

**Project Report
STK-254**

Proceedings of the 1999 Space Control Conference

**L.B. Spence
Editor**

13-15 April 1999

Lincoln Laboratory

MASSACHUSETTS INSTITUTE OF TECHNOLOGY

LEXINGTON, MASSACHUSETTS



Prepared with partial support of the Department of the Air Force
under Contract F19628-95-C-0002.

Approved for public release; distribution is unlimited.

DTIC QUALITY INSPECTED 4 1 9 9 9 0 4 1 6 0 2 6

This report is based on studies performed at Lincoln Laboratory, a center for research operated by Massachusetts Institute of Technology. The work was sponsored by the Department of the Air Force, AFSPC/DOY, under Contract F19628-95-C-0002.

This report may be reproduced to satisfy needs of U.S. Government agencies.

The ESC Public Affairs Office has reviewed this report, and it is releasable to the National Technical Information Service, where it will be available to the general public, including foreign nationals.

This technical report has been reviewed and is approved for publication.

FOR THE COMMANDER


Gary Tunungian
Administrative Contracting Officer
Directorate of Contracted Support Management

Non-Lincoln Recipients

PLEASE DO NOT RETURN

Permission is given to destroy this document
when it is no longer needed.

MASSACHUSETTS INSTITUTE OF TECHNOLOGY
LINCOLN LABORATORY

**PROCEEDINGS OF THE 1999
SPACE CONTROL CONFERENCE**

PROJECT REPORT STK-254

13-15 APRIL 1999

Approved for public release; distribution is unlimited.

LEXINGTON

MASSACHUSETTS

LEXINGTON

MASSACHUSETTS

PREFACE

The seventeenth Annual Space Control Conference sponsored by ESC and co-hosted by MIT Lincoln Laboratory and the AF Research Laboratory was held on 13, 14 and 15 April 1999. The purpose of this series of conferences is to provide a forum for the presentation and discussion of space control issues.

This *Proceedings* documents those presentations from this conference that were received in time for pre-conference publication. The papers contained were reproduced directly from copies supplied by their authors (with minor mechanical changes where necessary). It is hoped that this publication will enhance the utility of the conference.

Dr. Lee B. Spence
Editor

TABLE OF CONTENTS

A Mechanism for Evaluating Space Surveillance Networks <i>S.E. Andrews and R.C. Raup – MIT Lincoln Laboratory</i>	1
ALTAIR Radar Contributions to the Space Surveillance Network <i>G.F. Duff – MIT Lincoln Laboratory</i>	11
Performance of a Dynamic Algorithm for Processing Uncorrelated Tracks <i>K.T. Alfriend and Jong-II Lim – Texan A&M University</i>	17
Determining SSN operational System Capability (SYSCAP) <i>R.S. Daw – AFSPC/SWC/AES</i> <i>M.D. Hejduk – SenCom Corp.</i>	23
TELSTAR-401/Encounters with Telesat Canada Spacecraft <i>A.J. Grise – Telesat Canada</i>	35
Satellite Tracking Using Ambient RF (STAR) <i>M.F. Storz, W.M. Rezzonico, R.A. Racca and C.T. Krinsky – AFSPC/SWC</i>	39
Color Photometry of GEO Satellites <i>T.E. Payne & D.M. Payne – Schafer Corp.</i> <i>D.J. Sanchez – UPR</i> <i>S.A. Gregory – UNM</i> <i>L.G. Finkner and C.K. Davis – Boeing</i> <i>E. Caudill and L. Kann – AF Research Laboratory</i>	49
Ground-Based Imaging and Inspection of Commercial Satellites <i>L.A. Kann, D.G. Voelz and J.L. Kann – AF Research Laboratory</i> <i>J.M. Anderson – SAIC</i>	55
Active Lasing of Space Objects Using the HI-CLASS (High Performance CO ₂ LADAR Surveillance Sensor) Laser System <i>Capt. D.K. Werling, C.L. Matson, J. Gonglewski, S.R. Czyzak – Air Force Research Laboratory</i> <i>L.L. Crawford – Schafer Corp.</i>	63

Determination of Accurate Orbits for Close Encounters Between Geosynchronous Satellites	71
<i>R.I. Abbot and J. Sharma – MIT Lincoln Laboratory</i>	
Sequential Orbit Determination for the Catastrophic Decay of Object 13390	85
<i>R.S. Hujsak and J.F. Dicello – Logicon, Inc.</i>	
Relative Attitude Kinematics & Dynamics Equations and Its Applications to Spacecraft Attitude State Capture and Tracking in Large Angle Slewing Maneuvers	105
<i>G.Q. Xing, S.A. Parvez – Space Products and Applications, Inc.</i>	
Lincoln Near Earth Asteroid Research (LINEAR) Project: First Year Results	115
<i>H.E.M. Viggh, G.H. Stokes, F.C. Shelly, M.S. Blythe, M. Bezpalko</i>	
<i>J.S. Stuart, R.W. Sayer, C. Foo, K.S. Taylor – MIT Lincoln Laboratory</i>	
Haystack, TRADEX, TIRA/Effelsberg Radar Measurements of the Orbital Debris Environment During the 24-Hor Cooperative Beam Experiment, November 1996	131
<i>T.J. Settecerri – Lockheed Martin Space Operations Co.</i>	
<i>E.G. Stansbery – NASA/Johnson Space Center</i>	
NASA/JSC Optical Orbital Debris Program: Results from the Liquid Mirror Telescope (LMT) and the CCD Debris Telescope (CDT)	141
<i>J.L. Africano and J.V. Lambert – Boeing North America, Inc.</i>	
<i>T.J. Settecerri – Lockheed Martin Engineering & Sciences</i>	
<i>E.G. Stansbery – NASA/Johnson Space Center</i>	
Space Surveillance Operations with the Space-Based Visible	147
<i>Curt von Braun – MIT Lincoln Laboratory</i>	
Contributions of the Space-Based Visible Sensor to Catalog Maintenance	163
<i>J.G. Miller – The MITRE Corporation</i>	
<i>W.G. Schick – ITT Industries, Systems Division</i>	
SBV Uncorrelated Target (UCT) Processing	175
<i>G.R. Zollinger, J. Sharma, M.J. Lewis – MIT Lincoln Laboratory</i>	
SBIRS LOW Adjunct for Space Surveillance	189
<i>R.W. Sayer and G.H. Stokes – MIT Lincoln Laboratory</i>	

A Mechanism for Evaluating Space Surveillance Networks

S.E. Andrews and R.C. Raup
MIT Lincoln Laboratory

During 1997-98, MIT Lincoln Laboratory was tasked to support evaluation of future concepts for the US space surveillance network. The timeframe was for a network operating during the years 2005 to 2010. The DoD Office of the Space Architect had previously sponsored a broad study which included an evaluation of space surveillance concepts: our effort was to be a more focused follow-on study, with the particular charter to investigate the benefits of adding space-based sensors to the network mix. Col. Moulton, from the Joint Staff's, Sea-Air-Space Superiority Assessment Division, briefed the results of this mixed sensor study during the Space Control Conference held at MIT/LL last spring. This paper focuses on the mechanism used to perform the evaluation, which we believe may have utility beyond the study for which it was developed.

The first section of this paper provides background on the study itself, which defined both the boundaries for the network and the limits on the analysis performed for the study. The second section of the paper lists and describes the requirements on the evaluation system being used to support our analysis. The third section of this paper describes the mechanism in general, which is modular in design and versatile. The fourth and fifth sections describe specific aspects of the system (how scores are assigned to performance capabilities of a network and how the mechanism supports evaluation of the network in the context of different operating environments, respectively). The final section is a brief summary.

I. Background

The goal of the study was to identify and evaluate "realistic" space surveillance networks for the future, with particular emphasis on the trade-offs of using space-based sensors. The time frame set was the late part of the first decade of the new millennium, approximately 2005 to 2010. The term "realistic" was used to indicate that we focused on existing or demonstrated technologies, although some speculative systems were considered. Another aspect of the "realistic" networks was that we considered the transition path and its costs, rather than attempting to design completely new networks. To truly characterize the benefits and costs of space-based systems, we considered the range of possible networks from ones consisting of no space systems to ones comprising primarily space-based systems.

Among the things missing in the definition of the study was a set of defined requirements for this future network. We did not even have a defined view of the world scenario in which the network would be operating (e.g., high or low interest in ASATs, heavy or light involvement of government in commercial space, high or low population of man in space) to aid in the postulation of requirements. Given the significant changes in the political situation over the past ten years, assuming 'business as usual' was assessed to be a narrow-minded strategy. This missing component in the study definition had a significant impact on the design of our evaluation system, since it meant the system had to have sufficient flexibility to support evaluation of networks against a variety of possible futures.

We were able to leverage previous work done by Lincoln and by other organizations. As with most studies, there were constraints on the execution of our work. Both the available resources and the constraints affected our analysis plans.

We were able to draw heavily on the analysis from the study directed by the Space Architect's office in late 1996-early 1997. As part of this study, detailed cost analysis was performed on the majority of the existing and some of the proposed sensor systems, as well as some of the command, control and data processing functions. In addition, analysis was performed on the capabilities of some of the proposed sensor systems. Some of the work conducted for the SBIRS program was also useful to our work, as well as various studies on other sensor concepts.

Lincoln is involved in a variety of space surveillance areas, which has resulted in the availability of a variety of tools, data, and experience. We have large databases of observation data to support metric data and orbital

prediction accuracy analysis. We have a collection of simulation tools that overlapped the needs for this study. We have experience in the operations of a network. We have experiences with all aspects of operating a space-based space surveillance sensor (the Space-based Visible system on the Mid-course Space Experiment) and processing its data. The availability of tools, data, and experience affected the fidelity to which we could, and wanted to, evaluate a network.

We also received considerable support from personnel at USSPACECOM, AFSPC, and NAVSPACECOM. They provided input and comment on our analysis process, a requirements perspective, and some useful parameters. They and the Joint Staff were instrumental in providing some of our source documents.

Several constraints limited the scope of our work. The one with the greatest impact on the design of the evaluation system was that the study was scoped as a six month, 2 staff effort. This meant that we had to rely heavily on computing hardware and software already existing in-house. Software design was limited to simple programs and applications programs. This led to the choice of our evaluation system being designed as a Microsoft Excel application. The other major constraints on the study were a requirement to get consensus from the DoD space surveillance community on our approach and assumptions, and that we had to use published documents or new documents, as they became available. The former was useful, as well as being a constraint, since it resulted in community input to the process. The latter was an issue since there was on-going work on both the specifications of the SBIRS system and on a space control requirements review, and we wished to have the best available information for the study. In some cases, this meant being adaptable enough to accommodate late changes, in others it meant accepting that we could not wait for the newest results and still make our own deadlines.

Given the defined task, the support we received, and the constraints of the program, we were able to design an evaluation mechanism that provided a reasonable means for comparing one network to another and to an ideal. The tools we developed were manageable in a computational sense, but still allowed us to model network performance to a reasonable fidelity. They also supported evaluation against a range of requirement-sets, representative of the many different possible users and world-scenarios. The tool is extensible to higher fidelity modelling of the network and can take input from different simulators.

II. Requirements for Evaluation

The definition of the study, the constraints on it, and the support we received led to a set of requirements on the method of evaluating networks. These requirements can be divided into three areas: Input – what we needed to be able to handle in terms of cases, modelling, and parameters; Output – what we needed to be able to provide the study customer and reviewers; and Computing and Complexity – bounds on equipment, software, and fidelity of the analysis.

For input, there were three major requirements. The first is that we had to consider a reasonable selection of networks, enough that all the major network concepts were considered. The second was that the system had to capture the needs of the users of the network, including issues such as timeliness, data completeness, and data fidelity. The third is that we had to consider a reasonable range of potential operating environments for the network. An operating environment is the combination of the world socio-political-economic situation and the needs of the network users that define the network requirements.

For output, there were two major requirements. The first was that our method needed to produce a good scoring metric. It had to have a natural, or intuitive, feel (for example, a score as a number in the range from 0 to 100, with 100 being the best). It had to support comparison (for example, given two networks with numeric scores, the network with the higher score is better). The second requirement was that we had means to justify the final score. This supported three things: verification that the evaluation method was performing as desired; defense of our results; and review of the system parameters.

For the area of computing and complexity, there were three major requirements. The first was that the evaluation system provided a sensible balance between simplification and fidelity. We did not want a system so coarse-grained that subtle, but important, distinctions would be lost. We also could not afford, within the scope of our effort, to model every distinct detail. The second was that we were limited in software development time, and thus in the

complexity of the software. The third is that the system had to be computationally manageable, particularly from the standpoint of manual work.

III. General Evaluation Mechanism

This section provides an overview of the general mechanism we used to evaluate networks. Details are covered in Sections IV and V. There are two primary components to our evaluation mechanism. The first is a figure of merit system that follows the conventions of classical decision theory, given the assumption that user preferences are specified (i.e., how valuable it is to a user to have a certain capability, what the user's priorities are). This provides the base metric for comparing networks. The second is a system for easily allowing us to evaluate networks against the needs of a variety of possible operating environments. To evaluate every network for every operating environment of interest would be a burdensome task, and the system described reduces the manual and computer computational load. Note that network costs were considered in our analysis, but we chose to separate them from the performance-based scores. The cost aspect of our evaluation is not covered in this paper, however costs could have been treated in the same manner as performance parameters.

Figure 1 shows a flowchart of the evaluation process. For each candidate among the potential networks, the capabilities of that network are evaluated against a set of physical performance parameters. This process is independent of user preferences, since the set of parameters can include all anticipated needs. The scoring process assigns values to each capability and blends them to yield a single numeric score. This process takes the operating environment into account. A network is scored separately for each operating environment in the operating domain, which is the set of all possible environments anticipated for the study timeframe. For purposes of discussion, the term 'performance parameter' means the criterion against which performance is measured (e.g., how fast, how many, how accurate). The term 'capability' refers to the number (or other indicator) representing the network's actual performance in that parameter (e.g., 5 minutes).

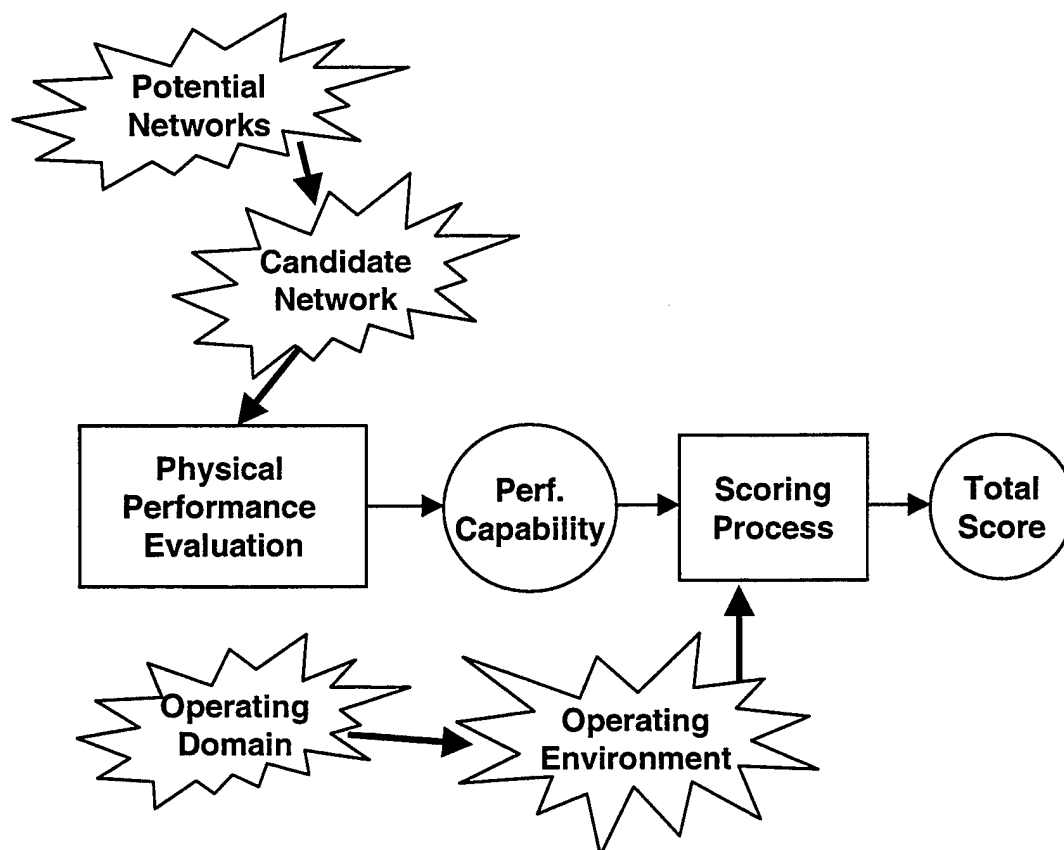


Figure 1 Flow of Evaluation Process.

The set of physical performance parameters used for the evaluation are based on existing or proposed requirements (e.g., task must be performed in n minutes). These are converted to measures on system capability (e.g., how fast can the specific task be performed?). For each performance parameter, every possible capability has a value assigned to it (e.g., assign a value of 5 to the fastest time of completion a specific potential user might desire, a value of 0 to a performance that would be unacceptable). Weights are also assigned that reflect the relative importance of one performance criterion to the others. Both the value and weight assignments are based on the specific user environment. For a given operating environment and performance parameter, the 'value function' specifies the value for each input performance capability appropriate to that environment. Similarly, for a given operating environment, the 'weight set' is the set of weights on parameters, as appropriate to that environment. The total score is formed by summing the weighted values assigned to the performance capabilities of the network. Performance parameters, value functions and weights are discussed in more detail in Section IV.

By separating the physical performance evaluation from the scoring, the network capabilities can be evaluated one time and different value and weights applied to the results to support evaluation of the network's merit in different operating environments. This modularization of the problem reduces some of the computational burden. To specify values and weights for each operating environment is a large and difficult task, however, and the multi-environment assessment technique we developed was designed to reduce the level of this task.

The concept behind this technique is that we can define the domain of possible operating environments for the years 2005 to 2010 by a set of independent factors. Each operating environment is then specified by the level to which each of these factors is relevant. The definition of the domain in this manner allows us to specify a set of functions that lets us calculate values and weights for any operating environment from the weights and values on a small set of specific operating environments. For our study, we characterized the possible operating environments by the four factors "Military Awareness", "Military Action", "NASA", and "Commercial". To illustrate the concept, we will consider the first three.

Military awareness represents the military's interest in knowing what is in space. The ideal case is to know everything about every space object in sufficient time to use the knowledge for its intended purpose. This is non-confrontational; acquisition of information is the key goal.

Military action represents the military's interest in using space-surveillance data to support actions such as deception, disruption, and destruction. Real-time data or near-real-time data might be required for targeting. Military awareness and military action were considered to be "independent" because we could envision situations in which the military was heavily monitoring space to support political activities and peaceful actions (deception and denial), but that there would only be a low level of military action involving space operations. While a high level of military action with a low level of military awareness seemed less likely, we could also envision a situation in which monitoring had been allowed to decrease and a sudden crises required quick military action based on the limited awareness data. To first order, the independence assumption was reasonable.

NASA represents US scientific activity in space. It includes the peaceful use of space for manned missions, which is a driver for many of the debris concerns. Science missions are expected to include prototype systems and non-redundant systems. It is possible to envision worlds with any combination of military and scientific activity, so the NASA factor is independent of the military ones.

Characterized in this way, the operating domain has a graphical representation, as shown in Figure 2. Each factor is represented by a coordinate axis. For a defined period of operation, we can define the extreme cases for each factor, and thus limit the operating domain to a hypercube (arbitrarily scaled to $[0,1]$ in each dimension). Each operating environment is then represented by a point in the hypercube. If, for example, we had an environment with moderate military awareness, low military action, and moderate scientific activity, the environment might be represented by the coordinate (0.5, 0.2, 0.5). Note that the sum of the component factors for an environment do not have to equal 1, this is not the relative component of each factor but the absolute amount of each. If military awareness, military activity, and US scientific activity are all high, the coordinate would be (1.0, 1.0, 1.0), which does not represent the same environment as the coordinate (0.33, 0.33, 0.33).

To determine the value functions and weights for a specific operating domain, value functions and weights are specified for the environments at the extreme points on each axis (i.e., at the 1's in Figure 2). These are the extreme environments where one factor is at the extreme and the other factors are not evident. We then use a combination rule to determine the weights and value functions for any other operating environment in the domain. The rule is described in more detail in Section V, but it balances the network needs due to the most demanding factor, the level of that factor in the environment, and the needs due to the other factors.

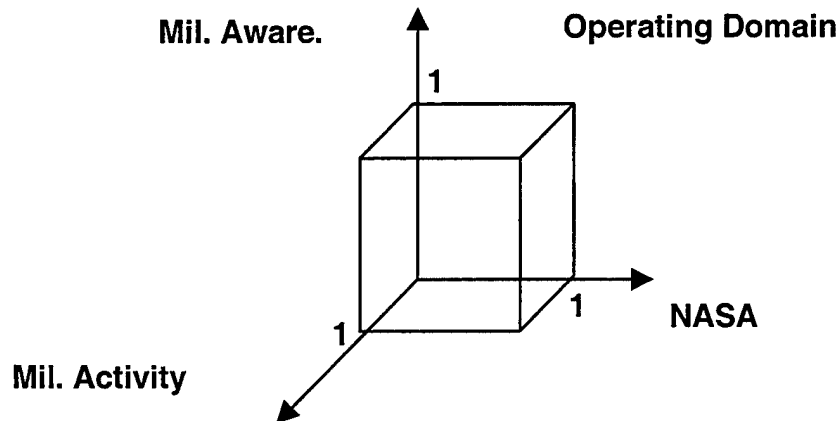


Figure 2 Example Graphical Representation of Operating Domain

IV. Scoring Performance

This section provides details on scoring a network, given a specified operating environment. How performance parameters are developed and used is covered first. How values are assigned to performance capabilities is covered second. Weighting of the scores on individual parameters is covered last.

The parameters for evaluating network performance are based on existing and potential requirements. Requirements consist of two components: a measurable quantity of network performance in some area and a threshold on that quantity. For example, one requirement might be that the maximum time for an object to be detectable is less than n minutes. A performance parameter is the measurable quantity (for example, the max time for an object to be detectable after an event). Note that having more requirements than necessary for a given operating environment is not a problem, since the impact of the network's performance against any parameter can be zeroed out in the weighting process. Cost can be included as a distinct parameter in this evaluation system, but we did not do so in our study.

To support assignment of values to different performance capabilities, we determined upper and lower bounds on each numeric performance parameter. These bounds were chosen to reflect the most stringent requirement that might be anticipated and the least stringent requirement that might be anticipated (i.e., the value of the toughest and easiest thresholds). In cases where we could envision that a network might be more valuable for exceeding a threshold than just meeting the toughest possible one, the boundary on the parameter was extended. Table 1 shows an example of some of the parameters we used and hypothetical bounds.

For every parameter, a specific user will have their own assessment of the value of a network performing to a certain level. This is captured by a value function, which assigns a numeric value to each level of a performance between the maximum and minimum bounds established earlier (functions can also assign values to non-quantifiable performance capabilities, such as the regions of space a network covers). The value functions for all parameters have the same maximum and minimum values (e.g., value of 5 is always best, 0 is always worst). Therefore, the set of value functions converts a set of performance measures with different units and scales to a set of consistent numeric measures, with best and worst always represented by the same pair of numbers.

Note that the value function on a parameter does not always have to be a simple scaling function. Twice as fast is not necessarily twice as good to a specific user. Similarly, the value function does not have to increase for increasing numeric performance capabilities. For example, if the parameter is a measure of time where faster is better, a higher value is assigned to a lower number of minutes.

Table 1 Parameters and Their Bounds

		NEAR EARTH (LEO)			DEEP SPACE		
Param Type	REQUIREMENT	UNIT	MIN	MAX	UNIT	MIN	MAX
<i>ACQUISITION TIMELINESS</i>	Maximum time for object detectable after event	min	0	600	min	0	2000
	Maximum time to cover visible LEO orbits	min	30	1440			
	Probability of finding min-size object in 24 hours	none	0.5	1	none	0.25	1
	Time to collect data for short-term orbital parameters	min	5	600	min	10	2800
	Maximum time to detect event under std operations	min	10	600	min	0	2000
	Maximum time to cover GEO belt				min	90	4320

The value function for a parameter is specific to the operating environment for which the network is being evaluated. It represents the increase in value to improving performance and the maximum and minimum relevant performance values.

Figure 3 shows a sample value function, where the parameter is the probability of detecting a LEO object in twenty-four hours. Both the lower and upper requirement bounds are shown, and they are given values of 0 and 5 respectively. The value for a 95% probability network is shown, as well.

To reduce the complexity of the process of developing value functions for the full set of parameters, we chose a set of eight representative function classes to cover the primary types of valuations. Four of the function classes increase with increasing numeric performance, and the other four are mirror images of the first. One is a step function, representing a hard threshold. One is a simple linear scaling (adjusted with a constant and negative scale factor for the increasing value with decreasing performance number cases). One function increases rapidly from the number representing the least stringent bound and levels off near the most stringent bound, representing environments where lesser performance is acceptable. The final function increases slowly from the number representing the least stringent bound and rises quickly near the most stringent bound, representing operating environments where performance has to be near the best possible to satisfy the needs of the users. Figure 4 shows the eight functions, where the negative signs indicate the functions with an inverse relationship. These eight provide a base sample of the variety of functions that can be used. Much more complex functions may be appropriate for certain cases

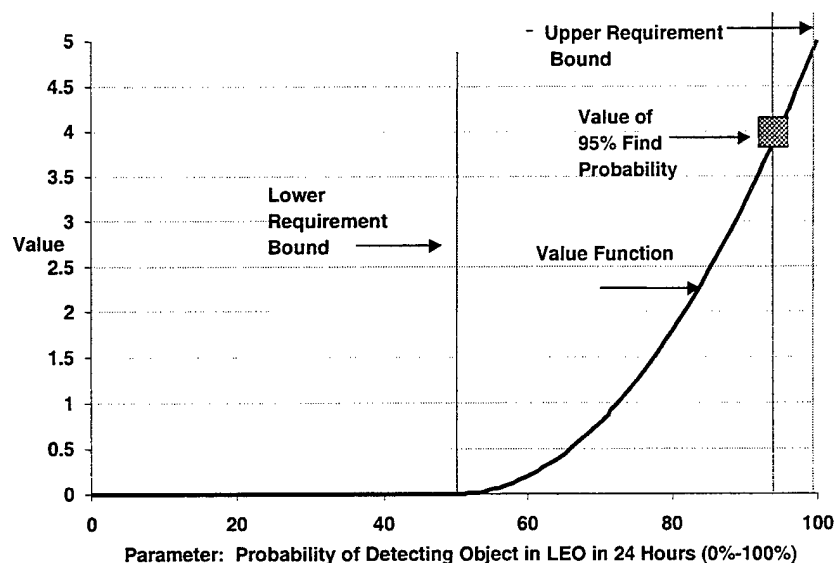


Figure 3 Value Function Example

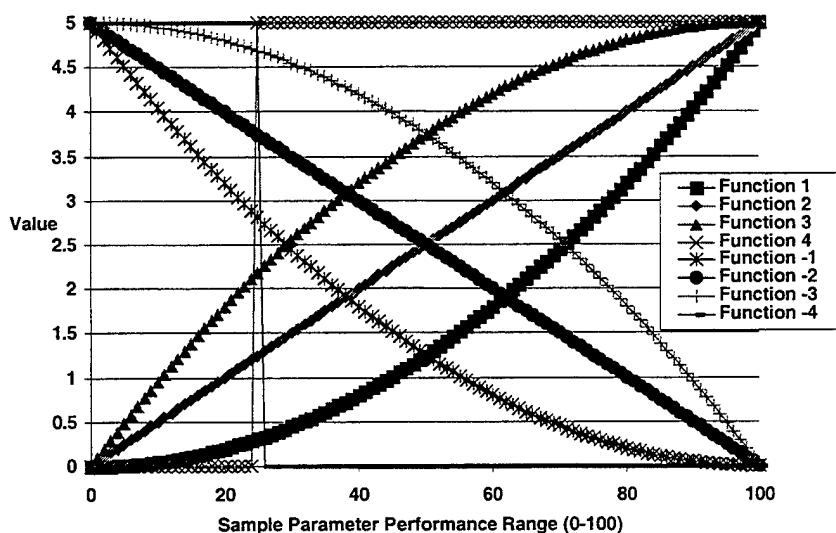


Figure 4 Nominal Value Function Set

The next stage of the process is to weight and sum the performance values to obtain a network score. Value functions convert a set of physical performance capabilities into a set of unitless numbers, all on the same scale. These sets of performance values support detailed evaluation of a network, but do not give a clear sense of which of two networks is better. To do such a comparison, it is easiest to have a single number that combines the information from the individual performance values. One effective way to combine the performance values is a weighted sum of the values. This not only creates a single measure on the network, but the weights are used to modify the impact of a performance parameter on the total score in proportion to the relative importance of that parameter to the network. Not all performance parameters are equally important, and a parameter that is half as important in an operating environment will be given half the weight.

As with the value functions, the weights are a function of the operating environment. For example, the military may place a high priority on having a high fidelity element set on active payloads and a lower priority on collecting data on small objects while NASA might place a high priority on characterizing the debris environment in the regime of the shuttle or space station and a lower priority on regularly having high fidelity element sets. Note that the coupling between the value function for a parameter and the weight is weak. A very important parameter might also require only a weak performance to satisfy the user needs for an environment. Similarly, a task for which it is difficult to suit user needs may not be important in the overall network performance.

IV. Dealing with Different Operating Environments

This section describes the mechanism for determining the value functions and weights for any operating environment using the value functions and weights for a small set of operating environments in the operating domain.

Recall the representation of the operating domain as a graphical space with axes corresponding to independent factors that define the domain. We considered four factors in our study, a military awareness component, a military activity component, a NASA component, and a commercial component (this last will be ignored for ease of representation). Figure 5 shows the graphical representation of the first three, along with the coordinate representation of a selected operating environment within the domain.

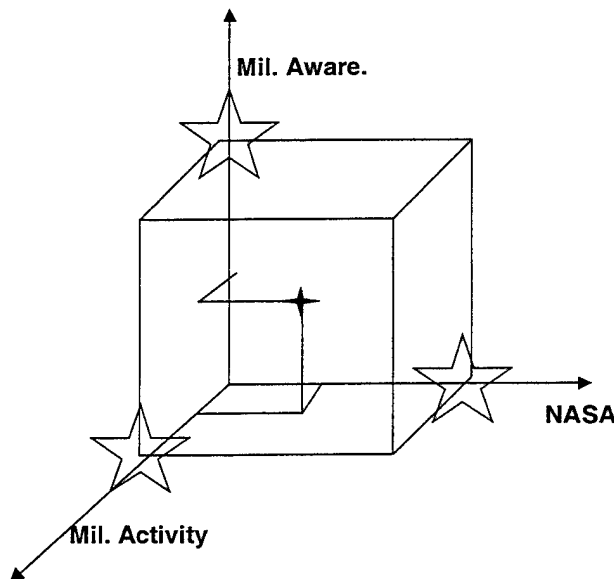


Figure 5 Sample Operating Domain with Selected Operating Environment at (0.6, 0.5, 0.5)

The following is the process for developing value functions and weight sets for any environment in an operating domain with M factors: Note that Step 3 can be done independently of the pair 4 and 5.

- 1) For each extreme point of each factor, i , (as represented by the stars at coordinates $\{0, 0, 1\}$, $\{0, 1, 0\}$, and $\{0, 0, 1\}$ on the graph) define the set of value functions, $(v_{i1}(c_j), \dots, v_{iN}(c_j))$ and weights (w_{i1}, \dots, w_{iN}) for the corresponding environments. The value $v_{ij}(c_j)$ represents the value a network, k , has for capability c_{kj} in parameter j (of N possible) in extreme environment i . The number w_{ij} is the weight on parameter j for environment i . These are the environments for which one factor is at its strongest possible and the others are not evident. For example, the extreme military awareness environment might be one where NASA has ceased operations in Earth-orbit space, the US has decided on a policy of no weapons against satellites, and the military wants near perfect knowledge about all satellites in Earth-orbit. Figure 6 shows the value functions used for the numeric example.

- 2) For the selected operating environment, determine the level of each factor. This is equivalent to determining the coordinate in the graphical space. Let x_i represent the level of factor i in the environment (equivalently, the factor i coordinate of the operating environment in the graphical representation).
- 3) Combine value functions according to the combination rule below.
- 4) Sum the coordinates for the operating environment and for each coordinate, determine the ratio, r_i , of the coordinate to the sum, $r_i = x_i / \sum_i x_i$.
- 5) The weight on each parameter, j , is the sum of the products of the weights, w_{ij} , for the extreme points times the ratio for the coordinate, or $\sum_i r_i w_{ij}$.

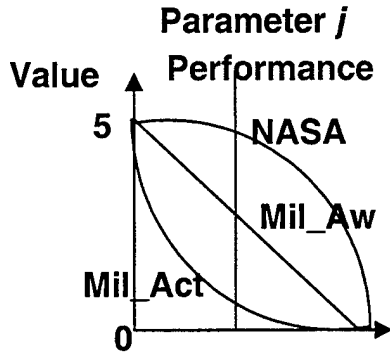


Figure 6. Value Functions for Example, for Parameter j

The combination function for value functions is one that takes the most stringent factor into account (the one that yields the lowest value for a given performance), in proportion to the level of the factor in the environment. Since there may only be a limited amount of the most stringent factor in the environment, other factors are taken into account as a function of their relative value for a given performance and the level of that factor in the environment. Note that the combined value for a given level of performance is not a linear combination of the values for the component factors. If, for example, the environment has 100% of the most stringent factor for a value for a given performance, then the combined values is equal to the most stringent value. Also note that the value function resulting from the combination is determined from the component functions on a point-by-point basis (with respect to capability, c).

The function that accomplishes this is presented below, using the notation described in this paragraph. A four-factor example is also given. Recall that $v_{ij}(c_{kj})$ represents the value a network has for capability c_{kj} in parameter j in extreme environment i , and select a specific c_{kj} . Without loss of generality, we can assume the values are ordered so that for $s < t$, $v_{sj}(c_{kj}) < v_{tj}(c_{kj})$. Thus, for increasing i , the operating environments become less stringent. Note that for $c_{uj} \neq c_{kj}$, which factor is most stringent may change. Therefore the new value function must be determined point-by-point over the range of possible capabilities unless the value functions for the extreme environments do not cross. Let v_{\max} represent the maximum possible value for a value function (the minimum is 0). Let v_{comb} represent the combined value. Let d_i be the discount, which is the amount the factor influences the combined value as a function of the level of that factor and the level of the more stringent factors.

$$v_{\text{comb}}(c_{kj}) = v_{\max} - \sum_i x_i (1 - d_i) (v_{\max} - v_{ij}(c_{kj}))$$

where $d_1 = 0$ and

$$d_i = d_{i-1} + x_{i-1} (1 - d_{i-1}) \quad \text{for } i = 2, \dots$$

For the four-factor case and a given capability, c_{kj} , let v_{ij} represent $v_{ij}(c_{kj})$. The combination function becomes

$$v_{\text{comb}} = v_{\max} - x_1(v_{\max} - v_{1j}) - x_2(1 - x_1)(v_{\max} - v_{2j}) - x_3(1 - x_1 - x_2(1 - x_1))(v_{\max} - v_{3j}) \\ - x_4(1 - x_1 - x_2(1 - x_1) - x_3(1 - x_1 - x_2(1 - x_1)))(v_{\max} - v_{4j})$$

Table 2 shows some example cases for the value function assessments of Figure 6. The first three rows show the value functions for the factor extreme points. Note that the value when all factors are at their maximums is equal to the value for the most stringent factor extreme. Note also that the value for the case in which all factors are at 50% is not the same as the value when all factors are at 100%, even though the relative contribution of the factors is the same. This is sensible since the 50% case indicates a case when there are fewer and easier demands on the network. Finally, note that the value for the case in which all factors are at 50% is lower than the value when only the most stringent factor is at 50%. This represents the increased demands of multiple 'users'. Note that it may be easier to determine the combined value functions for only those select capabilities that correspond to evaluated network performances than to determine the combined value function for the full range of possible capabilities.

Table 2: Examples of Values Resulting from Combination Function

Component Contribution			Value
Mil_Activity	Mil_Awareness	NASA	
100%	0	0	1
0	100%	0	2.5
0	0	100%	4
0	0	0	5
100%	100%	100%	1
0	100%	100%	2.5
50%	0	0	3
50%	50%	50%	2.25
60%	50%	50%	1.9

V. Summary

To support evaluation of space surveillance networks for a space surveillance network 'mix' study sponsored by the Joint Staff, we created a computationally reasonable tool for providing numerical network scores. While designed for the specific study, the tool's modular design would allow it to support other studies. With this tool, it is easy to add, subtract and revamp requirements. Different fidelities of simulation and evaluation can be performed.

The modular design has other benefits. Raw performance is separated from merit, and capability values are assessed separately from the weights that combine capability assessments into a single score. This supports analysis of the final score, since the components can be investigated. Different scoring functions and weights can be applied, but the network need only be analyzed for performance once.

This problem differed from those typical for classical decision theory in that the requirements and preferences of the network's users are largely unknown. Assembling individual weight and value sets to represent the breadth of possible operating environments would be prohibitive. We developed a mechanism for generation of a value and weight set for any environment based on the sets for a few specified environments. This mechanism in combination with the separation between network performance evaluation and network scoring allows for easy evaluation of the different operating environments of the different possible world futures.

Kwajalein Missile Range ALTAIR Radar Contributions to the Space Surveillance Network

Gary Duff
MIT Lincoln Laboratory

Abstract

The Kwajalein Missile Range (KMR) has four contributing sensors in the Space Surveillance Network: ALTAIR, ALCOR, MMW and TRADEX. The workhorse of these radars is ALTAIR, which performs the space surveillance mission 128 hours a week. The mission areas supported by ALTAIR are as follows:

1. New launches: ALTAIR was tasked by Space Command to provide support on 76 of the world's 86 space launches during FY98.
2. Support the warfighter: metric and SOI data provide Space Command with situation awareness.
3. Manned space flight missions: high metric accuracy supports rendezvous missions.
4. Conjunction tracks: tracking of resident space objects that pose potential threats to manned space flights.
5. Reentering objects: provide precision metrics during last hours before reentry.
6. Catalogue maintenance of deep space resident space objects: performed 37,752 tracks on deep space resident space objects in FY98, objects with a period of greater than 225-minutes.
7. Special space surveillance missions: supported the Space Improvements Program, interplanetary flybys, meteor shower activity and other special missions.

ALTAIR's near equatorial location, which is less than 30-minutes down-range of the Russian, Chinese, Japanese and potential Korean space launch sites, enables early detection, tracking and identification of new space launches from these countries. In addition, ALTAIR is well situated for tracking objects with low inclination. The world's busiest commercial launch site, Kourou in French Guiana, is located at 5° latitude and new launch sites with near equatorial locations are being constructed. ALTAIR is the only radar capable of tracking many of the objects associated with these launches.

Introduction

The Space Surveillance Network (SSN) consists of 23 sensors located around the world. There are three different types of sensors: radars, passive radio frequency (two are deep space, called the Deep Space Tracking System (DSTS), and two are near earth called Low Altitude Space Surveillance System [LASS]), and optical sensors. Maintaining current element sets on the almost 10,000 objects in the Space Control Center catalog is a challenging task. It is even more challenging to maintain element sets on the approximate 2,560 objects in deep space orbits, given the shortage of SSN resources. There are

five optical sensors (three GEODDS, TOS and SBV) that provide the majority of deep space metric observations to support catalog maintenance. Ground based optical sensors are limited to night operation, clear skies and to time intervals when satellites are illuminated by the sun. SBV is a space based optical sensor not limited by day/night or weather. However, commanding the satellite must be done at least 12-hours in advance. The data collected must then be downloaded to a ground station one to several hours after the data is collected. These limitations prevent optical sensors from

supporting high priority events such as launches and maneuvers. High priority events are typically tasked only to radars. There are four deep space radars in the network: ALTAIR, TRADEX, Millstone, and the FPS-85 at Eglin. ALTAIR, located near the equator in the middle of the Pacific Ocean, is frequently tasked for high priority tracks.

ALTAIR Overview

The ALTAIR radar, (Figure 1), is one of four SSN radars located at the Space and Missile Defense Command's United States Army Kwajalein Atoll; ALCOR, MMW and TRADEX are the other three. The ALCOR and MMW radars are used exclusively for the collection of Space Object Identification (SOI) data in their space surveillance roles. The role of TRADEX has been to backup ALTAIR. The ALTAIR radar performs 128 hours a week of dedicated space surveillance. During the remaining 40 hours, ALTAIR is subject to a 15-minute recall for SSN Category 1 tasking.

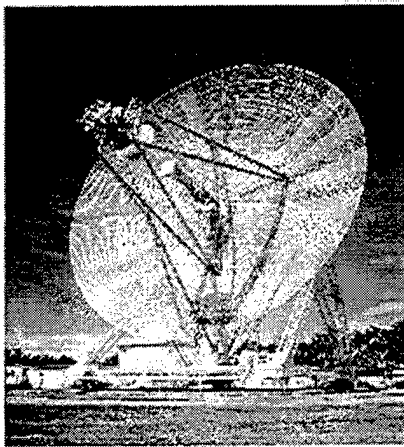


Figure 1. ALTAIR Radar

ALTAIR is a dual frequency radar (VHF and UHF) producing 12 megawatts of peak power, 6 megawatts in each frequency. The antenna is 150 feet in diameter and weighs 450 tons. Deep space tracks are performed with the UHF frequency only. Near earth tracks are performed with both frequencies. The range accuracy of the dual frequency, near earth tracks is better than 5 meters, making ALTAIR one of the most accurate sensors in the network. A new method for ionosphere correction used with the deep

space system was incorporated this year. A GPS receiver is used to measure ionosphere delays. This has improved the range accuracy on deep space metric observations from approximately 100 meters to approximately 25 meters.

During FY98, upgrades were completed giving ALTAIR additional capabilities with the VHF system. New capabilities include the ability to change frequency pulse-by-pulse between 154.5 and 161.5 MHz, and to transmit left/right circular, 45°/135° linear within the same pulse. ALTAIR users are currently utilizing these upgrades.

Funding for 128 hours a week to support space surveillance is provided by U.S. Army Space Command. Users of the radar include AFSPC 1CACS, AFSPC HQ/DOY, USSPC SCC, USSPC J2/CIC, NRL, and NASA.

ALTAIR's primary tasking is on deep space objects. In addition to the 37,752 deep space tracks performed during FY98, ALTAIR also performed 3,462 near earth tracks.

New Launch Support

ALTAIR was tasked on 76 of the world's 86 attempted space launches in FY98 (Table 1). Five of the planned launches failed to achieve orbit. Support was provided for 71 of the 81 launches that did achieve orbit. ALTAIR was the first radar to track 41 of the world's space launches in FY98.

ALTAIR's location is one of the reasons it is so important to the SSN. Located near the equator, at 9° latitude, ALTAIR is less than 30-minutes downrange from the Asian launch sites (Russia, China and Japan).

ALTAIR is the first sensor in the network with visibility of all the world's synchronous launches in their deep space transfer orbits. It has visibility of most injections into synchronous orbit.

In the case of a Russian synchronous launch, ALTAIR tracks the complex in its parking orbit 25 minutes after launch. Two hours after launch, ALTAIR is the first sensor to track the complex in its transfer orbit; ALTAIR observes the 4th-stage burn and the separation and injection of the payload into a synchronous orbit at the first apogee of the transfer orbit.

The world's busiest commercial launch site is the European Space Agency site located at 5° latitude in Kourou, French Guiana. ALTAIR is the first SSN sensor to observe all deep space launches from Kourou in their deep space transfer orbits. New, low latitude, launch sites will soon be active, such as Boeing's Sea Launch. ALTAIR is well positioned to track low inclination satellites and associated debris from these launch sites.

Launch Country	Total Launches FY98	ALTAIR Supported	ALTAIR support within 30 min. of launch
ESA	10	9	
Japan	3	3	3
China	7	5	3
Russia	28	27	13
US	33	27	
Total	81	71	19

Table 1. FY 98 Space Launches

The FY98 space launch activity reflects the changes taking place in the world today. Russian and Chinese launch vehicles are placing western payloads into orbit. Western launch vehicles are placing Russian payloads into orbit, such as the Bonum-1 payload. There are a number of data collection satellites, such as Helios, Landsat, and Spot, that sell the data on the open market.

These changes present challenges, as payloads must be identified and monitored. ALTAIR collects metric data and space object identification (SOI) data on new launches. The metric data tells where a satellite is; SOI data tells what the satellite is (payload, rocket body or debris). The metric and SOI data are transmitted to Space Command within five minutes after a high priority track is completed. Providing this information in a timely manner to Space Command is critical, especially during times of crisis.

Support to the Warfighter

The world realized the importance of space-based assets during the Gulf War in 1990. Our next adversaries are sure to attempt to disrupt use of these assets and use their own. Control of space must be maintained to assure access to space, maintain freedom of operations, and deny use of space to the enemy. Surveillance,

negation, prevention and protection are the mission areas that will make this possible.

ALTAIR supports the surveillance and negation missions by providing situation awareness of the ever-changing space environment. This can only be accomplished by knowing where objects are in space and what they are. ALTAIR provides metric observations and SOI data on over 75% of all Asian launches before they are catalogued. Radars are the only sensors to provide metric data ("where satellites are") and SOI data ("what satellites are") in all weather conditions, 24-hours a day. The information is sent to Space Command where reports are generated, such as the Space Order of Battle and SATRAN reports. These reports are transmitted to the Warfighter in the field (Figure 2). The Warfighter can use this information to protect against over-flights by reconnaissance satellites. Space Command also uses this information to put additional sensors on the payloads.

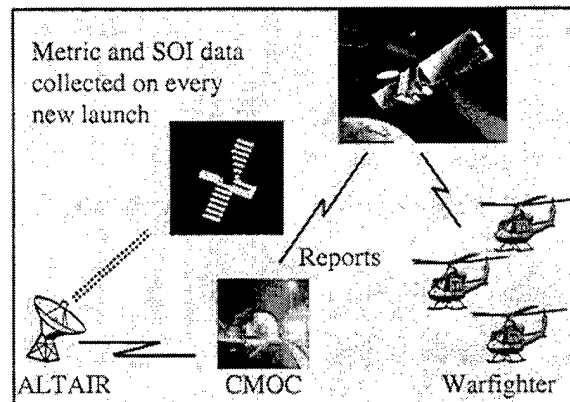


Figure 2. Support to the Warfighter

Reentering Objects

The decay time and location of decaying objects with high eccentricity orbits (eccentricity greater than .1) are difficult to predict. Many of these objects are large and dense, such as rocket bodies, SPELDA units and auxiliary motors that could survive reentry and cause damage upon impact. The SSN has limited resources to track these objects. In some cases, ALTAIR has been tasked Category 1 for every pass for up to 25 days on low inclination decaying objects. During the final days of decay, objects are often many minutes off their element set. ALTAIR uses its 75° scan, as shown in Figure 3, to locate these objects. The scan is designed to search large volumes of space, detect and characterize all

objects passing through the scan fence, and acquire objects that meet specified parameters. The scan is ideal for finding objects whose location is uncertain.

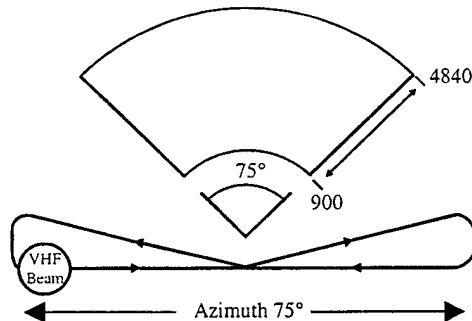


Figure 3. ALTAIR 75° scan

Manned Space Flight Mission Support - ALTAIR supports three aspects of manned space flight missions:

1. Early orbit determination.
2. Rendezvous missions.
3. Conjunction analysis.

Early Orbit Determination & Rendezvous - Shuttle launches are typically tasked Category 1 to ALTAIR. ALTAIR provides metric observations for early orbit determination.

ALTAIR's range measurement accuracy is of great value to Space Command when they need to maintain orbits on closely spaced objects. These include the Shuttle and MIR rendezvous missions, ISS construction support, and the release and retrieval of objects from the Shuttle.

Conjunction Analysis - Space Command looks for conjunctions between manned space missions and objects in the space catalog. Resident space objects with an element set age between 5 and 30 days that pose a potential threat to manned space systems are tasked to the SSN. The SSN success ratio for locating the objects on this list was less than desirable. A test was conducted at ALTAIR during the STS-89 / MIR rendezvous mission in January 1998 to demonstrate the contributions it could make in this mission area. ALTAIR's success ratio during this test was 53%, successfully tracking 65 of the 122 tracks attempted. Most of the objects tracked by ALTAIR were in highly eccentric orbits with low perigees.

On 12 June 1998 at 0130z, four hours prior to the reentry and landing of STS-91, ALTAIR was called out of antenna maintenance to track a SL12 auxiliary motor that was predicted to penetrate the shuttle protection box. ALTAIR tracked the auxiliary motor for 90 minutes. A decision was made, based on the high quality of ALTAIR's metrics, not to maneuver the shuttle and let the crew sleep in preparation for landing. The SL12 auxiliary motor was in a highly eccentric orbit.

Catalogue Maintenance - Tasking is received daily via a Consolidated Tasking List (CTL) generated by the 1st Command and Control Squadron at the Space Control Center. The CTL requests approximately 200 tracks a day. ALTAIR performed an average of 113 tracks per day during FY98. Even though the CTL-tasked objects are all Categories 1 or 2, higher priority real-time tasking is often received from U.S. Space Command via auto-tasking, forced tasking or by phone. This tasking takes priority over the CTL tasking.

During FY98, ALTAIR provided over 339,000 deep space and over 69,000 near earth metric observations to the SSN. The total number of tracks was 37,752 for deep space and 3,462 for near earth.

ALTAIR has coverage of over one third of the synchronous belt, between 90° and 240° East longitude. The synchronous belt has a number of areas where satellites are closely spaced. When ALTAIR points to one of these areas, more than one satellite often appears in ALTAIR's beam. These closely spaced satellites are called clusters. There are eight clusters in the synchronous belt in ALTAIR's coverage. Space Command dictates that when one object in the cluster is tracked, they all must be tracked. This is the only way to keep from confusing the satellites. Since all satellites have movement, the best time to track satellites in clusters is when they are farthest apart. Tracks on cluster satellites are scheduled at the times of greatest separation.

Special Space Surveillance Mission - ALTAIR often participates in unusual space surveillance activities, outside of normal tasking from Space Command. Three examples are Surveillance Improvement Program campaigns, the Hughes lunar flyby, and the Leonids meteor shower.

Surveillance Improvement Program - ALTAIR performed three data collection campaigns for the Surveillance Improvements Program (SIP) in FY98. SIP is a multiphase program designed to collect multi-spectral signature data on various satellites for Air Force Space Command. The collected signature data are used to evaluate space surveillance technologies and data analysis techniques.

Earth Flyby of Hughes Global Services (HGS-1), on 2 June 1998 - The Asiasat-3 satellite was launched on a Russian Proton launch vehicle on 25 December 1997 from the Baikonor Cosmodrome. The failure of the 4th-stage rocket body to inject Asiasat-3 into a synchronous orbit left it in an unusable 320 x 36,000-km transfer orbit. The original owner of the spacecraft, Asia Satellite Telecommunications Co. Ltd. of Hong Kong, received an insurance claim, as the insurers declared the spacecraft a total loss. Hughes Space and Communications Co. builders of the HS 601HP model satellite, salvaged the spacecraft. The spacecraft has been renamed Hughes Spacecraft (HGS-1).

The salvage mission used the moon's gravity to reposition the satellite into a geosynchronous orbit. Two orbits of the moon were completed. The first orbit occurred 14 May. ALTAIR, Millstone and a number of optical sites provided data on the first earth flyby.

HGS-1 made its second earth flyby on 2 June 1998. ALTAIR was the only SSN sensor to track the HGS-1 payload. The HGS-1 flyby was also tasked to five optical sensors as Category 1. Due to weather and time of day constraints, no optical data was collected. This highlights the importance of radars when timely data is needed. It should be noted that Millstone did not have visibility of this pass, and therefore was unable to collect data. The satellite is now in a useful orbit, catalogue number 25126.

Meteor Shower Support - To investigate the support ALTAIR could provide on the Leonids meteor showers in November 1998, data were collected on the Perseids meteor shower on 13 August. ALTAIR collected VHF meteor head-echo and trail data. Approximately 20 meteor hits per minute were observed. The data collected included position and signature data, which allow RCS determination. Doppler shift/spread, and ionized trail characterization

can also be determined. From this test it was concluded, ALTAIR could provide useful on the Leonids meteor storm.

On 18 November 1998, ALTAIR participated in a data collection effort to characterize the Leonids meteor storm. ALTAIR collected both VHF and UHF data at low elevations and also when the radiant was at its highest elevation (~77 degrees). Both on- and off-radiant data were recorded. ALTAIR recorded 11 periods of meteor activity, totaling 26GB of data. Although the storm did not reach the expected peak conditions, ALTAIR was successful in collecting head echo and trail data. Preliminary results indicate much stronger returns and longer trail duration. The head echo count varied, but more than one per second was observed during various periods.

Summary

The importance of a sensor can be measured in many ways. The number of metric observations collected and the number of tracks performed are two commonly used measures. These metrics do not adequately measure ALTAIR's contributions. ALTAIR's importance to the SSN is apparent when one examines the number of high priority tasks performed. During FY98, ALTAIR:

- Performed an average of over nine category 1 tracks per day (a total of 3,429).
- Supported 71 of 81 new launches within two hours after the launch, before they were catalogued.
- The first sensor to track 41 new launches.
- Tracked many decaying objects in their last hours of decay.
- A major contributor in supporting manned space flight conjunction tracks.
- Supported the development and testing of future technologies and analysis techniques.
- Provided 24-hour a day, all weather support on high priority events for both near earth and deep space activities.

Acknowledgment

A tribute is made to the many members of the ALTAIR team who maintain and operate the radar.

Performance of a Dynamic Algorithm For Processing Uncorrelated Tracks

Kyle T. Alfrend[‡]
Jong-Il Lim[†]

Tracks of space objects that do not correlate to a known space object are called uncorrelated tracks (UCTs). The association of UCTs to develop an ephemeris, and subsequently a new catalogued object, has typically been a manual process which requires significant time by the analysts. The algorithm used for track association is a static algorithm in that it does not directly take into consideration the uncertainties in the ephemerides determined from the individual tracks. In this paper a previously developed dynamic algorithm based on the track uncertainty (covariance) is evaluated. This dynamic algorithm is based on two new properties: a) The volume of the equiprobability ellipsoid is constant in time, even though the shape changes, and b) The probability of association is maximized by using this ellipsoid for association.

INTRODUCTION

There are currently about 9000 objects in the Space Catalog whose ephemeris is maintained by USSPACECOM. The sensors of the Space Surveillance System are tasked daily to track these objects. (The NAVSPASUR fence does detect objects but obtains observations, not a track.) When one of the sensors detects an object it checks to determine if the object is in the space object catalog¹. If it is in the catalog, and if the sensor has been tasked to track it, a set of observations (a track) is obtained. If it is a catalogued object which the sensor has not been tasked to track, then the object is not tracked. If it is not in the catalog, it is tracked. All observations are then passed to the Space Surveillance Center (SSC) denoting whether or not the object is a catalogued object. At the SSC another attempt is made to correlate the track with objects in the space catalog. The association algorithm is a position comparison. The two ephemerides are propagated to the same epoch and a rectangular parallelepiped is constructed about the estimated position in the radial, in-track and out-of-plane directions. If the two objects are in the box then the objects correlate. (There are different degrees of association that will not be discussed here.) If the tracked object does not correlate to any object in the catalog it becomes an uncorrelated track (UCT).

The primary sources of UCTs are breakups, operational satellites that have maneuvered, and small objects that are occasionally tracked. These small objects may be

[‡] Professor and Head, Aerospace Engineering, H. R. Bright Bldg., Room 701, Texas A&M University, College Station, TX 77843-3141, Ph (409) 845-5929, Fax (409) 845-6051, Email alfrend@aero.tamu.edu

[†] Graduate Student, Dept. of Aerospace Engineering, Texas A&M University

so small that only one radar can detect them, and depending on their orientation on some passes, that radar may not detect them. As a result an ephemeris may not be able to be developed, and the object cannot be entered into the Space Catalog. Consequently, each day numerous UCTs occur. It is then necessary to determine which of these tracks associate (correlate). Maintaining the ephemerides of the objects in the Space Catalog is an automated process. However, the processing of the UCTs to determine which ones associate in order to develop an ephemeris has primarily been a manual, time consuming process, which results in a strain on resources. Any improvements in this process would be helpful.

Catalog maintenance could become extremely difficult, if not impossible, if too many UCTs occur. Two situations in which this could occur are:

a) A computer failure, particularly during a time of high solar activity. During this down time the ephemerides of many of the objects in the drag region could degrade to such an extent that tracks of the same object would fail the association test. Each track would then become a UCT. If this occurred with enough objects reconstitution of the catalog might be required.

b) A requirement to track much smaller objects, down close to 1 cm in diameter. This would significantly increase, possibly by an order of magnitude, the number of objects which had to be tracked on a regular basis, and each track of each new object would become a UCT.

The purpose of this paper is to evaluate a previously method² that will improve the current method of correlating UCTs, and could be used in processing the UCTs in these situations.

In the current UCT association process four assumptions made about the data¹ are:

a) Each track of data resulted from observing "something" and is an accurate position for that "something" at the time it was observed. A track consists of both the observations and the element set that best represents the observations.

b) Each element set computed from only one track of data may not be accurate enough to predict a satellite's position within system standards, but the elements themselves are very near the true elements.

c) To consider the orbit determined, a minimum of three tracks of data are required on any object, if not solving for drag.

d) Four tracks are required if solving for drag.

The second assumption means that given a number of tracks on the same object there will be a small standard deviation in each individual element about the true value for that object. The standard deviation is not so small as to identify a particular object by merely picking one track elements. However, identifying objects by putting together tracks that have elements that "look" the same is a reasonable concept, and is the first step in the algorithm.

The process is that any track is selected as a reference track and all other tracks are compared to it. In contrast to RETAG¹, which is a position comparison, the UCT association is an orbital element comparison. Let e be the set of orbital elements. The two UCTs associate if

$$|e_i - e_{0i}| \leq \epsilon_i, i = 1, 2, \dots, 6 \quad (1)$$

This is an ordered process of comparison to minimize computation, and the problems of increased uncertainty in some of the orbital elements when the inclination is small. The candidate tracks do not associate if they fail any of the following:

$$\begin{aligned} |i - i_0| &< \varepsilon_1, \varepsilon_1 \text{ nominally } 0.3 \text{ deg} \\ \left| \frac{n - n_0}{n_0} \right| &< \varepsilon_2, \varepsilon_2 \text{ nominally } 0.0075 \\ |e - e_0| &< \varepsilon_3, \varepsilon_3 \text{ nominally } 0.008 \end{aligned} \quad (2)$$

If these tests are passed then the angle between the two orbital planes is checked, then the argument of perigee and finally, in some cases, the position in orbit.

The point to be made here is that this is a static association algorithm, it does not take into account the uncertainty or covariance of the track, nor how the element uncertainties change with time. In addition, the in-track error grows with time so the probability of association, Eq. (1), being satisfied for the in-track component, decreases with the time between the tracks. The proposed approach will consider these factors.

DYNAMIC ALGORITHM

Theory

This new dynamic association algorithm takes into account the changing uncertainty of the state variables. Before presenting the algorithm some terms will be defined.

Equiprobability Ellipsoid³

Given a system with state $\mathbf{x}(t)$, let $\mathbf{C}(t)$ be the covariance matrix, i.e.,

$$\mathbf{C}(t) = E(\mathbf{x}\mathbf{x}^T), E(\mathbf{x}) = 0 \quad (3)$$

where E denotes the expectation operator. Now consider the surface defined by the covariance $\mathbf{C}(t)$, that is the surface defined by

$$S(t) = \mathbf{x}^T \mathbf{C}^{-1} \mathbf{x} = k^2 \quad (4)$$

$S(t)$ is an n dimensional ellipsoid whose semi axes have length k times the standard deviation of the variable for that axis. This volume is called the equiprobability ellipsoid³ since the probability density is the same at all points on the surface.

Association Volume

The volume used to associate tracks is called the association volume. For example, the volume described by Eq. (1) is an association volume. The association volume used by USSPACECOM for associating tracks of known objects is a three dimensional box in

the in-track, radial and out-of-plane position space centered on the predicted object position. The nominal lengths of the half sides of this box are

$$\begin{aligned} \text{in track} &= \Delta t = 3 \text{ seconds} \\ \text{radial} &= \Delta h = 5 \text{ km} \\ \text{out of plane} &= \Delta \beta = 0.05 \text{ deg} \end{aligned} \tag{5}$$

Some multiple of these values, typically three or four, is used for track association.

To present the new approach it is first necessary to present the two theorems proved in Ref. 2. The following assumptions are made:

- The problem under consideration can be represented by a conservative system, i.e., the forces are derivable from a potential. Except for the atmospheric drag and solar radiation, the external forces on a satellite are derivable from a potential. For track separations of less than a day, which is the problem under consideration, the effects of these two non-conservative forces are usually very small compared to the size of the association volume, and can be ignored except for objects well into the drag region. Such objects will probably decay rapidly.
- The equations of motion can be linearized. Of concern is the deviation of the motion from the reference trajectory defined by the initial state determined from the observations. These deviations, except possibly for the in-track motion, are not large and can be represented by a linear system if the proper coordinate system is used. Ref. 2 shows that the linearized equations represent the motion even when large deviations occur in the in-track direction if the proper variables are chosen.

Theorem 1

For Hamiltonian systems the volume of the equiprobability ellipsoid is constant in time.

Theorem 2

Given an association volume, $S^*(t)$, and an equiprobability ellipsoid, $S(t)$, that have equal volumes, the probability of an object being within the association volume is maximized if the association volume is the equiprobability ellipsoid, that is $S^*(t) = S(t)$.

The first theorem shows that the volume of the equiprobability ellipsoid³ defined by the covariance matrix is constant in time if all the forces are derivable from a potential. The second theorem proves that for a volume of a given size the probability of being in an association volume is maximized if the association volume is some multiple of the equiprobability ellipsoid. These two theorems establish that the probability of being inside the association volume does not degrade with time as it does with a static position, or orbital element, association volume used for track association. A static association method is currently used for UCT association.

Distribution of k

Assuming the probability density function of the state $\mathbf{x}(t)$ is Gaussian, that is,

$$f_{\mathbf{x}}(\mathbf{x}) = \frac{1}{(2\pi)^{N/2}(\det C)^{1/2}} \exp\left(-\frac{\mathbf{x}^T C^{-1} \mathbf{x}}{2}\right) \quad (6)$$

where C is the covariance then the probability density function and distribution function of k are

$$\begin{aligned} f(k) &= \frac{1}{2^{(N/2-1)}\Gamma(N/2)} k^{N-1} \exp(-k^2 / 2) \\ F(z) &= \frac{1}{2^{(N/2-1)}\Gamma(N/2)} \int_0^k r^{N-1} \exp(-r^2 / 2) dr \end{aligned} \quad (7)$$

where $\Gamma(x)$ is the Gamma function defined by

$$\Gamma(x) = \int_0^{\infty} u^{x-1} \exp(-u) du \quad (8).$$

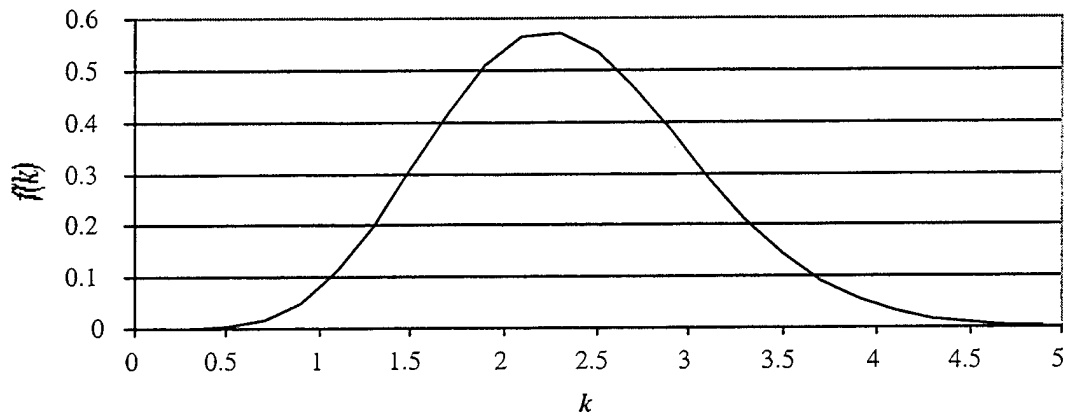
For $N=6$

$$\begin{aligned} f(k) &= \frac{1}{8} k^5 \exp(-k^2 / 2) \\ F(k) &= 1 - \frac{1}{8} (k^4 + 4k^2 + 8) \exp(-k^2 / 2) \end{aligned} \quad (9)$$

Figure 1 shows the theoretical probability density function $f(k)$. Comparison of the density function from numerical experiments with this plot will reveal how well the theory and real world compare. From the distribution function one can select a value of k to use to ensure from a theoretical basis a high probability of associating the tracks. Of course, as k increases so does the probability of false associations. These two concepts have to be balanced against each other. The size of the covariance is also a factor in the process.

NUMERICAL EXPERIMENTS

A set of non-operational objects in low Earth orbit (LEO) have been selected. The procedure is shown in Fig. 5. For each object each track is considered to be a UCT. The ephemeris and covariance for each track are obtained from the LSDC process with epoch as the time of the first observation. The ephemeris and covariance are then propagated to the epoch of each track that is within 24 hours. With the error being the difference in the two states and the covariance the sum of the covariances of the two tracks the value of k is calculated using Eq. (4). Treating these values of k as a random variable the



distribution is obtained and compared with the theoretical distribution given by Eq. (9). In addition, for each pair of tracks Eq. (2) is used to determine if the two tracks correlate using the current static algorithm.

REFERENCES

1. *Mathematical Foundation For SCC Astrodynamic Theory*, NORAD Technical Publication TPP SCC 008, 6 April 1982.
2. Alfrend, K. T., *A Dynamic Algorithm For the Processing of UCTs*, Paper No. 97-607, 1997 AAS/AIAA Astrodynamics Conference, Sun Valley, ID, Aug. 1997.
3. Battin, R., *An Introduction to the Mathematics and Methods of Astrodynamics*, AIAA, 1987.

Figure 1 Theoretical Probability Density Function $f(k)$ for $N=6$

This effort describes a scheme for reporting the operational Systems Capability (SYSCAP) of the Space Surveillance Mission. It includes details of the mission, its execution, the system as it is intended to be deployed, the systems' employment, the dependencies on other systems, the relationship between Force Structure and outage impacts, and the determination of overall SYSCAP. This summary and a more detailed paper (same title, Mar 99) accompany an EXCEL spreadsheet-based utility (which can be used as a prototype tool) for the immediate description of current mission SYSCAP based on reported site Operations Capability (OPSCAP), the insightful scheduling of planned outages, and insight into the resulting impact to warfighters and other users.

While this effort provides the justification for the deployment/employment of Space Surveillance Network (SSN) sensors/assets (i.e., Space Surveillance Force Structure), the impact of mission execution on users, and the rule base for determining SYSCAP, it also provides the means for describing and complying with JCS Volume VI direction. Effective 2 FEB 99, the JCS directed operational Space Surveillance SYSCAP up-channel reporting.

This analysis assumes requirements from the 10 July 1995 AFSPC Space Surveillance Requirements Document – provided by AFSPC to USSPACECOM, directing all AFSPC assets to use it until USSPACECOM produces a final capstone document (in progress). The Space Surveillance Performance Analysis Tool (SSPAT) was heavily referenced for space population and growth, and the performance of current Space Surveillance Network (SSN) assets. The threat is primarily derived from the AFSPC/IN document, Threat Input for Space Surveillance MAP (2 March 1995), but also includes information from the USSPACECOM/J2F document, Foreign Space Threat (23 June 1995), the National Air Intelligence Center (NAIC) Space Systems Threat Environment Description (TED) (11 September 1995), and the draft USSPACECOM Space Control Capstone Requirements Document (20 May 1996).

Approach

The underlying foundation of Space Surveillance and Space Control is to characterize the battlespace, maintain the space catalog and identify the Space Order of Battle, and support other Mission Areas (see chart, last page). If surveillance of space events and the space catalog are not maintained, a growing number of unknown trackable objects will begin to pass through the battlespace. Unknown tracks will increase until the ability to correlate tracks with known objects degrades and the ability to differentiate objects is lost. This is analogous to an AWACS aircraft which must survey and monitor the air battlespace. It must track and differentiate both friendly and hostile targets. If unknown targets exist, it must identify and correlate them and it must correlate unknown tracks with their respective objects. An incomplete database results in the inability of the AWACS to identify the targets of interest—it becomes unable to pick them out of the air population (a "chaff" effect results). A surveillance system must track and correlate all that is detectable to it. It must also detect and add to its surveillance frame all new craft, events, and unknown, unidentified, or hostile activity.

The traditional method used for determining the SYSCAP of surveillance systems is to base the "color changes" on regions of coverage. This works well for systems charged with perimeter defense surveillance such as air defense systems and even missile warning systems. It also works well for these "systems of systems" with only one mission.

Unfortunately, the business of Space Surveillance does not lend itself to deployment around a terrestrial perimeter—if a region on the earth were to change to SYSCAP RED, no information is actually conveyed; the effect on SSN operations is indeterminate. Nor does the mission consist of just one type of surveillance—the impact of a site outage may result in high impact to one process but no impact to another.

Therefore, to give meaning to a reported SYSCAP, a scheme of reporting in terms of mission impact was developed. This scheme begins with first understanding the mission of space

surveillance. Using a strategy-to-task approach to illustrate the fallout of requirements on the SSN, the mission requirements are ultimately described in terms of Mission Area Tasks (MATs). These MATs vary from year to year, and organization to organization, but they are essentially grouped in the same way. The groupings are always in terms of *product* and/or customer categories. From these MATs, an analysis of the actual operations of the SCC and SSN reveals how the SSN actually executes its processes to meet its requirements. Such an analysis shows the overall Space Surveillance mission in fact consists of several common *processes* called Mission Profiles (MPs).

Space Surveillance Mission Profiles and Mission Types

Common MPs are grouped into Mission Types to describe more simply the overall SYSCAP. Due to the nature of the available sensor technologies and the physics of Space Surveillance, sensors are deployed/employed differently for Near Earth (225 minute orbital Period or less) than for Deep Space (greater than 225 minutes in orbital Period), and as such there is a SYSCAP for NE and one for DS.

Mission Profile Mapping into Mission Types

	SPACE TRACK	SPACE INTELLIGENCE
ROUTINE PROFILES	- Routine Orbit Maintenance - Precision Orbit Maintenance - New/Lost Object Search	- Routine Space Intelligence
ALERT PROFILES	- NFLs - On-Orbit Events - Hostile Kinetic Attacks	- BDA/Initial MPA Support

Space Surveillance supports composite profiles consisting of more than one Mission Profile, in the accomplishment of its Mission Area Tasks:

- Orbital Safety—utilizes the Routine Orbit Maintenance, Precision Orbit Maintenance, and Routine Search Mission Profiles.
- Reentry Assessment—is a combination of Routine SOI and Status Collection (to determine which decaying objects, from the Routine Orbit Maintenance Mission Profile, to place on Reentry Assessment processing), and Precision Orbit Maintenance (to calculate the impact point).
- Pre-Planned Cooperative Launch processing—combines the Routine Search, Routine Orbit Maintenance, and Routine SOI and Status Collection Mission Profiles.

Attributes required for Space Surveillance

The reality of the Space Surveillance infrastructure is that most of the assets are already acquired based on geopolitics or inheritance from other missions. This effort includes the results of an analysis summarizing the details of current sensors' capabilities. From that list of assets, the functions required in the execution of the Mission Profiles are analyzed and the necessary attributes for mission success identified. Space Surveillance assets, suitable to performing the functions required of them, must be deployed and employed effectively to meet the performance requirements of the Space Surveillance Mission Area.

The following table lists the specific suitability parameters of the Force Structure which must be considered to complete the MATs effectively, and identifies the respective effectiveness and performance parameters to which they contribute. The applicable functions of each MP pertaining to a particular suitability parameter are indicated (M=Monitor, Detect, and Notify; A=Alert and Task; S=Search, Locate, and Report; C=Converge, Track, and Collect to obtain Product Criteria; P=Correlate, Identify, Process, and Transmit Product; X=Associated Effectiveness or Performance Parameter) Functions in parentheses are those performed by assets outside the Space Surveillance Mission Area. A dash following a letter indicates not all segments within the Force Structure would need to maintain that suitability characteristic. An asterisk is used to identify possible problem areas with the current Force Structure.

Space Surveillance Suitability Parameters, Associated Effectiveness Parameters, and Resulting Performance Requirements

MISSION PROFILES:	NFL Tracking and Processing	On-Orbit Event Detection, Tracking, and Processing	Routine Orbit Maint- enance	Precision Orbit Maint- enance	Kinetic Attack ID, Tracking and Processing	BDA/ Initial MPA Support	Routine Space Intelligence	New/Lost Object Search
APPLICABLE FUNCTIONS:	(M)ASCP	MASCP	ACP	ACP	(M)ASCP	AC(P)	AC(P)	ASP
SUITABILITY								
All-Weather Accessibility	(M)SC	M [*] S [*] C [*]	C ⁻	C	(M)SC	C [*]	C ⁻	
24-Hr Accessibility	(M)ASCP	M [*] AS [*] C [*] P	P	ACP	(M)ASCP	AC [*] (P) [*]		AP
Range Capability (NE, DS)	SC	MSC	C [*]	C	SC-	C	C [*]	S
Ranging Capable	C	C [*]	C-	C-	C			
Compatibility	(M)ASCP	MASCP	ACP [*]	ACP	(M)ASCP	AC(P)	AC(P)	ASP
Connectivity	(M)ASCP	SCP	ACP	CP	(M)ASCP	AC(P)	AC(P)	P
Spot Search Ability	C	SC	C		SC	C	C	S
Event Search Ability	(M)S	S			(M)S	S		S
New/Lost Object Search Capability								S
Metric Capability (accuracy, precision)	SCP	MSCP	CP	CP	CP	C(P)	C	S
Basic SOI Capability (fidelity)	(M)SC	MSC		C	(M)C	C(P)	C(P)	S-
Enhanced SOI Ability (resolution, fidelity)		M [*] C ⁻			(M)	C [*] (P) [*]	C ⁻ (P)	
Small Size Acquisition Ability			C [*]	C				S [*]
Multiple Object Tracking Capability	(M)C	C	C [*]		(M)C		C [*]	S
Multiple Search Capability	(M)S	S			(M)S			S
Correlation Capability (track integrity)	SCP	SCP	C [*] P	CP	(M)SCP	C(P)	C(P)	P
Routine Accessibility (12hrs-DS, 18-NE)			AC [*]				AC [*] (P)	S
Availability			ACP				AC(P)	
Dependability	(M)AS [*] CP	M [*] ASCP		ACP	(M)AS [*] CP	AC(P)		ASP
Reliability	(M)ASCP	MASCP	ACP	ACP	(M)ASCP	AC(P)	AC(P)	ASP

**Space Surveillance Suitability Parameters, Associated Effectiveness Parameters, and
Resulting Performance Requirements (cont.)**

MISSION PROFILES:	NFL Tracking and Processing	On-Orbit Event Detection, Tracking, and Processing	Routine Orbit Maint- enance	Precision Orbit Maint- enance	Kinetic Attack ID, Tracking and Processing	BDA/ Initial MPA Support	Routine Space Intelligenc e	New/Lost Object Search
APPLICABLE FUNCTIONS:	(M)ASCP	MASCP	ACP	ACP	(M)ASCP	AC(P)	AC(P)	ASP
SUITABILITY (cont')								
Responsiveness	(M)SCP	MSCP	C*	ACP	(M)SCP	AC(P)*	C(P)	AS
Discrimination Ability (pieces)	(M)CP	CP	CP	CP	(M)CP	C(P)	C(P)	
Track Capacity Rate			AC*P				AC*	ASP
Throughput	(M)		ACP		(M)	C(P)	AC(P)	ASP
Communications Integrity	(M)ASCP	MASCP	ACP	ACP	(M)ASCP	AC(P)	AC(P)	ASP
Processing Speed	(M)ASCP	MASCP		ACP	(M)ASCP	AC(P)	(P)*	
EFFECTIVENESS								
Coverage	X*	X*	X	X	X*	X	X	X
Capacity			X*				X*	X
Responsiveness	X	X	X*	X	X	X	X	X
Detectability (prob. of aq/success)	X	X	X*	X	X	X*	X*	X*
Accessibility (operating time)	X	X*	X*	X	X*	X*	X*	X
PERFORMANCE								
Timeliness	X*	X*		X	X*	X*		
Quality (accuracy, resolution, fidelity, stability)			X	X		X*	X*	
Unambiguity (correct correlations, discrete products)	X	X	X		X	X	X	X
Completeness (no lost/unidentified satellites or true UCTs)	X	X	X*		X		X*	X*

It is here that the final suites of sensors to be used for accomplishing each MP are picked. This is the determination of the Force Structure for each MP based on required capability and available attributes. It is the identification of how the SSN assets will be deployed and employed. It is analogous to picking the kicking, receiving, punting, offensive, and defensive teams from a list of football players. Each player's attributes are considered in light of the mission to be performed during the game. Each mission consists of several functions requiring certain attributes. Some functions are common to several MPs, and the same asset may be employed for both.

The Space Surveillance Force Structure

At this point, there is a departure from requirements. It is well known that the current documented requirements are not all attainable by the current SSN. It is not the intent of SYSCAP to describe a system's ability to meet requirements but instead to describe its ability to perform as intended—once it has been deployed as efficiently as it can to meet requirements as best it can. Therefore, once the Force Structure is chosen, requirements are set aside in lieu of a description of the impact to the capability of a suite of sensors to perform a particular MP. Green indicates little to no impact to mission execution, Yellow indicates a significant impact, and Red a critical impact—with reference to the *intended* Force Structure's abilities (this analysis accounts for programmed sites, such as HAVE STARE, which are funded and have definite delivery dates).

Synergy with Logistics

Since there is an unfortunate tendency to confuse SYSCAP with Logistics Dependability, Availability, and Reliability, this effort contains a short discussion of how to keep the two separate, while maintaining synergy. A sensor's sustainability and maintenance are directly influenced by its required Operational Dependability (D_o), Availability (A_o), Mission Reliability (MR), Operating Time, and capabilities.

The Operating Time requirement for a sensor is the time a sensor must be accessible to the SSN to execute its MPs. The Accessibility of the sensor must meet requirements to include contractual, weather, daylight, or other mission constraints. Availability is the logistics probability that a sensor will be operational to perform *routine* MPs during its Operating Time. Dependability is the logistics probability that a sensor will be able to respond to *Alert* MPs in the event of a recall to status during the Operating Time. Reliability is the probability that a sensor will not fail logistically during a track (mission time). These definitions are from the Draft 22 Jun 96 Space Surveillance Dependability, Availability, and Mission Reliability Document.

The Space Surveillance SYSCAP Utility

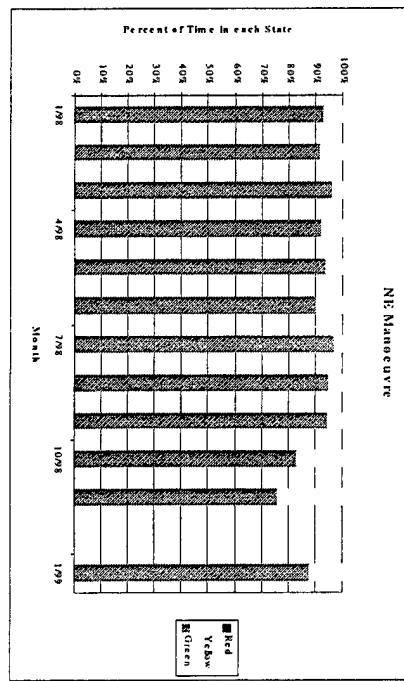
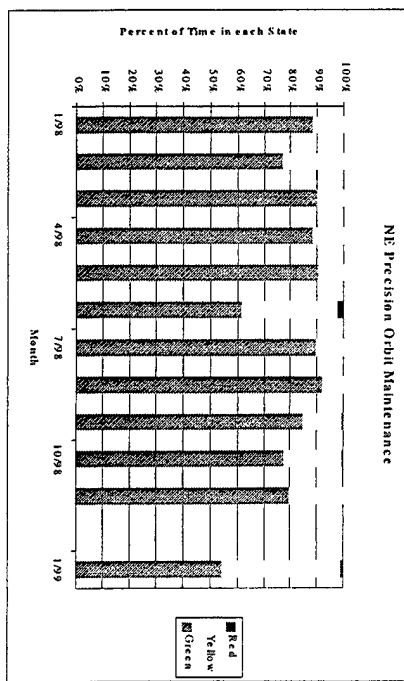
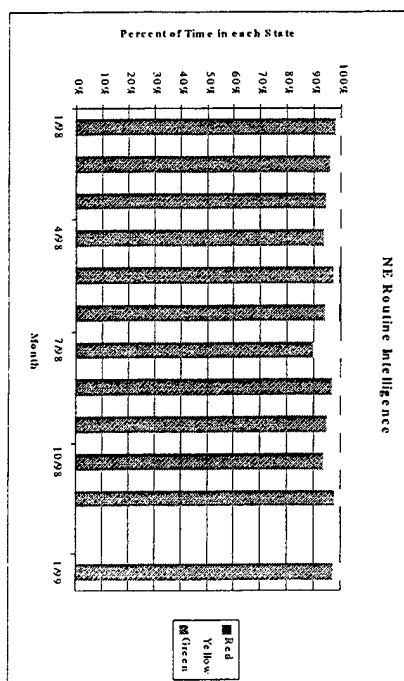
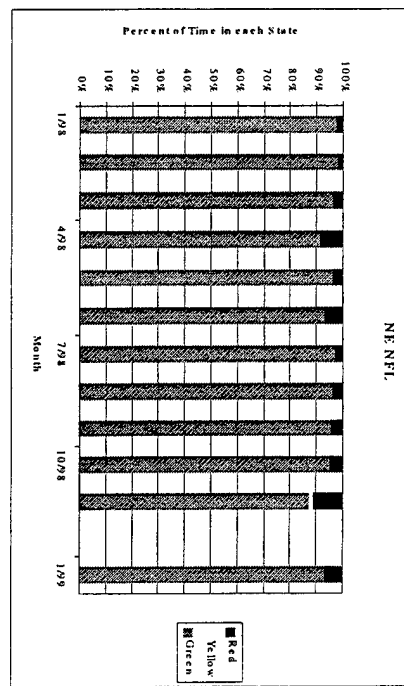
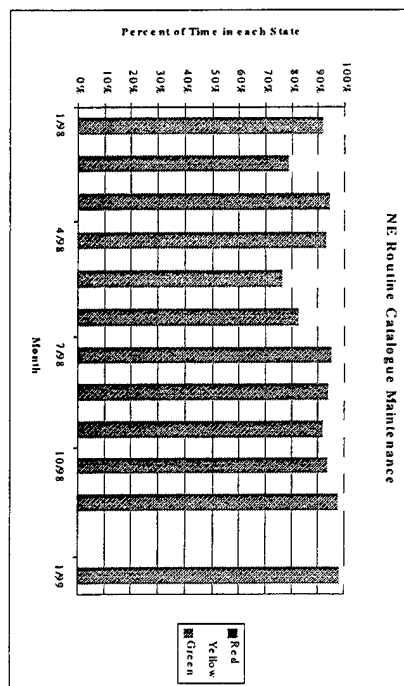
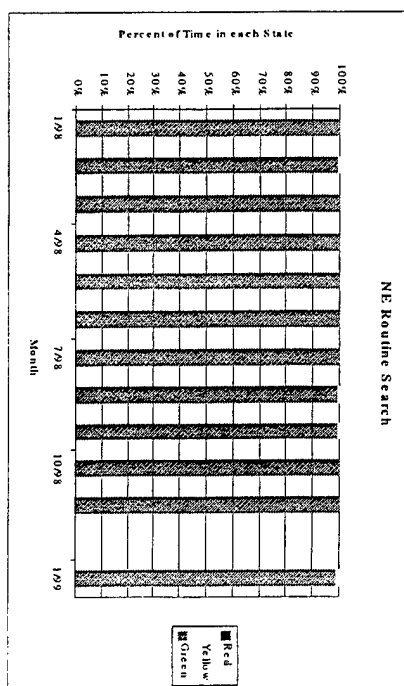
The SYSCAP Utility is an EXCEL spreadsheet (.xls) file enhanced by Visual Basic code. The conclusions of this effort concerning the use of SSN sensor sites and the rule base for determining SYSCAP are embedded in it. The enhancing code which automatically takes user inputs and applies the rule base to display SYSCAP has been locked-out to prevent misrepresentation of the Force Structure, a sensor's contribution, or the SYSCAP rule base without approval, coordination, or analysis. It runs on a PC using EXCEL '97 and has displays for the following purposes:

- a. A summary display with site OPSCAPs, resulting Mission Profile SYSCAPs, and derivative Mission Type SYSCAPs (for up-channel reporting);
- b. A summary display similar to the above but intended as an initial prototype display for a C² center which would need the Mission Profile SYSCAPs mapped into the Mission Type SYSCAPs, thus showing which MPs affect which MTs;
- c. Displays for the rule bases applied to determine color changes for each MP and the derivative MTs;
- d. A single display that identifies which sites affect which MPs, to be used for planning scheduled outages; and
- e. A display that illustrates which MPs directly contribute to the various user groups of the SSN, and the gradual degradation in SSN product delivery to those users

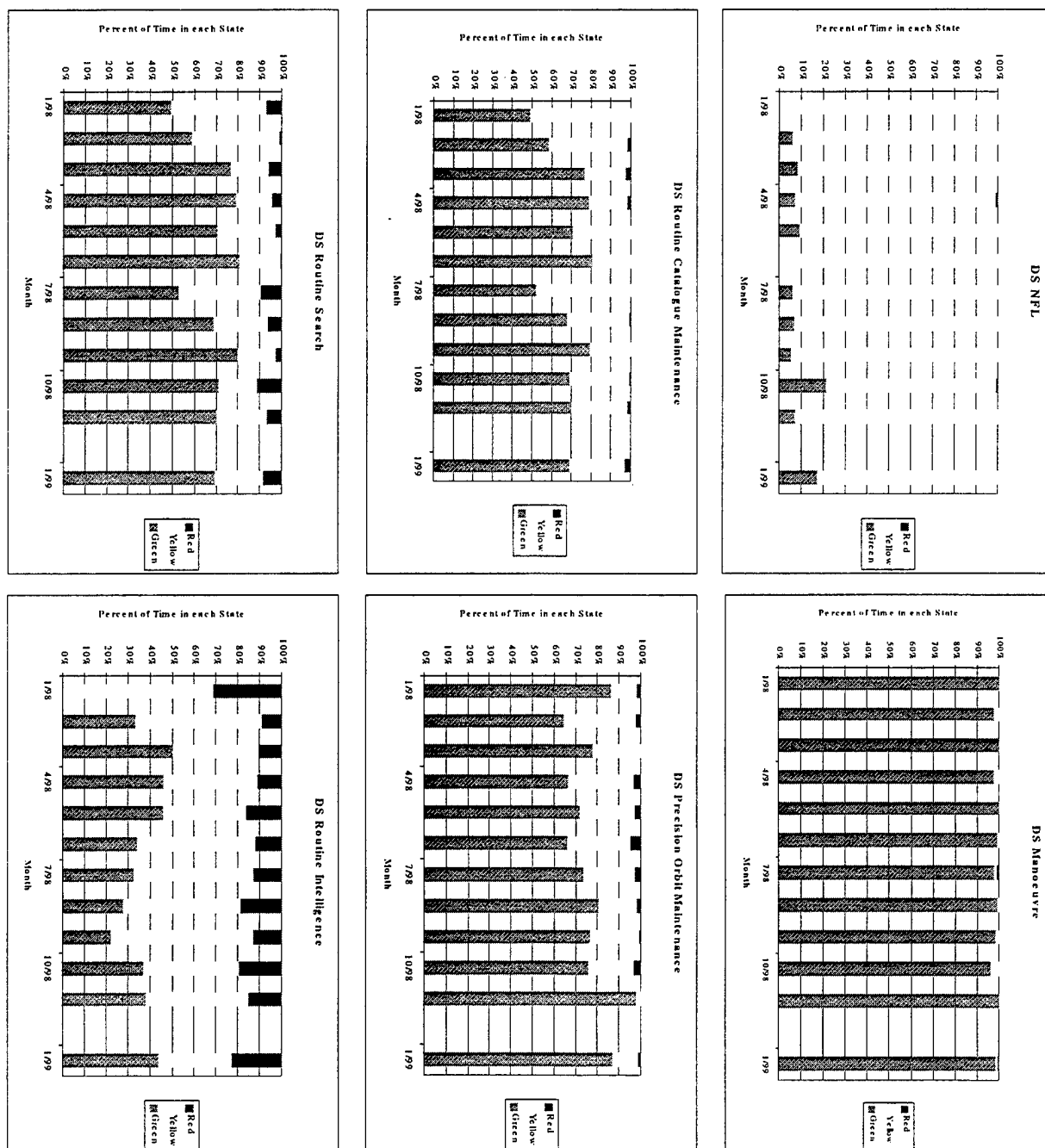
The following is the overall SYSCAP summary display from the utility, followed by an example display which shows the rule base as it is applied to the corresponding MP. There is a different rule base for each MP, and the colors change to reflect the impact of sensor OPSCAP inputs as they are entered by the user. Other displays in the utility show how the MP SYSCAPS map to the overall, up-channeling Mission Types.

The displays taken from the SYSCAP utility, including the one on the previous page, are designed for display in color and are far more easily understood when viewed this way. The colors green, yellow, red, blue, and gray, each with a distinctive meaning, can appear on any of these displays. The grayscale reprint here allows only an uncertain differentiation among colors. Interested readers are referred to the complete report, cited in the opening paragraph, for a more easily accessible treatment of displays.

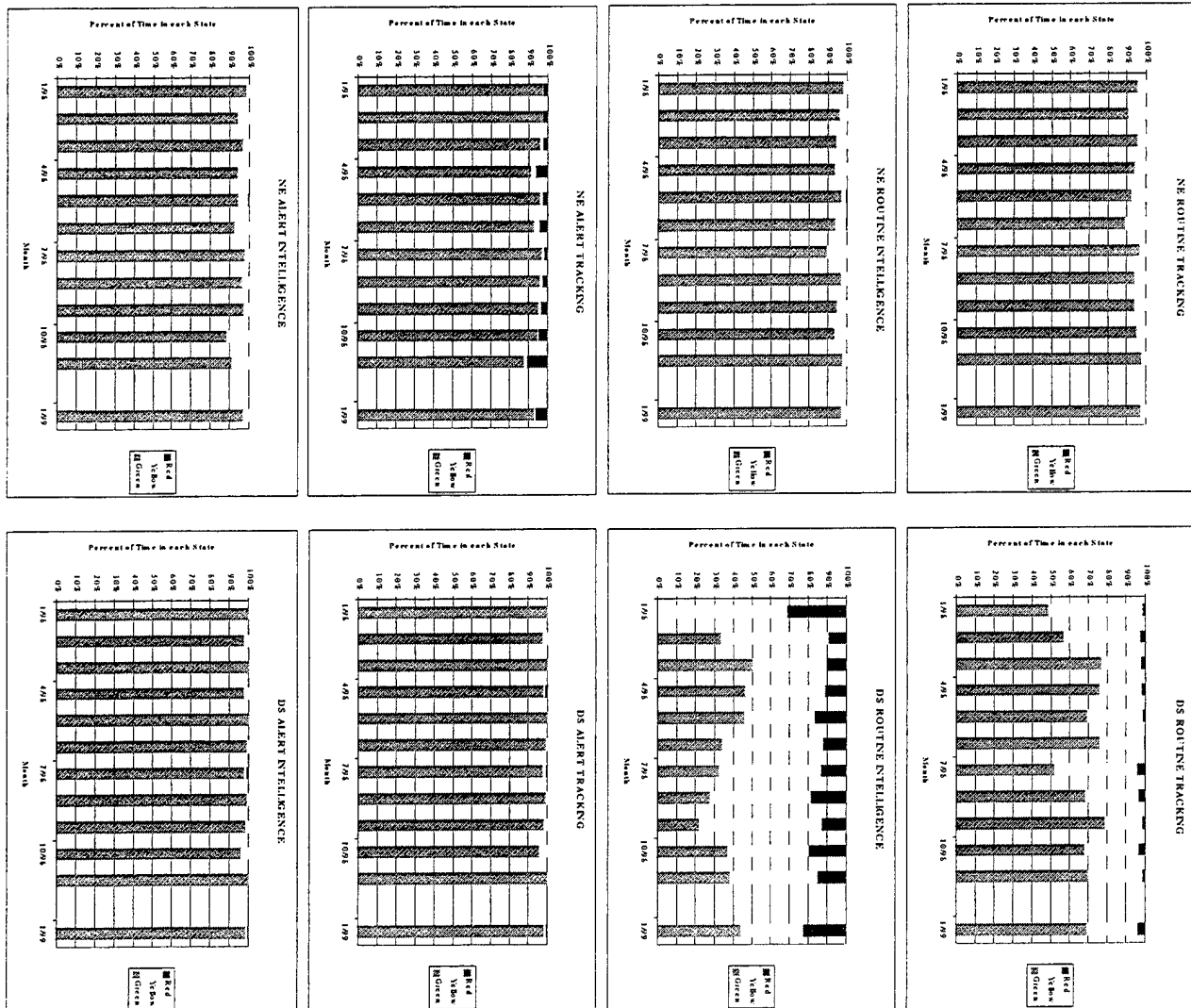
NE SYSCAP performance over the past year yields several conclusions. First, although in Space Surveillance it has become customary to view as acceptable performance that is primarily green, for any other Mission Area (such as Missile Warning) it would be considered grossly unacceptable. Second, the notable amount of non-green time for Precision Orbit Maintenance may indicate difficulties in any significant expansion of the number of satellites maintained as precision orbits (*i.e.*, SP). Finally, the predominance of green time, coupled with the known shortfalls in NE timeliness and catalogue performance, indicate that such shortfalls derive from inadequate SSN assets rather than problems with mission execution or site outages.



In deep-space, the lack of a completed DS radar ring (HAVE STARE or Pirincli) affects NFL performance significantly. Additionally, most DS missions place a high demand on the same high-capacity optical sensors, which are vulnerable to weather outages; much of the poor performance reflected in the bottom four graphs can be ascribed to this difficulty.



The following two columns of charts, one for NE and one for DS, reflect the higher-level Mission Types. As consolidations of Mission Profiles, they are used for up-channel SYSCAP reporting. As expected, the story told by these consolidated Mission Type charts is similar to that which is observed at the Mission Profile level: in NE, the predominance of green indicates that performance shortfalls are due to insufficient SSN assets rather than execution or outage problems; in DS, the heavy and overlapping reliance on a few high-capacity optical sensors makes the mission performance especially vulnerable to weather-induced outages.



Warfighter and User Display

Finally, it was determined by the operations community at the 14 AF's Guardian Tiger '98, that some means to describe Space Surveillance SYSCAP's effect on users is needed. The following display is an attempt to describe this relationship and its effects. As previously stated, the *process*-oriented Mission Profiles directly contribute to the *product*-oriented customer categories. Since it is not appropriate for a supporting mission to decide the SYSCAP of the mission being supported, the impact to the delivery of products to the users is described in terms of amount of expected products affected. As sensor OPSCAPs change, Mission Profile SYSCAPs change. Those Mission Profile SYSCAPs in turn affect the delivery of Space Surveillance products to the various categories of customer/user groups they support. It is unknown whether the percent impact is tolerable by the particular user or whether it is the essential portion that was affected.

SYSCAP Effects on Products to Warfighters and Users

MISSION PROFILE		SPACE SURVEILLANCE CUSTOMER/USER PRODUCT CATEGORIES							
		Maintain RSO	Maintain SOB	Support Theater	Assist Intel	Support Protection	Support Negation	Launch/ On-Orbit	Treaty Monitoring
NFL	NE								
	DS		□	□		□			
On-Orbit Events	NE								
	DS		□	□		□			
BDA/ MPA	NE		□	□		□	□		
	DS		□	□		□	□		
Routine Catalogue	NE	□	□	□					
	DS								
Precision Catalogue	NE								
	DS								
New/ Lost Search	NE								
	DS								
Routine Intel	NE		□	□	□			□	□
	DS		□	□	□			□	□
Percent of Products Available		88%	65%	63%	50%	67%	50%	67%	50%

Note: unless Routine Catalogue Maintenance is being performed fully, all other missions will degrade
 Routine Catalogue Maintenance SYSCAP:

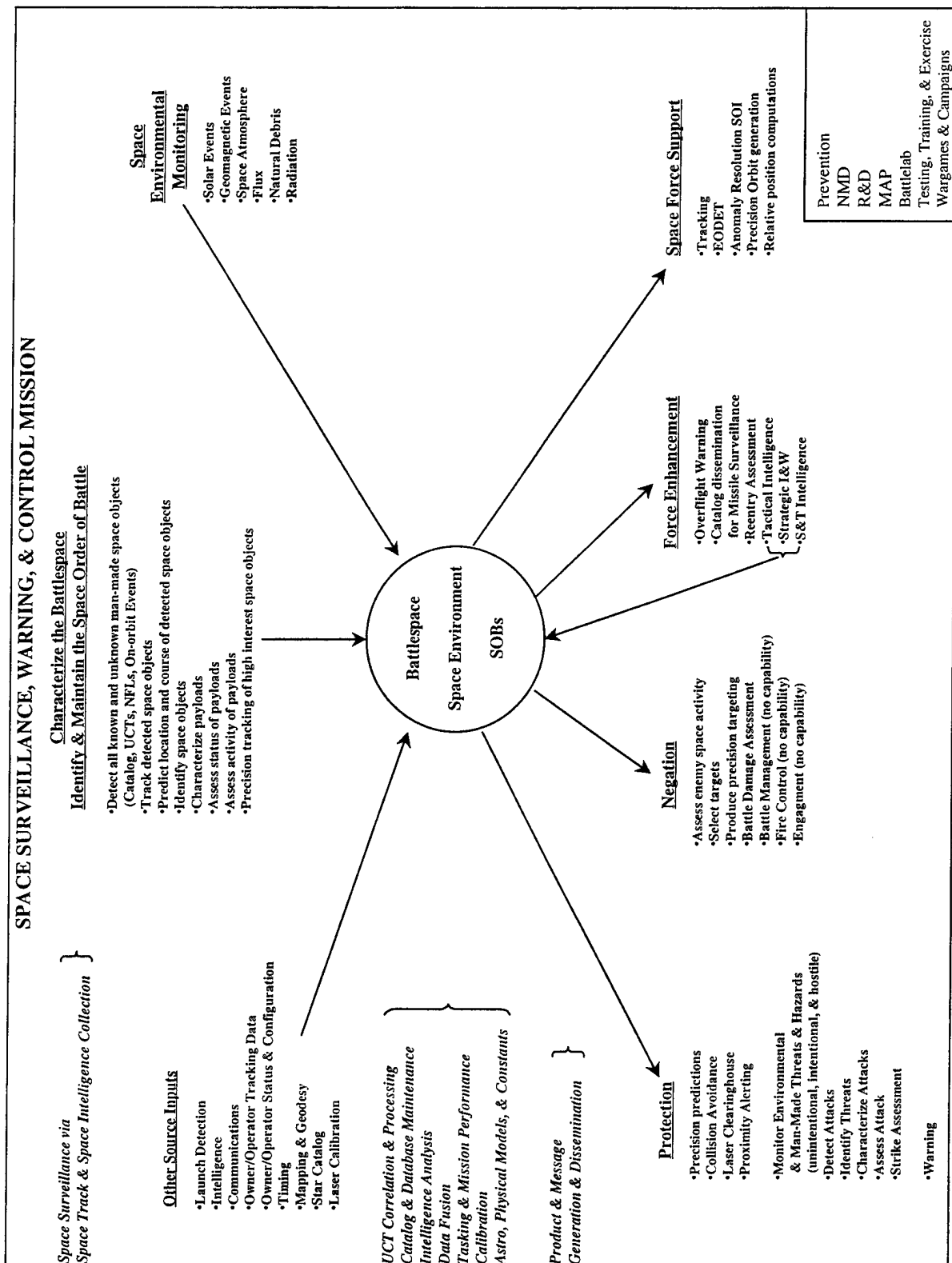
NE:

DS:

The Next Step

Now that a scheme for operational SYSCAP has been developed, the next step is to bring individual site OPSCAPs in line with the same scheme. A site's OPSCAP should take into account the overall OPSCAP of its multiple sensors on site. It should also reflect its contribution in terms of routine processing and alert response, as well as operating time and recall capability. Eventually, this will pave the way for improved dependability and availability performance in matters of logistics, and the same in matters of design (i.e., Line Replaceable Units, Maintenance Concepts, etc.).

While the insight into the resulting impact on the different user groups of Space Surveillance (given the SYSCAP changes in Mission profile and Mission Type) is illustrated above and in the actual utility, the eventual impacts to the users, especially the theater and space warfighters, must be studied. The SYSCAP Utility and this effort provide a beginning.



TELSTAR-401

ENCOUNTERS WITH TELESAT CANADA SPACECRAFT

With the in-orbit failure of TELSTAR-401 (January 1997) and its potential threat to synchronous satellite between 97°W and 113.5°W, a Cooperative Research and Development Agreement (CRDA) between various Satellite Operators and the Massachusetts Institute of Technology Lincoln Laboratory was created. Telesat is one of these Satellite Operators. The overall handling of the TELSTAR-401 encounters with the Telesat spacecrafts is presented along with the improvement/optimization made over the last two years towards reducing the work caused by these encounters.

Currently, Telesat controls four geosynchronous spacecrafts: Anik E1 at 111.1°W, Anik E2 at 107.3°W, MSAT M1 at 106.5 °W and Anik C1 at 106.3°W. The Anik E's are controlled within a stationkeeping box of 0.05°. MSAT M1 is controlled within 0.075° East/West and 0.05° North/South. Anik C1 is controlled within 0.1° East/West but without any North/South control (i.e. inclination Feb 1st, 1999 = 1.5°). The stationkeeping maneuvers are performed basically just before any control limit is reached (and weekend maneuvers are avoided). This is very different from many other Satellite Operators who perform stationkeeping maneuvers on a very regular by-weekly cycle.

One of the first activities between Telesat and MIT Lincoln Laboratory (more specifically with Millstone) was to define the basic parameters in exchanging orbit and performing orbit determination. Some of these parameters were: coordinate system; time system; constants, solar radiation force model (i.e. effective area and spacecraft mass) and tracking station locations. Initial spacecraft longitude discrepancies were reduce from 0.025° to around 0.0015°.

Initial orbit determination indicated solutions with latitude, longitude and radius discrepancies of the order of 4, 2.5 and 0.5 km respectively. With the effort of Millstone (using tracking data from Telesat and from Millstone) new Telesat ranging biases for each spacecraft were estimated relative to Millstone tracking system. Using these new range biases, Telesat orbit solutions now agree with Millstone to within 160 meters in the in-plane direction and 400 meters in the out-plane direction. On a weekly basis, Telesat is sending its tracking data measurements and its maneuver parameters to Millstone.

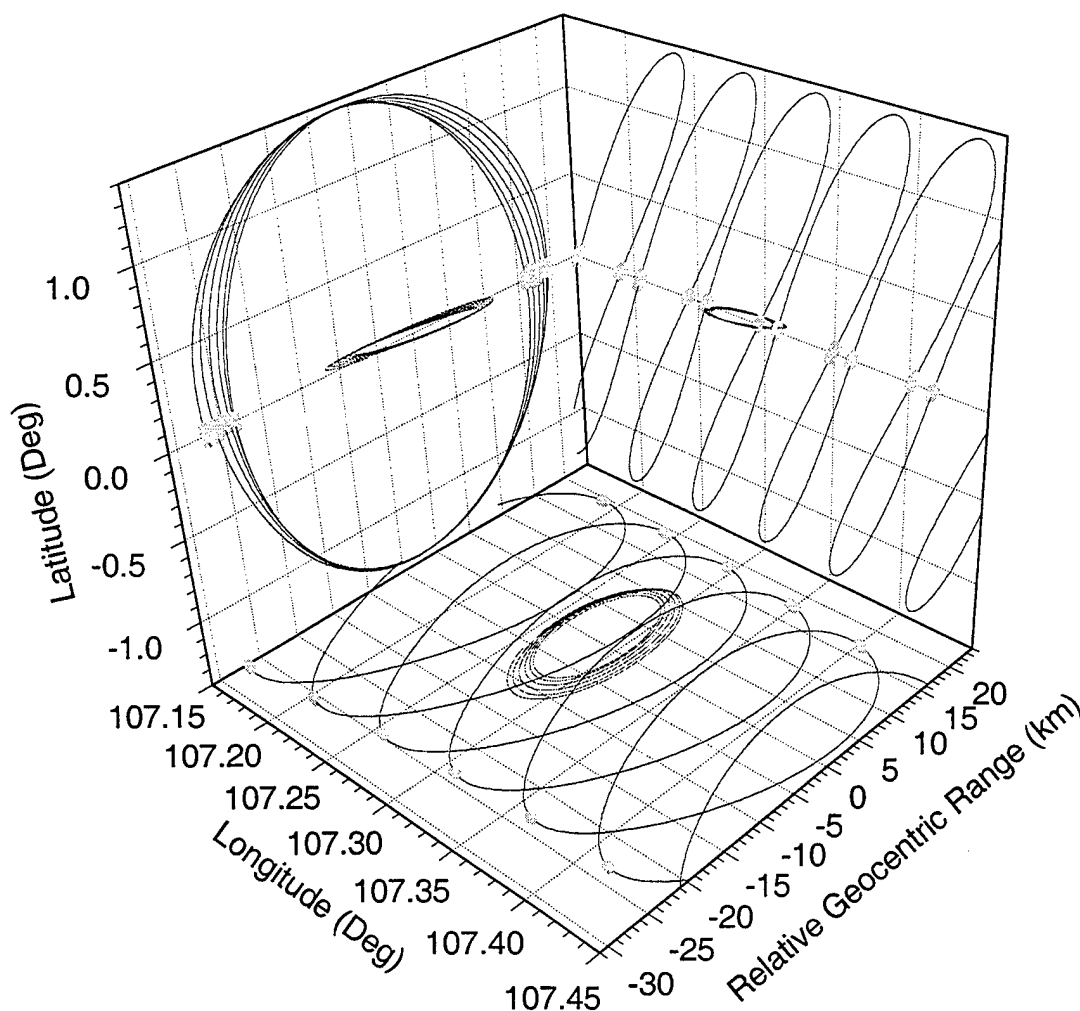
Since October of 1997, Telesat spacecrafts has had eight encounters with TELSTAR-401. They are summarized below:

Telesat S/C	Encounter Date	Spatial Separation
MSAT M1	October 6, 1997	14.1 km
Anik E2	October 21, 1997	17.4 km
Anik E1	January 9, 1998	8.6 km
Anik C1	June 1, 1998	27.2 km
Anik E1	August 12, 1998	12.4 km
Anik E2	October 31, 1998	14.9 km
MSAT M1	November 15, 1998	15.1 km
Anik C1	November 20, 1998	14.9 km

On the initial encounters, Telesat/Millstone had the following basic 15-day activity plan as follows:

T -15 days	Millstone provides TELSTAR-401 orbit
T -14 days	Telesat performs E/W maneuvers to maximize distance
T -14 days	Millstone starts tracking Telesat S/C
T -7 days	Millstone provides: <ul style="list-style-type: none">- TELSTAR-401 Orbit- Telesat S/C Orbit- Spatial Separation Plot
T – 7 days	Telesat performs E/W adjustment if required
T – 1 day	Millstone confirms final separation value
T	Millstone monitors encounter in real-time
T + 1 day	Millstone reports on results of real-time monitor

As time progress, the inclination of TELSTAR-401 increase (0.73° per year), the eccentricity of its orbit changed (cyclic over a year) and the overall geometry of the encounters were much better understood, and thus some of the encounters became of low concerns. A good example of this is the Anik E2 encounter on October 31st, 1998. As is well indicated in the Latitude/Radial plane of **Figure 1**, the large inclination and eccentricity of TELSTAR-401 makes it impossible for the two spacecrafts to collide.



From: MIT Lincoln Laboratory

Figure 1 TELSTAR-401/Anik E2 Encounter

On the other hand, the Anik C1 inclination (which is not being controlled) is only about 0.1° different from TELSTAR-401. In this case, the TELSTAR-401 encounter will always be of extra interest.

During the last few encounters, the two orbits' differences (i.e. Telestar-401 orbit from Millstone OD and Telesat S/C orbit from Telesat OD) are separated into three components (i.e. latitude, longitude and radial directions). Because of the large TELSTAR-401 inclination, any closes approach to geostationary spacecrafts will occur at equator crossing. At this equator crossing, if a significant radial separation exists then the encounter is declared safe (independent of longitude). The radial separation uncertainty is estimated to be close to 100 meters. In most cases, Telesat will maximize the longitude separation as part of its routine stationkeeping East/West maneuvers and will avoid any stationkeeping maneuvers seven days prior to any encounter.

Within the last year, other encounters (other than with TELSTAR-401) have been flag by Millstone with the Telesat spacecrafts. A specific example of this was the COSMOS 2282 body encounter with Anik C1 on September 26th, 1998. Initial computation indicated a spatial separation of only 6 km. Telesat performed a small East/West maneuver to increase this separation to 14 km. Therefore a larger scope (outside of TELSTAR-401) of encounter analyses is also currently being addressed.

One day semi-annual meetings between MIT Lincoln Laboratory and the Satellite Operators within the CRDA have also occurred. At these meeting MIT Lincoln Laboratory summarized the overall work that they performed and the Satellite Operators provided feedback from their end. Interchange of information between Satellite Operators was also very useful.

In conclusion, the Cooperative Research and Development Agreement (CRDA) between Telesat (plus other Satellite Operators) and the Massachusetts Institute of Technology Lincoln Laboratory has been very successful in minimizing the risk of collision between the TELSTAR-401 and active spacecrafts. Over the last few years, an improvement in exchanging orbit solutions, removing range biases in orbit determination process, and with the overall effect of perturbations on the TELSTAR-401 orbit, has made the TELSTAR-401 encounters very simple, routine and safe.

Satellite Tracking Using Ambient RF (STAR)

Mark F. Storz, Wayne M. Rezzonico, Robert A. Racca, and Charles T. Krinsky (Space Warfare Center)

INTRODUCTION

Satellite Tracking Using Ambient RF (STAR) demonstrated the capability to detect and track Low Earth Orbit (LEO) satellites (typically 150 to 3,000 km) with a passive, stand-alone space surveillance capability. The system relies on ambient radio frequency (RF) energy from existing broadcast transmitters (such as television) to illuminate target satellites. Orbiting satellites reflect this energy which is collected by a ground-based receiver. The STAR concept uses a "multistatic" geometry where multiple sources of RF energy, which are geographically displaced from a receiver, illuminate the satellite of interest. The resulting returns were used to extract kinematical information on the satellite.

Currently, there are thousands of commercial TV transmission towers worldwide which send transmissions into space. During the STAR effort, these reflected TV transmissions were collected with a mechanical dish receive antenna and subsequently processed to determine the trajectory of orbiting satellites. The components of an operational system based upon this concept are now essentially commercial-off-the-shelf (COTS) and take advantage of recent advances in computing power and digital signal processing.

OBJECTIVES

The STAR demonstration was structured to show the capability to augment existing Air Force Space Surveillance Network (SSN) sensors. The following objectives were addressed during the STAR effort:

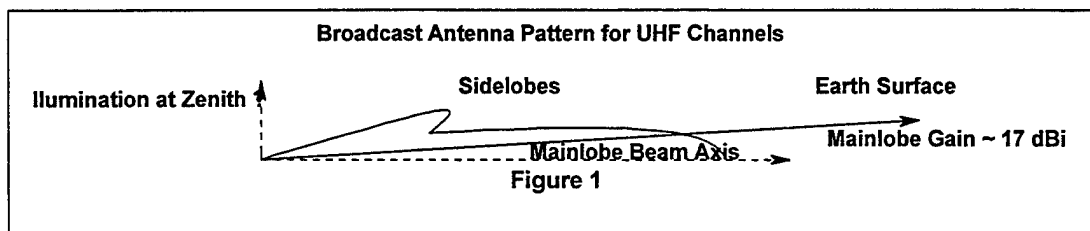
- Characterize the environment to determine the availability of RF energy and determine performance- limiting constraints.
- Detect and track space objects using existing element sets as a basis for initial position determination and sensor track initialization.
- Detect and track space objects assuming no a-priori knowledge of the element set to demonstrate a capability to detect and track unknown objects.
- Investigate the capabilities, limitations, and cost of the proposed equipment needed for the STAR system.

METHODOLOGY

The STAR demonstration addressed four separate tasks that are discussed below:

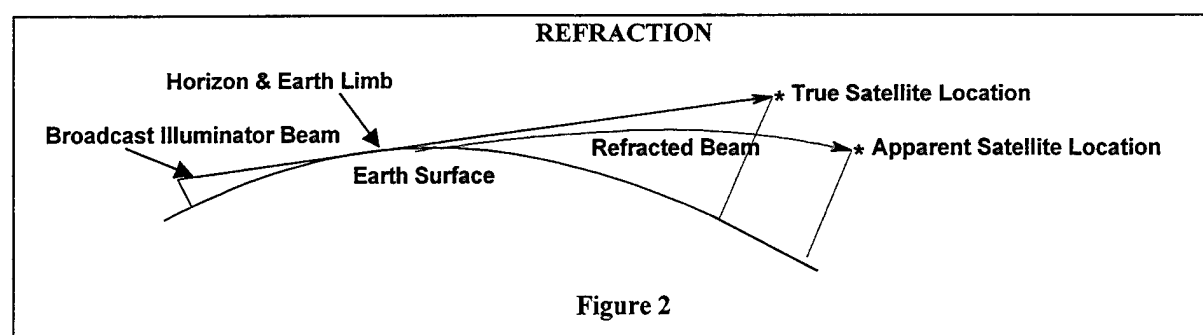
Task 1: Environment Characterization

Doppler range-rate and range data were obtained by collecting echoes from selected satellites to characterize antenna elevation patterns, co-channel signal environments, sources of interference, and propagation anomalies. The antenna elevation pattern is defined as the volume of space where existing TV transmitters provide usable energy to illuminate orbiting satellites. Since these transmitters are designed to provide energy to consumers on the ground, ground based receivers collect the majority of this energy. Figure 1 illustrates this concept.

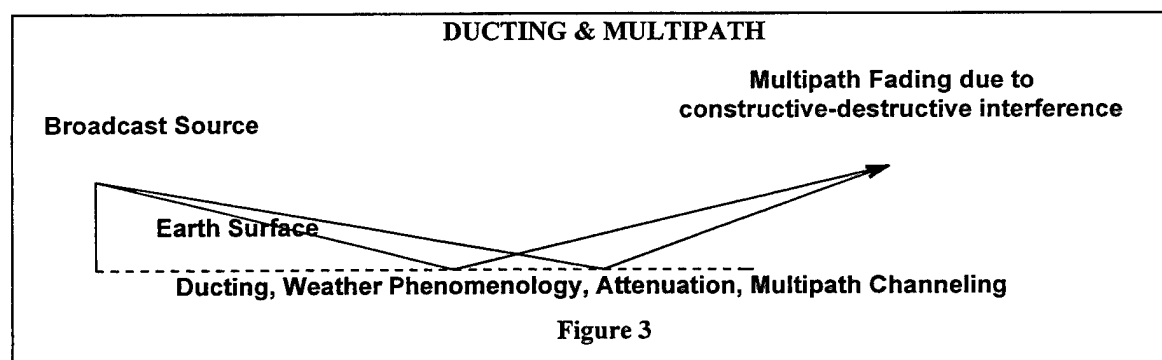


Another goal of this task is to develop a method for determining the origin of a received satellite echo. In order to make use of the Doppler velocity and range, the satellite returns must be associated with the correct transmitter. This is not a trivial task since the FCC issues broadcast licenses to multiple transmitters at the same, or at very nearly the same frequencies. Consequently, several of these transmitters may simultaneously produce detectable returns.

The final goal was to evaluate the data in order to characterize the impact of refraction, ducting, multipath and other propagation anomalies. These phenomena, which may potentially impact the accuracies of the system, are illustrated in Figures 2 and 3.



Ducting and multipathing affect the amount of energy that can be reflected from a target. As shown in Figure 3, the energy transmitted by a television station can be reflected from the ground. This reflection can increase the effective range of a transmitter without increasing output power. As this energy is reflected back into space, the signals interfere with each other both constructively and destructively. This effect results in satellites being visible when they would not have been expected (constructive interference) or not visible when they were expected (destructive interference). These aspects of the signal environment define the performance envelope of what is required to illuminate orbiting satellites with sufficient energy for reliable detection and tracking.



For the purposes of data collection, Syracuse Research Corporation (SRC), with the assistance of Air Force Research Laboratory (AFRL/SNRD), installed government-owned recorders into the 30-meter Naval Research Laboratory (NRL) dish antenna system located at Pomonkey, MD. Due to technical limitations and scheduling constraints, only UHF data was collected. The satellites observed during this task were chosen based on their stable orientation and orbit, along with a relatively large radar cross section (RCS).

Table 1 contains the satellite passes collected in support of this task. For each pass, the rise, culmination and fade time are provided as well as the maximum elevation and minimum range (km). "Ch 1" and "Ch 2" show the two frequencies that were exploited for that pass. The column labeled "# Traces" shows the number of returns which were detected in the recorded data. A blank space denotes that either the data was not analyzed or the data was not saved due to a problem with the data collection process. The RCS column shows the radar cross section of the satellite in square meters as reported by the FPS-85 radar at Eglin AFB.

Table 1. Task 1 Satellite Data Collection Summary

#	SSC No	Date	Rise	Mid	Elev.	Range	Fade	Ch 1	Ch 2	# Traces	RCS
A	16609	17-Mar	12:50:17	12:55:25	86.4	379.77	13:00:32	19	15		396.55
B	24670	16-Mar	15:38:03	15:43:22	39.7	633.25	15:48:38	15	N/A		18.02
C	23019	16-Mar	18:32:49	18:38:30	55.9	572.84	18:44:08	15	16		37.56
D	23560	17-Mar	16:27:22	16:34:42	47.6	1024.4	16:42:00	19	17		30.96
5	16609	6-Apr	22:00:21	22:05:29	64.4	422.6	22:10:39	19	15	12	396.55
30	16609	7-Jul	15:50:49	15:55:54	63.3	414.1	16:00:56	34	38		396.55
46	16609	9-Jul	15:21:06	15:26:05	37.8	581.9	15:31:01	36	38	11	396.55

Task 2: Satellite Catalog Maintenance

Satellite Doppler range-rate and range data were collected on a variety of targets, for several illuminator-satellite-receiver geometries, including simultaneous multiple illuminators. This task was designed to demonstrate the potential contribution to satellite catalog maintenance, a function performed by the AF Space Surveillance Network. Achievable satellite position accuracies were determined as a function of the number of illuminators being exploited and the length of time in track. SRC collected target echo data from a variety of space objects of different sizes and orbit altitudes. All data in this task was processed to determine the number of transmitter echoes received.

For some passes having sufficient reflected energy, additional processing to derive range measurements was applied. These range values were created using a Time Difference of Arrival (TDOA) approach. This technique relies on matching the time phase of the direct path with the reflected signal. Due to the very weak reflected signals, only the horizontal synchronization pulses of the TV waveform were exploited. This technique yields range measurements that are ambiguous to 19.06667 km and accurate to 1200 m.

These range rate and range observations were compared to a "reference truth." For this comparison, a special set of laser calibration satellites was used with accuracies of better than ± 5 meters in position and a few millimeters per second in velocity. The calibration satellites used in the STAR demonstration include ERS-2 (23560), Topex/Poseidon (22076) and EGP (16908). Another critical component of this task was to quantify the minimum detectable object size as well as the maximum range of the system. This was accomplished by collecting data from various satellite sizes and at various ranges.

Task 3: Search Demonstration

This task was designed to demonstrate a rudimentary search capability. In addition to the catalog maintenance role, operational sensors should be capable of performing a search for new objects resulting from a launch or for reacquiring an object after an orbital maneuver. The required hardware and computational loading to perform this task was also evaluated and included in the design phase of the demonstration.

The demonstration used the results from Tasks 1 and 2 to develop an approach for the search case and appraise the expected performance. This appraisal examined trade-offs in integration time, detection sensitivity, and processing complexity. Also included was the ability to measure look angles, as well as range measurements and their impact on multistatic operations. The demonstration collected seven separate data passes to demonstrate the application of the multistatic approach to the search case. The data collection is summarized in Table 2.

Table 2. Task 2 Satellite Data Collection Summary

#	SSC No	Date	Rise	Mid	El	Range	Fade	Ch 1	Ch 2	# Traces	RCS
54	22076	9-Sep	13:47:13	13:58:19	88.3	1346.0	14:09:20	16	19	6	19.35
57	23179	9-Sep	17:27:34	17:36:11	48.9	1267.0	17:44:52	19	19		3.79
60	24297	9-Sep	20:23:48	20:31:47	39.7	1245.0	20:39:42	16	19		8.39
61	23189	10-Sep	12:35:11	12:44:09	52.8	1228.0	12:53:06	16	19		3.06
62	23342	10-Sep	13:53:26	14:00:14	84.0	669.0	14:06:58	16	19		5.33
63	23560	10-Sep	15:24:55	15:32:17	42.6	1098.0	15:39:34	16	19	6	30.96
65	25040	10-Sep	17:23:07	17:30:34	43.6	1074.0	17:37:57	16	19	4	14.91

During data processing, a series of assumptions were generated concerning the satellite's expected Doppler motion. Due to the very weak signals received, the presence of a satellite echo is not apparent without integration processing. When this integrated information was coupled with the look angles (azimuth and elevation), a first approximation of the satellites orbit could be derived.

Task 4: System Design

Consideration was given to the top-level design of a low-cost, transportable system for space object detection and tracking based on multistatic principles. Included in this phase was the development of an operations and maintenance (O&M) estimate and a plan to support the development of a concept of operations (CONOPS).

Using the data collected from the previous three tasks, the design of a real-time search and track multistatic sensor for space object surveillance was formulated. This design addressed a passive, receive-only, transportable phased array antenna incorporating electronic beam steering and multiple beam processing. The antenna configuration allows for the collection of angular information (to support search processing), unknown space object track and search filters and algorithms. The sizing of the antenna was parametrically scaled to space object range and size combinations. Signal processing, sizing, and the accuracy of satellite position processing algorithms were also appraised. From this system design, AFRL/SNRD and SRC developed an operations plan to support government CONOPS development. The plan includes system features and limitations, tracking accuracies, O&M cost estimates, and the availability of existing broadcast illuminators for use in worldwide, operationally realistic locations.

RESULTS

Demonstration data was collected during four periods from March to September 1998. The data reduction of 71 collection attempts is summarized in the following paragraphs. The information is categorized by task, and then by the specific goals of each task.

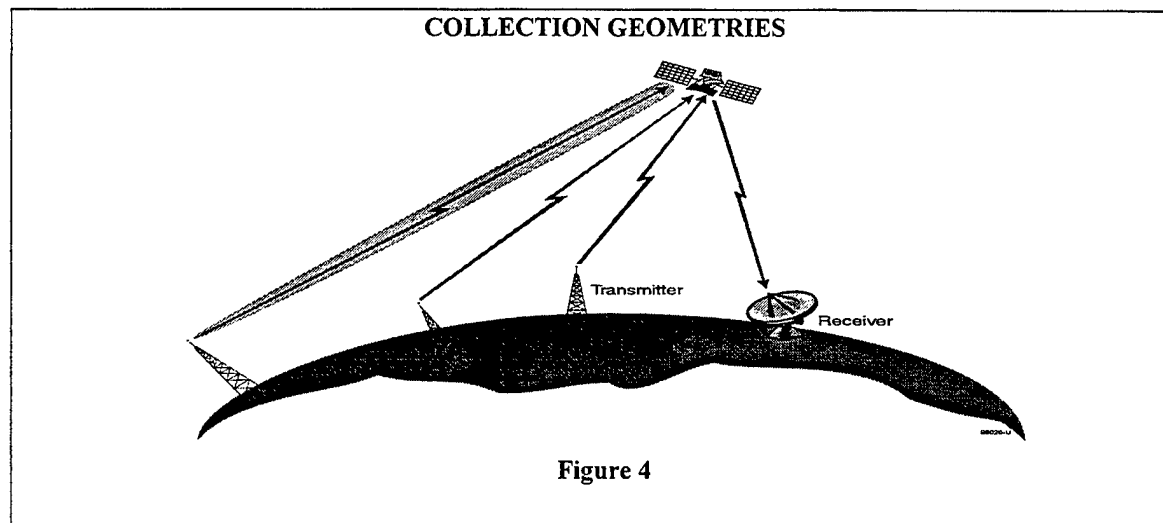
Task 1: Environment Characterization

Television transmitters are designed to transmit power to customers on the ground. In order to use this energy to detect and track satellites, it was first necessary to determine the amount of energy available for illuminating LEO satellites. To answer this question, data from four MIR passes were analyzed. Comparing the strength of the received signal as a function of elevation angle (relative to the transmitter) and adjusting for the range losses, a first order estimation of the actual antenna pattern was derived. Because of its large size, MIR was visible over a greater extent of elevation angles. Unfortunately, MIR has a complex shape with varying radar cross sections and the distribution of signal strengths did not produce as smooth a curve. Variations in the transmitted power (as much as 11 dB based upon the video content) represent an additional uncertainty in the analysis.

The optimum geometry with respect to the receive antenna is for an overhead viewing geometry. This minimizes both the range losses and the array loss factors (assuming a phased array pointed upward) for the receive leg. There are two basic collection geometries relative to the transmitters that must be considered which are illustrated in Figure 4. The optimum geometry from a detection point of view is the one illustrated by the left-most transmitter in the figure where the satellite is in the mainbeam of the transmitter. The additional energy supplied by the transmitter compensates for the additional range loss relative to the other geometry, which is illustrated by the right-most transmitter in the figure. In this latter geometry, the satellite is in the transmit antenna sidelobes. Consequently, the most favorable geometry now occurs when the satellite is nearly overhead minimizing the range losses, although the elevation sidelobes are lowest overhead. Since the elevation sidelobes are very nearly uniform at high elevation angles (above 30-40 degrees), this gives the next best geometry after the mainbeam geometry.

There was very little evidence of satellite detections in mainbeam geometries during this effort. Some data, which originated from the transmitter mainbeam, was obtained. However, the primary problem is that at UHF frequencies, the mainbeam of the antenna is too narrow and is pointed downward. This makes the geometry very susceptible to terrain masking of the mainbeam.

The geometry of the satellite ground trace with respect to the transmitter and receiver uniquely defines the expected Doppler offset. The bistatic range rate is the sum of the monostatic range rate of the satellite relative to the transmitter and the range rate of the satellite relative to the receiver.¹ When the resulting expected curve is scaled for the expected frequency, this frequency can be determined as a function of time. While element sets do not perfectly represent the motion of the satellite, this technique is sufficient for correlating satellite Doppler echoes to the transmitter.



Task 2: Satellite Catalog Maintenance

The first question to resolve was the minimum size satellite and maximum range that can be reliably detected. Unfortunately, traditional RCS measurements reflect an average monostatic cross section over a time period (usually a month). Due to the multistatic nature of the STAR demonstration, a satellite illuminated from various aspect angles provides different effective radar cross sections. For purposes of this analysis, the Eglin published RCS values were assumed to represent the actual size of the satellite.

Each pass was assigned a Figure of Merit (FOM) that equals the RCS in dB minus the range losses in dB, assuming a range equal to the average altitude of the satellite. The data points were then sorted into 5 dB bins by FOM and are summarized in Table 3. The probability of detection for a particular satellite pass can be calculated by computing the FOM and referencing the table. This analysis was repeated using actual ranges to determine the probability of detection for a given pass. Table 4 summarizes the results. The low number of samples in some bins reduce the confidence in the detectability percentage. Assuming a smooth curve of detection percentage vs FOM, a detection percentage is presented which may be more reasonable.

Using this approach, typical LEO satellites were evaluated. Roughly 64% of these objects should be detectable using a setup comparable to the demonstration equipment. If the antenna size is scaled upward, the percentage of these satellites detectable also increases. For example, a 63m x 63m (36 dBsm) antenna yields a capability to detect and track 89% of these satellites, a 100m x 100m (40 dBsm) antenna has sufficient sensitivity to see 94% of these satellites. Note that these detection estimates only apply when the maximum elevation angles with respect to the receiving antenna are comparable to those of the STAR experiments, i.e., above 30-40°.

Table 3. Detection Sensitivity Based on Altitude

FOM (dBsm)	# of Passes	Percent Dets
<-240	2	10
-240 to -235	5	30
-235 to -230	8	50
-230 to -225	13	85
-225 to -220	9	94
-220 to -215	4	100
-215 to -210	2	100
> -210	4	100

Table 4. Detection Sensitivity Based on Minimum Range

FOM (dBsm)	Number of Passes	Percent Dets	Smoothed %
<-240	9	28	27
-240 to -235	3	83	40
-235 to -230	6	50	50
-230 to -225	11	83	83
-225 to -220	14	92	91
-220 to -215	1	100	98
-215 to -210	2	75	99
> -210	2	100	100

The measurement accuracy is a function of several considerations including how well the broadcast frequency is known, the location of the transmitters and receiver, coordinate system incompatibilities, timing errors, and ionospheric propagation effects.

During the STAR demonstration, it was noted that transmitted frequencies were not necessarily constant but can vary with time. These uncertainties in the transmitted frequency require that a means to monitor the actual transmitted frequency as a function of time be established. In the demonstration, the direct path from the transmitters was collected through the sidelobes of the receiving antenna. In an operational system, a dedicated receiving antenna is recommended where possible. For transmitters outside of the radio horizon of the receiver, the direct path would be sampled remotely and the frequency transmitted back to the receiver station for inclusion in the data reduction.

Transmitter location and time registration errors cause Doppler shift errors on the returns from all transmitters. These errors manifest themselves as Doppler errors which are greatest near the zero Doppler crossover time. Doppler measurements are most insensitive to deviations in position or time at the beginning and end of the pass, when the Doppler shift remains relatively constant. At these locations, the satellite is far enough from the transmitter and receiver so that slight position offsets are relatively unimportant.

Some of the Doppler errors may be due to atmospheric fading on the direct path which, in general, is coming from a diffracted path over the horizon. Fading of less than 1 Hz on better paths has been measured at UHF frequencies during other programs². While this may be a factor, it is thought that direct-path fading would not cause systematic errors in the STAR data.

The errors experienced in this effort are dominated by systematic errors and are almost certainly caused by some combination of the above factors. With time and careful investigation, the systematic errors may be considerably reduced, leaving only random measurement errors. However, due to the time constraints of the STAR demonstration, these errors remain a subject for future work.

Table 5 shows the root-mean-square (rms) of the residuals between the observed and computed bistatic range rates for each of the satellite passes. The computed quantities are based on the available truth orbits. The rms for each transmitter is displayed as well as the average rms for the whole pass. The transmitter positions as supplied by the FCC database were used to compute the residuals. Notice that certain transmitters are associated with higher rms values than others. When these transmitters contribute to more than one pass, the rms values from the same transmitter tend to be consistent across passes. For example, transmitter WLTX has rms values of 3.334, 1.783, and 4.585 meters/sec which are relatively high values. Likewise, the transmitter WNPA has consistently high rms values of 5.209 and 3.269 meters/sec. This appears to indicate that certain transmitters have more residual error than others. The systematic nature of the residuals seems to point to errors in the transmitter position, but could also be due to a poor direct measurement of the transmitting frequency³.

Estimating and removing these errors is a cost-effective way to improve the observation accuracy. Correcting the transmitter position error and other errors could play an important role in improving the accuracy of the satellite trajectories especially in situations where accurately surveyed transmitter positions are unavailable.

STAR was expected to generate observations accurate to 40 cm/sec. An examination of Table 5 reveals that this was not realized. However, due to the multistatic nature of the demonstration, these errors did not reduce the ability of the demonstration to accurately generate satellite state vectors.

Individual state vectors were estimated from the observed data for each of the five passes in Table 5 and were compared with corresponding truth data. Figure 5 shows the best state estimates that were achieved by optimizing the temporal length of the batch interval in the differential correction process. All of the position errors are less than 2 km. Passes 12 and 19 yielded results that were less than 250 m.

Table 5. Doppler RMS Values.

Pass 3 Satellite 23560 6 April 1998 Average RMS = 2.166 m/sec				
Transmitter	Latitude (deg)	Longitude (deg)	Height (meters)	RMS (m/sec)
WLTX	34°.09694	-80°.76417	614	3.334
WUNM	35°.10500	-77°.33750	575	1.365
WNPA	40°.18083	-79°.16278	936	5.209
WOIO	41°.38750	-81°.69530	614	0.612
WCDC	42°.63722	-73°.16861	1116	1.201
Pass 12 Satellite 23560 9 April 1998 Average RMS = 1.407 m/sec				
Transmitter	Latitude (deg)	Longitude (deg)	Height (meters)	RMS (m/sec)
WLTX	34°.09694	-80°.76417	614	1.783
WUNM	35°.10500	-77°.33750	575	0.555
WGPX	36°.24833	-79°.65580	461	0.901
WBOC	38°.50444	-75°.64310	310	0.606
WNPA	40°.18083	-79°.16278	936	3.269
WOIO	41°.38750	-81°.69530	614	0.663
WCDC	42°.63722	-73°.16861	1166	1.080
Pass 19 Satellite 23560 10 April 1998 Average RMS = 2.392 m/sec				
Transmitter	Latitude (deg)	Longitude (deg)	Height (meters)	RMS (m/sec)
WLTX	34°.09694	-80°.76417	614	4.585
WUNM	35°.10500	-77°.33750	575	0.396
WNEP	41°.18278	-75°.87250	889	0.989
WCDC	42°.63722	-73°.16861	1116	0.963
Pass 25 Satellite 22076 6 July 1998 Average RMS = 1.134 m/sec				
Transmitter	Latitude (deg)	Longitude (deg)	Height (meters)	RMS (m/sec)
WATL	33°.80750	-84°.34060	617	1.654
WCNC	35°.34690	-81°.17080	830	0.908
WUNP	36°.29110	-77°.83610	433	0.657
WTVQ	38°.03420	-84°.39420	598	0.989
WOLF	41°.43583	-75°.72917	735	1.404
Pass 36 Satellite 23560 8 July 1998 Average RMS = 3.196 m/sec				
Transmitter	Latitude (deg)	Longitude (deg)	Height (meters)	RMS (m/sec)
WMMP	32°.78750	-79°.85000	234	3.478
WNEH	34°.37250	-82°.16750	415	2.655
WPXR	37°.19306	-80°.15806	1197	1.706
WBAK	39°.23278	-87°.39694	462	4.164
WADL	42°.55417	-82°.88750	370	3.620

Extensive parametric studies were conducted by SRC to assess the orbit estimation process in terms of the accuracy of the computed orbits. The differences between the estimated satellite positions and the true positions, as shown in Figure 5, are not correlated with the average rms values for each pass. In general, the accuracy of the results depend on several interrelated factors. These include the number of observations, the inclusion of bistatic range in conjunction with range-rate, the number of transmitters used in the multistatic configuration, the aspect angles associated with the multistatic viewing geometry, and how thoroughly the systematic biases have been removed from the observations.

When processing only Doppler information, and assuming that measurement errors are about 1 m/s, eight to twelve transmitters are required to provide a state estimate that is within 100 m of the truth. When range measurements are also available (limited by the available signal strength and the availability of the transmitted direct path for a zero range reference), four to six transmitters are required for the same 100 m accuracy. The number of transmitters required also depends on how uniformly the transmitters are geographically distributed relative to the receiver.

Task 3: Search Demonstration

Search mode refers to the tracking and estimation of unknown satellite orbits where an initial state vector estimate is not available. This mode is much more difficult than tracking and updating known satellite orbits. In the most general unknown satellite case, nothing is known *a-priori*; and the search is conducted by initially using look angles and subsequently using bistatic observed quantities.

Because of the large antenna size required for sensitivity and the correspondingly small size of the beamwidths, performing an actual search by scanning an antenna beam is not practical. There are too many beam positions required for a reasonable amount of search space. Update times are too long, considering that a satellite can move at rates on the order of 1° per second and that dwell times are on the order of two seconds. It is more efficient to use a fixed angular region of coverage. A fixed set of beams could be steered to cover some region of angular space which is long enough to intercept a number of satellites and sufficiently wide to collect enough data on a satellite passing through so that an angles-only track can be determined. The angle track can then be used to predict the look angle of the satellite and thus steer a beam or cluster of beams towards the satellite in real-time. Once this crude two-line element set is generated, the search task simplifies into the satellite catalog maintenance task described previously⁴.

One method of search used for STAR was to provide a search volume. In this case, only a time to start collecting data (not necessarily the start of the pass), and a general pass direction, such as north to southwest, was provided. The Pomonkey antenna was steered as usual, following the known satellite orbit. This was necessary to ensure that sufficient data was collected since the analysis was not done in real-time.

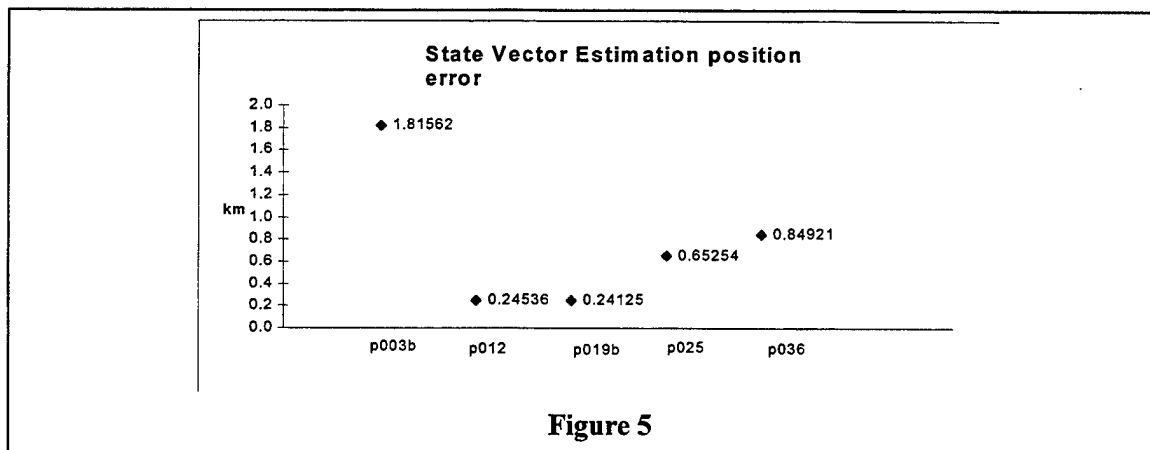
Since *a-priori* information on the satellite was not available during the demonstration, the technique used to detect the satellite is to construct a bank of range-rate filters that are matched to a series of discrete Doppler rates (matched filter). The reflected signal is not ordinarily visible without performing a coherent integration. Since the Doppler profile is not known, this integration cannot be accomplished. This bank of matched filters will not provide a satellite track, but discrete detections when the integration is coherent with the assumed Doppler rate. The process is illustrated graphically in Figure 6.

Each matched filter has a constant Doppler slope. The filter is matched to the satellite dynamics when the slope of the matched filter equals the slope of the satellite Doppler curve. Figure 6 shows a characteristic S-shaped Doppler curve for the satellite and three parallel lines representing the matched filter. The matched filter history is represented by the center line. The others are simply shifted versions of the actual matched filter history and illustrate the points in time when the filter is matched to the satellite Doppler shift. At the times when the slopes are equal, a match is obtained and maximum processing gain is achieved. The match, and consequently the signal-to-noise ratio (SNR), typically degrades quickly with time around the time of match. At this time, the satellite returns from a curve whose knee occurs at the time of match for the given filter. The measured frequency of the knee is the frequency difference between that of the nominal filter (illustrated by the center line in the figure) and the actual frequency of the satellite at the time of match.

Task 4: System Design

The STAR demonstration was conducted with a 30-meter mechanical reflector antenna. The experimental results showed that this hardware was somewhat limited in flexibility and sensitivity relative to the desired operational performance goals. However, the experimental results can be used as a basis for extrapolating to a more useful operational system. The fundamental method for improving sensitivity is to increase the antenna aperture.

The proposed STAR system consists of a large-aperture passive phased array antenna with centralized steering, beamforming, and signal processing. Although the beamforming must be local to the antenna, the beam signals can be transmitted to a remote signal and data processing location, and the array can be controlled from the remote location. A similar interface could be made between the signal processing and data processing functions. Because of the large array dimensions, active electronics must be provided at the element level, to establish the system noise figure, and to overcome RF cabling losses.

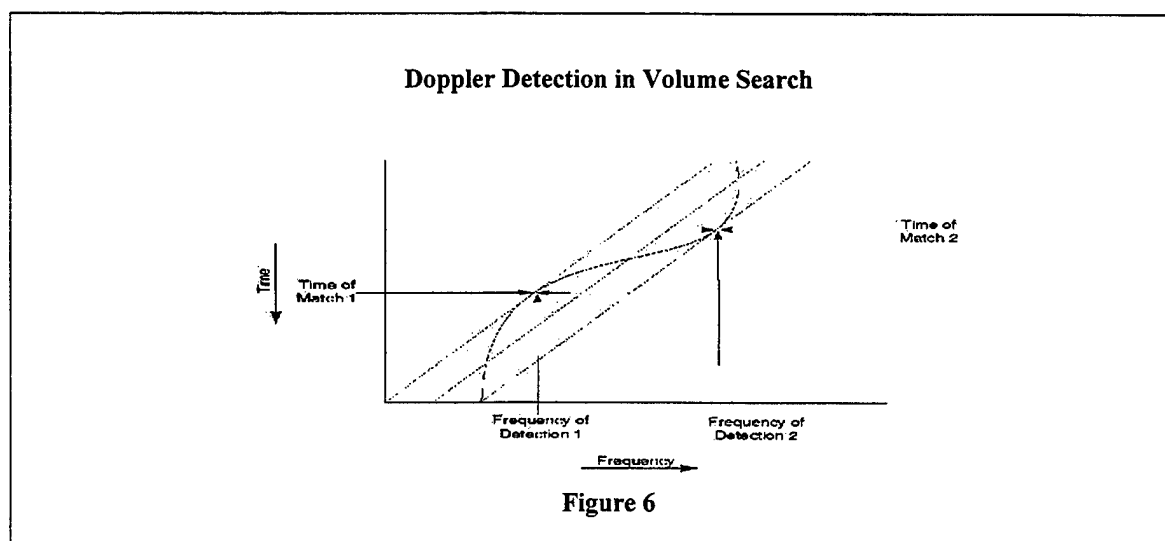


Although the antenna and RF hardware can be made somewhat wide in bandwidth, a single cost-effective antenna array cannot be made to cover both the UHF and VHF television bands. As a result, two similar designs are proposed: one for the UHF band and one for the VHF band.

Auxiliary horns or small dish antennas will be used to collect direct-path signals. These will be mechanically steerable to point them at the transmitters of interest. Separate receivers and digitizers will be required for each antenna. The digitized data will be used as a processing reference as previously discussed.

Concept of Operations

The STAR concept is designed to fill coverage gaps within the current SSN. These gaps have a significant impact on the maneuver detection capability. STAR was not designed for, nor is it capable of supporting, debris cataloging and catalog maintenance on very small objects. STAR is not a volume surveillance system; it must instead be cued and supplied with an approximate space-time target location, or with a specified and limited search volume. The niche STAR fills within the SSN is the ability to accurately track objects within existing coverage gaps in a cost-



effective and transportable manner. This can be done since maneuvering satellites generally adjust orbit period. This type of maneuver changes the satellite's arrival time at a particular sensor. However, when predicted look angles are adjusted with respect to inertial space, the STAR system can provide observations to update the satellite element set.

The STAR concept relies on available ambient energy to illuminate a target. The availability of this energy depends on the number of nearby transmitters, their broadcast schedule and the amount of energy they typically produce. In

addition, the location of other TV broadcast assets must be addressed due to their ability to interfere with receiving satellite echoes.

To make efficient use of the STAR receiver and signal processor, it is desirable to be able to produce a multistatic localization solution using multiple transmitters in a single TV channel. This minimizes the hardware requirements (and the cost). Therefore, we are interested in finding a location where at least six transmitters are operating on the same television channel and where the direct path transmission can be received.

Most TV transmitters radiate omnidirectionally in azimuth. However, station owners do not wish to spend money radiating in directions where there is no audience, and the azimuth coverage is sometimes modified accordingly. For example, coastal stations tend not to radiate out to sea. All of these factors must be considered when selecting a site to exploit broadcast television signals.

There are three basic kinds of television transmitters: regular broadcast transmitters, translators, and low power transmitters. Regular broadcast transmitters are high-powered and suitable for use as sources of illumination. Conversely, translators and low-power television transmitters are not suitable sources. Nevertheless, along with translators, low-powered transmitters must be taken into consideration when determining a site for a system, since they can potentially cause co-channel interference or receiver saturation. During the demonstration, if a TV transmitter was closer than 100 km to the receiver, that frequency generally could not be used. This is due to the direct path signal saturating the receiver and degrading the sensitivity to receive the much weaker reflected satellite return.

SUMMARY

The data collected within the STAR demonstration has shown great promise for operational utility. This demonstration was intended to show a quick 'proof of concept' for STAR. Although no residual capability exists as a result of this demonstration, the lessons learned can lead to a cost-effective procurement or follow-on demonstration.

It is important to note that the STAR system is not as capable as other, more expensive systems. The STAR system instead provides a somewhat lesser capability at a significantly lower cost. The STAR concept should be evaluated not as a standalone solution but in terms of its augmentation potential.

REFERENCES

- [1] Racca, Robert A., "Satellite Tracking Using Ambient RF (STAR): Orbit Estimation", 10 February 99
- [2] Ogrodnik, Robert, "Satellite Tracking Using Ambient Radio Frequencies (STAR)", 4 January 99
- [3] Storz, Mark, "Satellite Tracking Using Ambient RF (STAR): Calibration Methodology", 10 February 99
- [4] Thomas, Dan, "Satellite Tracking Using Ambient RF Final Report", AFRL Contract F30602-97-C-0237, P00002, January 99
- [5] Sennitt, Andrew G., editor-in-chief, *World Radio TV Handbook*, 1998 Edition, Windsor Books International, Oxford, UK, 1998.

Color Photometry of GEO Satellites

T. E. Payne (Schafer), D. J. Sanchez (UPR), S. A. Gregory (UNM), L. G. Finkner (Boeing), E. Caudill (AFRL), D. M. Payne (Schafer), L. Kann (AFRL), C. K. Davis (Boeing)

Abstract

The Air Force Research Laboratory Directed Energy Directorate (AFRL/DE) Space Surveillance Technologies Branch is pursuing non-imaging techniques to obtain information on the identity and status of geosynchronous (GEO) satellites. On-going experiments have provided visible color photometry data on several GEO satellites for space object identification (SOI) purposes. These data have been analyzed using statistical probabilities to produce quantified identifications of satellite bus types and the satellites themselves. Additional analysis has been performed to ascertain the relative usefulness of each photometric bandpass in order to optimize this color photometry technique. The results and conclusions of this work to-date are presented.

Introduction

GEO satellites pose unique challenges to the Space Surveillance Network to track, identify, and to determine anomalous behavior because the majority of them are three-axis stabilized and have no relative motion with respect to the observer. This stability makes radar tracking and imaging not feasible unless the satellite has become unstable, parts of the satellite move, or the orbit is not truly geosynchronous. Therefore, optical tracking and photometric signatures are the tools that are used most often to track, identify, and determine status or anomalies. Space object identification (SOI) of GEO satellites is a difficult task given the faint, unresolved character of the optical signal. Surveillance deficiencies have been identified related to detection of changes of status of GEO, anomaly resolution, general GEO intelligence, and the lack of global coverage. SOI needs include identification of class and type, status determination (operational or not), and anomaly resolution. Potential solutions have been identified with color photometry as one possibility to aide in resolving cross-tags and status determination. [1]

Color photometry, also known as multi-spectral photometry, and in some circles as hyperspectral which connotes very narrow bands has its origins in astronomy. Astronomical photometry is defined as the measurement of the apparent brightnesses of an object in various wavelength bands in the optical or infrared regions of the electromagnetic spectrum. The brightnesses are usually referred to in magnitudes

where $m_1 - m_2 = -k \log_{10} \left(\frac{f_1}{f_2} \right)$. The magnitudes assigned to the objects are m_1 and m_2 with energy

fluxes f_1 and f_2 and k is a constant. The minus sign is chosen so that brighter objects have smaller numeric values of m . Since the definition of magnitude involves two objects, magnitude is a relative concept. If a photometric system with several filter bands at different wavelengths is used, by taking the difference in magnitudes measured in two different bands, color or a color index can be formed. For instance, if the standard Johnson broadband filter system is used, the filter bands are denoted U, B and V. The wavelengths corresponding to those bands are shown in Figure 1. Then a color index can be defined as

$$B - V = K - 2.5 \log \frac{\int_0^{\infty} F_B(\lambda) d\lambda}{\int_0^{\infty} F_V(\lambda) d\lambda}; \text{ where } K \text{ is a constant. } F_x \text{ is the observed energy flux through filter}$$

x. In reality, the infinite integral is cutoff by the finite extent of the filter bandpass. So a color index essentially measures the ratio of flux between characteristic wavelengths. [2] A larger numerical value for the color index indicates a redder color, while a smaller numerical value indicates bluer color.

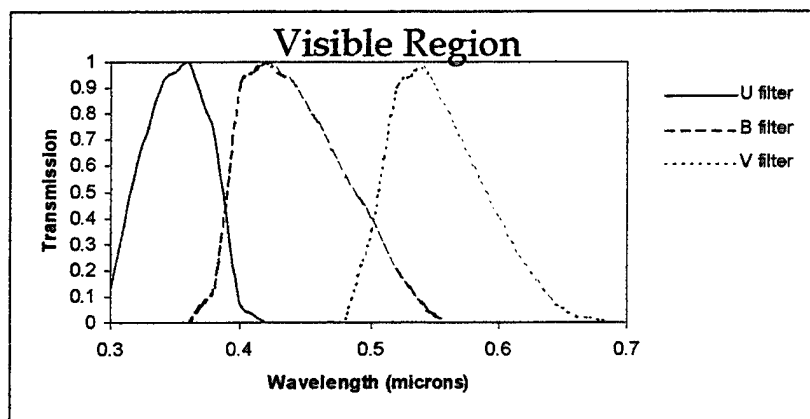


Figure 1. Standard Johnson filter bands U, B, V

Previous work supported by the AFRL Directed Energy Directorate (DE) on simulations of spectral signatures (reflected electromagnetic spectrum off GEO satellites) concluded that color photometry was a promising technique for addressing problems in GEO SOI. [3] [4] Additionally, color photometry observations were sponsored by AFRL/DE showing that different satellites had different color characteristics. [5] Prior photometric works by John V. Lambert (Boeing) and W. I. Beavers (MIT/LL) have also shown that information about the satellite was available in the brightnesses and the colors. The difficulty in any optical non-imaging technique is how to exploit that information and yield quantified variables about the satellite's identity and status. This has been the goal of the current on-going effort supported by AFRL/DE.

The current work presented here has endeavored to classify the satellite type by using its photometric colors. The extended standard Johnson system has been used to-date. These filters are designated B, V, R, and I. The properties of these filters are summarized in Table 1. [6] The current observations are being made at the Capilla Peak Observatory (CPO) outside of Albuquerque, NM. The U filter has not been used to-date due to lack of transmission at these wavelengths at this observatory. The current set of observations span from June 1998 to the present. As of this writing, 175 observations have been taken on 10 satellites, some of which are in a cluster. Table 2 contains the list of satellites.

Table 1. Johnson Filter Characteristics

Filter	Mean Wavelength (Å)	FWHM (Å)
B	4417	960
V	5505	827
R	6690	1744
I	8000	1425

Table 2. Satellites.

Satellite Name	Type
Solidaridad 1	Hughes 601
Solidaridad 2	Hughes 601
Anik E1	GE Satcom 5K
Anik E2	GE Satcom 5K
DBS 1	Hughes 601
DBS 2	Hughes 601
DBS 3	Hughes 601
AMSC 1	Hughes 601
Gstar 4	LMAS 3000
Spacenet 4	LMAS 3000

Data Reduction and Analysis

The data is obtained using a CCD camera with the B, V, R, and I filters. Observations of stars are made for radiometry and color calibrations. Sky flat fields, bias, and dark frames are taken and used in the data reduction to minimize noise and errors in the photometric data. The instrumental magnitude is calculated using the Image Reduction and Analysis Facility (IRAF) software package. IRAF contains a large selection of computer programs for general image processing, reduction and analysis of optical and IR CCD data. [7] The instrumental magnitude ($m_{instrument}$) is obtained by measuring the intensity on (I_{on}) and off (I_{off}) the object of interest using the IRAF software and using the relation

$$m_{instrument} = -2.5 \log \left(\frac{(I_{on} - I_{off}) \times N_{pixels}}{t_{exposure}} \right); \text{ where } N_{pixels} \text{ is the number of pixels subtended by the}$$

object and $t_{exposure}$ is the exposure time of the observation. The instrumental magnitude is then converted to a standard magnitude using a relation between the standard magnitude and the instrumental magnitude as shown in Figure 2. All other filters are similarly treated. This process removes the effects of the Earth's atmosphere and the telescope. The final standard magnitudes have an uncertainty of .03 magnitudes and are exoatmospheric.

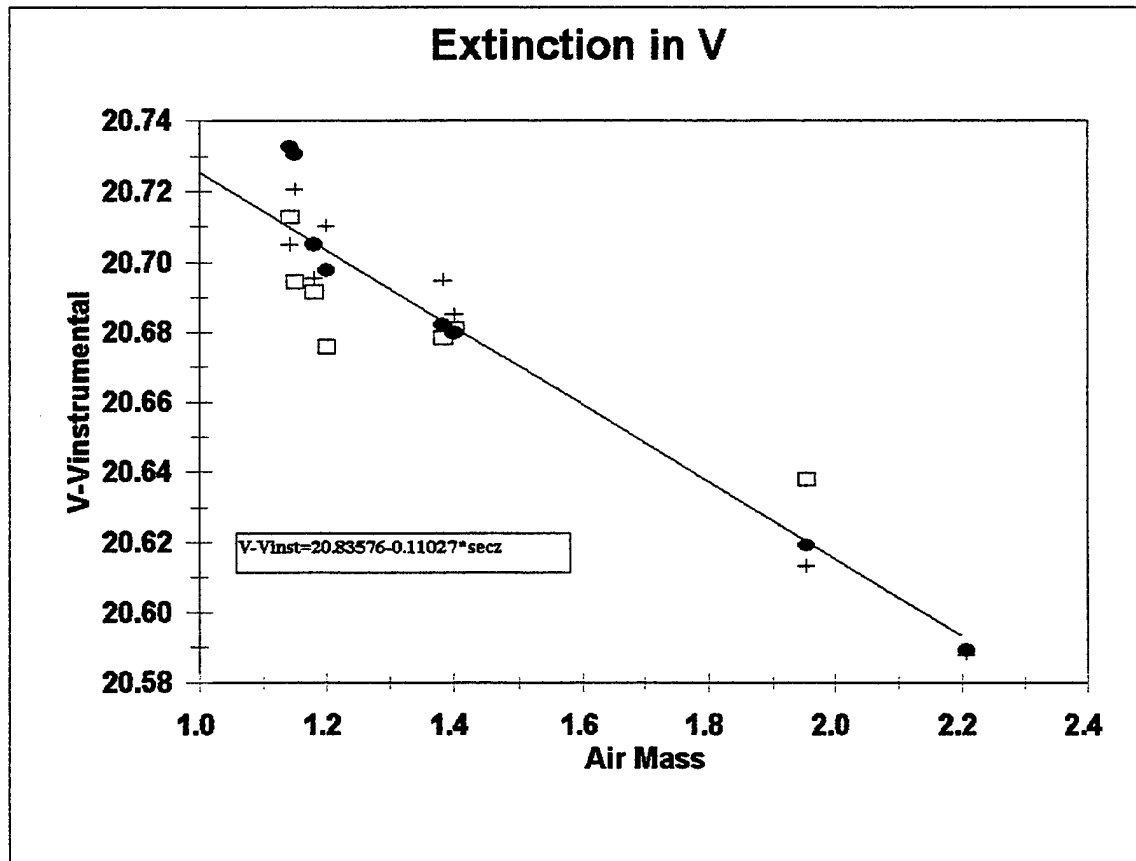


Figure 2. Extinction in the V filter.

Photometric Analyses and Results

As can be seen in Table 2, all the satellites under consideration are three-axis stabilized. Their features are very similar as is apparent in Figure 3. The color photometry data taken on these satellites was processed using two different types of groupings. One group separates the 10 satellites into 3 classes by type of

payload. The second group separates the satellites into 5 classes by type of satellite. Table 3 shows these groupings.

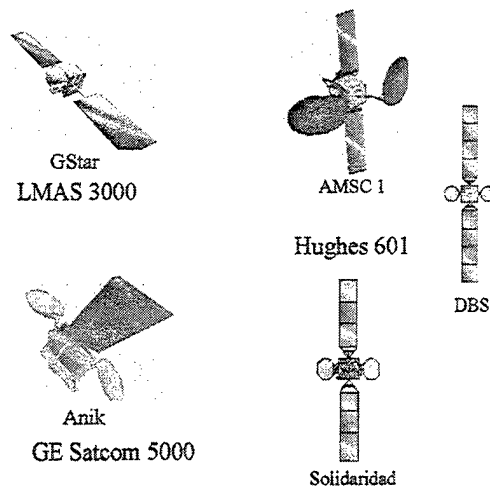


Figure 3. Depictions of some of the satellites.

Table 3. Satellite groupings.

Satellite Name	Type	Group 1	Group 2
Solidaridad 1	Hughes 601	1	1
Solidaridad 2	Hughes 601	1	1
DBS 1	Hughes 601	1	4
DBS 2	Hughes 601	1	4
DBS 3	Hughes 601	1	4
AMSC 1	Hughes 601	1	5
Anik E1	GE Satcom 5K	2	2
Anik E2	GE Satcom 5K	2	2
Gstar 4	LMAS 3000	3	3
Spacenet 4	LMAS 3000	3	3

For illustrative purposes, Figures 4 – 5 plot the data when magnitudes and colors are plotted against one another. The data is plotted using Group 1 designations. By themselves, these data do not separate out the satellite classes completely.

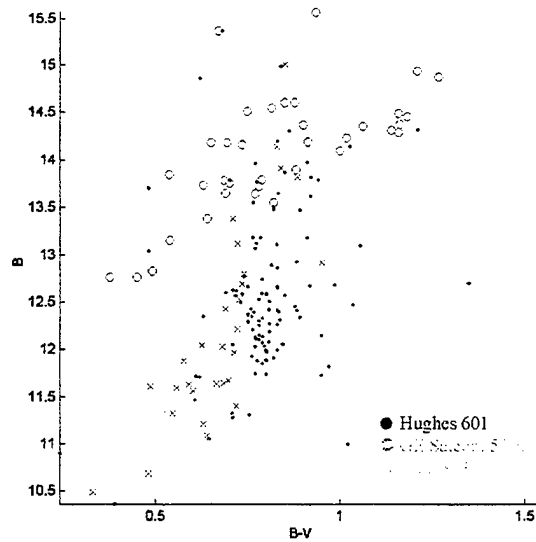


Figure 4. Color-Magnitude Plot

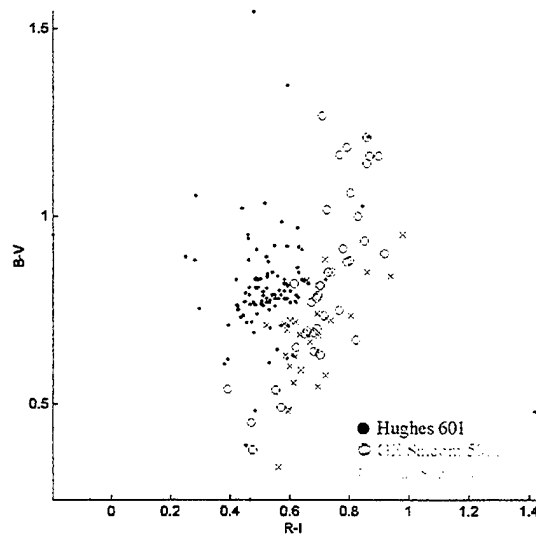


Figure 5. Color-Color Plot

Therefore, it was determined that pattern recognition algorithms may be applicable to this problem and may separate the classes better. In addition, the application of these algorithms would enable quantified confidence levels to be calculated on the ability to correctly identify the satellite class. Three different discriminants or classifiers are currently being tested: K-nearest neighbor, Gaussian classifier, and Mahalanobis distance. These are each used in combination with principal component analysis to obtain a percentage of correct identification of each group. A brief description of each algorithm follows.

In pattern recognition terminology, the magnitude and color data creates a feature space. A feature space is defined by the different features of the data. These features describe the data in terms that are of interest for a specific problem. For instance, medical data on people can define a feature space whose dimensions are height, weight, age, and sex. In this case, the dimensions of our feature space are the magnitudes B, V, R, I, and the colors, B-V, V-R, and R-I. Feature space, in general, is a n-dimensional space that is defined by the properties that describe the population of interest.

Principal component analysis is a common type of preprocessing that aims at reducing the number of input variables or the dimensions of the feature space while maintaining the most significant relationships reflected by the data. This technique attempts to identify an m -dimensional subspace of the n -dimensional feature space that seems most significant, and then projects the data onto this subspace. [8]

K-nearest neighbor is a classifier in which the position in feature space of the k -nearest neighbors whose identities are known is compared with the position of the data point whose identity is to be determined. This relative position is used to determine the identity of the unknown data point, where k is an integer variable ranging from 1 to the number of data points minus one. With the current data, the best results are obtained when $k = 3$. For example, if the three closest data points in the feature space to the unknown data point are identified as Hughes 601 (using Group 1), then the unknown data point is identified as Hughes 601 with 100% probability.

The Gaussian classifier fits a Gaussian with a mean and standard deviation in feature space to each class. An unknown data point's location in feature space is then compared with the position, shape, and extent of the Gaussians in the feature space. If the unknown data point is at a location in feature space that is described by only one Gaussian, then its identity is known to 100% probability. If that location is shared by two Gaussians, then the Euclidean distance from the mean of each Gaussian is computed and relative probabilities are generated that the unknown data point belongs to each population represented by each Gaussian. [9]

The Mahalanobis distance is used in the algorithm above instead of the Euclidean distance. When the Gaussian classifier is used, there is a possibility of error unless all the Gaussians have the same shape and extent and the probabilities are equal that the unknown data point is any of the classes. So, classification based on the nearest Gaussian may be near optimum only if appropriate additional weights are introduced by using a Mahalanobis distance. [10]

These color photometry data were processed using the above techniques. Their results were then studied to determine which filter combinations, groups, and classifiers yielded the best results. When the data was combined using Group 2, the results were much poorer than when the data was combined using Group 1. One major factor is the limited amount of observations. The results for Group 1 using the three classifiers are shown in Figures 6 - 8. They show correct identification using k-nearest neighbor, 81.14% using the Gaussian and 86.29% using the Mahalanobis distance. The results for Group 2 using k-nearest neighbor are 52.00% correct identification, using a Gaussian they are 45.71%, and the results are 55.43% using the Mahalanobis distance.

Ground-Based Imaging and Inspection of Commercial Satellites

L.A. Kann, D.G. Voelz, J.L. Kann, (Air Force Research Lab, Phillips Research Site, Kirtland AFB, NM)
and J.M. Anderson (SAIC, Albuquerque, NM)

Abstract

For 25 years the US Air Force has investigated methods and technology for obtaining high-resolution optical images of satellites using ground-based telescopes. Optical imaging of low-earth-orbit (LEO) spacecraft requires the use of specialized assets such as fast-tracking telescopes, low-light camera systems, and image recovery and processing expertise. Currently, these assets exist almost exclusively in the DoD - primarily in the Air Force. Optical images of commercial spacecraft could aid in diagnosing satellite malfunctions and failures. A small program has been established to explore the use of Air Force ground-based optical imaging technologies and assets to detect potential anomalies that may occur on commercial satellites, while driving new image analysis software to improve the capabilities of current ground-based optical systems. In this paper we present an overview of the project and discuss the motivations and expectations for the effort. We will describe the technical efforts underway, including hardware and software development.

1.0 Introduction

Imaging through the atmosphere requires highly specialized equipment, very large telescopes, and specialized post processing algorithms among other things. There are two different techniques to achieve imaging through the atmosphere - active imaging and passive imaging. Active imaging consists of illuminating the object in space with an artificial source of light, such as a laser. Passive imaging relies on natural light, such as sunlight or earthshine, to illuminate the object. This effort will deal strictly with passive imaging for reasons which include the fact that the active imaging technology is not yet perfected, it is much more expensive, and passive imaging has proven to provide better imaging results so far. At the present time, there is no easy way to look at a LEO satellite orbiting the earth. LEO satellites typically orbit at a distance of 500 to 1000 miles (800 to 1600 Km) above the earth. Currently, most existing commercial telescopes are not powerful enough to resolve features on satellites at these distances through the turbulent atmosphere.

This year the number of commercial satellite launches has outpaced those of the military, with an accelerated trend expected. Historically, the Air Force has been responsible for identifying and tracking all man made objects in space. The Air Force Research Laboratory (AFRL) has supported this activity by providing research and development in the advancement of ground based optical imaging of satellites. By exploring and quantifying the utility of optical imaging assets and technologies to commercial satellite stakeholders, AFRL is taking a step in the direction of providing a valued service to the commercial community, and at the same time offering the possibility of reduced cost and greater efficiency to the Government.

In addition to benefiting the commercial sector, byproducts of this program should help the USAF as well. Ongoing development of atmospheric correction algorithms to improve image quality and image exploitation algorithms to assist in detecting spacecraft anomalies will greatly improve the USAF's capability to gather, process and exploit space surveillance imagery for military intelligence gathering purposes. Other military benefits include improved understanding of ground based imaging capabilities, improved techniques to fuse satellite models with imagery to detect and understand anomalies using real field data, and potential improvements in the fidelity of current simulations codes such as TASAT (Time-Domain Analysis and Simulation for Advanced Tracking). All of these improvements will help the commercial and military sector's long range space surveillance capabilities. In this paper, we provide the background and approach for a dual use space surveillance effort.

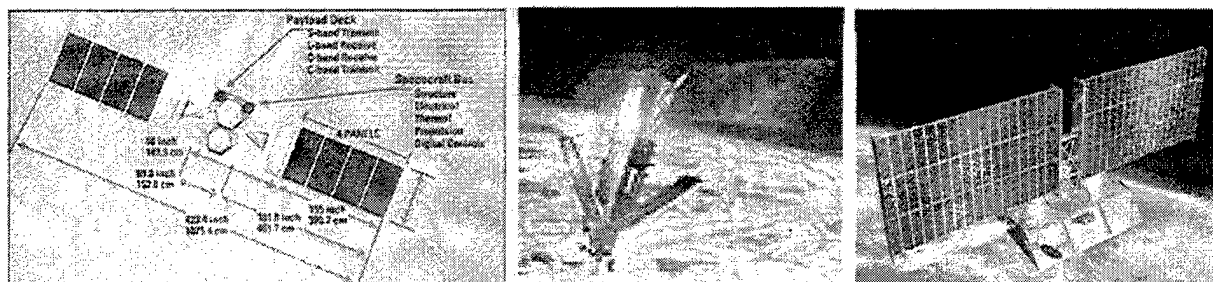
2.0 Motivation for the Commercial Marketplace's Interest in Satellite Imagery

The commercial satellite market is of interest to many parties, including satellite developers, manufacturers, insurers, constellation owners, and even the US Government. While commercial satellites are of great interest to satellite owners, manufacturers, and insurers, they are also of interest to the US forces as a potential primary means of communication. It is estimated that the launch services and space insurance market alone generated

approximately \$10 billion in revenues for 1998. With more than 250 satellite launches planned, the investment in commercial, military, and science satellites is forecasted to boom in the new millennium [1]. With the aggressive growth of satellite constellations and applications, the satellite marketplace is becoming a dynamic, high-growth environment, creating a highly competitive environment. According to Jane's Military Communications 1996-97, one estimate of the amount of money that US forces currently spend on commercial satellite use is \$250 million. Therefore, there remains the long-term possibility of substituting bought-in commercial capacity rather than spending an estimated cost of \$30 billion replacing all US dedicated military spacecraft in the period from 2003-2015 [2].

LEO satellites typically cost millions of dollars per vehicle. When taking into consideration the entire cost of the constellation, including design, production and deployment of the satellite constellation, the price is generally in the billions of dollars. Most LEO satellites are insured for problems such as an unsuccessful launch, collisions, and "in-orbit" failures amongst other things. Knowing why a satellite has failed could have impact upon future design specifications, creating more efficient satellites. In addition, such information could help keep the costs of insurance down. The ability to examine spacecraft from the ground (using optical and/or radar systems) can aid the commercial sector by helping to resolve or explain unknown on-orbit problems, assess the status of satellites presumed to be non-operational, verify telemetry diagnostic data, and provide information for design improvements and insurance claims.

For illustrative purposes, we take a closer look at a few LEO constellations that are currently in-orbit or are destined to be there in the near future. Satellites in these large constellations are potential targets for this effort. These satellite constellations are divided into three basic categories, based upon the satellite's operating frequency. Little LEOS operate in the 0.8 GHz range, big LEOs operate in the 2 GHz or above range, and Mega-LEOs operate in the 20-30 GHz range [3].



Figures 1-3: The Globalstar satellite [4], the Iridium satellite [5], and the Teledesic satellite [6].

The following chart describes some details of three major LEO constellations, with Iridium being the forerunner for the LEO satellite constellation completed in 1998 [7].

	Globalstar	Iridium	Teledesic
Category	Big-LEO	Big-LEO	Mega-LEO
No. of Satellites	48 active + 4 in-orbit spares	66 active + 6 in-orbit spares	288 active + 12 in-orbit spares
No. of Planes	8 planes (6 satellites/plane)	6 planes (11 satellites/plane)	12 planes (24 satellites/plane)
Altitude	1410 km	780 km	1350 km
Cost*	\$2.2 Billion	\$3.7 Billion	\$9 Billion
Period (minutes)	113	100.1	98.8
Satellite visibility	16.4 minutes	11.1 minutes	3.5 minutes
Size	10.75m x 1.5m	13m x 4 m	not available

* Cost includes design, production and deployment of the satellite constellation.

Figure 4: Chart describing three major LEO satellite constellations.

Since the number of LEO satellites/constellations orbiting the earth is rapidly increasing, and the rate at which they travel is great (~17,000 mph), the risk of a satellite colliding with another satellite or space debris is steadily increasing. According to the United States Space Command (USSPACECOM), which closely tracks all space objects, there are currently more than 8,000 objects orbiting the earth [8]. A lot of these objects are not satellites but space junk, which could be anything from a non-functional satellites to a satellite part to garbage from the shuttle. At the rates of speeds these satellites travel, the smallest object, such as a nut or bolt, could cause tremendous damage to the satellite. A visual inspection of a LEO satellite might provide information that could help determine if the satellite has collided with something or if the satellite has physical damage to it's exterior. In addition, any other changes to the satellite's structure and/or it's orientation could be verified from ground based imagery.

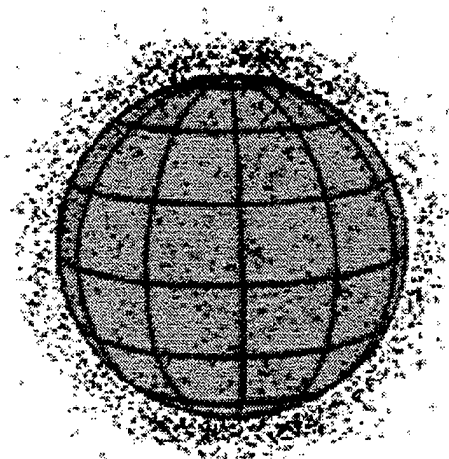


Figure 5: Graphical display representing all of the 8,000+ objects larger than a softball currently circling the globe.

In 1997, a small bit of debris the size of a paint fleck collided with the space shuttle Discovery punching halfway through its windshield, and a French-made Cerise satellite was completely destroyed when it collided with a discarded rocket body [9]. When a satellite collision occurs, the satellite is not just destroyed but generates more space junk, further increasing the risk of a collision. Because of this increasing problem, improved space surveillance/tracking capabilities is becoming increasingly important to both the military and commercial sectors. Therefore, the necessity to better understand the potential "worth" of such data against real space objects is critical to characterizing and improving existing and future systems.

3.0 Air Force Research Laboratory's Assets and Technologies

In this section we describe the existing AFRL's assets as well as simulation and analysis tools, that may be used on this effort.

3.1 The Starfire Optical Range

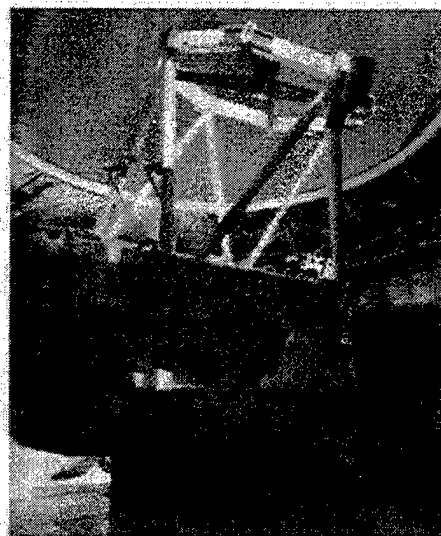


Figure 6:
SOR's 3.5-meter telescope

The Air Force Research Laboratory's Starfire Optical Range (SOR) is a world-class optical research site located on Kirtland Air Force Base, New Mexico. The primary mission of the SOR division is to develop and demonstrate optical imaging and wavefront control technologies to support Air Force aerospace missions. Experiments in adaptive optics and beam control for laser propagation and imaging applications are conducted on four major optical mounts, which are briefly described below. All three mounts are elevation over azimuth designs, and all are capable of tracking low earth orbit satellites [10].

3.1.1 The SOR 3.5 Meter Telescope

The SOR 3.5-meter telescope is currently the world's largest operational telescope capable of tracking low-earth orbit satellites. Using adaptive optics, the telescope is capable of resolving basketball-sized objects 1,000 miles out in space. A detailed description of the telescope and adaptive optics system is available in two previous papers [11,12]. The telescope is a classical Cassegrain optical design with a coude path. It has an f/1.5 parabolic primary mirror and a hyperbolic secondary mirror producing 1 milliradian of unvignetted field. The honeycomb-design borosilicate glass primary mirror weighs 4,500 pounds and has a one-inch thick glass facesheet. The surface is polished to a precision of 21

nanometers, 3,000 times thinner than a human hair. The mirror is supported by a system of 56 actuators that maintain the figure of the mirror as the gravity vector changes. An image derotation K-mirror is installed in the vertical path at the ground floor, and a fold flat below the K-mirror rotates to select one of several optical paths. Sensors and other instrumentation can be mounted at one of two Naysmyth optical breadboards on the telescope or in one of four coudé laboratories. To minimize thermally-induced turbulence, the facility is cooled by a closed-cycle water system chilled by an ice plant located away from the telescope. The telescope enclosure is fully collapsible, leaving the telescope completely exposed to the atmosphere in order to minimize dome seeing effects [10].

The telescope is equipped with a 941-channel, 1,500 Hertz frame rate adaptive optics system which has produced near-diffraction-limited visible images of both satellites and astronomical objects. The tracking system, with wavefront sensor and image track sensors and two beam steering mirrors, has shown 50-60 nrad RMS track jitter (one axis, one- σ). Figure 7 illustrates the performance of the SOR 3.5-meter telescope with an example binary star with measured point spread function (FWHM) of 0.59 arcseconds ($2.8 \mu\text{rad}$). Performance improvements on dim targets will be achieved within the next few years through the addition of a hybrid laser beacon system, which will combine two low-altitude Rayleigh beacons with a mesospheric, sodium resonance beacon.

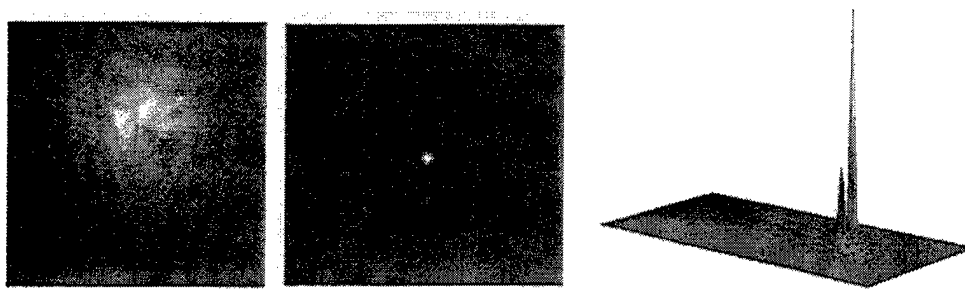


Figure 7 (a-c): Two 0.6 second exposures of the Binary star 104 Tau. The uncompensated image is shown on the left, and the image compensated with adaptive optics in the center. The peak intensity is 71 times greater in the compensated image as illustrated by the histogram on the far right.

The total cost of the 3.5-meter telescope, enclosure, laboratories, physical plant and all supporting facilities was \$27 million. The research and operations staff is comprised of approximately 50 military, civilian, and contractor personnel. The staff includes physicists, mathematicians, astronomers, electronic and mechanical engineers, optical designers and technicians, sensor and computer specialists, laser technicians, a site meteorologist, electricians, plumbers, welders, machinists, and a variety of other specialists.

3.1.2 The 1.5 Meter Telescope

The 1.5-meter telescope is also a classical Cassegrain optical design with a coudé path and a single coudé laboratory. It has an $f/1.5$ parabolic primary mirror and a hyperbolic secondary mirror producing 300 microradians of unvignetted field. Mounting options for instrumentation are similar to those of the 3.5-meter telescope. This telescope has a maximum rotation rate of $30^\circ/\text{second}$. The telescope includes a 241-channel natural guide-star adaptive optic system that has produced very near diffraction limited under typical atmospheric turbulence conditions. The design of the adaptive optics and tracking systems are similar to those of the 3.5m telescope.

3.1.3 The 1.0 Meter Beam Director

The beam director is a coelostat used primarily to transmit laser beams for in which the 1.5m or the 3.5m telescope is used as a receiver. It is occasionally used for making wide field images of astronomical objects. The coelostat is capable of pointing over a complete hemisphere while allowing lasers and sensors to remain stationary in the attached laboratory. The beam director mount holds two 57-inch flat mirrors in an elevation over azimuth configuration with a one-meter clear aperture. The elevation mirror is supported by an active pneumatic system of 36 bellows that maintain the figure of the mirror as the gravity vector changes. Both axes are equipped with direct drive DC torque motors, high-resolution position encoders and fluid bearings.

3.1.4 The 25 Centimeter Beam Director

The 25-cm beam director is also a coelostat used to transmit laser beams for multi-mount experiments. The mount holds two 30-cm flat mirrors in an elevation over azimuth configuration; the clear aperture is 25 cm. This mount is not normally used as an imaging receiver.

3.1.5 Cameras

The SOR mounts have accommodated a wide variety of cameras from visible through near infrared wavelengths for experiments with specialized requirements. Visible wavelength CCD cameras in routine use at the SOR for acquisition and imaging include high frame rate (2500 frames/sec) 64x64 and 128x128 shuttered and non-shuttered cameras as well as several low frame rate Photometrics cameras of up to 1024x1024 pixels. Xybion intensified video cameras are also in use at all mounts.

3.2 Maui Space Surveillance Site (MSSS)

The Maui Space Surveillance Site (MSSS) is the U.S. Air Force's premier optical space observing site. In addition to its military mission, the site is home to an ongoing program of research in high-resolution imaging techniques and astronomical research. The Maui Optical Tracking and Identification Facility (MOTIF), and a Ground-based Electro-Optical Deep Space Surveillance (GEODSS) site operated by US Air Force Space Command. The site is the only one of its kind in the world, combining operational satellite tracking facilities (MOTIF and GEODSS) with a research and development facility.

Air Force Maui Optical Station (AMOS) consists of the observatory's premier optical instrument, the 1.6-meter telescope, the sensors mounted on it, and two smaller telescopes. The Maui Optical Tracking and Identification Facility (MOTIF) a primary sensor of the USAF SPACETRACK network operated by Headquarters Air Force Space Command (HQ AFSPC) [13]. The MOTIF mount is actually a pair of co-mounted 1.2-meter telescopes. In 1994, MOTIF was used to demonstrate fiber optic coupling of the two telescopes' output. Fringes were recorded while observing the star alpha Boo.

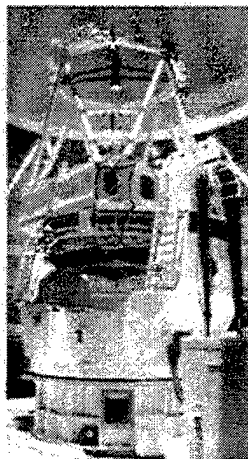


Figure 9: 3.67-meter

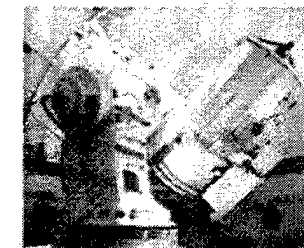


Figure 10: 1.6-meter

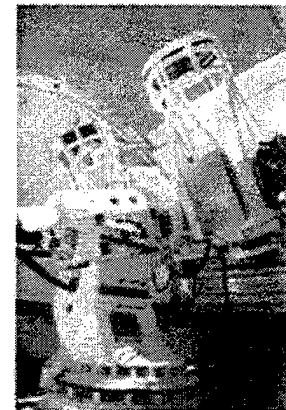


Figure 8: Twin 1.2-meter

The 3.67-meter Advanced Electro-Optical System (AEOS) advanced instrumentation includes a four-array (visible, NIR, MWIR, and LWIR) camera/radiometer. A 741-actuator adaptive optics system is expected to operational by summer of 1999.

The 1.6-meter mount houses the one-of-a-kind GEMINI instrument package, a three-camera system designed to collect data for such advanced image reconstruction schemes as phase-diverse speckle imaging. The 1.6 was used during STS-95, the space shuttle mission carrying U.S. Senator John Glenn, to image the section of the shuttle where the drag chute door had fallen off during launch [14].

3.3 Current Software Capabilities

In addition to its impressive ground based hardware, AFRL has developed simulation tools, image analysis tools, and post processing algorithms and atmospheric correction algorithms that are currently being utilized. These tools will continue to be enhanced and characterized under this effort. Some of the current capabilities and limitations based on existing AFRL technologies are discussed in this next section.

3.3.1 Image Analysis Tools

3.3.1.1 Time-Domain Analysis and Simulation for Advanced Tracking (TASAT).

The Time-Domain Analysis and Simulation for Advanced Tracking (TASAT) software is an Imaging and Tracking Systems Simulation and Modeling Environment developed by Logicon, under contract with the US Air Force, to allow analysts to create detailed models of satellites (or other space object) that are detailed enough to include their shape, materials, and thermal properties [15]. The system then generates radiometrically accurate images for tracking, imaging, algorithms and system performance analysis. The models created can then be viewed either passively by sunlight or actively from a laser simulation.

Full fidelity control system modeling allows active optical elements to compensate for the effects of atmospheric turbulence and jitter. Realistic engagement scenarios can be generated using a wide variety of trajectory and attitude control models and a wide variety of imagery, including high resolution pristine objects, optically degraded images, sampled focal plane array (FPA) images, and point spread functions (PSF). TASAT is capable of performing both target modeling and sensor modeling.

3.3.1.2 Intelligence Data Analysis System for Spacecraft (IDASS)

The Intelligence Data Analysis System for Spacecraft (IDASS) software is a toolkit designed to provide visualization and analysis tools that combine multiple sources of data (visual, radar, etc.) together with space object models to assist in determining the health and status of space objects [16]. The toolkit was designed by TASC under contract with the USAF. IDASS has four primary analysis functions, which include attitude and motion estimation, image simulation, image comparison, and orbit visualization. IDASS will probably be used to overlay a model of the commercial satellite onto the actual imagery collected for comparison purposes in detecting and classifying satellite anomalies.

3.3.2 Atmospheric Correction Algorithms

Even with a telescope as large as the 3.5m telescope at SOR, post-processing techniques are still required on the imagery in order to achieve acceptable resolution. Resolution achieved through any telescope is generally limited by atmospheric turbulence more than the optical design and optical quality of the telescope. Regardless of the size of the telescope, angular resolution is limited to approximately 1 arcsec at visible wavelengths due to the effects of the atmosphere.

Adaptive optics is an atmospheric correction technique that uses mechanical means to sense and correct for turbulence effects as they occur (i.e. in "real time"). Adaptive optics provide a means of sensing aberrations induced by the atmospheric turbulence and correcting them in real time. This technique results in a more narrow point spread function, meaning improved resolution and improved image quality [17]. However, adaptive optical techniques are limited in practice due to various effects such as finite temporal close loop bandwidth and finite spatial sampling of the atmospheric aberrations and noise in the detection process. Because of this, post-processing algorithms are often used to improve the image quality. Algorithms using various deconvolution and superresolution techniques are currently being studied and have potential for use in this effort.

4.0 Proposed Direction

In order to have a successful program, be a successful team needs to put together first. The team should contain members with various areas of expertise, including those knowledgeable in image exploitation algorithm development, atmospheric correction algorithm development, satellite stakeholders, and persons already intimately familiar with existing AFRL assets and technologies.

The next step will be to assess the current capabilities and current assets to determine what existing hardware and software would be most appropriate to utilize for this effort. Factors such as weather conditions, availability of telescope time, position of the desired satellites, required resolution and other conditions all play a valuable role in determining which telescope would be the most appropriate telescope to use.

The target database needs to be established, but first the target set needs to be defined. Since this intent of this effort is to benefit the commercial satellite world, it is appropriate that our target set contain existing commercial satellites. As discussed earlier, there are plenty of potential candidates in various orbital slots, so finding one that falls in the footprint of the telescopes being utilized should not be difficult. Since there are so many Iridium satellites and the constellation is already completed, this satellite would be a good commercial satellite to work with.

In conjunction with the imagery collection process, atmospheric correction and image enhancement algorithms will be developed/refined. These algorithms will contribute to the overall resolution achieved under this effort. Based on the resolution of the collected imagery, visual analysis should provide a wealth of information in regards to what physical properties of the satellite can be distinguished. This information will be gathered together in a conclusive report, indicating what physical properties, possible physical defects, and other anomalies can be resolved using this technique. The satellite owners, manufacturers and insurers involved in this project will help in assessing the value of this information to each stakeholder, which will determine the successfulness of this effort.

4.1 Utilizing Existing AFRL Software Tools

Both TASAT and IDASS will play a major role in assessing the state of commercial satellites imaged under this effort. With detailed design information obtained from the satellite manufacturer and AFRL's TASAT modeling and simulation package, a detailed model of the proposed target satellite can be created. The TASAT system will then generate radiometrically accurate images that can be used for image analysis. Once data is collected, the hi-fidelity-generated model can be overlaid on the actual image data using IDASS. This will provide image comparison information and motion analysis information together which can be used to diagnose the health and status of the target satellite. The motion analysis information can determine whether the satellite is assuming proper orbital motion, or if it is spinning or tumbling. The model overlaid onto the actual image data of the satellite will help determine if there is any physical damage to the satellite based on the fidelity of the model.

There are some risks associated with this new effort. The major risk is getting insufficient resolution and/or Signal-to-Noise Ratio's (SNR) in the imagery to diagnose any problems with the satellite, or not getting a sufficient quantity of data to obtain any meaningful results. There are currently some images of LEO objects taken from both SOR and MSSS that appear to indicate sufficient image resolution for the task. In the event that the resolution is not sufficient for the purpose of this effort, this information would still be valuable in assessing the limitations of the current technology area. A successful data collection is also imperative to the success of this effort. Varying factors such as weather conditions, atmospheric turbulence, time of day and position of the desired satellites, and availability of the telescope are all factors in collecting the data. An insufficient data collection will not provide any useful information, thus the need to determine the target database and start the collection process early in the program.

5.0 Conclusions

Upon completion of this effort, a system capable of performing commercial satellite inspections should be in place, with the role of the Air Force and the role of the contractor more formally defined. The ability to examine spacecraft from the ground can aid the commercial sector by helping to resolve or explain unknown on-orbit problems, assessing the status of satellites presumed to be non-operational, verifying telemetry diagnostic data, and providing information for design improvements and insurance claims. The results of this effort should provide better insight to the value that optical imagery of LEO satellites can provide to commercial satellite stakeholders. In addition to a system, the results of this effort should provide both the commercial community and the Air Force with more advanced image processing and atmospheric correction algorithms, and more knowledge and insight of potential problems with LEO satellites that can be resolved using optical imagery.

References:

1. "World Markets for Commercial, Military and Science Satellites", Frost & Sullivan, Feb 1998, Website: <http://www.prgguide.com/reports/cellular/r1-719w.html>
2. Jane's Military Communications 1996-97 Website, <http://www.janes.com/defence/editors/jmc96/jmc9604.html>
3. "How Do Satellite's Work?" Website: <http://www.attek.com/satellite/work.html>, Copyright 1996, William C. Cook
4. Globalstar Website, <http://www.globalstar.com/>
5. Iridium Website, <http://www.iridium.com/>
6. Technical Overview of the Teledesic Network, The Teledesic Satellite, Teledesic Website, <http://www.teledesic.com/tech/details.html>
7. Lloyd's Satellite Constellations Web Site, Big LEO tables, Website: <http://www.ee.surrey.ac.uk/Personal/L.Wood/constellations/tables/tables.html>
8. Lockheed Martin's The Tech Museum of Innovation Website: <http://www.thetech.org/hyper/satellite/4/4a/4a.1.html>
9. Techmall Web article, "Space Clutter Increases Risks For Insurers of Satellites", Website: <http://www.techmall.com/techdocs/TS971104-11.html>
10. FAS Space Policy Project, Military Space Programs, Starfire Website: <http://www.fas.org/spp/military/program/track/starfire.htm>
11. J. Fugate, et al., 'First Observations with the Starfire Optical Range 3.5 meter Telescope,' Symposium on Astronomical Telescopes and Instrumentation for the 21st Century, SPIE Proc., 1994.
12. K. Spinherne, et al., "The Starfire Optical Range 3.5m Telescope Adaptive Optical System", SPIE Proceedings, volume 3353-03.
13. AMOS User's Manual Website: http://ulua.mhpcc.af.mil/Manual_intro.html
14. MHPCC ADASS General Information Website, <http://wailea.mhpcc.edu/ADASS/>
15. Logicon Products Webpage for Time-Domain Analysis and Simulation for Advanced Tracking (TASAT), Website, <http://www.logicon.com/tasat/>
16. W. Meyers, D. Phillipson, "Intelligence Data Analysis System for Spacecraft User's Guide for IDASS Version 3", TASC TR 7941-4-3.
17. Michael C. Roggemann, Byron Welch, "Imaging Through Turbulence", CRC Press, 1996.

Active Lasing of Space Objects using the HI-CLASS (High Performance CO₂ LADAR Surveillance Sensor) Laser System

Deborah K. Werling, Charles L. Matson, John Gonglewski, Stanley R. Czyzak
Air Force Research Laboratory, Directed Energy Directorate,
Surveillance Technologies Branch (AFRL/DEBS)
3550 Aberdeen Ave. SE
Kirtland Air Force Base, NM 87117-5776

Linda L. Crawford
Schafer Corporation, 2000 Randolph Rd, SE, Albuquerque, NM 87106

ABSTRACT

The HI-CLASS system, located at the Maui Space Surveillance System, is a high power, wideband, coherent laser radar (LADAR) for long range detection, tracking, and imaging of space objects and remote sensing. Hardware and software were developed for two modes of operation: a LADAR mode for active imaging of space objects, and a lidar mode for remote sensing atmospheric measurements. Data were collected to demonstrate the system capabilities and to validate technology and designs for fielding operational lidar systems. The demonstrations for operational utility provide the groundwork to an upgrade program. One demonstration includes high accuracy tracking of specific space objects in position and velocity simultaneously to ultimately provide size, shape, and orientation information. The future plans for lidar development, based on the results of the HI-CLASS demonstrations, will be discussed.

1. OVERVIEW

The HI-CLASS (High Performance CO₂ Laser Radar Surveillance Sensor) system is located at the Maui Space Surveillance System (MSSS) atop Haleakala in Maui, Hawaii (Figure 1). The current HI-CLASS system is coupled to the 0.6m Laser Beam Director (LBD) telescope at MSSS. Design and development for a HI-CLASS-type system on the 3.67m Advanced Electro-Optical System (AEOS) telescope began in early 1999. The objectives of the HI-CLASS program are to demonstrate with a high performance laser radar active remote sensing, high precision near earth (NE) and deep space (DS) object tracking, and imaging of space objects for Space Object Identification (SOI). The HI-CLASS system will also demonstrate lidar and laser radar capabilities to validate technologies and designs for operational systems. This effort can further lead to compact laser radar systems applications for airborne and spaceborne surveillance platforms.



Figure 1. HI-CLASS System at MSSS

The HI-CLASS system is a wide bandwidth, waveform agile, high power, compact, coherent laser radar capable of two modes of operation. The laser radar (LADAR) mode is designed for long range high precision hard-body acquisition, tracking, and imaging. The lidar mode is used for long-range remote detection of chemical vapors using natural terrain returns. This paper will focus on the LADAR capability and its ability to provide real-time, high precision satellite ranging, tracking and imaging. HI-CLASS illuminates low-earth orbit (LEO) satellites with the CO₂ laser and receives the reflected light back from the satellites to obtain information such as size, structural information, and accurate orbital positional data. Although HI-CLASS illuminates only LEO orbit satellites, an analysis is on-going to determine how well this system could illuminate satellites at geosynchronous (GEO) orbits if it had a higher-power laser and a larger telescope/receiver. The HI-CLASS system provides real-time precision range that describes the altitude of a satellite, and range-rate information that describes the velocity of a satellite in its orbit. This information can also be processed to create high-resolution images of satellites. This paper will describe an overview of the HI-CLASS system, the demonstration of its capabilities, and future plans for the system.

2. SYSTEM DESCRIPTION

The HI-CLASS system consists of a CO₂ laser oscillator, receiver/processor, and a beam train that couples the transceiver to the 0.6m LBD telescope (Figure 2). It uses a power-oscillator amplifier and has the capability to produce a 30 Joule transmitter output energy at a 30 Hz repetition rate. The receiver/processor is a wide-band heterodyne detection system and is the controller for HI-CLASS. It is also the controller for all communication to and from the LBD, as well as the entire mount control system that goes through the processor. The beam train has the ability to switch from transmit to receive mode so the system is able to operate in a monostatic mode. The beam is shaped by the beam train optics and is expanded and slightly overfills the 0.6m circular aperture of the telescope. The HI-CLASS system also has an analog to digital converter and a real time digital processing system.

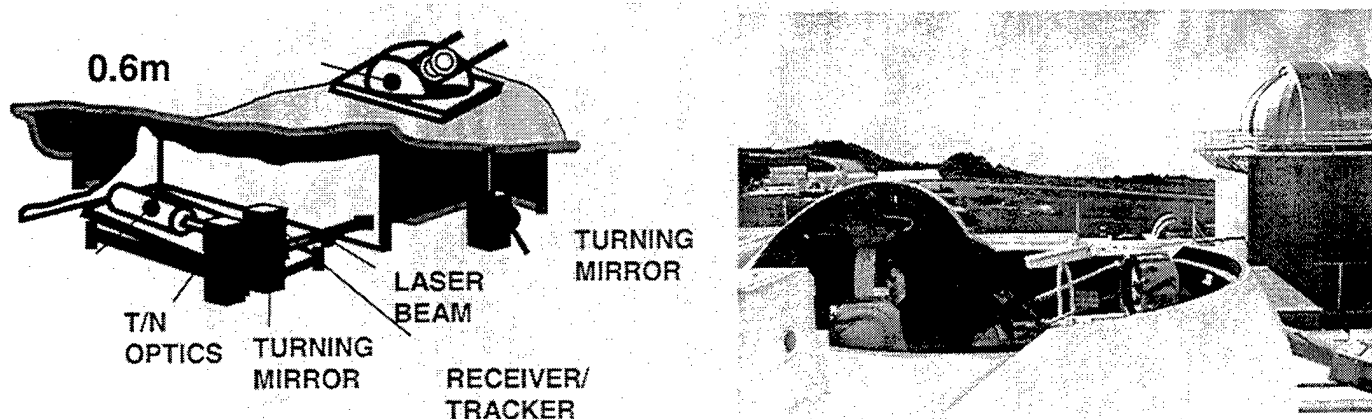


Figure 2. HI-CLASS System on 0.6m LBD

The transmitter produces two waveforms necessary for the generation of the data for acquiring and tracking the hardbody targets. The system produces a sequence of high power pulses in a pulse burst waveform that is used for imaging or a pulse tone waveform that is used for tracking. The initial target acquisition parameters of range and velocity are produced with the pulse-tone waveform. Once the target is acquired, the system switches to the pulse-burst waveform; each pulse hits the target at a different position in the sky. This waveform is used to generate fine range resolution and fine cross-doppler resolution that is associated with target spin. The return pulse can be transformed into the intensity projection of the satellite at that particular angle. These returns can be used to reconstruct images using tomographic imaging techniques.¹

The receiver/processor system consists of a heterodyne receiver subsystem and a processor subsystem. The receiver subsystem includes a local oscillator, an optical frequency shifter, an optical pulse monitor, and an analog receiver. The processor subsystem includes a digital processor, a wide-band waveform processor, operator displays, and the system controller.

Certain functions are performed in the front-end optical heterodyne detection system including frequency shifting of the return beam using an acousto-optic modulator. The returned optical signal is combined with a signal from the local oscillator to form a heterodyne signal. This signal is incident upon a quad (four element) HgCdTe infrared detector. The four individual elements of the quad detector are used to track the target. All four signals produced by the elements of the quad detector are summed to generate the high-resolution range and Doppler products.

The optical system must shift the frequency of the return signal so the whole body Doppler signal will not interfere with or obscure the wide-band imaging data. The imaging bandwidth is ~500 MHz. It rides on the carrier generated by the whole body Doppler that is greatest at the horizon and gradually goes to zero at culmination. As long as the imaging bandwidth does not fold over on itself, fine Doppler details can be unambiguously resolved. Re-shifting the return beam when the naturally occurring Doppler approaches the imaging bandwidth will ensure that the bandwidth does not fold over. This effect keeps the imaging bandwidth away from the fold over region by first shifting plus 500 MHz, then minus 500 MHz.

The receiver subsystem contains a RF analog receiver. This analog electronics subsystem performs several critical signal-conditioning functions prior to analog to digital conversion. The analog receiver performs various functions including amplifying detected optical signals, generating four narrow-band channels for the pulse tone processing and one wide-band sum signal for pulse burst processing, and removing whole body Doppler frequency shifts under input control by the system processor. The receiver also coherently replicates the baseband content of the signal generated by the LADAR detector, compensates for Doppler frequency shift, and amplifies and outputs the signal processing.

The processor consists of three major sub-elements, the controller, the core or targeting algorithm processor, and the operator workstation. Although all three sub-elements can be independently programmed and used for separate functions, they are all linked through shared memory architecture. This shared architecture results in a mission and system controller and a target

acquisition-imaging real-time display capability. The target tracking (range and Doppler) vectors and the imaging parameters (range-doppler, amplitude, energy absorption vs. wavelength, etc) are both installed in the processor. These algorithms can be upgraded and re-programmed as required. The processor passes on the relevant targeting parameters for display to the operator workstation during the targeting mission. Feedback and updates are then sent to the mount control system of the 0.6m telescope.

The processor function is to extract range and Doppler shift from the output of the analog receiver. Range and velocity products are both obtained by correlating the return with the optical pulse monitor. Fourier Transform techniques can be used in this process to provide more efficient and accurate results.²

3. SYSTEM CAPABILITIES

Four phases of development and demonstration have been completed for the HI-CLASS system. Phase 0 was the initial system development and check out. During Phase 0 the system utility was determined and specifications were defined while the key technology components of the transmitter and beam pointing were demonstrated.³

The Phase 1 system consisted of the CO₂ laser oscillator and its associated optics table, the CO₂ receiver and the beam train coupling the HI-CLASS transceiver to the 0.6m aperture telescope. During Phase 1, breadboard hardware was built which lead to a fully integrated, complete, pulsed 100-watt class laser radar system at the MSSS. The Phase 1 test objectives were met with returns obtained from the satellites observed during this testing.

During Phase 2, the system oscillator and receiver-processor were built and integrated. The receiver/processor generated real-time target trajectory data and the transmitter operated at about 12J-output energy. The Phase 2 system produced real time generation of returns of cooperative targets for range and range-rate.⁴ It also accomplished detection of return signals from cooperative satellites as well as from uncooperative satellites, which have no retro-reflectors. Remote sensing experiments were also conducted.

The Phase 3 system was completed in summer 1997. This phase added a power amplifier to the transmitter, bringing the system capability to a 30 J transmitter output energy at a 30Hz repetition rate. Phase 3 added the capability to produce real-time Doppler imaging. The Phase 3 system demonstrated the capability of reaching 30 J transmitter output at 30 Hz.

The HI-CLASS system is currently in the final phase (Phase 4) of its research and development effort which began in fall 1997 and is anticipated to continue through the end of 1999. The objective of this phase is to demonstrate state of the art technology and how a HI-CLASS-type system can contribute to the maintenance of the space catalog, to include high accuracy LADAR data to improve satellite orbital state vectors, NE space debris study, and Geosynchronous tracking study. The results from these demonstrations and studies will provide the groundwork to develop an operational HI-CLASS-type system.

The goal of the Space Catalog Maintenance demo is to evaluate the potential of LADAR to augment the Air Force Space Surveillance Network (SSN) that maintains the catalog of orbiting objects. This task is comprised of four elements: system model, capacity analysis, risk-reduction experiments, and demonstration experiments. The system model was developed to evaluate potential targets for the system and perform diagnostics. The capacity analysis estimates the effectiveness of a LADAR operating as part of the SSN. It takes into account the hardware reliability, the weather, availability of satellites to track, and supporting acquisition and track sensors. The risk-reduction experiments are structured to work out procedures and calibration issues prior to a demonstration. Each experiment consists of two nights of satellite passes and data collection. On the first night the satellite is tracked and LADAR data is collected (Figure 3). The data collected is then used in an Air Force orbital model that propagates the orbit for the following night. The following night this data is used to acquire and track the same target.

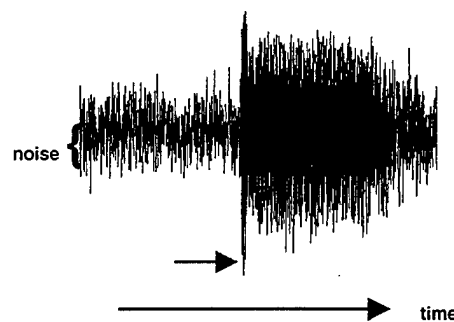


Figure 3. LADAR returns from satellites

The Phase 4 effort also involves the design, development, and utilization of HI-CLASS-type hardware on AEOS (Figure 4). This effort began in Jan 98. Studies were completed and included determination of the utility and feasibility of putting hardware similar to the current HI-CLASS system on the 3.67m AEOS telescope at the MSSS. One option for such hardware options is putting receiver hardware on AEOS for bistatic operation with the current HI-CLASS system. In such a configuration, the laser transmitter would go through the 0.6m telescope and the return light would be collected using the AEOS telescope.

Such a configuration would allow data collection for dimmer targets than those that can be currently seen with the HI-CLASS system. Another option being explored is a complete HI-CLASS type system on AEOS including transmitter hardware for use with AEOS in a monostatic mode. The configuration would be robust and capable of being used by operators who are not highly-trained scientific personnel. The actual design, development, and utilization of such hardware on AEOS was started in 1999, starting with the installation of an AEOS Filter Wheel.

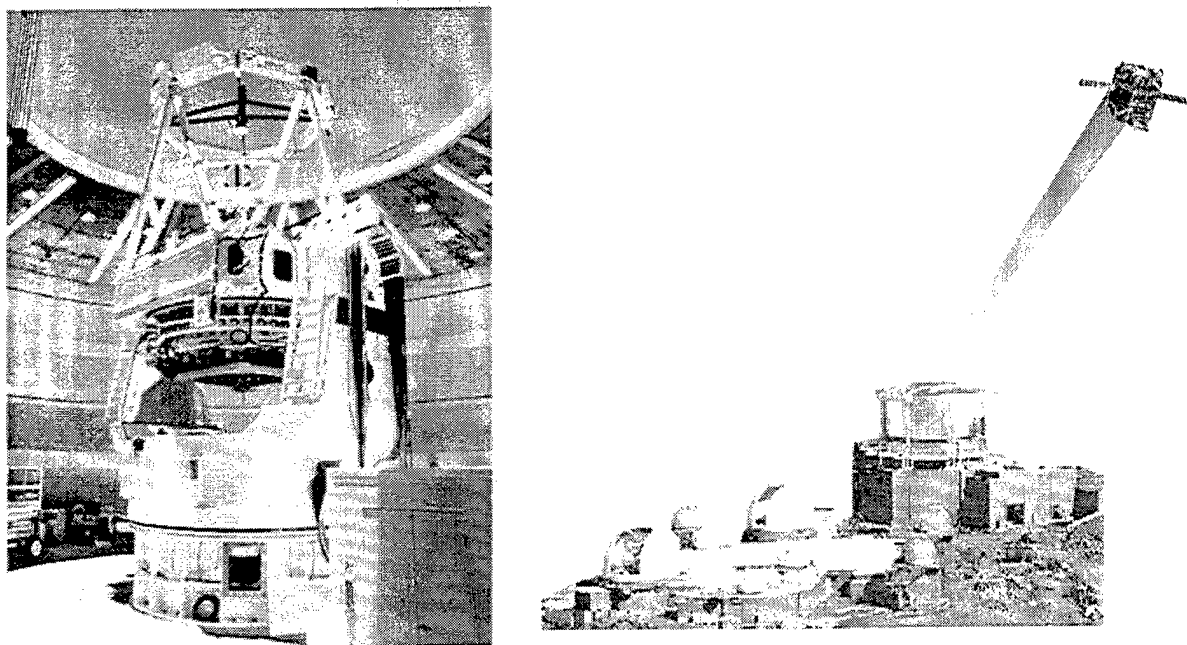


Figure 4. 3.67m AEOS

4. POTENTIAL APPLICATIONS FOR LADAR SYSTEMS

Potential applications may apply to other LADAR systems, but this paper will focus on HI-CLASS-type systems. This term refers to a LADAR system that incorporates HI-CLASS features and characteristics but differs from the current HI-CLASS system. The HI-CLASS-type system would be an operational system possibly with higher transmitter output energy. In its current configuration, the system requires a team of physicists and technicians who have a very thorough knowledge of the HI-CLASS system and the physics and electronics involved in its operation. The term HI-CLASS-type system refers to a similar system, but one that could be used by trained operators who do not have expertise in physics or optics.

The follow-on HI-CLASS work is focused on providing the groundwork for operational applications for LADAR. The first step to determine these applications is to perform a requirement analysis of the current space surveillance requirements, such as the 1995 AFSPC Space Surveillance Requirements Document and the 1998 USSPACECOM Space Control Capstone Requirements Document. Next, applicable needs that a LADAR can mitigate will be specified along with a definition of the technologies a LADAR can demonstrate for operational utility. For example, a LADAR can support areas such as high accuracy observations for theater space surveillance support and for maintenance of satellite orbits using special perturbation orbit determination algorithm. A Concept of Operations will be developed to document how an operational LADAR system can support the user requirements. Experiments and demonstrations will be defined using the current HI-CLASS system and/or the HI-CLASS-type system on AEOS. Results from these experiments will determine the types of modifications required to the system in order for it to become operational.

6. CONCLUSION

The HI-CLASS system is a research and development effort that is demonstrating state of the art technology as well as making accomplishments that have not been previously capable on LADAR systems. While this technology demonstration is continuing, a demonstration of the potential application of this and similar systems needs to be performed. The follow-on effort that began in mid-1997 will provide the groundwork for such demonstrations.

REFERENCES

1. C. Matson, E. Magee, and D. Stone, "Reflective tomography for space object imaging using a short-pulselength laser", *SPIE Proceedings*, vol.2302, pp. 73-82 (1994).
2. M. Kovacs, G. Dryden, V. Hasson, D. Ruffatto, R. Pohle, R. Wendt, S. Czyzak, D. Mosley, and M. Fox, "The Field LADAR Demonstration (HI-CLASS) Program: A review of the phase 2 testing effort".
3. V. Hasson, R. Wendt, S. Czyzak, "Overview of the Field Ladar Demonstration Program Developing a High-Resolution Imaging and Remote Sensing", *SPIE Proceedings: SPIE 10th Annual AeroSense Symposium Laser Radar Technology and Applications*, (April 1996).
4. M. Kovacs, D. Ruffatto, F. Corbett, S. Ghoshroy, V. Hasson, R. Pohle, R. Wendt, S. Czyzak, and M. Fox, "A Review of the HI-CLASS Test Program", *IRIS Proceedings: 1996 Meeting of the IRIS Specialty Group on Active Systems* (May 1996).
5. D. Mosley, C. Matson, S. Czyzak, "Active imaging of space objects using the HI-CLASS (High Performance CO2 ladar surveillance sensor) laser system", *SPIE Proceedings: Laser Radar Technology and Applications II*, (April 1997).

Determination of Accurate Orbits for Close Encounters between Geosynchronous Satellites

R. I. Abbot and J. Sharma (MIT Lincoln Laboratory, Lexington MA 02173)

INTRODUCTION

With an increased number of drifting geosynchronous satellites, the threat to active geosynchronous satellites has been growing. As one example of this, on January 11 of 1997, the Telstar 401 satellite failed while on orbit at 97 degrees West longitude and is now resonating in the geopotential well from 97-113 degrees West longitude. Figure 1 shows the frequency of encounter distances to date of Telstar 401 with active satellites in the well. Many of the encounter distances shown are after avoidance maneuvers, and without these would have been less than 10 km. Telstar 401 will continue to resonate indefinitely in the geopotential well and therefore will pose a serious and long-term potential threat to active satellites there.

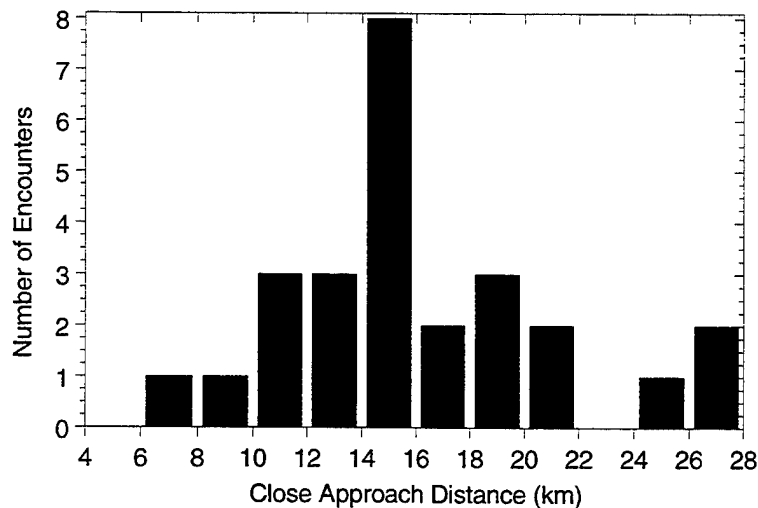


Figure 1. Frequency of Close Approach Distances for Telstar 401 Encounters

Because of the threat of Telstar 401, MIT Lincoln Laboratory has entered into a Cooperative Research and Development Agreement (CRDA) with the owner/operators of 15 commercial satellites that occupy the region between 97-113 degrees West longitude. The CRDA partners are GE Americom, PanAmSat, SatMex, and Telesat Canada. This effort, in part, involves maintenance of orbits of both the CRDA partner satellites and Telstar 401. This information is used by the CRDA partners to determine if possible avoidance maneuvers are required and what an optimum maneuver strategy might be if necessary.

There are several research areas involved with the CRDA, but one of the primary ones is to quantify the orbit accuracy that can be determined for geosynchronous satellites and to examine the means of improving it. Under the CRDA agreement the primary tracking resource for Telstar 401 is the Millstone Hill radar in Westford MA. Three methods have been used to evaluate the orbit accuracy achievable with the Millstone tracking. The first is the traditional overlap of two

consecutive long-arc orbit fits that have part of the fit span in common. The second is the use of an external set of high quality measurements that are used to evaluate the orbit accuracy. These measurements are from the SBV (Space Based Visible) optical telescope, which is a space based contributing sensor to the SSN (Space Surveillance Network) and is operated by MIT Lincoln Laboratory. The third method is the use of an external very high accuracy reference orbit from TDRS [1] with which orbits computed with Millstone data can be compared.

From the accuracy assessment analysis, which will be discussed below, it was determined that the orbit accuracy for Telstar 401 and the CRDA satellites generally is between 0.5 and 2 km. This is of concern since if the accuracy of the orbits for Telstar 401 and a CRDA satellite was each 2 km, then this could sum to 4 km in the worst case. This certainly detracts from the confidence of an encounter distance of 4 km and, with the high value assets involved, even encounter distance estimates of 6-10 km often have led CRDA partners to maneuver their satellites. This level of orbit uncertainty has led to the examination of how to improve the accuracy of Telstar 401 and CRDA satellite orbits in order to provide an increased confidence in encounter distances. The CRDA partners collect transponder range data in order to maintain their orbits, and this has been obtained from them for study. The goal was to check and improve the calibration of this data if possible and to see how well it with the Millstone data could determine a geosynchronous orbit. Since Telstar 401 km is not an active satellite, no transponder range data are available. However, data have been routinely collected by SBV and an examination has been made to see how it can enhance the orbits determined from Millstone data for Telstar 401. The following sections will simultaneously discuss the various methods for quantifying and enhancing orbit accuracy.

TELSTAR 401 ORBIT ACCURACY

Telstar 401 has been tracked for CRDA encounter analysis since its first encounter with PanAmSat's Galaxy IV on May 12, 1997. Telstar 401 and CRDA satellites are tracked densely by Millstone for about a month for each encounter. This insures that enough tracking is collected so that at two weeks before the predicted encounter an orbit accurate to an estimated 2 km or better has been computed. CRDA partners then have enough time to decide if any maneuver strategy is required. Tracking is also continued a few days after the encounter to compute a post-encounter orbit to confirm encounter predictions. Encounters are generally close enough in time that Telstar 401 is tracked almost continuously. This permits a long history of Telstar 401 orbit accuracy to be maintained. This is done by computing 14 day orbits with one day in common for an overlap accuracy assessment. All the orbits in this paper, unless indicated otherwise, were computed using an MIT Lincoln Lab developed special perturbations orbit determination software known as Dynamo.

Table 1 provides a sample of the overlap orbit accuracy assessment for Telstar 401 with just the Millstone tracking. The number of Millstone tracks for the two overlapped orbit fits are also shown. Millstone, on average, takes two tracks of 5-10 observations per track per day. The overlapped orbits are considered independent since one day in common is less than ten percent of the fit span. The overlap is quantified by computing the difference of ECI (Earth Centered Inertial) coordinates at 15 minute spacing from both orbits on the day in common. These differences are transformed to radial, along track (along the velocity vector), and cross track

(perpendicular to the first two) components. Then the RMS (Root Mean Square) is computed for the differences of each component. Assuming, on average, that half the difference is due to errors in each orbit, the RMS difference is divided by two. The resulting quantity is the overlap measure of orbit consistency, and experience has shown that it is also a good measure of accuracy.

Table 1. Telstar 401 Orbit Improvement Using SBV Observations

Day of Year	MH Tracks Arc1/Arc2	Without SBV Obs			SBV Tracks Arc1/Arc2	With SBV Obs		
		Δ Rad RMS(m)	Δ Cross RMS(m)	Δ Along RMS(m)		Δ Rad RMS(m)	Δ Cross RMS(m)	Δ Along RMS(m)
314 (1997)	23/26	179	1525	365	15/16	32	229	131
327 (1997)	26/20	153	1314	329	16/8	18	216	76
27 (1998)	4/4	48	301	615	8/15	31	95	172
40 (1998)	4/12	109	722	238	15/14	72	361	201
53 (1998)	12/22	85	647	196	14/9	28	147	108
66 (1998)	22/26	67	672	343	9/8	41	468	97
79 (1998)	26/15	171	1520	347	8/9	28	284	60
92 (1998)	15/8	215	2034	467	9/12	54	496	216

Table 1 also shows the accuracy assessment when SBV observations are added to the orbit fit. The number of SBV tracks are shown for the orbit fits. An SBV track consists of four right ascension and declination measurements. Note from the table that without SBV observations, the largest error component is in the cross track direction, and this is contributing to a large part of the 2 km orbit error. This is an error in the determination of the inclination of the geosynchronous orbit. The reason for this is that Millstone has azimuth and elevation angle errors from 5 to 10 millidegrees and these are mapping into errors of determining the inclination. When SBV observations are added, which have typical angular accuracies of one mdeg, the cross track component is reduced to under 0.5 km. Figure 2 illustrates the improved total position when SBV data are included.

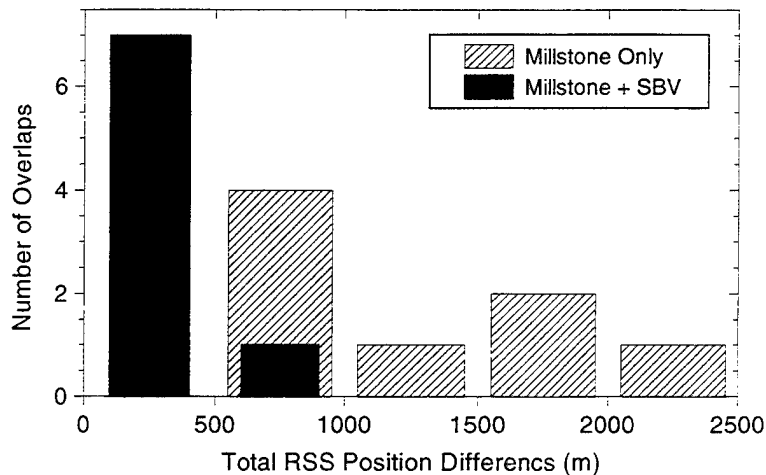


Figure 2. Improved Telstar 401 Orbit Accuracies with the Addition of SBV data.

ORBIT ACCURACY USING CRDA DATA

Transponder range data were received from all CRDA partners for analysis. Before it could be used the calibration of the range biases had to be examined. A range bias between a ground station and satellite can be due to the station hardware, the satellite transponder, and atmospheric refraction. The CRDA partners have two tracking stations, and it is difficult to determine range biases for both station-satellite pairs from just that ranging data alone. The biases can be absorbed into the orbit solution and incorrect values may result. At best, the bias for one station-satellite pair can be determined if the other is fixed at some value. To determine both station-satellite biases, another source of tracking data is necessary to provide an independent source of orbit control.

During encounter periods, Millstone is providing significant tracking of CRDA satellites, and this helps provide an orbit that can be used to calibrate the CRDA data. Millstone orbits alone with errors up to 2 km are not adequate to calibrate the CRDA range data to the level of its measurement error which is from 4-16 m. This was seen when the CRDA range data were differenced against corresponding ranges from the Millstone orbit, and the resulting residuals showed diurnal signatures of 100-200 m. Therefore the CRDA data were given a-priori errors for weights and included in the orbit fits instead of just being compared with them. The orbits were iterated until biases converged. The standard deviation of the residuals was used as the measurement error of the data. After the CRDA data was calibrated, it was used to examine orbit accuracy enhancement.

Two examples are presented of the orbit analysis in which CRDA range data are combined with the Millstone data. The CRDA range data in these examples are from Telesat Canada. One set of Telesat data is from Anik E1 over Day 343 of 1997 to Day 011 of 1998. The other set is from Anik E1 between Days 203 to 225 of 1998. The Telesat data are from two stations: Allen Park near Toronto and Edmonton in Western Canada. Measurements from this data were made from

these stations roughly every two to four hours. Millstone was supporting Telstar 401 encounters with Anik E1 and was tracking on average twice per day, with 5-10 observations per track.

The Telesat data were calibrated with uncertainty in the range biases equal to the measurement error of the data, which was 8 m. The accuracy of the Anik E1 orbits was then evaluated using orbit overlap. For the overlap analysis, two 18 day orbits were computed; one from Days 343-360 of 1997 and the other from Day 359 of 1997 to Day 011 of 1998 with Days 359 and 360 in common. In one case, CRDA data were not used with the Millstone data and in the other it was. Table 2 shows the summary of the overlap statistics. The RSS (Root Summed Square) is the total error.

Table 2 Orbit Accuracy Assessment of Anik E1 by Overlap on Days 359-360

Tracking Case	Δ Rad RMS(m)	Δ Cross RMS(m)	Δ Along RMS(m)	Δ RSS (m)
Millstone Only	132	1236	268	1272
Millstone + Telesat	9	61	17	64

The Telesat range data improved the accuracy in all three components, although the cross track improvement was most dramatic. With the Telesat range data, orbits accurate to better than 100 m were obtained.

During this period there were SBV measurements with errors of 0.5 mdeg or better. This was better than the stated accuracy for SBV and was good enough to provide an independent assessment of orbit accuracy to the few hundred meter level. The high accuracy SBV data provided an external means of evaluating orbit accuracy by not being used in the orbit fits but rather compared with the orbits computed without and with the Telesat data. SBV residuals in right ascension and declination were computed by differencing the measurements with corresponding theoretical ones that were derived from the orbit. The resulting residuals, without and with Telesat data in the orbits, are shown in Figures 3 and 4 respectively. The SBV residuals show significant improvement when the Telesat data were added. The mean of the right ascension measurements is reduced from 1.10 mdeg to 0.15 mdeg, and the sigma of the declination measurements is reduced from 3.12 mdeg to 0.58 mdeg. One millidegree at the distance of a geosynchronous satellite from SBV is about 700 m. These residuals are either due to orbit or measurement error, but in either case they bound the orbit error in right ascension and declination to 400 m.

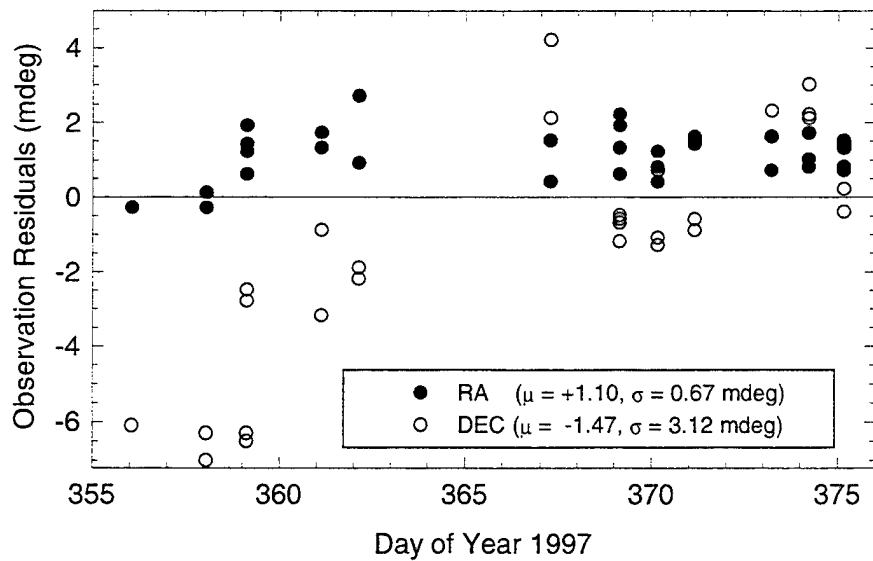


Figure 3. SBV RA and DEC residuals for Anik E1 on Days 356-376 without Telesat range data.

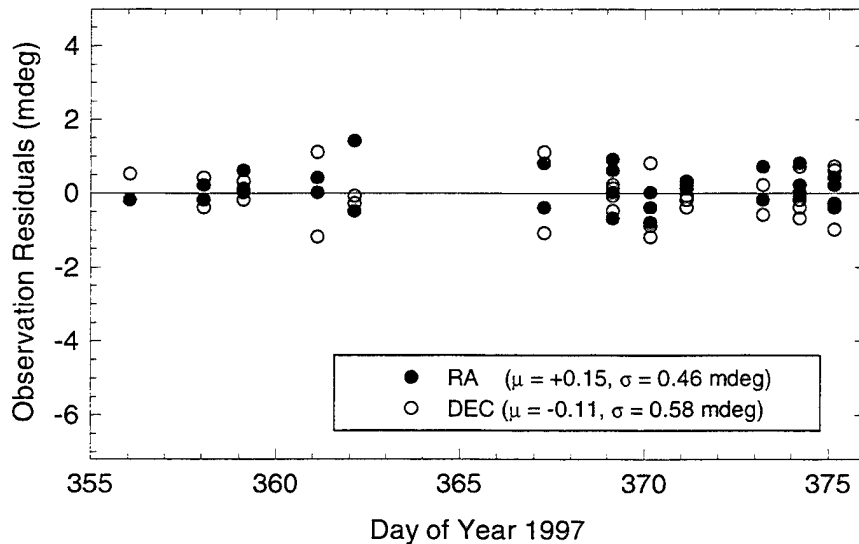


Figure 4. SBV RA and DEC residuals for Anik E1 on Days 356-376 with Telesat range data.

In the second example, with Anik E1 again, orbits with data from Days 203 to 225 of 1998 were computed, and again evaluated with overlap. The SBV data showed measurement errors more typical of the stated accuracy, one mdeg. This level of accuracy could not evaluate the orbit accuracy to the few hundred meters as in the first example, so instead it was actually used in the orbit fits to see how this more typical data could enhance orbit accuracy. To assess orbit accuracy, three scenarios of tracking data were considered for orbit determination: 1) Millstone only tracking data 2) Millstone and SBV tracking data, 3) Millstone, SBV, and Telesat range

data. MH tracked twice per day on average, SBV tracked roughly once every two days, and Telesat tracked continuously every two to four hours.

The Telesat range data first had to have its calibration reviewed. The biases turned out to be the same as in the first example within the measurement uncertainty that was again determined to be 8 m. After calibration, two orbits were computed for the overlap, over Days 203 to 214 and Days 214 to 225 with Day 214 in common. Table 3 shows the orbit accuracy of the three cases. The addition of SBV data significantly reduced the cross track error as well as helped an already small radial error. The Telesat range data then reduced the overall orbit quality to the 100m level (RSS).

Table 3. Orbit Accuracy Assessment of Anik E1 by Overlap on Day 214

Tracking Case	Δ Rad RMS(m)	Δ Cross RMS(m)	Δ Along RMS(m)	Δ RSS (m)
Millstone Only	82	718	238	761
Millstone + SBV	40	293	212	364
Millstone + SBV + Telesat	10	67	75	101

TDRS TRACKING EXPERIMENT

An alternate method to assess orbit accuracy is to compare the orbit to a more accurate reference orbit. The use of a reference orbit also permits analysis of the growth rate of these errors when the orbit solution is propagated. This section will also expand on the benefits of combining optical and radar tracking to improve the orbit quality. Unfortunately, there are no satellites in geosynchronous orbit which are tracked by lasers and have a submeter ephemerides available. The Goddard Space Flight Center (GSFC) routinely generates a precise orbit for their Tracking and Data Relay System (TDRS) satellites. The published TDRS orbits are accurate to 50-60m (1σ) in position [Ref 1 & 2]. The precise element sets for TDRS are published routinely on the web. The element sets have to be transformed from a earth centered relative (ECR) to a J2000 earth centered inertial (ECI) coordinate system by applying the appropriate nutation and precession rotations. Ephemeris data provided by GSFC, for comparison, revealed that the solar radiation pressure scale parameter required an adjustment when used as an input to Dynamo. The ability to accurately generate a precise ephemeris using the TDRS element sets is illustrated in the figure below. Figure 5 shows the position differences between a J2000 ephemeris for TDRS-4 generated at GSFC and a similar ephemeris generated by transforming and propagating a GSFC element set with Dynamo.

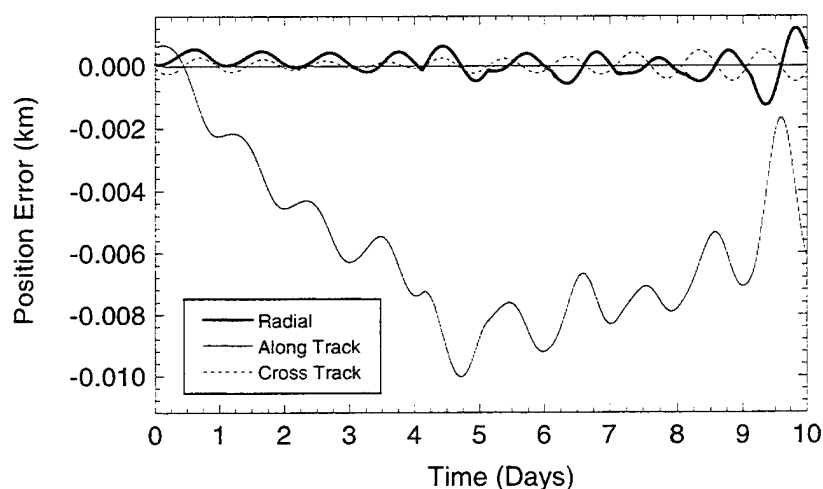


Figure 5. Comparison of Dynamo Propagation of TDRS-4 Element Sets

This figure shows the difference between the two ephemerides are less than 10 meters over 10 days. In practice GSFC generates a precise element set for TDRS-4 every Monday-Wednesday-Friday, so an element set is never propagated for more than 3 days.

The TDRS-4 satellite was tracked frequently by both the Millstone Hill Radar and SBV during a maneuver free period between day 302 and 362 (1998). The tracking data were used to compute orbits for TDRS-4, and the accuracy of these orbits was determined by comparing these orbits with the reference orbits computed from GSFC element sets. Having a reference orbit also allows the assessment of the growth of position errors when the orbit solutions were propagated. The first case illustrate the capabilities of optical and radar sensors in maintaining geosynchronous orbits. Figure 6 shows the orbit quality of an orbit generated from 6 SBV tracks collected over 14 days. The horizontal bar indicates the period during which the observations were collected. In this fit only the state of the spacecraft was estimated. The solar radiation pressure is modeled using nominal area and mass values, but a radiation scale parameter was not estimated. The orbit solution has been propagated backwards to accommodate the largest propagation interval with data collected. The cross track errors are less than 1km, and indicate that the orbit plane has been accurately determined. This is consistent with the precision of the SBV observations of one mdeg, which is approximately 700m at the geosynchronous belt.

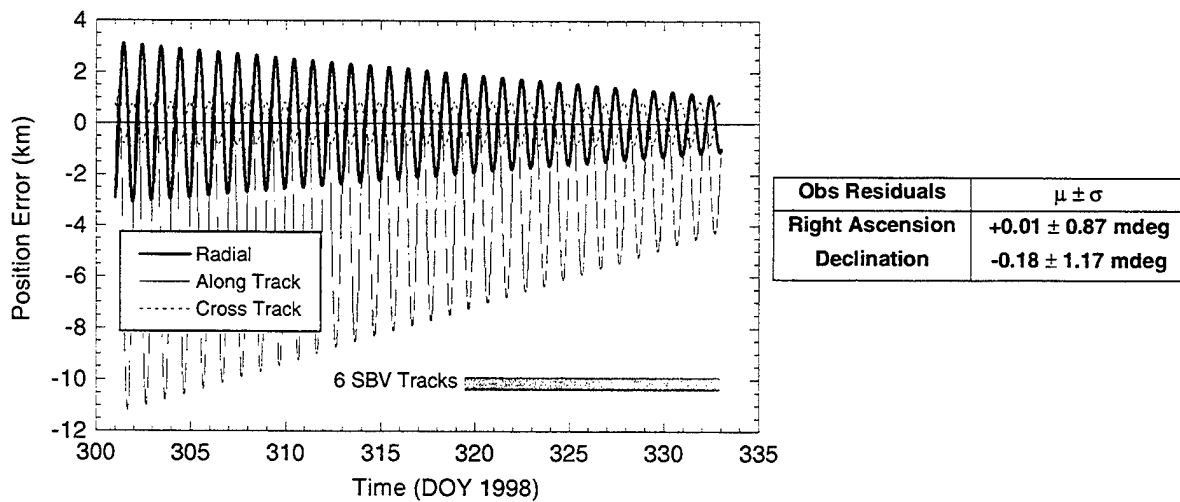


Figure 6. Two week SBV only tracking orbit comparison

The periodic variations in radial and along track position indicate that the eccentricity of the orbit has not been well determined. The near zero mean of the radial position does indicate that the semimajor axis has been well determined. The total position error after 18 days of propagation is approximately 12 km. The next figure shows the quality of orbit obtained from three Millstone Hill Radar Tracks over the same two week period. The first significant feature is the accuracy and long term stability of radial and along track position errors. The direct measurement of range and range rate significantly improves the ability to accurately estimate the solar radiation pressure scale parameter, and thereby improving the estimate of the semimajor axis and eccentricity. Unfortunately the determination of angular position is less precise than the SBV. The mean and one sigma standard deviation for the radar measurements are also listed in Figure 7. The lower angular precision and accuracy of the radar limits the ability to accurately determine the orbit plane, resulting in larger cross track errors than the optical data derived orbits.

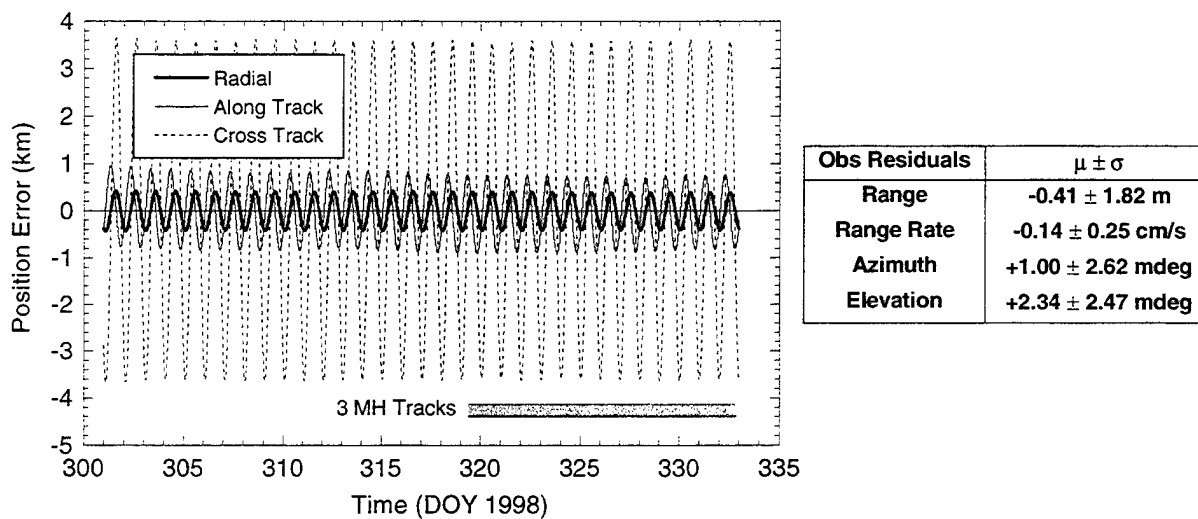


Figure 7. Two week Millstone only tracking orbit comparison

One way to improve the quality of the orbit is to combine the strength of optical and radar data. Figure 8 shows the orbit position differences for an orbit generated from the previous 6 SBV tracks and 3 Millstone tracks.

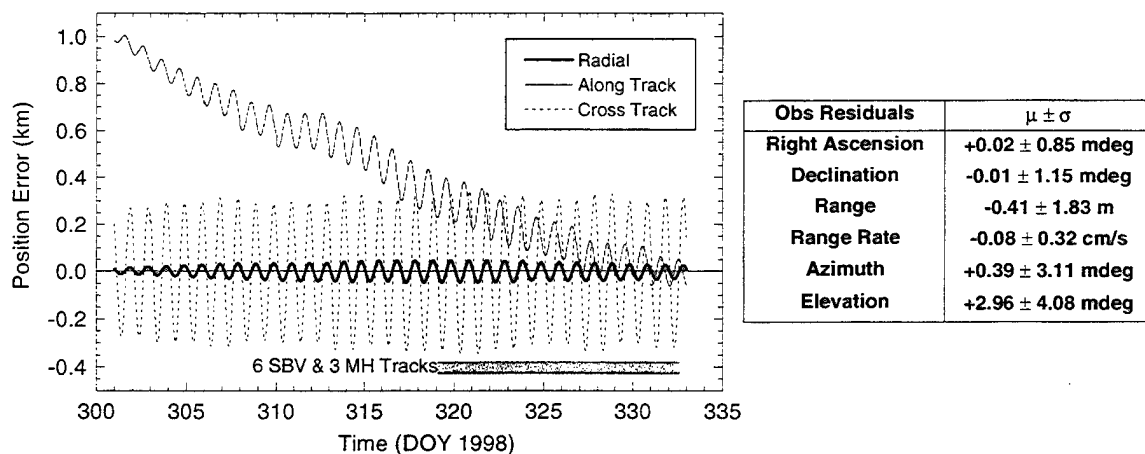


Figure 8. Two week SBV and Millstone tracking orbit comparison

By combining both measurements a significantly more accurate orbit was obtained in all three dimensions. There was slight degradation in the azimuth and elevation residuals indicating the lower accuracy of these measurements. The error growth rate, although not zero, is significantly reduced to less than one half kilometer over 18 days. This result demonstrates the complementary nature of optical and radar observations.

The next two figures illustrate the capability of extended single sensor tracking. Figure 9 shows an example of dense Millstone tracking with 17 tracks collected over a two week period. This

figure shows that the limitations of poor angular measurement precision can be overcome by sufficient collection of precise range and range rate data.

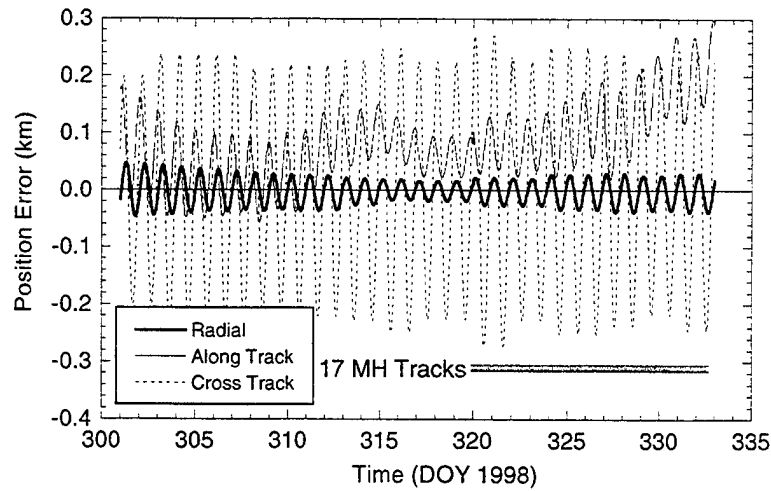


Figure 9. Two week dense Millstone only tracking orbit comparison

Figure10 shows that with a long arc of only SBV observations it is possible to accurately estimate the radiation pressure scale parameter and generate sub-kilometer orbits.

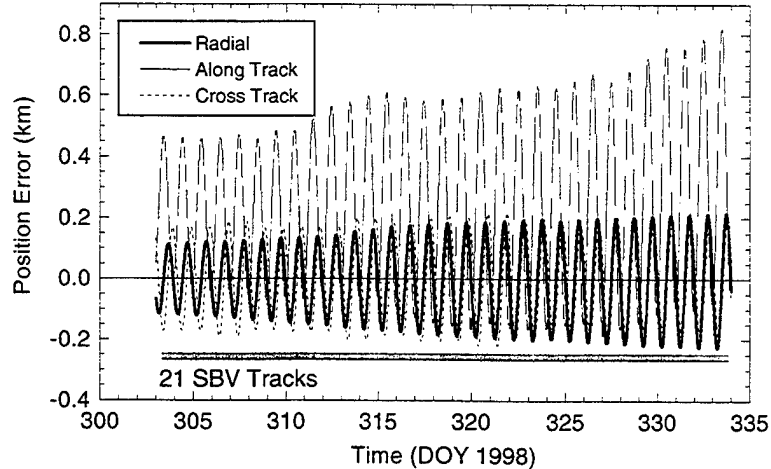


Figure 10. 31 day SBV only tracking orbit comparison

The final two figures show the quality of element sets obtained from analytical orbit determination methods. Figure 10 shows the orbit comparison using a MIT Lincoln Lab developed ANalytical Orbit Determination (ANODE) software. The data used is identical to that used for Figure 8. The position errors are stable over the observation span, but grow quickly when the orbit solution is propagated.

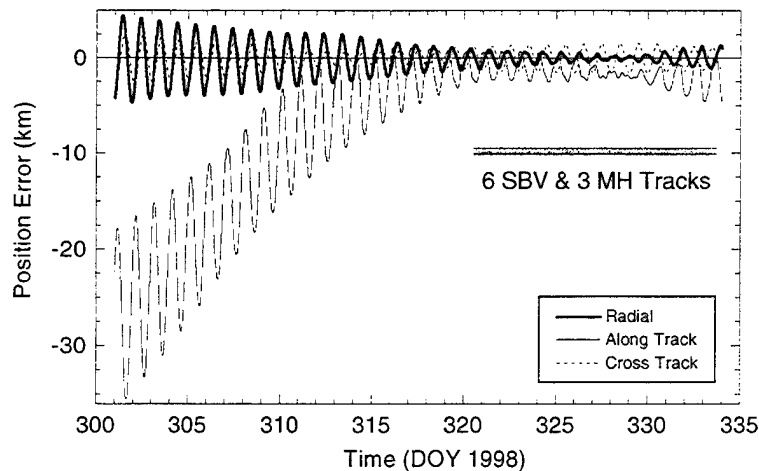


Figure 11. Accuracy of an ANODE orbit solution

Similar results are obtained for a SGP element generated by Space Command, and are shown in Figure 12. The figure shows the position error for an ephemeris generated by propagating a SGP element using a SGP4 propagator. This figure also shows the amount of data that were transmitted to Space Command for TDRS-4.

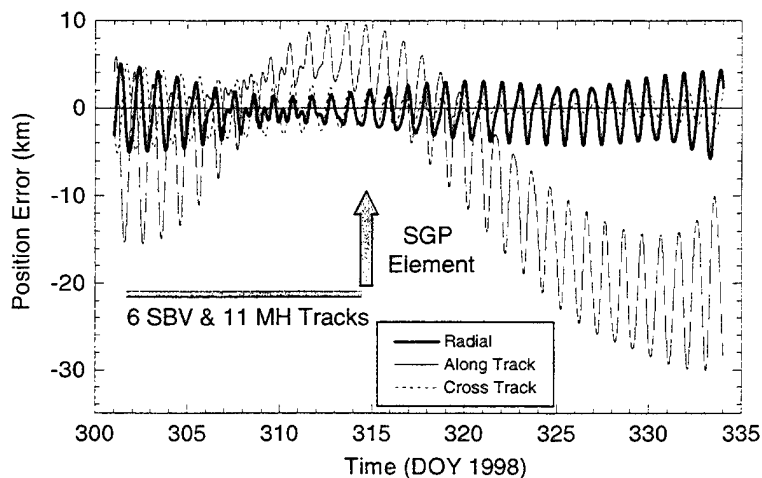


Figure 12. Accuracy of a SGP element set

CONCLUSION

The experience with Telstar 401 has demonstrated the necessity of highly accurate special perturbation orbits to confidently predict small miss distances between geosynchronous satellites. The overlaps of Telstar 401 orbits indicate that orbit accuracies of 0.5 – 2.5 km are

achieved with only Millstone Hill tracking. The addition of optical SBV data significantly improves the quality of the orbits to 500 meters. These results are supported by the TDRS orbit comparisons. The addition of well calibrated operator ranging data for the active satellites further improves the orbit quality to less than 100 meters. The TDRS analysis has also demonstrated the ability to determine accurate geosynchronous orbits using sufficient amounts of optical data only, and has illustrated the limitations of orbit solutions using analytical orbit determination methods.

ACKNOWLEDGEMENTS

We would like to acknowledge Tony Grise of Telesat Canada for providing range data and related information for this analysis. We would also like to acknowledge the assistance of Osvaldo Cuevas at GSFC in using the precise TDRS element sets published by GSFC.

REFERENCES

1. Oza, D.H., et. al., *Accurate Orbit Determination Strategies for the Tracking and Data Relay Satellites*, AIAA Paper N95-27768.
2. Haines, B.J., et. al., *A Novel Use of GPS for Determining the Orbit of a Geosynchronous Satellite: The TDRS/GPS Tracking Demonstration*, Proceedings of ION GPS-94, Salt Lake City, Utah, September 20-23, 1994.

Sequential Orbit Determination for the Catastrophic Decay of Object 13390

R. S. Hujsak¹ and J. F. Dicello III (Logicon Inc.²)

NORAD object 13390 was a Molniya rocket body, launched into a high eccentricity orbit in July 1982 and reentered on March 28, 1995. This object is typical of high eccentricity decaying objects, with high velocities at very low perigee altitudes (< 100 km), yielding very strong drag effects. High velocities, low perigees, and unknown vehicle attitude, coupled with atmospheric model uncertainty makes orbit prediction difficult, and as a consequence orbit determination is difficult. There were two objectives in this analysis, to demonstrate the capability of a sequential filter to automate the orbit determination process and to investigate the dynamics of a catastrophic event on March 14, 1995. Both objectives are met. The filter automatically processed all tracking data from November 16, 1994 through March 13, and the filter predicted reentry on March 14. However, the Space Surveillance Network tracked 13390 until March 28. The filter was reinitialized on March 14 and automatically processed the remaining tracking data. An investigation of the events of March 14 indicate that a breakup probably occurred, followed by the immediate reentry of a massive fragment and continuing orbit of a second fragment for 14 days, which explains both the filter prediction of reentry and the continuation of tracking by the SSN. This analysis demonstrates the degree of automation, reliability, and accuracy achievable with a sequential filter under stressing conditions and demonstrates the power of a filter as an analysis tool in complex dynamical problems.

1 INTRODUCTION

In this analysis the term "decay" refers to the long term, drag-induced circularization of the orbit, while "reentry" refers to the last few minutes as altitude drops from orbit altitude to impact. This terminology may be somewhat different than that used by the space surveillance community or the Space Surveillance Center (SSC).

The motivation for this effort is the anticipated commercialization of space surveillance services, where automated data processing will be required to minimize cost, and where cost effectiveness will be critical for business success. There are a few technical challenges to meet before full automation of space surveillance data processing can be achieved. One such challenge is the automation of the orbit determination process for decaying satellites with strong drag perturbations. And one of the most challenging decaying orbits is the catastrophic decay of a high eccentricity satellite.

The name "catastrophic decay" has origins in the space surveillance community, however the actual author is unknown. In general a catastrophic decay indicates a high eccentricity satellite with a very low (~ 105 km) perigee and a tremendous range of dynamics at play during the decay process. A decaying high eccentricity orbit crosses through the operating altitudes for all low altitude satellites, including Shuttle and Space Station, and for higher altitudes, including the GPS constellation.

The catastrophic decay orbit determination problem is very difficult. Prediction is completely dominated by drag (and lift) effects for satellites that are randomly tumbling and subject to drag forces in a region where the atmospheric density models have substantial uncertainties. Poor prediction accuracy, coupled with sparse radar coverage makes orbit determination difficult. This study uses special perturbation techniques to improve orbit prediction accuracy, and, hopefully, lead to improved automation of the orbit determination process with sparse data.

Drag dynamics are severe for objects in catastrophic decay. Apogee can decay at over 1000 km per day. A 20% random error in atmospheric density can easily lead to a 20% prediction error in period decay, with intrack prediction errors growing at 10,000 km per day. Drag accelerations may cause the satellite to break up or suffer some other structural damage before re-entry. Lift accelerations can cause satellites to skip off the atmosphere. All of these problems combine to make the orbit determination for a catastrophic decay very difficult.

Our approach is to use a sequential filter to perform the orbit determination, anticipating the need to account for large random unmodeled forces stochastically. We seek to demonstrate automation, accuracy, and reliability. If a

¹760 Constitution Dr. Suite 30, Exton, PA, 19341, (610) 458-3330, dhujsak@logicon.com.

² Logicon Inc. is a Northrop Grumman Company.

filter can be demonstrated to solve the automation problem for this class of objects, then it is sure to provide better accuracy and reliability for easier orbit classes.

The Space Surveillance Network (SSN) provided tracking data for this analysis. Satellite 13390 (international designator 82-074D) was selected because tracking data is available throughout the entire decay period, because there is a catastrophic event in the analysis interval, and because there is substantial tracking data over the last ten days of orbit life. This data set also includes some very long data gaps, which challenge the orbit determination process. Previous work by Fischer (Ref. 1) with this data set provides a convenient independent check of our findings.

The filter automatically processed all tracking data from Nov 16 through March 13, through a wide range of dynamics and tracking coverage. Then the filter predicted reentry early on March 14. However the SSN continued to track 13390 for another 14 days, until March 28. The filter was reinitialized on March 14, and subsequently processed all tracking data automatically until reentry on March 28.

Our current hypothesis is that the filter correctly predicted reentry on March 14. However 13390 broke into two major fragments late on March 13 or early on the 14th, due to repeated hammering by drag effects. It appears that the breakup actually kicked one fragment into a higher orbit, while the second fragment reentered immediately. The orbiting fragment subsequently decayed on March 28. Evidence of a breakup includes a jump in perigee from 95 km on March 13 to 109 km on March 14. Filter estimates for ballistic coefficient, lift coefficients, and the orbit provide evidence that the reentering fragment may have had greater mass than the fragment remaining in orbit.

In addition to a successful automation of the orbit determination process and analysis of the breakup, this analysis: (a.) rates the Jacchia 70 and Jacchia-Roberts density models as unsatisfactory for this application, (b.) rates the MSIS-90 model as sufficient, to the accuracy achieved, (c.) and identifies and quantifies significant random lift perturbations before and after breakup.

It will be necessary to process more of these test cases to establish whether the lessons learned with 13390 are repeatable, to automate the filter tuning process, and to enable automated processing everywhere.

Other Molniya rocket bodies have been observed to behave in a similar fashion, rapidly decaying until reentry is apparent, only to slow the decay rate with reentry many days later. If our hypothesis is correct, there is a massive fragment that reenters early. It is recommended that the SSN select another decaying Molniya rocket body and begin TIP tracking earlier. Dense tracking data and radar cross section data could be used to assess the breakup hypothesis and confirm the mass and size of the reentering fragment..

2 SATELLITE 13390 TEST CASE DESCRIPTION

2.1 Element History

Satellite 13390 is the insertion rocket body for Molniya 1-55 (international designator-82-074), launched into a high eccentricity orbit on July 21, 1982. Throughout the orbit lifetime the perigee rose and fell due to lunar and solar gravity perturbations. Toward the end of life the perigee is driven to a very low altitude by the same gravitational effects, and atmospheric drag causes rapid circularization and reentry.

The element histories, derived from SGP4 elsets for perigee, apogee, and period are given as "♦" in Figure 1 - Figure 3, below. These graphs provide some indication of the difficulties encountered in the orbit determination process.

In Figure 1 perigee is computed above the flattened earth. Although the SGP4-generated perigees have some scatter it is apparent that perigee decays steadily for 118 days (until March 14) and then appears to jump. Although it is difficult to state precisely when or how much perigee changes, due to the noise in the SGP4 solutions, it is apparent that a lower perigee altitude before March 14 is suddenly a higher perigee after March 14. The jump in perigee is unusual, and will motivate a hypothesis of a breakup on March 13, with immediate reentry of one piece, with the remaining piece surviving until March 28.

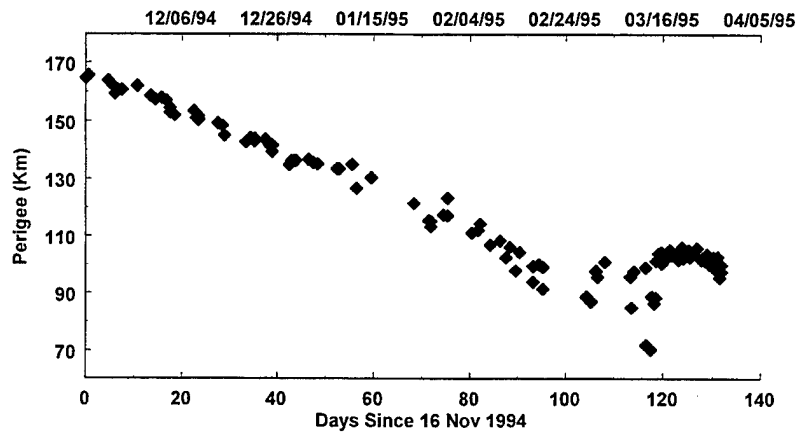


Figure 1: SGP4 Perigee Height Above Geoid

In Figure 2, apogee decay rate increases as perigee decays until suddenly, on or before March 14, the rate of apogee decay changes substantially. Both apogee and perigee point to a significant event on or near March 14.

The element sets reported in Figure 1 and Figure 2 have varying frequency. There are 74 elsets in the first 95 days (until Feb 18), an update rate of almost once per day. Then, from day 95 to day 118, there are three distinct gaps of 9 days, 5 days, and 2 days, reflecting sparse tracking data and difficult orbit dynamics. Finally, after day 118, elset density increases dramatically, reflecting both the high tracking rates associated with TIP (Terminal Impact Prediction) tasking.

In Figure 3 the SGP4 history of orbit period also shows a distinct abrupt event on March 14. Since orbit period is a function of semi-major axis, while apogee and perigee are functions of both semi-major axis and eccentricity, this clearly shows a major impulsive perturbation in semi-major axis.

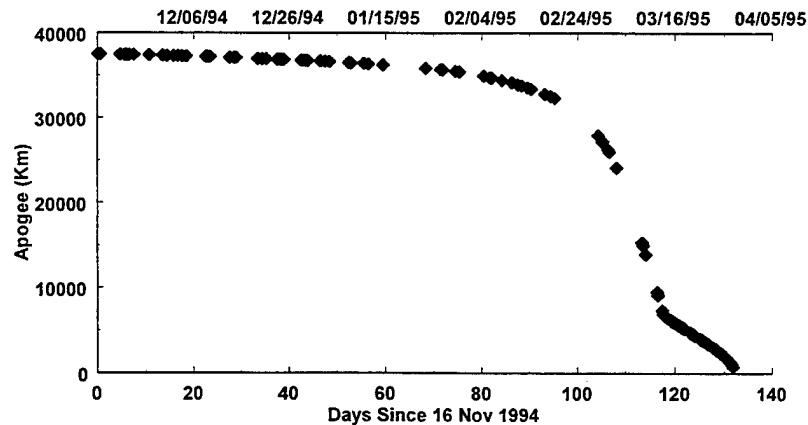


Figure 2: SGP4 Apogee History

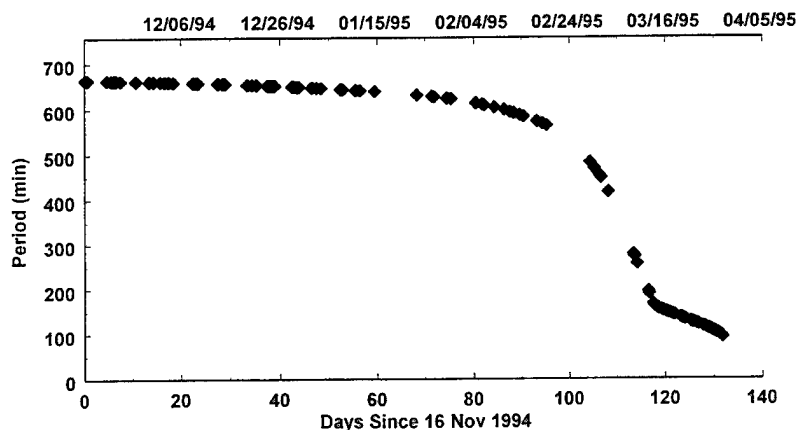


Figure 3: SGP4 Orbit Period History

Using these graphs we assign four distinct periods of dynamical behavior, which we arbitrarily call the Easy Decay Phase (before Feb 14), Rapid Decay Phase (Feb 14 – March 14), a Catastrophic Event (March 14), and TIP Phase (after March 14).

2.2 Tracking Data

Tracking data was collected by the Air Force Space Surveillance Network (SSN), and was archived in the 1st CACS archives. The data set consists of tracking data, station coordinates, data format description, and historical SGP4 element sets. Calibration statistics (noise and bias statistics) for the radars were not provided.

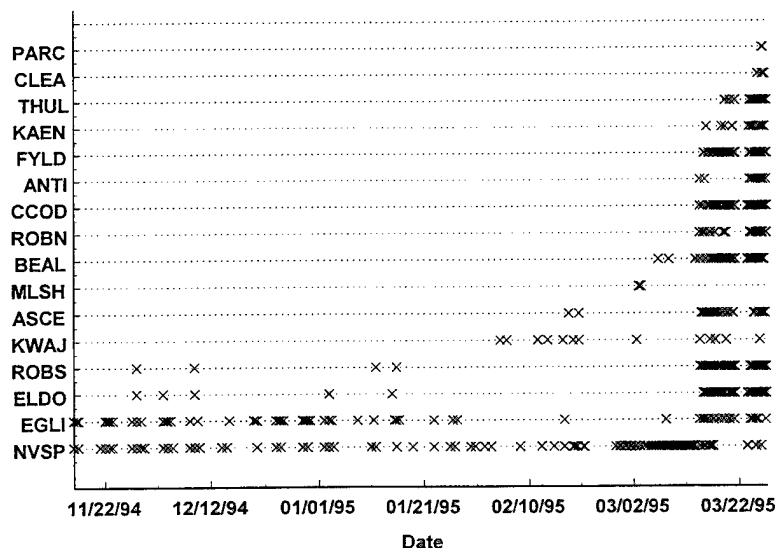


Figure 4: Tracking History

The tracking data density and distribution is evident in Figure 4, with sparse data until 13390 was placed on TIP status after March 14, 1995. Notice that NAVSPASUR is practically the only contributor of data in early March. Figure 4 reports all tracking data, and on this scale it is difficult to identify the data gaps, however there are several, some on the order of 6 days, and one critical gap two days long in the midst of the TIP Phase.

The NAVSPASUR data archived and provided for this analysis is "triangulated" data, derived from the native direction cosines reported by the instrument. According to Dr. Schumacher of Naval Space Command this triangulation process introduces additional error, and that error becomes worse as altitude increases. Dr. Schumacher recommended using the direction cosines data and particularly advised against using the triangulated range data for a high altitude object like 13390. He also advised that the triangulated angles data also degrades as range increases. Unfortunately the native direction cosine data for 13390 has been deleted. Given this advice, all ranging data from NAVSPASUR was discarded for this experiment, only the angles data was utilized, and it was deweighted. An attempt was made to discard NAVSPASUR data altogether, but it proved critical to automating the orbit determination process; some data gaps were simply too long without NAVSPASUR observations.

3 SOFTWARE DESCRIPTION

The software used in this analysis consists of a sequential filter and a matched smoother. The filter provides the orbit determination process. The smoother is an analysis tool, used to test the statistical integrity of the filter solution and to provide a reference against which filter predictions can be compared. The smoother is also necessary because there was no definitive SSC ephemeris included with this test case.

3.1 Filter

The filter is a Modified Extended Kalman Filter, locally linearized about the last estimate (i.e. a current-time implementation). In the Extended Kalman Filter the state is predicted via numerical integration of the equations of motion, using standard force models. Modifications are made to both the Kalman Time Update and the Kalman Measurement Update. The Time Update discards the Kalman white noise hypothesis and employs a physically connected process noise structure, as defined by Wright (Ref. 7). The Measurement Update uses a non-linear measurement representation (Ref. 2). State space consists of six orbit parameters, a drag coefficient, two lift coefficients, and one time-varying bias state for each sensor measurand being processed (e.g. Eglin would have 3 states, one for range and one for each angle).

Measurement states are added when a new station enters state space and are dropped after the tracking data has been processed and the correlations to the state estimate become negligible. This means that state space is continually expanding and contracting, adapting to the tracking scenario.

Measurement errors are quantified in terms of white noise sigma, a constant bias, and a time-varying bias, characterized as an exponentially correlated Gauss Markov process. Measurements are rejected or accepted automatically, based on an "n-sigma" rejection criterion, where the sigma is computed from the filter covariance. This is important, since it depends on a realistic filter covariance. If the covariance is too small, then too much tracking data is rejected, and if the covariance is too big, the filter will accept "bad" tracking data.

3.2 Smoother

The smoother is a Modified Rauch-Tung-Striebel formulation (Ref. 3). The smoother uses the filter outputs (state and covariance) as inputs, and processes these in reverse chronological order. The modification made to the Rauch-Tung-Striebel smoother consists of an additional process noise term defined by Wright (Ref. 4). The smoother state space also grows and collapses, in agreement with the filter state space, the mechanism of which is embodied in McReynolds' Extended Gauss Markov Theorem (Ref. 5). As in the filter, the orbit substate is propagated by numerically integrating the equations of motion.

3.3 The Integrator, Force Models, and Coordinate Systems

The integrator and force models used are summarized below.

The use of observed values for atmospheric density model inputs represents a slight advantage over real-time operations however the predicted values which were used in SSC operations were not archived.

Parameter	Model	Remarks
Propagator:		
• Perturbation Method	Special Perturbations	Variation of Parameters
• Integrator	Runge-Kutta (4,4)	
• Step Size	Variable	
Force Models		
• Earth Gravity	JGM-2 (40,40)	
• Sun Gravity	Point mass	JPL DE200
• Moon Gravity	Point mass	JPL DE200
• Drag	Spherical assumption, with solve-for coefficient	
• Density Model	MSIS-90	
• Flux	Observed a_p and $F_{10.7}$	
• Lift	No modeling, strictly solve-for components, see text	Rapid Decay Phase and TIP only
• Solar Pressure	Sphere	Constant coefficient
• Solid Earth tide	1 st order only	
Coordinate Systems		
• Standards used	J2000.	Uses complete IAU definition (Ref. 6)
• Earth Orientation Parameters	Polar offset and ΔUT	Observed daily USNO values

3.3.1 Drag and Lift Models

Drag is modeled for a spherical object, using the classical formulation as an acceleration in the anti-direction of the of the satellite's velocity with respect to the rotating atmosphere:

$$\ddot{\underline{r}}_D = -\frac{1}{2} C_D (A / M) \rho |\dot{\underline{r}}_a| \dot{\underline{r}}_a$$

Lift was introduced because the filter consistently diverged when solving for drag alone. It was observed that the filter was attempting to correct the orbit plane just prior to diverging, and that, together with the intuitive description of a slowly tumbling object presenting a variable cross-section and orientation to the atmosphere, seemed to suggest that lift effects might be significant. Lift accelerations are only applied in the integrator if the filter solves for a non-zero coefficient value.

3.3.2 Atmospheric Density Model Selection

The MSIS-90 atmospheric density model is used throughout this analysis. Two other models were considered and discarded, the Jacchia '70 and the Jacchia-Roberts '72 models.

The Jacchia-Roberts density model was our first choice, because of the computational efficiency of the analytic integration of density with altitude. However, the analytic density integrals are defined in altitude bands, and functions are discontinuous where altitude bands abut. The GTDS version of Jacchia-Roberts uses splines at these boundaries to enforce continuity, and that is usually sufficient for nearly circular satellites. For 13390, however, the satellite passes through these altitude bands so quickly that the splines are ineffective, and density would appear to have step functions in it. Using the Jacchia-Roberts model actually caused the filter to diverge within the first 30 days of this analysis, and motivated a search for a replacement.

Similarly the Jacchia '70 model does not extend below 90 km altitude, and requires that some other model be applied below 90 km, which will create a step function at 90 km. This analysis requires a prediction of terminal impact, making the step function at 90 km, and hence the Jacchia '70 model unacceptable.

The search for a continuous model included a conversation with Dr. Frank Marcos of AFRL. He recommended the MSIS-90 model because it is continuous across all altitude bands, including reentry.

The decision to use the MSIS-90 model is a key step in the success of the filter in this application.

4 ORBIT DETERMINATION PROCESS

4.1 Radar Calibration Statistics

Radar calibration data was not provided with this test case, so it was necessary to obtain radar calibration statistics elsewhere. Fortunately we have an archive of tracking data provided by the former commander of 1st CACS, Col. Muolo, which contains tracking data for each DMSP satellite for 30 days in Nov-Dec 1994. The orbits for two of the DMSP satellites were determined, using the filter and smoother, and the post-fit residuals were computed versus the smoothed ephemeris. Calibration statistics were extracted and used to support the analysis of the catastrophic decay of 13390.

The calibration activity was intended to generate approximate statistics, sufficient for an analysis of the catastrophic decay of 13390, where force model errors clearly dominate tracking data errors. As a consequence the statistics for some of the radars are questionable, and the need for a better calibration is evident in this analysis.

Specifically, Ascension and Fylingdales reported very little tracking data on DMSP satellites and, consequently, the calibration statistics are probably poorly determined. (In the TIP Phase, Section 4.5.3, below, these stations will have a high percentage of tracking data rejected by the filter.)

All range residuals from NAVSPASUR were ignored in the calibration process (recall Section 2.2, above) and the noise statistics for angles measurements were further inflated to reflect increasing uncertainty in the triangulated angles with increasing range.

4.2 Initialization

The assignment of initial statistical values for the filter is often referred to as "tuning", which is somewhat of a misnomer. The following sections describe the "tuning" process as an attempt to assign physically reasonable statistical values for physical processes.

The stated objective of this analysis is to demonstrate automation, and in that spirit a single set of statistics is assigned and used for the entire 133 days. Better accuracy could have been obtained if the filter was tuned for smaller and smaller subsets of tracking data, but that would not be an automated process.

Since many of the parameters cited here were manually selected, the next step in automating the orbit determination process will be to functionalize and automate the tuning process.

4.2.1 Orbit Initialization

An initial orbit determination was performed using the Herrick-Gibbs method, followed by a one-day six-element three-iteration batch least squares fit to all tracking data on Nov 15 and Nov 16.

4.2.2 Drag and Solar Pressure Coefficient Initialization

The initial value for ballistic coefficient ($B=1/2 C_D A/m$) was set to 0.002 and the initial value for solar pressure scale factor ($S=1/2 C_R A/m$) was set to 0.0009 (consistent with a C_D value of 2.2 and a C_R value of 1.0). After the filter was run over the first 30 days, it was apparent that the filter was driving B to 0.006, so the starting value was reinitialized to 0.006. It was also apparent that S was weakly observable, so the S value was set to 0.0025 (approximating the ratio of $C_D = 2.2$ and $C_R = 1.0$) and the solar pressure solve-for flag was turned off.

Lift coefficients are initially set to zero.

4.3 Orbit Covariance Initialization

The a priori orbit error covariance was arbitrarily set with the following sigmas (with zero off-diagonals):

R (m)	I (m)	C (m)	Rdot (m/s)	Idot (m/s)	Cdot (m/s)
2500.	3000.	6000.	6.	10.	6.

4.3.1 Gravity Process Noise

Gravity process noise is computed using Wright's (Ref. 7,8) formulation for time-correlated gravity model errors. Wright's model is based on the original work of Kaula (Ref. 9), Gersten, Gore, and Hall (Ref. 10), and Pechenick (Ref 11).

4.3.2 Drag Process Noise

Drag is modeled as a time-varying coefficient, subject to random changes in the satellite cross-section and to random errors in the density models. Nominally the atmospheric density models are quoted as being accurate to $\pm 15\%$, however the filter did not perform well with 15 % (one-sigma) errors for ballistic coefficient uncertainty. The analyses reported here use a 10% uncertainty (one-sigma) for drag. The correlation half-life for drag was set to ten days for the entire analysis.

4.3.3 Lift Process Noise

Lift is defined to be in two directions, each orthogonal to the direction of drag (which aligns with satellite velocity with respect to the rotating atmosphere). L_1 is defined to be in the orbit plane, perpendicular to the drag direction, and positive "up". L_2 is directed orthogonal to drag and to L_1 , and positive in the same direction as the orbit crosstrack. The drag-lift coordinate system is similar to, but slightly rotated from the Frenet coordinate system.

Lift states were introduced as a mechanism to "pump" the covariance for random lift effects, expecting that the lift acceleration would be independent from perigee passage to perigee passage, but might be fairly constant over any single perigee pass. That characterization demands a short half-life, and a value of 20 minutes was assigned.

The Gauss Markov r.m.s. values were obtained by trial and error, since we have no prior experience with lift effects at this altitude. Originally we expected L_1 to dominate L_2 , but when the filter was run with L_1 r.m.s. values larger than L_2 values, the filter behaved poorly. Large r.m.s. values for L_1 and for L_2 also caused the filter to fail, and we finalized the r.m.s. uncertainty on L_1 and L_2 to be $0.001 \times B$ and $0.01 \times B$. These tuning values were used from Feb 3 until reentry.

4.4 Processing Strategy

The filter was initialized on Nov 15, 1994 as described above. The filter was run as a continuous process until it started to diverge in February 1995. After some analysis we noticed that the filter was trying to correct orbit inclination just prior to diverging, and so the software was modified to introduce two new states, one for each component of lift.

The analysis was repeated, processing from Nov 16 to Feb 3 without the lift states and then, beginning on Feb 3 the lift states were added. The result was a continuously running filter until March 13, when the predicted orbit indicated reentry on March 14.

To reinitialize the filter after March 13 required a good track of data for a Herrick-Gibbs orbit initialization. The first such track was found on March 14, leaving a one-day data gap where the filter did not process the data. After reinitialization the filter automatically processed all tracking data until reentry on March 28.

This report does not determine the appropriate technique for automating processing from March 13 to 14, however it does provide a diagnosis of the problem, and future work will address improving on these results.

4.5 Filter Accuracy Assessment

There is no "truth ephemeris" available for 13390. For this analysis a smoother was applied to generate a smoothed post-fit ephemeris. The smoother processes the filter state and covariance in reverse chronological order and generates an ephemeris which should be of better accuracy than the filter ephemeris. Filter accuracy is measured as the difference between the filter and the smoother.

Filter-smoother differences are similar to classical differences between a prediction and a post-fit ephemeris over the same interval, when the differences are large, e.g. during a prediction, then the difference can be reliably interpreted as filter error. However when the differences are small, e.g. over tracking intervals, then the magnitude of the error in the smoothed ephemeris must be considered.

Sections 4.5.1 through 4.5.3 provide an assessment of the filter error over each of three segments of the analysis, Slow Decay, Rapid Decay, and TIP Status. The Catastrophic Event will be discussed separately in Section 5.5.

4.5.1 Filter Accuracy During Slow Decay

Figure 5 provides the vector magnitude of the filter-smoother position differences, together with the tracking data distribution for the Slow Decay Phase. The saw-toothed pattern is characteristic of filter accuracy, with small errors over tracking and classical error growth over prediction intervals. Over this period perigee drops from 170 km to 130 km, and the prediction accuracy becomes more sensitive to gaps in the tracking data as perigee drops.

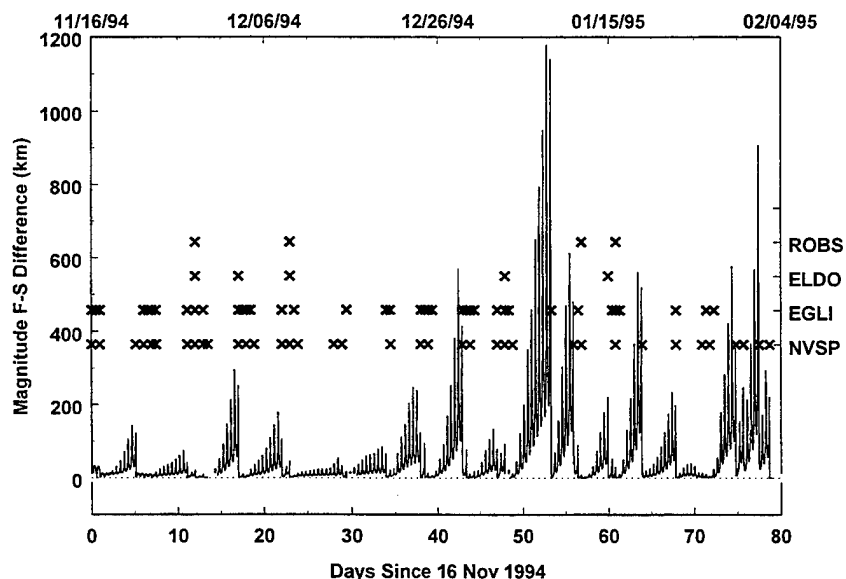


Figure 5: Filter Position Error RSS During Slow Decay Phase

Beginning in February (toward the end of Figure 5) orbit accuracy degrades, probably because NAVSPASUR is the only sensor reporting tracking data, and that data is severely dewighted (see Section 4.1). The filter remains stable across all gaps in the tracking data and responds immediately to new tracking data.

There was no manual editing of tracking data during the Slow Decay Phase and the filter accepted all tracking data.

4.5.2 Filter Accuracy During Rapid Decay

Figure 6 depicts position error magnitude during the Rapid Decay Phase. The dominant feature of this graph is the large error incurred over a seven-day data gap. During these seven days apogee dropped 3000 km, while orbit error grew to 25,000 km (practically one-half rev), and yet the filter successfully predicted through the data gap and continued the automatic orbit determination process.

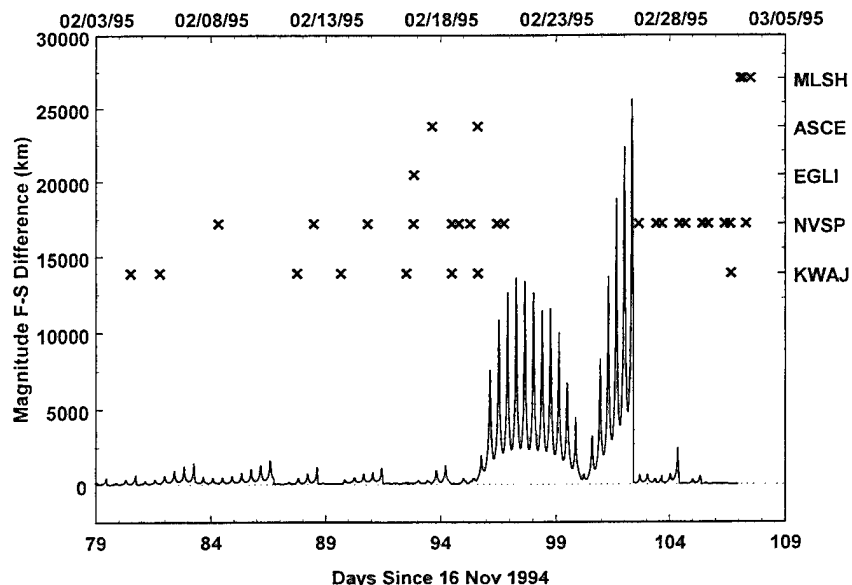


Figure 6: Filter Position Error RSS During Fast Decay Phase

There are no filter-smoother differences for the interval March 5-14 because the filter predicts reentry on March 14 and the smoother is not designed to smooth backwards from a reentry.

During the Rapid Decay Phase, between Feb 18 and March 14, it was necessary to manually edit out two NAVSPASUR hits, one Eglin fence observation, and one short Millstone track. Over this interval the filter automatically rejected almost all elevation data from Ascension, due to poor calibration (see Section 4.1).

4.5.3 Filter Accuracy During TIP Phase

Figure 7 provides the vector magnitude of the filter-smoother position differences, together with the tracking data distribution for the TIP Phase. A two-day gap in the tracking data generates differences as large as 20,000 km, however the filter was able to recover following the gap. (This data gap is most likely a glitch in the archive process, and does not reflect on space surveillance operations.)

Comparing Figure 7 to Figure 5 illustrates the effect of dense tracking data. Even though perigee is lower and atmospheric model uncertainties are larger and (as discussed later) there are pronounced lift effects during TIP Phase, the accuracy is substantially better than the Slow Decay Phase.

Over the TIP Phase there were 7570 observations collected of which 6 were edited manually (all single fence observations from phased array radars, which were probably mistagged). The filter rejected approximately 10% of the tracking data. Fully one-half of the rejected data was from Fylingdales and Ascension, which were poorly calibrated in our radar calibration activity (Section 4.1). The remaining rejections are immediately after the gap in tracking data, while the filter is trying to recover from a 20,000-km prediction error.

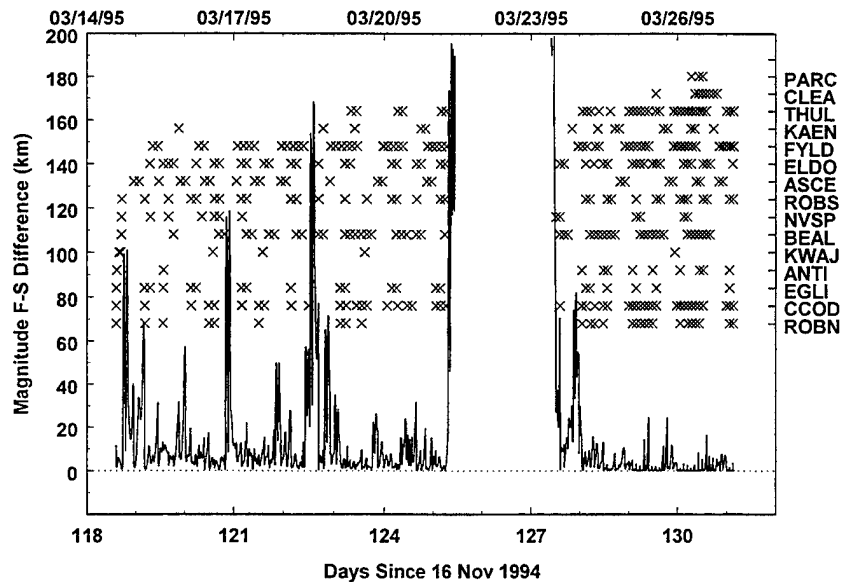


Figure 7: Filter Position Error RSS During TIP Phase

5 DECAY AND REENTRY ANALYSES

5.1 Filter Solution for Apogee

The end-to-end solutions for apogee are given in Figure 8. The filter values are graphed for the intervals over which the filter processed autonomously, and a one-day gap appears where the filter predicted reentry on March 14. Apogee decay rate changes significantly during the data gap, as indicating a catastrophic event.

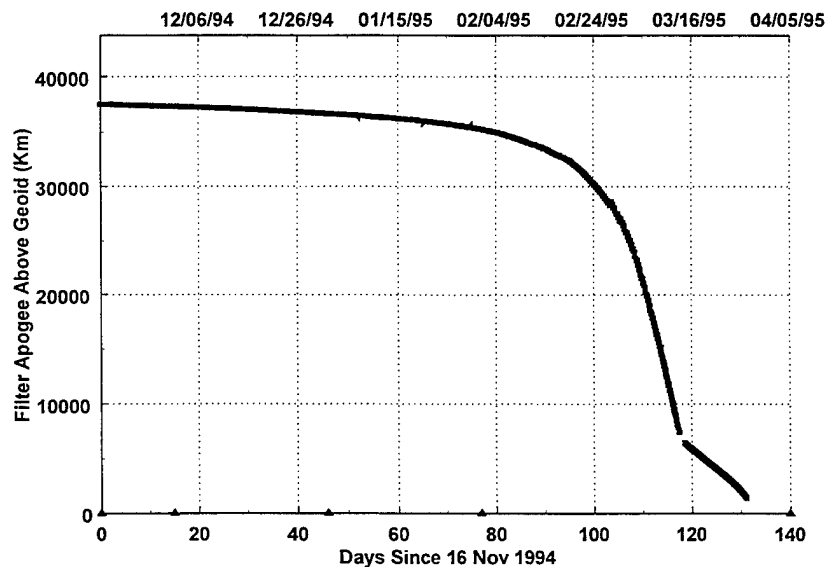


Figure 8: Filter Solution for Apogee

5.2 Filter Solution for Perigee

An end-to-end solution for perigee is given in Figure 9. The filter values are graphed versus the left-hand scale and the SGP4 values are graphed against the right hand scale. The scales are slightly offset so that neither result is obscured.

The perigee graphed here is derived from the osculating position and velocity, as determined sequentially, with J_2 periodic effects removed. The value graphed here is derived from the following procedure:

- Convert the osculating position and velocity (at any point in the ephemeris) to classical elements, using the standard transformations.
- Convert osculating classical elements to mean classical elements by subtracting the J_2 short term periodics (using Liu's formulation for the periodics (Ref 12)).
- Set the mean value of mean anomaly to zero, approximating mean elements at perigee.
- Convert mean classical elements at perigee to osculating, again using Liu's equations.
- Compute osculating position and velocity from the osculating classical elements at perigee.
- Compute altitude of perigee above the oblate spheroid.

This calculation gives a consistent value for perigee, and agrees with the osculating perigee at perigee. If the osculating perigee is computed directly, without removing J_2 periodic effects, then the value can vary by ± 10 km over a single orbit period.

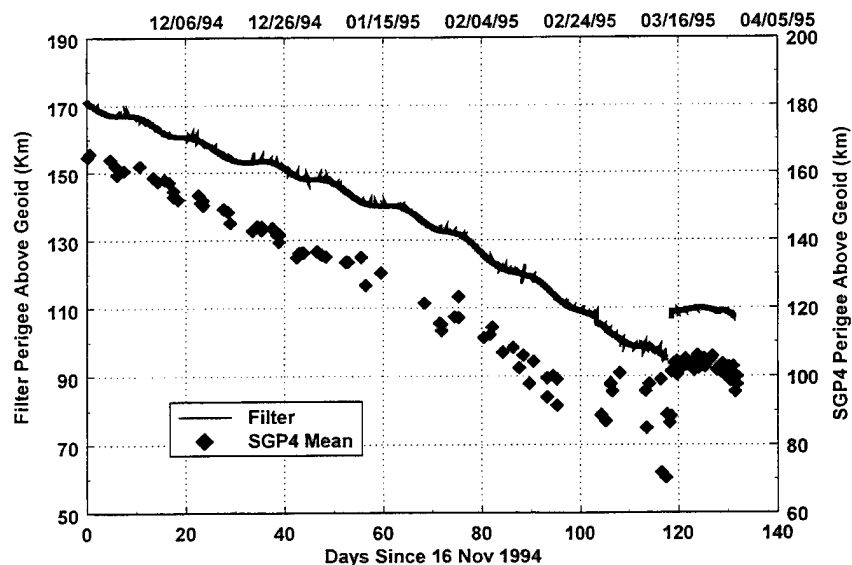


Figure 9: Solutions for Perigee Height above Geoid

Again, Figure 9 points to a catastrophic event occurring late on March 13 or early on March 14. Clearly, after reinitialization, the filter estimate of perigee is higher than before the gap, indicating unusual activity. The SGP4 elsets confirm the diagnosis.

5.3 Solution for Ballistic Coefficient (B)

Recall that a single set of "tuning" parameters are assigned for the entire analysis, seeking automation over possible accuracy advantages from selective tuning of smaller sub-intervals. In Section 4.2, the filter used a nominal value for B of 0.006, and assumed a time-varying process with one-sigma magnitude excursions of $\pm 10\%$ of B . Figure 10 provides evidence of a more complex set of tuning rules will improve accuracy.

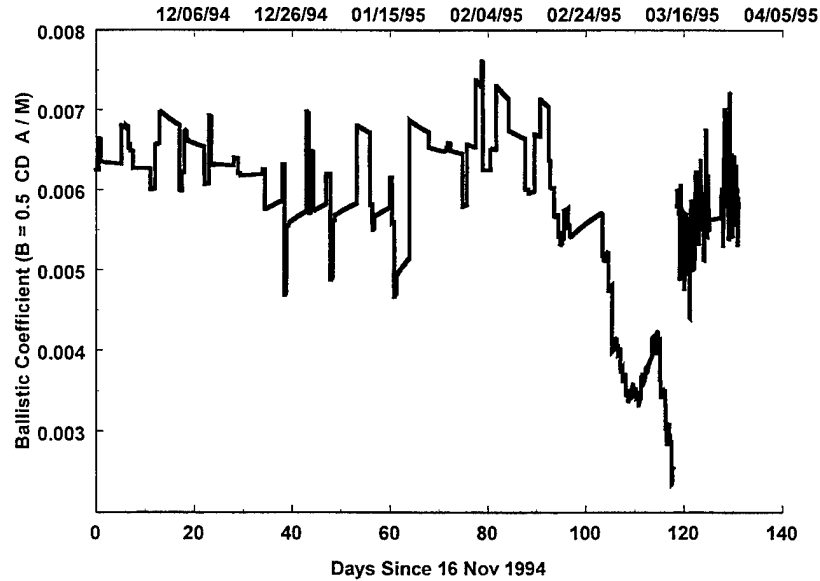


Figure 10: Ballistic Coefficient Solutions

Figure 10 provides the point-by-point filter solutions for B. Figure 11 focuses on twenty days of Rapid Decay.

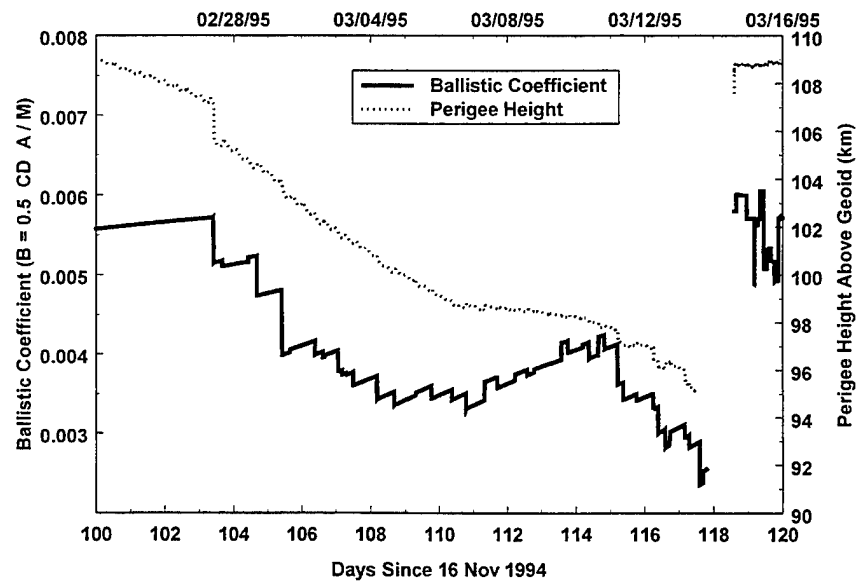


Figure 11: Ballistic Coefficient Detail

5.3.1 B Solutions During Slow Decay

During the Slow Decay Phase (before Feb 2.) the average value for B is 0.0065, with variations as large as $\pm 25\%$. This behavior is consistent with an a priori uncertainty of $\pm 10\%$. Given the long term stability of B, it might have been possible to improve prediction accuracy across data gaps by using a tighter constraint than $\pm 10\%$.

5.3.2 B Solutions During Rapid Decay Phase

Over the Rapid Decay Phase, following Feb 3, the ballistic coefficient drops, then rises, and finally plunges as the filter predicts reentry on March 14. Since 13390 does not reenter this behavior motivated a more detailed investigation.

One hypothesis for the erratic behavior of B is that the MSIS-90 model is in error by as much as 50% below 106 km altitude. However there are other, equally likely hypotheses discussed below.

Perigee dropped below 120 km and decayed monotonically to 95 km (see Figure 9). The estimate for B systematically decreases as perigee drops deeper into the transition region between free molecular flow and laminar flow for the atmosphere, precisely as predicted by hypervelocity drag theory (Ref. 13).

After March 6, B increases. This too is possible under hypervelocity drag theory, since the ballistic coefficient is a function of the angle-of-attack between the satellite and the atmosphere, and the angle of attack at perigee decreases as apogee drops. Alternatively the satellite could be coming apart, actually increasing the drag cross-section as shrouds or struts begin to tear away.

Between March 11 and March 14 the ballistic coefficient drops rapidly. It is not clear if this behavior is explainable based on hypervelocity drag theory. Perhaps the satellite structure begins to collapse from repeated hammering by atmospheric drag. Due to the fact that only correlated tracking data is archived, it is not possible to determine if unknown targets were also detected, indicating fragmentation. The filter fit to the tracking data is quite good, indicating a single piece being tracked, and indicating that the MSIS-90 model is continuous below 106 km altitude, if not correct.

Reentry is predicted for March 14, but 13390 is later tracked with a perigee of 109 km, a mysterious behavior.

This analysis and that of Fischer (Ref. 1) agree that reentry is predicted to occur on March 14.

5.3.3 B Solutions During TIP Phase

During the TIP Phase, B has rises slowly and, suddenly, has an apparent diurnal behavior (see Figure 12). The source of the diurnal behavior is not known, but the magnitude is $\pm 16\%$ about the average value for B, which is on the order of the "state of the art" in empirical density models. On the other hand, the B solution was fairly smooth before March 14.

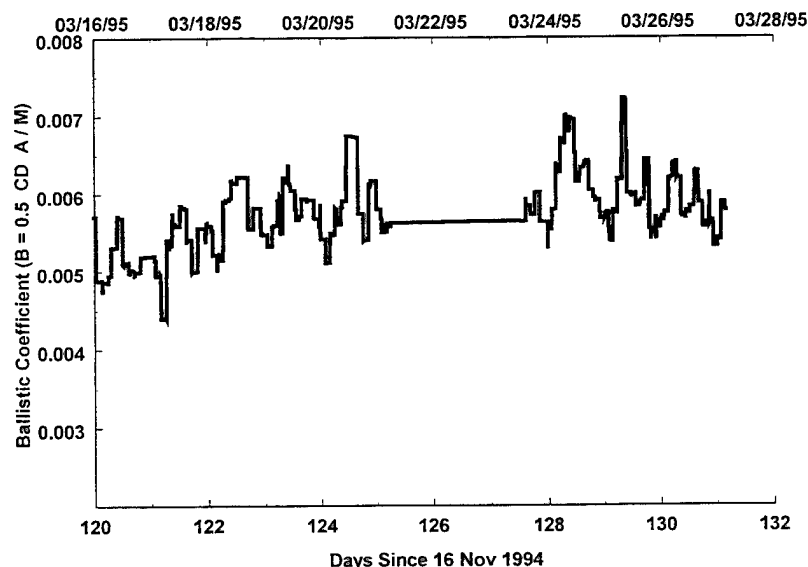


Figure 12 Drag Coefficient During TIP Phase

5.4 Solution for Lift

Recall that lift states were introduced to provide a mechanism for accounting for random lift effects due to a randomly tumbling object, specifically as an easy method of generating process noise without having to derive a stochastic function. We did not expect to be able to actually estimate lift coefficients which could be used to improve orbit prediction (i.e. values that remain constant for multiple revs).

The filter does assign corrections to the lift states, even though the r.m.s. statistics are small and the half-life is short. These solutions are graphed in Figure 13 and Figure 14.

Both solution parameters have similar macro-behavior, differing significantly before and after March 14. Lift effects in both components are an order of magnitude large after March 14 than before. This is difficult to explain based on a tumbling hypothesis, particularly since perigee is higher after March 14 by 14 km. Lift could increase if the shape of the object changed, but it is doubtful that the structure could be distorted sufficiently to generate an order of magnitude more lift. One reasonable hypothesis is that the object broke up and the mass of 13390 after the breakup is significantly less than before March 14.

Since both lift states exhibit large solutions, the effect will perturb the orbit plane as well as the motion in-plane. This provides some explanation why solutions that only account for perturbations in the drag direction perform so poorly.

These solutions for lift coefficients are visibly random. This may explain why least squares orbit determination is such a difficult process for these objects, that a process that solves for constants of integration cannot solve for random variables of integration. This is an important consideration in choosing an orbit determination process for commercial space surveillance applications.

The solutions for lift over the Rapid Decay Phase are much smaller than over the TIP Phase, however lift states were required before the filter would successfully process through the Rapid Decay Phase automatically. The estimates for L_2 are almost an order of magnitude larger than the estimates for L_1 , indicating that cross-track lift perturbations were more significant than "radial" lift perturbations.

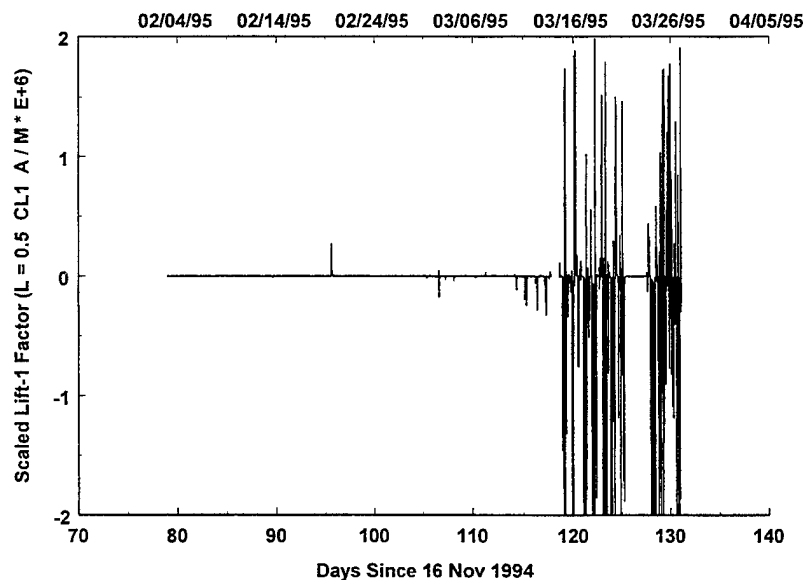


Figure 13: Lift 1 Solutions

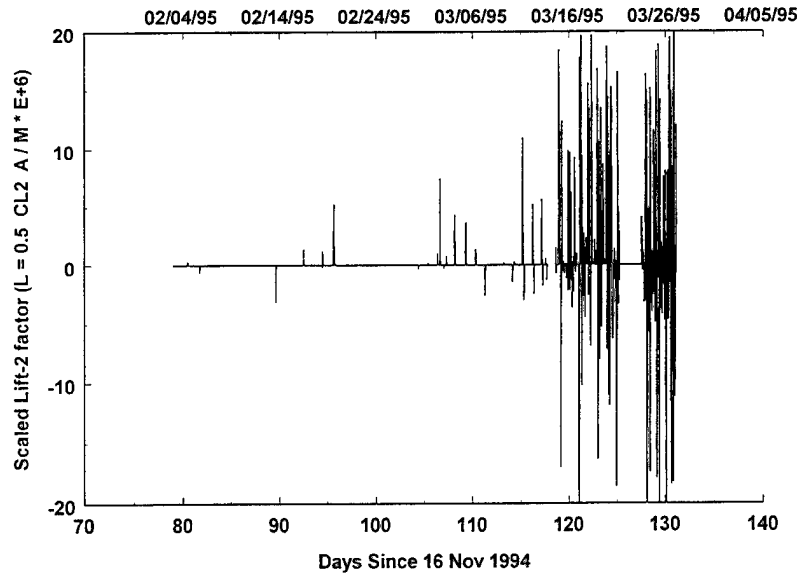


Figure 14: Lift 2 Solutions

5.5 Analysis of the Catastrophic Event

The big mystery with 13390 is the sudden change from a reentering trajectory with perigee at 95 km to an orbit with perigee at 109 km. Our hypothesis is that 13390 broke into at least two large fragments late on March 13 or early on March 14. One fragment reentered immediately, while the other fragment continued to orbit the earth with a higher perigee.

Using the vis-viva integral the velocity of the combined masses and the velocity of the individual pieces can be computed at the instant of breakup.

$$v^2 = \mu \left(\frac{2}{r} - \frac{1}{a} \right)$$

If the breakup occurs on March 14 at 00:00 Z (arbitrarily selected), then (Figure 16) the apogee pre and post breakup is approximately the same at 6500 km. The parent object has a perigee of 95 km (Figure 15). Suppose that a single event, due to breakup, raises the perigee of the high orbit to 109 km. A breakup must occur between 109 km and 6500 km altitude, within the altitude range of the orbiting fragment., and is most likely near 109 km.

Assuming a breakup at $r = 109$ km altitude, the velocity of the parent object would be 9.038 km/sec and the post-breakup velocity of the surviving fragment would be 9.040 km/sec, requiring a velocity change of 2 m/sec.

There is no active source of thrusting to generate a velocity impulse, but the conservation of linear momentum does result in a change in velocity when objects break up. If the breakup is instantaneous and if there are two pieces, then the conservation of linear momentum yields

$$m_p \underline{v}_p = m_1 \underline{v}_1 + m_2 \underline{v}_2.$$

The exact time of breakup is unknown, however for any candidate time of breakup, the velocity vector (\underline{v}_p) of the parent object is given by the filter estimate and the dry mass is known ($m_p=870$ kg, Ref.). The velocity vector of the orbital fragment can also be obtained after the breakup can also be derived by predicting backward from filter estimates on March 14 after reinitialization. The unknowns in the conservation of momentum are the masses of each fragment and the velocity vector for the reentering fragment.

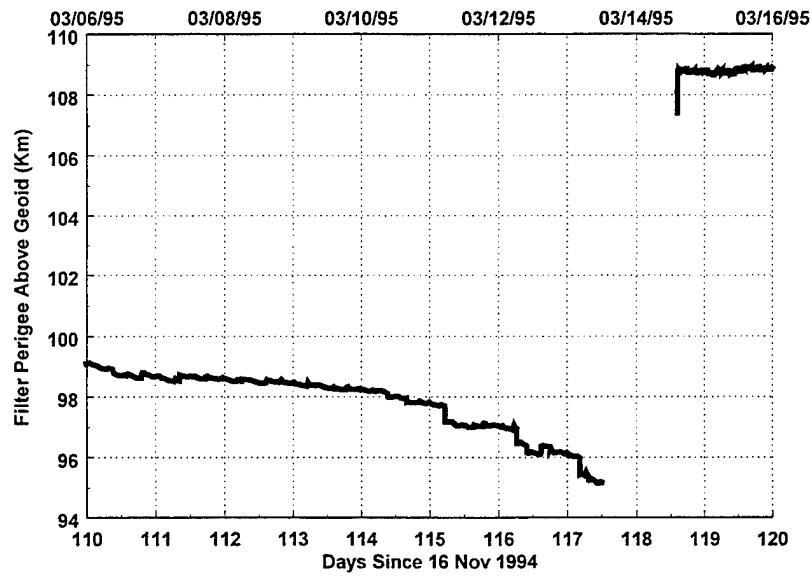


Figure 15: Perigee Step Function

To simplify the problem, we computed the delta-velocity necessary to raise perigee by 14 km for the orbital fragment, while conserving apogee at 6500 km. Depending on where in the orbit the delta-v is applied, a delta-v magnitude of 2-3 meters/sec is sufficient. The delta-v is a very small fraction of the total velocity (9+ km/sec), so, regardless of direction that the delta-v is applied, the post-breakup velocity vector for the orbiting fragment is almost collinear with the pre-breakup velocity vector of the parent at the instant of breakup.



Figure 16: Apogee Step Function

If the reentering fragment's velocity vector is also almost collinear with the velocity vector for the parent object, then the vector equation for conservation of linear momentum is approximated by a scalar equation:

$$m_p v_p \approx m_1 v_1 + m_2 v_2.$$

Substituting mass of the parent $m_p=870$ kg, and scalar velocity of the parent $v_p=9.038$ km/sec at 109 km altitude, and the velocity of the surviving fragment $v_1=9.040$ km/sec at 109 km altitude, then the masses of the orbiting fragment (#1) and reentering fragment (#2) can be parametrically evaluated, while conserving masses, $m_p = m_1 + m_2$. Postulating the mass of the orbiting fragment, and holding apogee at 6500 km, we can compute the perigee altitude of the reentering fragment:

m_1 (kg)	m_2 (kg)	v_2 (km/sec)	Perigee ₂ (km)
800	70	9.015	-101
600	270	9.0336	+54
400	470	9.0362	+76
200	670	9.0374	+86
100	770	9.0377	+89

These calculations show that if a breakup occurs at 109 km altitude that a wide range of mass distributions are possible, yielding immediate reentry of one fragment and continuing orbit of the second fragment. In fact, 90% of the total mass of the parent could reenter and satisfy the breakup hypothesis.

Does it make sense for 90% of the total mass of the parent to reenter? The lift coefficients determined by the filter are an order of magnitude larger following the breakup, indicating a significantly less massive surviving fragment (Section 5.4). The drag coefficient is also significantly perturbed, exhibiting a diurnal behavior that is not evident before the breakup. Given these indicators, it appears that a massive reentry might have occurred on March 14, however without supporting evidence, such as radar cross-section signature data, it remains a hypothesis.

5.6 Reentry Predictions

Figure 17 is the result of repeated attempts to predict reentry. The predictions were performed by selecting the filter state at each 0000Z, 0600Z, 1200Z, and 1800Z, every day for the last 5 days of life, and predicting until altitude falls to 10 km above the geoid. The first seven predictions coincide with the gap in tracking data (recall Figure 7). The next three predictions are not very good, principally because the filter is recovering from 20,000 km of error incurred across the data gap. Thereafter the predictions trend nicely toward the last, best estimate of reentry time.

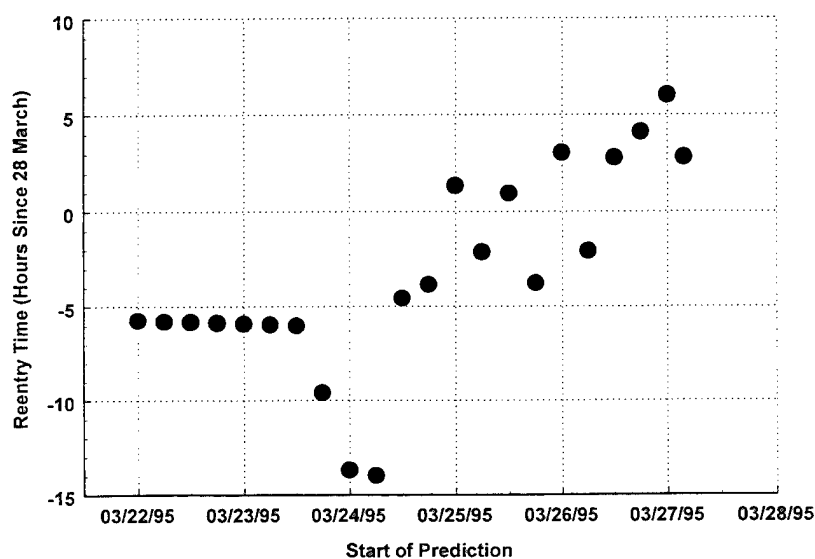


Figure 17: Repeated Predictions of Reentry Time

There is no information available to indicate the true time of reentry. Our best estimate, based on the last prediction is reentry occurred on March 28 at 0230Z. However, based on the general trend in the last few reentry predictions, the actual reentry time may be as late as 0600Z.

Successive reentry predictions trend toward the eventual reentry time.

6 CONCLUSIONS

The capability of a filter to automatically process this most difficult of decay cases has been established. The filter was run with a single set of tuning parameters through a variety of drag conditions and tracking scenarios, and produced a continuous solution throughout the decay process. This makes the filter a viable candidate for automating the orbit determination process for commercial space surveillance applications.

The catastrophic decay of this Molniya rocket body appears to result in two separate reentry events, one during a suspected breakup on March 14 and another on March 28. Based on the pre-breakup and post-breakup orbit characteristics, as determined by the filter, evidence is provided indicating that the first reentering object could be more massive than the second. The breakup hypothesis explains why perigee appears to suddenly jump by 14 km. It also explains the order-of-magnitude increase in random lift effects detected by the filter after March 14.

The behavior of 13390 through March 14, with rapid decay followed abruptly by slower decay is typical of most Molniya rocket bodies. It is likely that they all break up and it may be the same massive piece that reenters each time (perhaps the rocket motor assembly). If a massive object reenters, then the SSC may want to predict reentry and impact under the TIP mission. We recommend that the SSN extend TIP tasking for the next Molniya rocket body reentry to collect and evaluate dense radar tracking and radar cross section data before and after the apparent catastrophic event.

The breakup hypothesis was a direct result of the capability of the filter to detect and solve for random lift effects and to provide a detailed, sequential history for the ballistic coefficient. It is doubtful that any other approach (e.g. batch least squares) could provide comparable information.

This analysis was made possible, in part, by adopting the MSIS-90 atmospheric density model. The model provides a continuous density profile and, according to the ballistic coefficient solution, provides a consistent solution through all altitudes down to 106 km. Below 106 km altitude the behavior of the ballistic coefficient solution might be due to mis-modeling of density in MSIS-90, but there are other, equally likely, explanations. There is an apparent diurnal behavior in the drag coefficient detected during the TIP phase, which needs to be explained through further analysis.

The decision to include lift states in the filter was critical to successful automation of the orbit determination process. It was also an enabling technology in support of the analysis of the breakup hypothesis.

The filter solution over the TIP Phase is consistently better than 100 km throughout, and better than 20 km most of the time, and reentry predictions were all within 12 hours of the final prediction, beginning 7 days before reentry occurs.

7 ACKNOWLEDGEMENTS

Thanks to US Space Command / J3 for providing the tracking data and approving the public release of this report. Dr. Frank Marcos' recommendation of the MSIS-90 model was critical to this success. Jim Wright reinforced our decision to use lift states and suggested using the conservation of linear momentum to explore the mass allocation at breakup.

8 REFERENCES

- 1 Fischer, J. D., "The Evolution of High Eccentricity Orbits," MS Thesis, Massachusetts Institute of Technology, June 1998.
- 2 Gelb, A., *Applied Optimal Estimation*, The M.I.T. Press, 1974.
- 3 Rauch, H., "Solutions to the Linear Smoothing problem," IEEE, *Trans. Autom. Control*, Vol. AC-8, 1963, pp. 371.

- 4 Wright, J. R., "Algorithm Definition Report for Simultaneous Orbit Determination," NASA TR-NAS5-29417-1, September 1988.
- 5 McReynolds, S. R., "Multipoint Smoothing Algorithm for Discrete Linear Systems," *Journal of Guidance, Control, and Dynamics*, Vol. 12, No. 6, Nov.-Dec. 1989, pp 920.
- 6 *Explanatory Supplement to the Astronomical Almanac*, U.S. Naval Observatory, University Science Books, Edited by P. Kenneth Seidelmann, 1992.
- 7 J. R. Wright, "Sequential Orbit Determination with Auto-Correlated Gravity Modeling Errors," *Journal of Guidance and Control*, Vol. 4, No. 3, May-June 1981, pp. 304.
- 8 J. R. Wright, "Orbit Determination Solution to Non-Markov Gravity Error Problem," *Spaceflight Mechanics 1994*, Vol. 87, Part II, 1994, pp. 1153.
- 9 W. M. Kaula, "Statistical and Harmonic Analysis of Gravity," *Journal of Geophysical Research*, Vol. 64, Dec. 1959, pp. 2411.
- 10 R. H. Gersten, R. C. Gore, W. S. Hall, "Statistical Properties of Orbit Perturbations Induced by the Earth's Anomalous Gravity Field," *Journal of Spacecraft*, Vol. 4, Sept. 1967, pp. 1150.
- 11 Pechenick, K.R., "A Derivation of the Gravity Error Covariance Formulas Including the Off-Diagonal Components," Applied Technology Associates, Inc., Sept. 1988.
- 12 Liu, J. J. F., "A Semi-Analytic Theory for the Motion of a Close-Earth Artificial satellite with Drag," AIAA 79-0123, 17th Aerospace Sciences Meeting, Jan 1979.
- 13 Regan, F. J., *Re-Entry Vehicle Dynamics*, AIAA Education Series, 1984.

Relative Attitude Kinematics & Dynamics Equations and Its Applications to Spacecraft Attitude State Capture and Tracking in Large Angle Slewing Maneuvers

G. Q. Xing, S. A. Parvez (Space Products and Applications, Inc.)

In this paper the relative attitude kinematics equations and relative dynamics equations are developed. These results will provide the basis for developing relative navigation necessary for virtual platform and spacecraft formation flying. The nonlinear Lyapunov attitude controller and nonlinear robust sliding controller are presented for the direct applications of the relative kinematics and relative dynamics equations to the spacecraft large angle slew maneuver problems. In comparison with papers published on similar subjects, these nonlinear controllers will realize the attitude state capture and tracking in the large angle slew maneuvers.

Introduction

Guidance and control for the spacecraft formation flying need the relative attitude information. The attitude rotation matrix (called attitude matrix) and the kinematics relationship of attitude matrix are defined with respect to the inertial reference frame. Therefore, the first problem is to define the kinematics relationships when the attitude matrix is defined with respect to a non-inertial frame. The second problem is defining the relative attitude dynamics. To the best of the author's knowledge, the complete answer to these problems have not appeared in the published papers and books. Even though the concept of relative attitude has been discussed in [3-5], the complete answers to the problems noted above have not been provided. In fact, there are some formulas and developments in these references that are in error and require corrections in order to be applied.

The attitude of a rigid-body with respect to the inertial frame is determined by a rotation transformation matrix from the inertial frame to body frame. This rotation matrix is referred to as the attitude matrix. In practical design, the attitude matrix is parameterized to be 4-dimension parameters such as axis/angle variables, quaternion, and 3-dimension parameters such as Rodrigues (Gibbs vector), Euler angles and the modified Rodrigues parameters. All these parameters are all called as the attitude parameters.

As a natural extension of the attitude matrix, the rotation matrix of the body-frame with respect to a non-inertial frame can be defined as the relative attitude matrix. Development of the kinematics and dynamics of the relative attitude should resolve the following questions:

- (1) What is the kinematics equation for relative attitude matrix ?
- (2) What is the kinematics equation for the relative attitude parameters ?
- (3) What is the relative attitude dynamics equations ?

In this summary, the results of problems (1)-(3) will be presented, although this will be done without the proofs due to space limitation. In addition, as examples of application, two examples are presented in this paper.

The first example is the application to design of a nonlinear controller for large angle maneuvers or the attitude state tracking, using Lyapunov Second Method. While Refs. 3-5 provide a study of these nonlinear controller design, there are some errors in development of the relative attitude kinematics and dynamics equations in these papers. In order to draw attention and initiate discussions on this matter among researchers in this field, the nonlinear control law will be redesigned using Lyapunov method for the relative attitude kinematics and dynamics equations. These developments can be compared with the results presented in [3-5].

The second example is the application of the sliding robust nonlinear controller for design of controller for spacecraft large angle maneuver and attitude state tracking. There are some existing papers that study the nonlinear

sliding control problem of large angle maneuvers [10-12]. However, these literature use the sliding control law for attitude tracking only. On the other hand, the sliding control law provided in this paper can be used for attitude state tracking. This means, in addition to attitude tracking, this design can also realize the angular velocity tracking for target satellite.

Relative Attitude Kinematics

It assumed that

$$\mathcal{F}_I = \begin{bmatrix} \dot{l}_I \\ \dot{j}_I \\ \dot{k}_I \end{bmatrix} \quad \mathcal{F}_T = \begin{bmatrix} \dot{l}_T \\ \dot{j}_T \\ \dot{k}_T \end{bmatrix} \quad \mathcal{F}_S = \begin{bmatrix} \dot{l}_S \\ \dot{j}_S \\ \dot{k}_S \end{bmatrix} \quad \mathcal{F}_B = \begin{bmatrix} \dot{l}_B \\ \dot{j}_B \\ \dot{k}_B \end{bmatrix} \quad \mathcal{F}_D = \begin{bmatrix} \dot{l}_D \\ \dot{j}_D \\ \dot{k}_D \end{bmatrix} \quad (1)$$

\mathcal{F}_I = the vectrice [9] of the inertial reference system

\mathcal{F}_T = the vectrice of the local horizontal reference system for target satellite

\mathcal{F}_S = the vectrice of the local horizontal reference system of the chasing spacecraft

\mathcal{F}_B = the vectrice of the body-fixed reference system of the chasing spacecraft

\mathcal{F}_D = the vectrice of the body-fixed reference system of the target attitude

The attitude of the rigid spacecraft is the orientation of its reference frame with respect to another reference frame. The most convenient reference frame is a dextral, orthogonal triad which is fixed with the rigid body of spacecraft. The other reference frame can be an inertial reference frame, or it can be a movable reference frame which is fixed to another rotating body. The attitude with respect to the inertial reference frame is the absolute attitude. The attitude with respect to a movable rotating reference frame is the relative attitude.

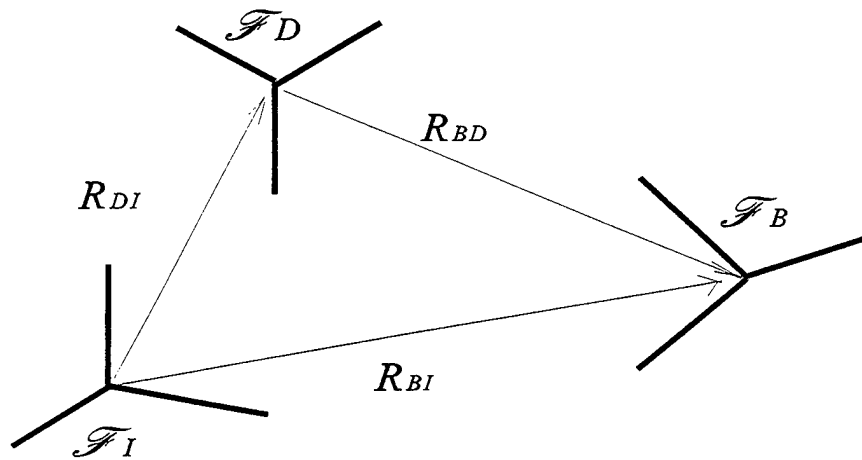


Fig.1. Relative Attitude Geometry

In order to study the relationship between two rotating reference frames, the relative attitude can be defined as a transformation matrix between the two reference frames. For example:

$$\mathcal{F}_B = R_{BD} \mathcal{F}_D \quad (2)$$

The transformation matrix R_{BD} is the relative attitude matrix of the reference frame \mathcal{F}_B with respect to the reference frame \mathcal{F}_D . Similarly, the relative attitude matrix can be also parameterized. These attitude parameters, such as Quaternions, Rodrigues, modified Rodrigues, and Euler angles, are known as relative attitude parameters. Use of these parameters require the following solutions:

- (1) Kinematics relationship for the relative attitude matrix
- (2) Kinematics relationship for various attitude parameters

It is assumed that \mathcal{F}_I , \mathcal{F}_B , \mathcal{F}_D are the inertial reference frame, body reference frame and the desired attitude reference frame, respectively. The angular velocity of \mathcal{F}_B and \mathcal{F}_D with respect to the inertial reference frame are ω_b and ω_d , and may be defined as:

$$\underline{\omega}_b = \mathcal{F}_B^T \omega_b \quad \underline{\omega}_d = \mathcal{F}_D^T \omega_d \quad (3)$$

The relative attitude between the reference frames \mathcal{F}_I , \mathcal{F}_B and \mathcal{F}_D are as follows:

$$\mathcal{F}_B = R_{BI} \mathcal{F}_I \quad \mathcal{F}_D = R_{DI} \mathcal{F}_I \quad \mathcal{F}_B = R_{BD} \mathcal{F}_D \quad (4)$$

The kinematics equations for R_{BD} and R_{DB} in the Body reference frame \mathcal{F}_B are as follows:

$$\frac{dR_{BD}}{dt} = -\omega_{bd} \times R_{BD} \quad (5)$$

In response to problem (1) above, the attitude kinematics equation for relative attitude matrix R_{BD} can be written in a compact form in the body reference frame \mathcal{F}_B

$$\underline{\omega}_{bd} = \underline{\omega}_b - \underline{\omega}_d = \mathcal{F}_B^T \omega_{bd} \quad (6)$$

where

$$\omega_{bd} = (\omega_b - R_{BD} \omega_d) \quad (7)$$

and

$$\frac{dR_{A_0}}{dt} = R_{A_0}[\omega_{rc}^\times] \quad (8)$$

In response to Problem (2) above, the following developments are provided:

1. The relative kinematics equations in Quaternion:

$$\dot{q}_{rc} = \frac{1}{2}(q_{rc}^\times + q_{rc} I)\omega_{rc} \quad (9)$$

$$\dot{q}_{rc\infty} = -\frac{1}{2}\omega_{rc}^{\mathcal{F}} q_{rc} \quad (10)$$

and

$$\omega_{rc} = 2(q_{rc\infty}\dot{q}_{rc} - \dot{q}_{rc\infty}q_{rc} - q_{rc}^\times \dot{q}_{rc}) \quad (11)$$

where the relative Quaternion attitude are defined as

$$q_{rc} = \begin{bmatrix} q_{rc0} \\ q_{rc1} \\ q_{rc2} \end{bmatrix} = \sin \frac{\phi_{rc}}{2} a_{rc} \quad \bar{q}_{rc} = \begin{bmatrix} q_{rc0} \\ q_{rc\infty} \end{bmatrix} \quad q_{rc\infty} = \cos \frac{\phi_{rc}}{2} \quad (12)$$

a_{bd} , ϕ_{bd} are the relative axis/angle attitude parameters of the body reference frame \mathcal{F}_B respect to desired frame \mathcal{F}_D . The relationship with the relative attitude matrix R_{BD} is

$$R_{oA} = (q_{rc\infty}^2 - q_{rc}^{\mathcal{F}} q_{rc})I + 2q_{rc} q_{rc}^{\mathcal{F}} - 2q_{rc\infty} [q_{rc}^\times] \quad (13)$$

2. The relative kinematics equations in Rodrigues parameters:

$$\dot{g}_{rc} = \frac{1}{2}(g_{rc}^\times + g_{rc} g_{rc}^{\mathcal{F}} + I)\omega_{rc} \quad (14)$$

and

$$\omega_{bd} = \frac{2}{(1+g_{bd}^T g_{bd})} (I - g_{bd}^{\times}) \dot{g}_{bd} \quad (15)$$

where the relative Rodrigues attitude parameter is defined as

$$g_{bd} = a_{bd} \tan\left(\frac{\phi_{bd}}{2}\right) \quad (16)$$

The relationship between the relative Rodrigues attitude parameters and the relative attitude matrix is

$$R_{BD} = \frac{1}{(1+g_{bd}^T g_{bd})} ((1 - g_{bd}^T g_{bd})I + 2g_{bd} g_{bd}^T - 2[g_{bd}^{\times}]) \quad (17)$$

3. The relative kinematics equations in modified Rodrigues parameter:

$$\dot{p}_{bd} = \frac{1}{4} [(1 - p_{bd}^T p_{bd})I + 2[p_{bd}^{\times}] + 2p_{bd} p_{bd}^T] \omega_{bd} \quad (18)$$

or

$$\omega_{bd} = \frac{4}{(1+p_{bd}^T p_{bd})^2} [(1 - p_{bd}^T p_{bd}) + 2p_{bd} p_{bd}^T - 2p_{bd}^{\times}] \dot{p}_{bd} \quad (19)$$

where the relative modified Rodrigues attitude parameter is defined as

$$p_{bd} = a_{bd} \tan\left(\frac{\phi_{bd}}{4}\right) \quad (20)$$

The relationship between the relative modified Rodrigues parameters and relative attitude matrix is

$$R_{BD} = \frac{1}{(1+p_{bd}^T p_{bd})^2} [(1 - 6p_{bd}^T p_{bd} + (p_{bd}^T p_{bd})^2)I + 8p_{bd} p_{bd}^T - 4(1 - p_{bd}^T p_{bd})[p_{bd}^{\times}]] \quad (21)$$

4. The relative kinematics equations in Euler angles:

$$\dot{\theta}_{bd} = S^{-1}(\theta_{bd2}, \theta_{bd3}) \omega_{bd} \quad (22)$$

or

$$\omega_{bd} = S(\theta_{bd2}, \theta_{bd3}) \dot{\theta}_{bd} \quad (23)$$

where

$$S(\theta_2, \theta_3) = \begin{bmatrix} \cos\theta_3 \cos\theta_2 & \sin\theta_3 & 0 \\ -\sin\theta_3 \cos\theta_2 & \cos\theta_3 & 0 \\ \sin\theta_2 & 0 & 1 \end{bmatrix} \quad (24)$$

$$S^{-1}(\theta_2, \theta_3) = \begin{bmatrix} \frac{\cos\theta_3}{\cos\theta_2} & -\frac{\sin\theta_3}{\cos\theta_2} & 0 \\ \sin\theta_3 & \cos\theta_3 & 0 \\ -\frac{\cos\theta_3 \sin\theta_2}{\cos\theta_2} & \frac{\sin\theta_3 \sin\theta_2}{\cos\theta_2} & 1 \end{bmatrix} \quad (25)$$

The attitude matrix R_{BD} in Euler angles is defined as R_{321} rotation matrix, i.e.,

$$R_{BD} = R_3(\theta_{bd3}) R_2(\theta_{bd2}) R_1(\theta_{bd1}) \quad (26)$$

Relative Attitude Dynamics Equations

Assume \underline{J}_b , ω_b , \underline{L}_b and \underline{J}_d , ω_d , \underline{L}_d are inertial dyadics, angular velocity, applied external torque (including control torque) of the chase satellite and target satellite, respectively. Then

$$\underline{J}_b = \mathcal{F}_B^T \underline{J}_b \mathcal{F}_B \quad \omega_b = \mathcal{F}_B^T \omega_b \quad \underline{L}_b = \mathcal{F}_B^T \underline{L}_b \quad (27)$$

and the relative velocity is defined as follows :

$$\omega_{bd} = \omega_b - R_{bd} \omega_d \quad (28)$$

$$\underline{J}_d = \mathcal{F}_D^T J_d \mathcal{F}_D \quad \underline{\omega}_d = \mathcal{F}_D^T \omega_d \quad \underline{L}_d = \mathcal{F}_D^T L_d \quad (29)$$

then the relative attitude dynamics equation in the chasing satellite body reference frame \mathcal{F}_B is

$$J_b \dot{\omega}_{bd} + \omega_{bd} \times J_b \omega_{bd} + \omega_{bd} \times J_b R_{BD} \omega_d = L_b - R_{BD} (L_d + \Delta J_d \dot{\omega}_d + \omega_d \times \Delta J_d \omega_d + 2\omega_d \times J_b \omega_{bd}) \quad (30)$$

where

$$J_d \dot{\omega}_d + \omega_d \times J_d \omega_d = L_d \quad (31)$$

$$\Delta J_d = R_{DB} J_b R_{BD} - J_d \quad (32)$$

Applications to Attitude State Tracking for Large-Angle Maneuvers

Case 1. Nonlinear Lyapunov Attitude Controller

In order to avoid the singular point, the modified Rodrigues parameter p is selected to describe the orientation of the satellite attitude. It is assumed that p_b , ω_b and p_d , ω_d are the absolute attitudes of the chase satellite and target satellite, respectively. The goal is to find a control law which can transfer the state (p_b, ω_b) of the chase satellite to the state (p_d, ω_d) of the target satellite. Based on the definition of the modified Rodrigues attitude parameters, the relationship between absolute attitude and relative attitude is

$$p_{bd} = p_b \otimes p_d^{-1} \quad (33)$$

where

$$p'' = p' \otimes p^{-1} = \frac{p(p'^T p' - 1) + p'(1 - p^T p) - 2p \times p'}{1 + p^T p p'^T p' + 2p^T p'} \quad (34)$$

In order to simplify development, let

$$\delta x = p_{bd} \quad \Delta \omega_b = \omega_{bd} \quad (35)$$

the relative kinematics equation and relative dynamics equations are as follows.

$$\delta \dot{x} = M \Delta \omega_b \quad (36)$$

$$J_b \Delta \dot{\omega}_b + \Delta \omega_b \times J_b \Delta \omega_b + \Delta \omega_b \times J_b R_{BD} \omega_d = L \quad (37)$$

where

$$M = \frac{1}{4} [(1 - \delta x^T \delta x) I + 2[\delta x^\times] + 2\delta x \delta x^T] \quad (38)$$

$$L = L_b - R_{BD} (L_d + \Delta J_d \dot{\omega}_d + \omega_d \times \Delta J_d \omega_d + 2\omega_d \times J_b \Delta \omega_b) \quad (39)$$

Eq. (36-37) can be written as follows

$$J \delta \ddot{x} + C \delta \dot{x} = M^{-T} L \quad (40)$$

where

$$J = M^{-T} J_b M^{-1} \quad (41)$$

$$C = M^{-T} J_b \dot{M}^{-1} - M^{-T} [(J_b \Delta \omega_b)^\times] M^{-1} - M^{-T} [(J_b R_{BD} \omega_d)^\times] M^{-1}$$

$$M^{-T} L = M^{-T} (L_b - R_{BD} L_d - 2R_{BD} [\omega_d^\times] J_b M^{-1} \delta \dot{x}) \quad (42)$$

The state vector of this system can be selected to be

$$X = \begin{bmatrix} \delta x \\ \delta \dot{x} \end{bmatrix} \quad (43)$$

The virtual mechanical energy V

$$V = \frac{1}{2}(\delta x^T K_p \delta x + \delta \dot{x}^T J \delta \dot{x}) \quad (44)$$

can be a Lyapunov function where K_p and K_d are two constant symmetric positive definite matrices. Using Lyapunov method it can be proven that nonlinear asymptotically stable control law is

$$L_b = -M^T(K_p \delta x + K_d \delta \dot{x}) + R_{BD}(L_d + \Delta J_d \dot{\omega}_d + \omega_d \times \Delta J_d \omega_d + 2R_{BD}[\omega_d^x]J_b M^{-1} \delta \dot{x}) \quad (45)$$

Case 2. Sliding robust nonlinear controller

It is assumed that the relative dynamics equations are given by Eqs. (40-43). Using the sliding condition for multi-input system from [11]

$$\frac{1}{2} \frac{d}{dt} s^T s \leq -\eta (s^T s)^{\frac{1}{2}} \quad (\eta > 0) \quad (46)$$

We can define vector s as

$$s = \delta \dot{x} + \Lambda \delta x \quad (47)$$

where Λ is a symmetric positive definite matrix, or more generally a matrix such that $-\Lambda$ is Hurwitz. The vector s conveys information about boundedness and convergence of δx and $d\delta x/dt$, since the definition (47) of s can also be viewed as a stable first-order differential equation in δx , with s as an input. Thus, assuming bounded initial conditions, showing the boundedness of s also shows the boundedness of δx and $d\delta x/dt$, and therefore of x and dx/dt ; similarly, if s tends to 0 as t tends to infinity, so do the vectors δx and $d\delta x/dt$.

Let us define

$$V = \frac{1}{2} [s^T J s] \quad (48)$$

Using Lyapunov method, the nonlinear sliding robust control law which satisfied the sliding condition is

$$L_b = -M^T(\hat{J}\Lambda \delta \dot{x} + \hat{C}\Lambda \delta x) - M^T K \operatorname{sgn}(s) + R_{BD}(L_d + \Delta J_d \dot{\omega}_d + \omega_d \times \Delta J_d \omega_d + 2[\omega_d^x]J_b M^{-1} \delta \dot{x}) \quad (49)$$

where

$$\hat{L} = -\hat{J}\Lambda \delta \dot{x} - \hat{C}\Lambda \delta x \quad (50)$$

$$\hat{J}-J=\Delta J \quad \hat{C}-C=\Delta C \quad (51)$$

$$\operatorname{sgn}(s)=\left\{\begin{array}{ll} 1 & s>0 \\ -1 & s<0 \end{array}\right. \quad (52)$$

$$K_i \geq |[\Delta J \Lambda \delta \dot{x} + \Delta C \Lambda \delta x]_i| + \eta_i \quad (i = 1, 2, \dots, n) \quad (53)$$

Eq.(53) is a sufficient condition for satisfying the following sliding condition

$$\dot{V} \leq -\sum_1^n \eta_i |s_i| \quad (54)$$

Acknowledgment

This work was supported by NASA Goddard Space Flight Center, Greenbelt, Maryland, under Contract NAS5-98092.

References

- [1] Battin, Richard H., An Introduction to the Mathematics and Methods of Astrodynamics, AIAA Education Series, J.S. Przemieniecki/ Deries Editor-In-Chief, Published by AIAA, Inc.1987.
- [2] Kaplan Marshall H., Modern Spacecraft Dynamics and Control, John wiley & Sons, New York, 1976.
- [3] Wen, John T-Y. And Kreutz-Delgado, K. K., "The Attitude Control Problem", IEEE Trans. On AC, Vol. 36, No.10, Oct. 1991, pp.1148-1162.
- [4] Fjellstad, O., and Fossen, T.I., "Comments on The Attitude Control Problem," IEEE Transactions on Automatic Control, Vol. 36, No. 3, March 1994, pp. 699-700.
- [5] Wang, P. K. C. and Hadaegh, Coordination and control of Multiple Micro Spacecraft Moving in Formation," The Journal of the Astronautical sciences, Vol. 44, No. 3, July-Sept. 1996, pp. 315-355.
- [6] Isidori, A. Nonlinear Control System, Third Edition, Springer -Verlag London Limited 1995.
- [7] Shuster, Malcolm D., "A survey of Attitude representations," The Journal of the Astronautical Sciences, Vol. 41, No. 4, October-December, 1993, pp. 439-517.
- [8] Peter C. Hughes, Spacecraft Attitude Dynamics, John Wiley & Sons, Inc., 1986.
- [9] Wertz, J. R., Spacecraft Attitude Determination and Control, Kluwer Academic Publishers, Dordrecht/Boston/London, 1980.
- [10] Vadali, S.R., "Variable-Structure Control of Spacecraft Large-Angle Maneuvers", journal of Guidance Control & Dynamics, Vol. 9, No.2, 1986, pp. 235-239.
- [11] Dwyer, T. A. W., and Ramirez, H. S., "Variable-Structure Control of Spacecraft Attitude Maneuvers", Journal of Guidance Control & Dynamics, Vol. 11, No.3, 1988, pp.262-269.
- [12] Crassidis, J.L., and Markley, F.L., "Sliding Mode Control Using Modified Rodrigues Parameters", Journal of Guidance Control & Dynamics, Vol. 19, No.6: Engineering Notes, 1996, pp. 1381-1383.

Lincoln Near Earth Asteroid Research (LINEAR) Project: First Year Results

H. Viggh, G. Stokes, F. Shelly, M. Blythe, M. Bezpalko, S. Stuart, R. Sayer, C. Foo, S. Taylor
MIT Lincoln Laboratory

Abstract

The LINEAR project operates a wide area asteroid search program employing an advanced electro-optic search system developed for Air Force space surveillance applications. The technology was originally developed, and is operated, by MIT Lincoln Laboratory at the Lincoln Laboratory Experimental Test Site in Socorro, NM. Recent advances in large format, highly sensitive CCDs with fast readout rates, combined with customized, high throughput data processing systems, allow the LINEAR project to search more than 10,000 square degrees per month to a limiting visual magnitude exceeding 19th using a 1 meter GEODSS type telescope. This coverage, combined with an effective moving object detection algorithm, has allowed LINEAR to be quite productive when searching for Near Earth Objects (NEOs), comets, and main belt asteroids. The LINEAR program has been consistently operating during the lunar dark period of each month since March 1998. During this period, LINEAR has been responsible for the discovery of more than 70% of the NEOs found worldwide. This paper provides an overview of the project, summarizes the results to date and discusses planned future work.

Introduction

Lincoln Laboratory has a long history of developing technology for the Space Surveillance Network (SSN) run by Space Command. Space surveillance involves detecting and tracking Earth orbiting satellites and space debris, as well as maintaining a catalog of such objects. At the dawn of the space era in 1957, Lincoln's Millstone Hill radar provided the first radar tracks of the first artificial satellite, Sputnik. Since then, Lincoln has used the Millstone Hill facility to develop and transfer radar and software technology to the Air Force for use in the SSN, which operates several radars around the world.

Similarly, Lincoln Laboratory has also developed opto-electronic technology for use in the SSN at Lincoln Laboratory's Experimental Test Site (ETS) on the White Sands Missile Range in Socorro, NM. Much of this technology has been developed for the operational space surveillance system called the GEODSS (Ground-based Electro-Optic Deep Space Surveillance) system. Currently, a number of GEODSS systems are deployed around the world as part of the SSN. Each GEODSS site is currently equipped with 1-meter class telescopes and EBSICON detector systems based on 1970's studio television technology. Over the past several years, the US Air Force has been developing new devices and technology for the detection and tracking of Earth orbiting satellites, is now in the process of upgrading the GEODSS system to achieve the performance offered by state of the art detector systems. Under Air Force sponsorship, Lincoln Laboratory has developed a new generation of sensitive, large format, frame transfer CCD focal planes for GEODSS. The Lincoln Laboratory focal plane and camera system provides considerably improved sensitivity, which reduces integration times and allows tracking of fainter objects, fast frame transfer readout which allows the integration of the next image to be started

while the previous image is readout, and stringent blemish specifications, which minimize the loss of detections attributed to focal plane defects. These focal planes have been installed in a new generation of cameras and are currently undergoing testing at the ETS. The ETS is shown on the left side of Figure 1 across the parking lot from one of the operational GEODSS sites. Figure 2 shows the telescope used for the CCD camera tests and asteroid searching.

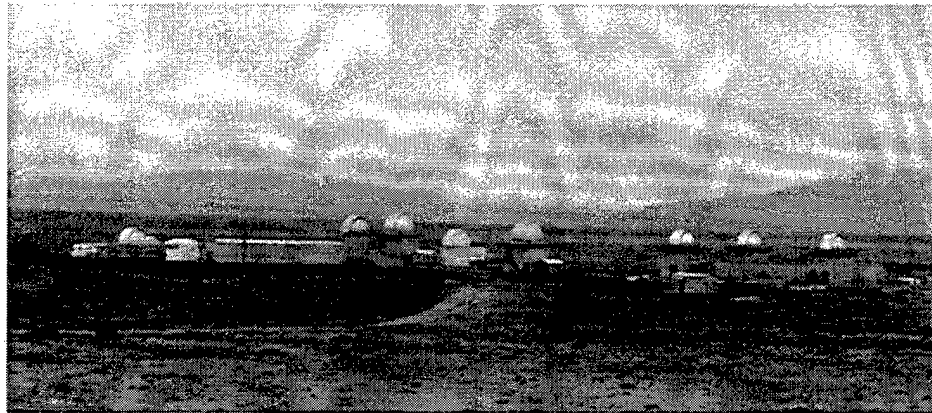


Figure 1. Lincoln Laboratory operated Experimental Test Site, Socorro, NM

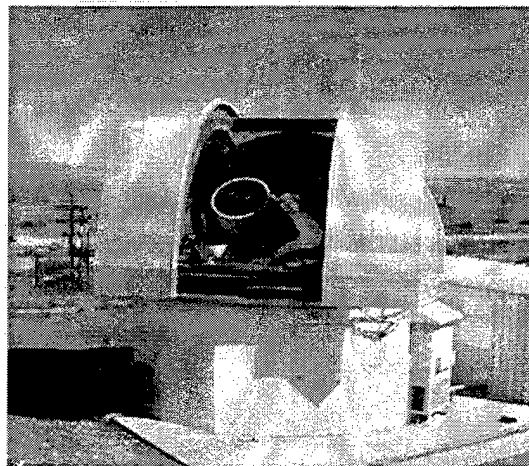


Figure 2. A close up of the ETS telescope used for the CCD testing and asteroid searching. The telescope is identical to that used at the operational GEODSS sites.

When equipped with the new focal plane and camera technology, the modest sized 1-meter GEODSS telescopes have considerable capability to conduct sensitive, large coverage searches for space surveillance applications. With some modifications, these capabilities can be extended to searching for Earth crossing asteroids. Further details regarding the new generation CCD and camera may be found in Reference 1.

The LINEAR Program

Initial field tests of the CCD and camera system were conducted over a period of several months, starting in August of 1995. These initial efforts were directed toward determining the

capability of the system to meet its design specifications for satellite surveillance as well as the capability of the system to detect asteroids.

During these initial tests, conducted at the ETS in August 1995 and July 1996, a small amount of observing time was dedicated to searching for asteroids. That effort yielded a total of 177 observations of asteroids that were sent to the Minor Planet Center (MPC) in Cambridge MA. In the course of these observations, 49 new objects were discovered that received new designations from the MPC, including a confirmed Near Earth Object (NEO), which was given the designation 1996 MQ. In addition, observations of 79 known objects were also collected and used by the MPC to maintain their catalog.

The initial results were modest in terms of the amount of sky covered and the numbers of asteroids discovered, however, they were made with a preliminary camera and data system that provided only a small fraction of the possible discovery rate of an operational system using the same CCD technology. The results were, however, sufficient to convince the Air Force that the approach had considerable merit and potential. Thus, a modest asteroid search effort, known as LINEAR (Lincoln Near Earth Asteroid Research), was started.

For LINEAR, a new data acquisition and processing system was implemented to achieve a much higher rate of search, processing, and discovery through the appropriate integration of existing real time hard disk storage, more tightly coupled signal processing, and automation of data management tasks. This system, along with the algorithms used for asteroid detection, are described in Ref. 1.

All asteroid observations generated by the LINEAR program are sent to the Minor Planet Center (MPC). The MPC is part of the International Astronomical Union and is located at the Harvard Smithsonian Astrophysical Observatory in Cambridge, MA. The MPC maintains a catalog of all known asteroids, comets, and other minor planets. The role of the MPC for asteroids is analogous to the role of Cheyenne Mountain for satellite tracking and cataloguing. In support of their cataloguing efforts, the MPC receives asteroid and comet observations from professional and amateur observers around the world. The MPC also maintains the NEO Confirmation Page, on which new NEO candidates are posted to facilitate follow-up observations by professional and amateur astronomers worldwide. LINEAR program interactions with the MPC are described in Ref. 1.

LINEAR Sky Coverage and Search Strategy

A prototype of the LINEAR system was tested during March through July 1997 to determine its search effectiveness. Because of limited equipment availability at that time, a smaller 1024X1024 CCD was used (the smaller chip is 1/5th the area of the full-scale GEODSS chip). In spite of the fact that a small format camera was employed during the search operations, the productivity was quite high during each of the observing runs – in fact the performance was comparable with other existing search programs such as NEAT and Spacewatch. During this five-month trial period 3 new NEOs and 1,367 main belt asteroids were discovered (MPC designations issued).

LINEAR began preliminary search trials with the large format 2560x1960 pixel CCD on October 22, 1997. LINEAR search operations are conducted during the period of the month when the moon is $\frac{1}{2}$ or less illuminated in order to reduce the background noise and increase the sensitivity of the search. In the initial 10 nights of operations LINEAR generated 52,542 observations and detected 11 NEO candidates – of which 9 were confirmed and received new designations from the MPC. Two of the NEO candidates were lost in subsequent follow-up attempts by the worldwide network of astronomers that track new objects.

LINEAR resumed observations with the large CCD during the dark of the moon period of March 1998. During March, LINEAR produced in excess of 150,000 observations and detected 22 potential NEOs – 13 of which were confirmed and received new designations. We believe that one of the reasons for the loss rate for NEO discoveries during this interval is that we stressed the capacity of the follow-up observers. During subsequent operations we have followed up our own NEO discoveries to avoid this problem, and have had a very small loss rate. During the March 1998 dark period, the MPC indicates that LINEAR provided in excess of 90% of the worldwide total of asteroid observations.

The impressive results achieved in March 1998 were the result of technical maturation of the underlying detector and processing technologies needed for LINEAR asteroid search operations. What followed during the next nine months of 1998 was a development effort concentrating on how best to use this technology to detect new NEOs through efficient search techniques.

Table 1 summarizes the observing statistics for the LINEAR program during 1998. Note the number of square degrees searched during each monthly lunar dark period. For the months since March 1998, LINEAR has averaged 10,000 square degrees of search. This number is 11,000 if the month of July 1998 is ignored, which was essentially a down month due to weather and equipment problems.

TABLE 1
Recent LINEAR Observation Statistics

PERIOD	OBS GENERATED	Sq. Deg. Collected	NEOs Discovered	Comets Discovered
10/97	52,575	3,060	9	0
3/98	151,035	9,906	13	0
4/98	91,495	7,124	8	1
5/98	51,068	12,124	12	6
6/98	26,289	12,170	10	1
7/98	2,027	800	1	0
8/98	60,917	10,132	16	1
9/98	161,169	11,586	26	0
10/98	85,738	9,298	8	4
11/98	61,297	12,174	19	1
12/98	69,873	13,874	18	2

Figure 3a contains a plot of the sky coverage achieved during March 1998. While 9,906 square degrees of data were collected, the area of sky depicted is only 3,064 square degrees, since much of sky was covered multiple times, some areas as many as five or six times. The initial

LINEAR search strategy was to search near solar opposition on the ecliptic for better solar phase angle and denser population of asteroids. Multiple nights were gathered to ensure enough detections on each asteroid for the designation to be credited by the MPC to LINEAR in a single month. However, many of the excessive repeats were the result of poor search planning. The hole in the coverage plot was due to bad weather.

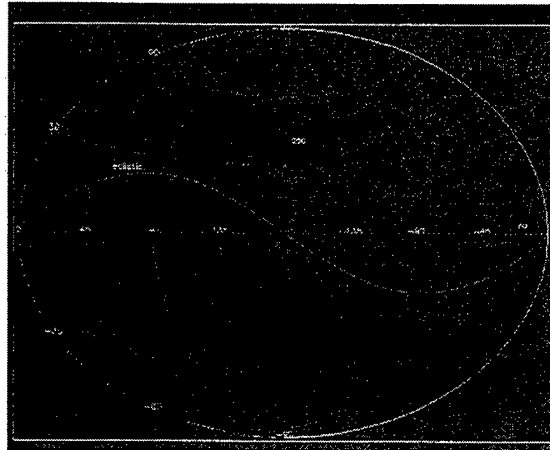


Figure 3a. LINEAR Sky Coverage March 1998

Figure 3b shows a similar plot for April 1998. In this month, we set out to reduce the excessive repeats through improvements in the planning system. In this month, 30% fewer search fields were collected (7,124 deg^2 vs. 9,906 deg^2), yet more sky was covered (3,546 deg^2), with an area collected to area covered ratio of about 2 to 1. Only a small area was covered four times, with the majority covered two to three nights, and some only one night. The sky coverage for May 1998 is depicted in Figure 3c. The repeat ratios were similar for May (12,068 deg^2 vs. 6,812 deg^2), yet more observing was done.

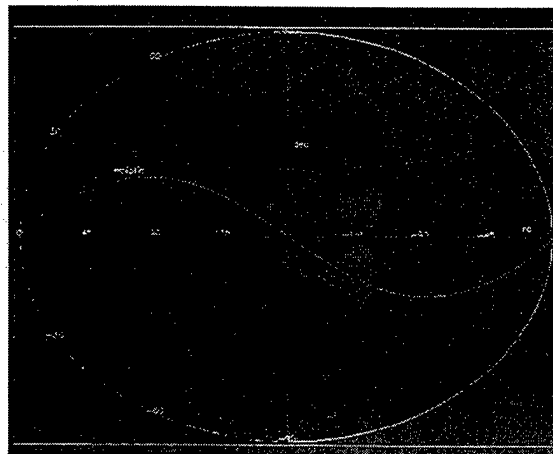


Figure 3b. LINEAR Sky Coverage April 1998

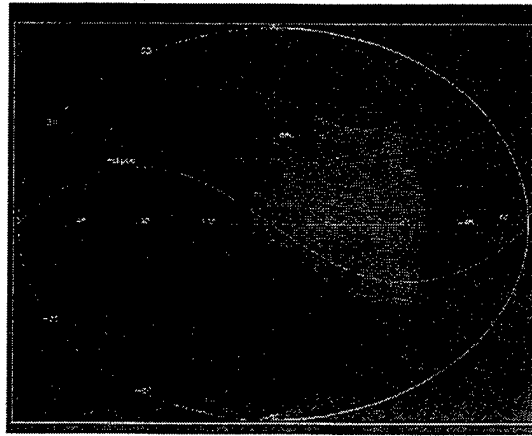


Figure 3c. LINEAR Sky Coverage June 1998

Up to this point in the LINEAR project evolution, our goals had been to collect two nights on all objects. This was because not all NEOs are recognizable from a single night's observation and therefore do not make it on to the NEO Confirmation Page for immediate follow-up. In addition, two nights in a single month are needed for the MPC to award a discovery designation for non-NEO asteroids. Performance analysis leads us to the conclusion that the productivity of the search is enhanced by searching as much new sky as possible and accepting the loss of some NEOs due to non-recognition. We therefore endeavored to maximize the amount of sky covered in more recent LINEAR searches. However, LINEAR still attempts to cover the ecliptic near opposition twice a month due to the high density of asteroids in the main belt, with the hope that some may turn out to be NEOs and to accrue a large number of discovery designations.

Figure 3d shows the sky coverage for June 1998. While the total area collected was the same as May 1998 (12,170 deg²), the amount of actual sky covered was much greater, at 8,612 deg². Most of this increase was accomplished by searching along the ecliptic, far to the west and east of opposition. The central areas were covered two times, while the east and west portions only once. No area was covered more than twice. Figure 3e shows the small area done in July 1998, which was severely hampered by bad weather and equipment issues.

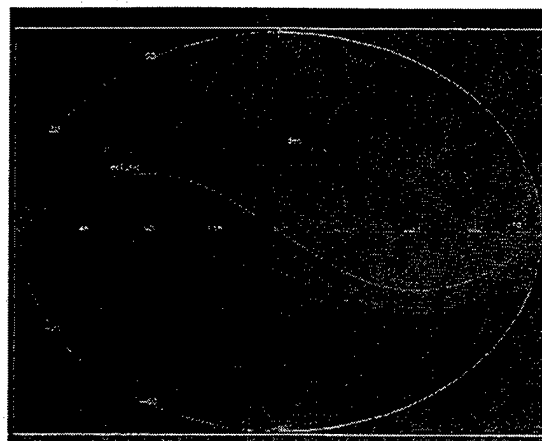


Figure 3d. LINEAR Sky Coverage July 1998



Figure 3e. *LINEAR Sky Coverage August 1998*

Figure 3f show the August 1998 sky coverage. In addition to going east and west of opposition, areas high up near the pole were also searched.

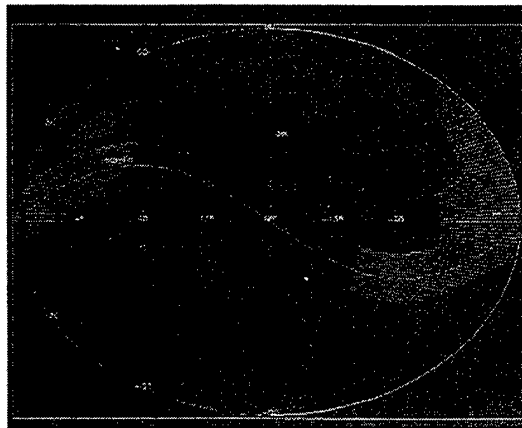


Figure 3f. *LINEAR Sky Coverage September 1998*

Figures 3g-3i, display the coverage for September, October, November, and December of 1998. They are similar to the August 1998 pattern, since our search planning had matured and the pattern stabilized. Note that in October-December the pattern reaches far north while still maintaining coverage east and west of opposition. Figure 4 depicts a composite of all the area searched by LINEAR during March through December 1998. The wide east to west coverage done each month allows each area of the sky on the ecliptic to be searched at least three months in a row.

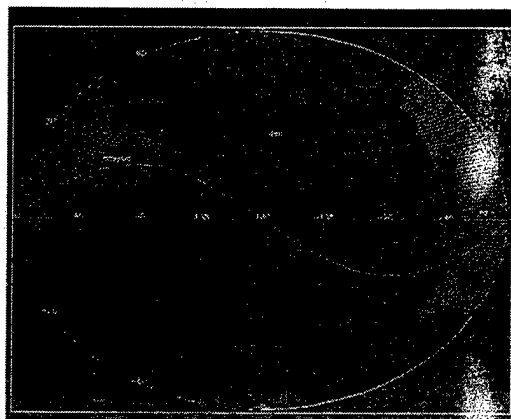


Figure 3g. *LINEAR Sky Coverage October 1998*

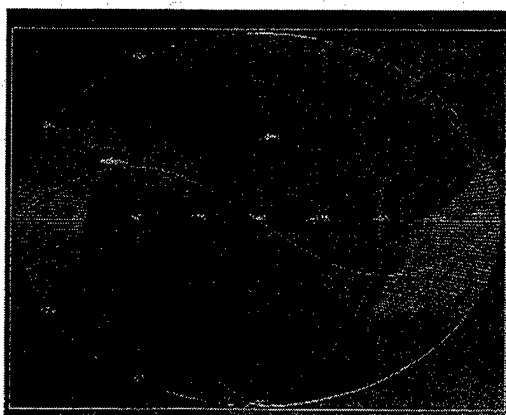


Figure 3h. *LINEAR Sky Coverage November 1998*

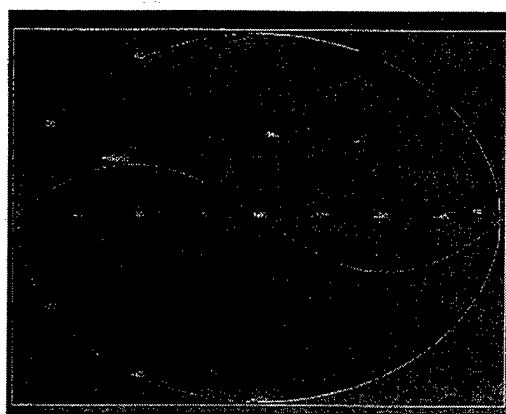


Figure 3i. *LINEAR Sky Coverage December 1998*

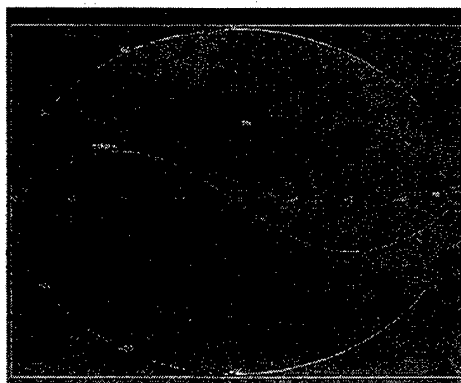


Figure 4. LINEAR Sky Coverage March-December 1998

LINEAR Discovery Statistics

The currently known catalogue of asteroids has been generated over a period exceeding a century and its content is a reflection of the capabilities of the search programs that generated the catalogue. Figure 5 contains a view of how the capability of LINEAR compares to those searches that generated the current catalogue. The figure contains a histogram of all of the detections of asteroids, known or newly designated, made by LINEAR through June 1998. The X-axis of the figure is the estimated diameter of the objects detected and the Y-axis is the number of asteroids in each size range. Diameters are estimated based on absolute magnitude assuming an average surface reflectance. Note that the new objects discovered by LINEAR are generally fainter than the known objects seen. By advancing the state of the art for detection sensitivity, LINEAR is better sampling the asteroid population, which increases sharply with decreasing size. The peak

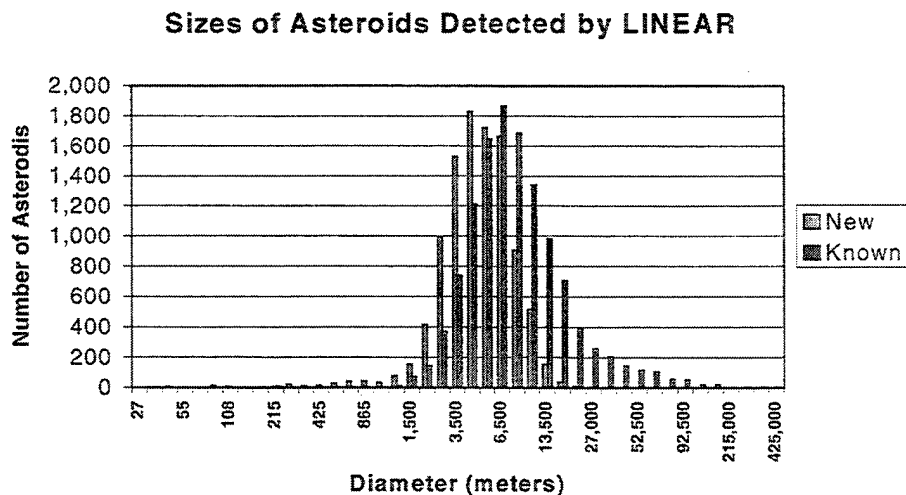


Figure 5. Histogram of all asteroids detected by LINEAR through June 1998, including new discoveries and known objects.

of the population discovered by LINEAR is approximately two visual magnitudes fainter than the peak for the known population. This represents a major advance in detection capability.

Figure 6 shows a similar histogram of the sizes of NEOs discovered by LINEAR through December 1998. LINEAR is finding a significant number of objects with estimated diameters exceeding 1 km. An impact of one of these objects with the earth would have globally catastrophic affects. LINEAR also has discovered significant numbers of objects in the 200 m - 1 km size range, which would initiate wide spread regional damage in the event of a collision with the Earth.

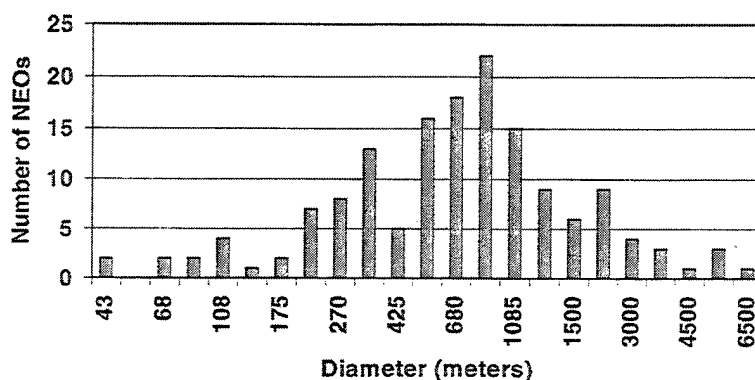


Figure 6. Histogram of Sizes of LINEAR NEO Discoveries. The amount of sky covered and total square degrees of data collected are also shown.

An analysis was done to explore the expected correlation between increased sky coverage and NEO discovery. Figure 7 plots the sky coverage, the amount of data collected, and the number of NEOs discovered for each month in 1998. There is no immediately obvious correlation, but several interesting inferences can be drawn from the data. NEO discoveries are

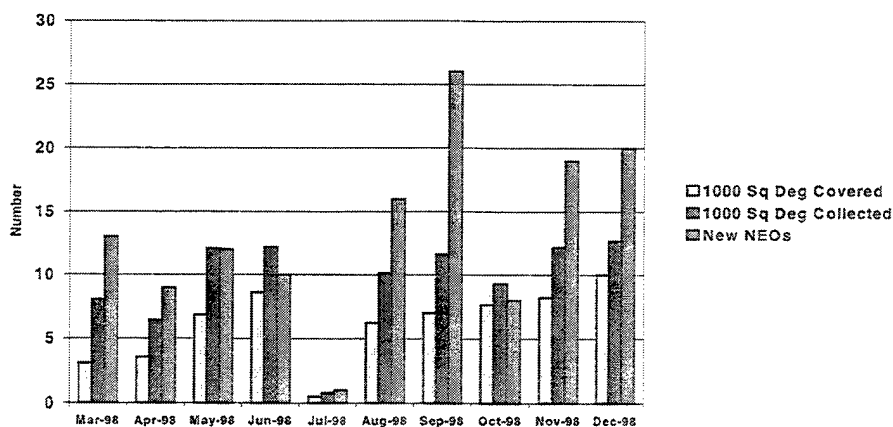


Figure 7. Number of NEOs discovered by LINEAR each month. The amount of sky covered and total

square degrees of data collected are also shown.

generally higher in the August-December period when the wide east to west, and high north searches were done, indicating that covering more sky generates more NEO discoveries. The jump in performance during the months of August and September may be attributable to discovering NEOs missed during July, but similar performance was obtained again in November and December.

Weather conditions are most likely the cause of the variations from month to month as indicated by Figure 8. In general, both the number of new NEOs discovered and known NEOs detected rise and fall together from month to month. If the distribution of NEOs is assumed to be uniform, the detection system is not changed, and the search pattern is roughly the same, then observing conditions will dominate how many NEOs are detected, and therefore discovered.

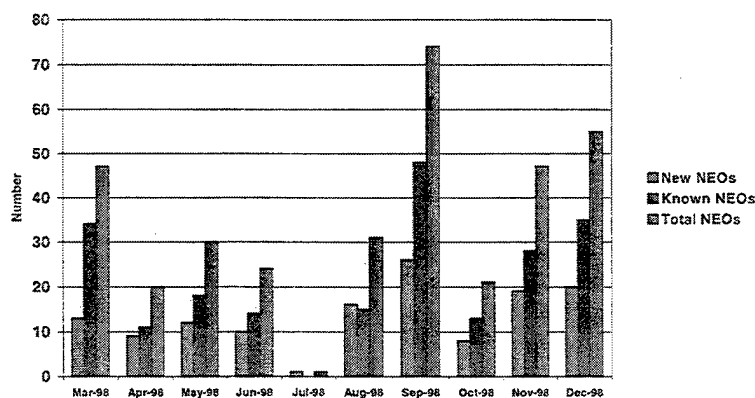


Figure 8. Number of NEOs observed by LINEAR each month. Both new and known NEOs are plotted, along with the total.

LINEAR has become the single largest contributor of asteroid observations to the MPC. Table 2 summarizes the percentage of worldwide discoveries that LINEAR has made in 1998. PHAs are Potentially Hazardous Asteroids, which are NEOs whose size and potential close approaches to the Earth make them the most threatening out of the NEO population. The list of PHAs is populated and maintained by the MPC.

Table 2 shows that LINEAR currently accounts for over 70% of all NEO and PHA discoveries since March 1998, including NEOs with diameters greater than 1 km. Overall, LINEAR has discovered roughly one quarter of known NEOs and PHAs. This is impressive given that the other $\frac{3}{4}$ of the catalogue took over 100 years to discover. LINEAR has also become a major discoverer of comets, accounting for more than 40% of the world wide comet discoveries.

Table 2.
LINEAR Percentages of World Wide NEO and Comet Discoveries as of 12/30/98

Discovery	LINEAR	Total World Wide	Percentage
NEOs	153	650	24%
NEOs since 3/98	135	190	71%
NEOs > 1 km	43	282	15%
NEOs > 1km since 3/98	40	55	73%
PHAs	39	159	25%
PHAs since 3/98	36	51	71%
Atens	13	46	28%
Atens since 9/98	13	15	87%
Comets since 3/98	16	38	42%

Also notable in Table 2 is the fact that since 9/98, LINEAR has found 13 out of 15 Aten asteroids discovered. Atens are difficult to detect, since they spend most of their orbit less than 1 AU from the Sun. They are therefore best detected far from opposition, nearer the Sun. Figure 9 splits the LINEAR NEO discoveries for 1998 into the three families of Atens, Amors, and Apollos. LINEAR had not discovered an Aten until September 1998. However, shortly after adopting our wide area search pattern in August 1998, LINEAR has become the world leader in Aten discoveries, increasing the known population by 28% in only four months.

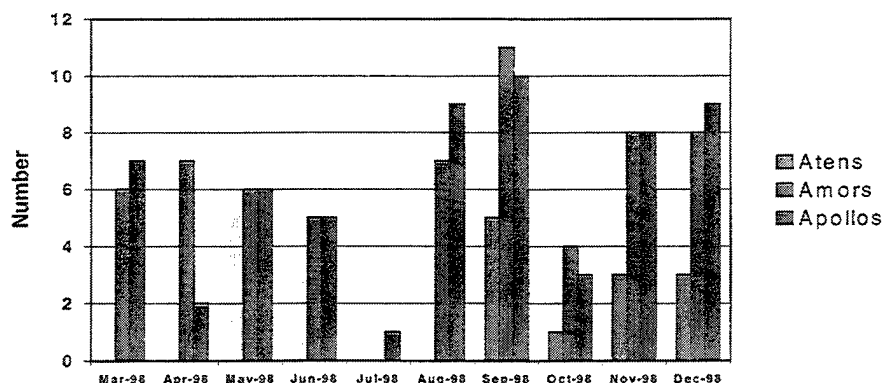


Figure 9. LINEAR NEO discoveries by asteroid family.

LINEAR Detection Sensitivity

The capability of the LINEAR system depends crucially on the detection sensitivity achieved during a search. The sensitivity determines the search volume for objects of a particular brightness. The sensitivity is determined by the telescope optics, the detector efficiency, the capability of the detection software, the site seeing and the weather, among other factors. We estimate the sensitivity achieved by LINEAR is approximately 19.5 visual magnitude when using

10 second integration period during good seeing. However, since the actual sensitivity achieved is a complex function of many variables, the actual performance of the search provides the best determination of the sensitivity. Figure 10 contains a histogram of 137 NEOs discovered by LINEAR, binned by their magnitude at discovery. The discovery magnitude is determined by taking the magnitude estimates made by other astronomers in the follow up process and combining them with a knowledge of the orbit to determine the apparent brightness as of the discovery date. Figure 10 indicates that the LINEAR system achieves sensitivity of ~19.5 visual magnitude as expected.

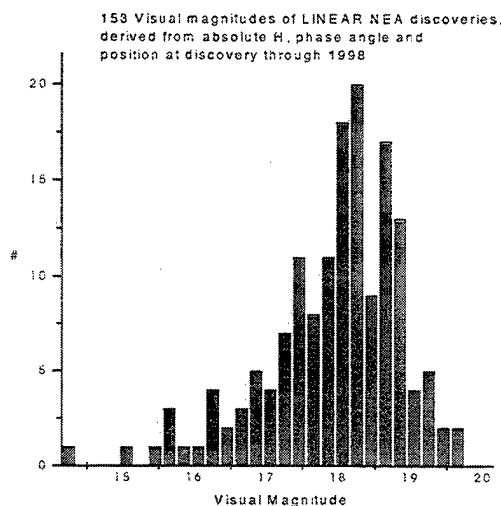


Figure 10. Apparent brightness of LINEAR NEOs at discovery.

Comparison with Other Asteroid Search Efforts

In addition to LINEAR, there are a number of search efforts ongoing around the world focused on the detection of near Earth asteroids. These include the following:

Spacewatch - Operated by University of Arizona Lunar and Planetary Laboratory, using a 0.9 m telescope, equipped with a scanning CCD, located at Steward Observatory on Kitt Peak.

NEAT (Near Earth Asteroid Tracking) – Operated by NASA/JPL, using a 1 m GEODSS telescope, equipped with a front illuminated imaging CCD, located on Maui.

LONEOS (Lowell Observatory Near-Earth-Object Search) – operated by Lowell Observatory, using a 0.59 M Schmidt telescope, equipped with front illuminated imaging CCD, located at the Lowell Observatory.

Figure 11 displays the near earth asteroids discovered by each of these teams on a plot of discovery date (day of year 1998) verses the absolute magnitude of the objects discovered. The absolute magnitude is the measure of the brightness of the object under a standard set of observation conditions and is related to the size of the object by the albedo. Typically an 18th

magnitude object is considered to have a diameter of about 1km. As can be seen by the figure, LINEAR has been quite productive over the interval starting in March 1998, and has found a large number of 1km and larger objects.

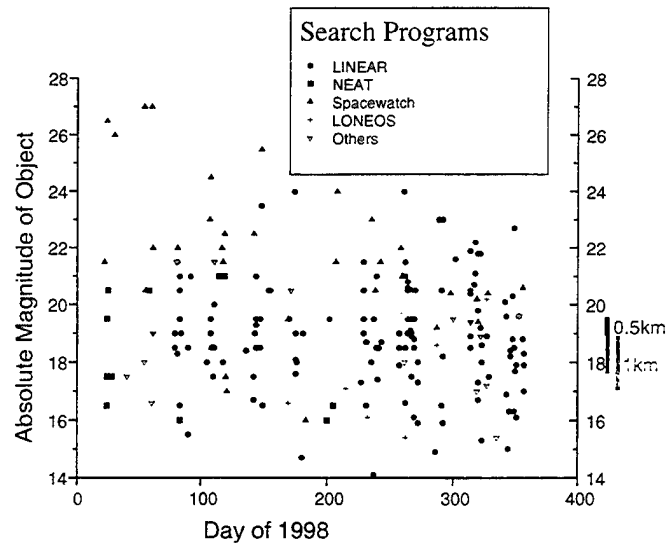


Figure 11. Plot of the discoveries of the major NEA search programs as a function of date of discovery and absolute magnitude

Future Plans

Future plans for LINEAR include the addition of a second telescope, nearly identical to the existing LINEAR system, for wide area search applications. This telescope will allow LINEAR to integrate longer to increase sensitivity, while maintaining coverage of large areas of the sky. New real-time data processing systems are currently under development that will remove certain constraints on the amount of data that can be collected in a single night, which will increase the amount of data collected and sky covered. A third telescope system is also under development, primarily for Air Force applications, which will be operated on a non-interfering basis for follow-up of NEO candidates and other interesting objects. This third telescope will utilize a smaller format CCD (1024X1024), which supports a narrower field of view than the search system. A follow-up scheduler software system is under development to automate the use of this third telescope in support of the wide area search units.

Summary

The LINEAR program has been using Air Force developed space surveillance technology to consistently search a large portion of the night sky for asteroids from March through December 1998. Substantial improvements in the search strategy executed during this period have made LINEAR the worldwide leader in the discovery of NEOs and comets. Future improvements to the LINEAR observing system should continue to increase the program's productivity and contribution to the cataloguing of dangerous NEOs.

References

Stokes, G.H., H.E.M. Viggh, J.S. Stuart, F.C. Shelly M.S. Blythe, "Lincoln Near Earth Asteroid Research Program – LINEAR", *Lincoln Laboratory Journal*, Volume 11, Number 1, pp 27-40, 1998.

Haystack, TRADEX, TIRA/Effelsberg Radar Measurements of the Orbital Debris Environment during the 24 Hour Cooperative Beam Experiment, November 1996

T. J. Settecerry (Lockheed Martin Space Operations Company), E.G. Stansbery (NASA/JSC)

Introduction

NASA initiated the formation of an international agency-level organization (the Inter-Agency Space Debris Coordination Committee, IADC) to facilitate the exchange of technical information on space debris. The United States, Russia, Japan, European Space Agency (ESA), France, Germany, United Kingdom, China, and India have representation on the committee. The IADC was chartered to report on four major areas related to orbital debris: measurements, modeling, risk assessment, and mitigation. The measurements group reports on data collected by ground based radar, optical systems, and spacecraft returned surfaces. In addition, they coordinate international measurement campaigns to further the knowledge of space debris. The first coordinated measurement campaign was planned for November 1996. The only participants were the United States and Germany. The US used the Haystack and TRADEX (Target Resolution and Discrimination Experiment) radars. Germany used the Tracking and Imaging Radar (TIRA) and the Max-Planck-Institute for Radio Astronomy's Effelsberg radio telescope in a bistatic configuration. The Haystack radar is located in Massachusetts, the TIRA/Effelsberg radar/radio telescope are located near Bonn, Germany, and the TRADEX radar is located on the island of Roi-Namur in the Kwajalein Atoll, in the Pacific Ocean.

The parameters measured/calculated in order to compare the data are: detection rate, flux, size distributions, orbital inclination and altitude. For the comparison, inclination, altitude, and estimated size are plotted versus time of day. This uniquely shows the specific families of debris associated with the NaK and HAPS debris.

Haystack Measurements

Figure 1 shows the time line for the 24-Hour, Haystack measurement campaign. The horizontal lines depict the data collection periods and the small circles are when Haystack tracked a calibration satellite. The satellite's X-band radar cross section (RCS) is shown in brackets following its satellite number.

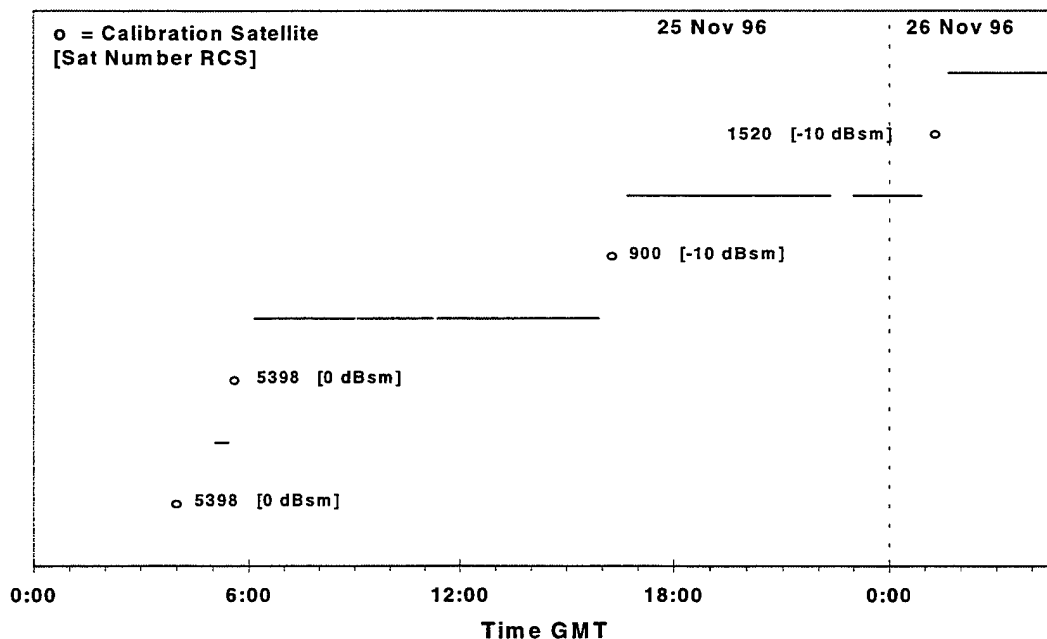


Figure 1. Haystack 24-Hour Measurement Campaign Time Line

A total of 19,605 hours of debris data were collected and 126 objects were detected. Figure 2 shows the altitude distribution (detection rate versus altitude) for the CoBeam campaign and for fiscal years 94-96. FY96 data is from Oct 95 through May 96. The FY distributions are in close agreement except above 600-km altitude. This increase is attributed to the breakup of the Pegasus-HAPS upper stage just prior to this campaign. The 'hump' in the data between 800 to 1000 km altitude is due to the RORSAT NaK debris.

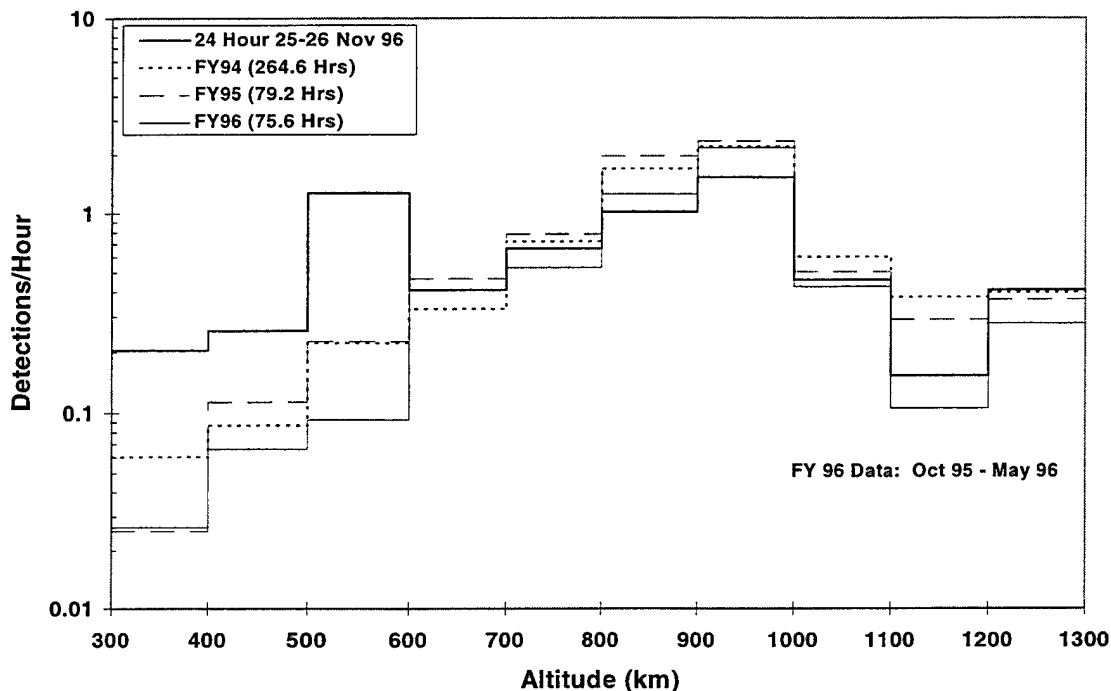


Figure 2. Altitude Distribution

Figure 3 shows the same data in terms of flux. The 100-km altitude bins are divided by the detection surface area for each bin. This data set is useful to determine the flux incidence upon a spacecraft. The spacecraft surface area divided by a length of time in orbit would yield the potential hits per unit time.

Figure 4 shows the detection altitude versus Doppler inclination. As depicted, orbital debris is not uniformly distributed. Typically, space debris is located near the same inclination and altitude as intact satellites. But, due to on-orbit explosions, orbital debris spread out from the initial orbit. The densely packed data groups are associated with the two major debris sources discussed previously.

The Haystack radar collects data from two polarizations. The radar transmits energy that is right circularly polarized and receives both right and left polarizations. The principal polarization (PP) channel is designated when the radar transmits right circular polarization and receives left. The orthogonal polarization (OP) channel is designated such when the radar transmits right circular polarization and receives right polarization. Energy received in the PP channel occurs when the energy is reflected from a single surface, such as a flat plate or a sphere. The OP channel receives energy when the target de-couples the signal. This occurs when the energy is reflected from a dipole or a multi-faceted object. The ratio of the energy received in the two channels can be attributed to the shape of an object. A high PP/OP ratio (> 8) is usually associated with spherical objects. An object reflecting energy with a polarization ratio greater than 2 and less than 8 is most likely ellipsoidal; a ratio less than 2 is usually dipole shaped or elongated. An object that reflects a very low PP/OP ratio is multi-faceted. Using these criteria, the symbols in figure 4 represent spherical 'o', ellipsoidal 'Δ', and dipole '—' shaped objects. This has been confirmed by analyses of the NaK droplets and HAPS debris.

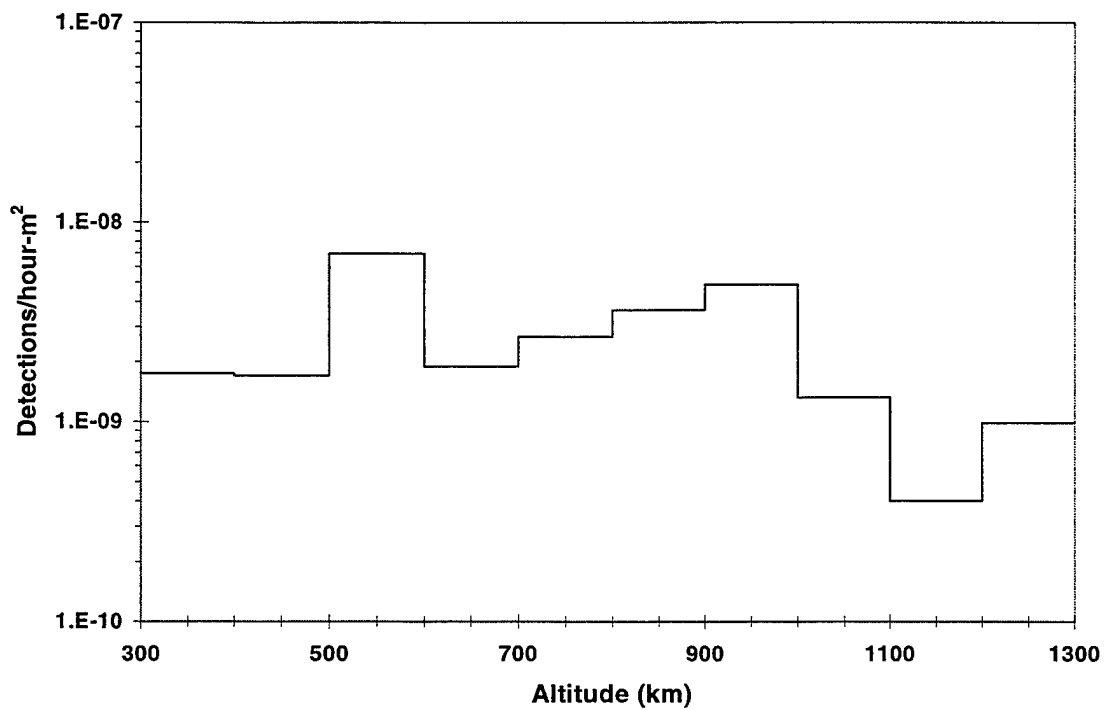


Figure 3. Haystack Flux Distribution

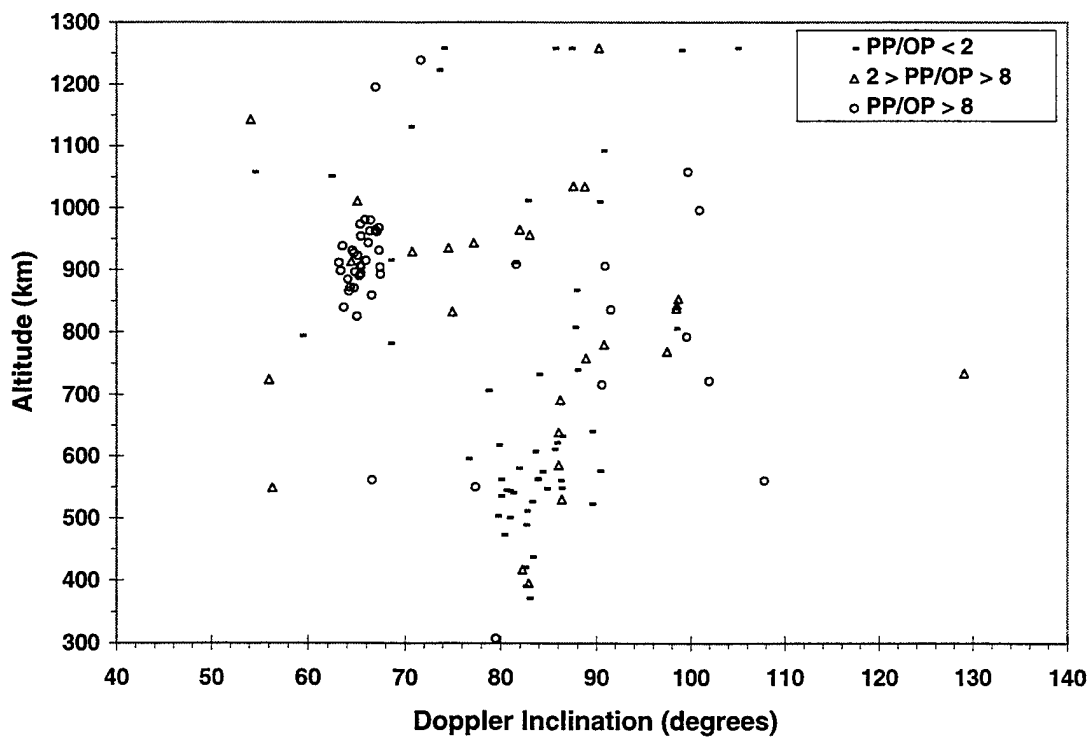


Figure 4. Altitude versus Inclination

In order to compare each radar's result, altitude, inclination, and size estimates are plotted as a function of time-of-day. The same orbital debris families should be visible from each radar but with a time difference that corresponds to the difference in longitude. The Haystack data in Figure 5 shows the altitude for each detection. The different symbols represent the shape of the object determined from the ratio of the PP and OP energy received as discussed above. Again, the detections between 800 and 1000 km altitude are mostly spherical and can be associated with NaK. The vertical lines represent the time window that the HAPS debris was visible from Haystack. They are paired starting from left to right in this figure. The lines were determined from the USSPACECOM cataloged HAPS objects. After the breakup in June 1996, the SSN identified and tracked nearly 700 objects related to this upper stage explosion. The orbital element sets for these objects were propagated using the SATRAK program through the Haystack field-of-view. The time windows are determined from the first and last observable object. The darker vertical dashed-lines show the start and stop times of the data collection period. The horizontal arrows indicate the time windows. Again note that the dipole shaped objects were primarily detected in the time and altitude windows associated with Pegasus-HAPS debris.

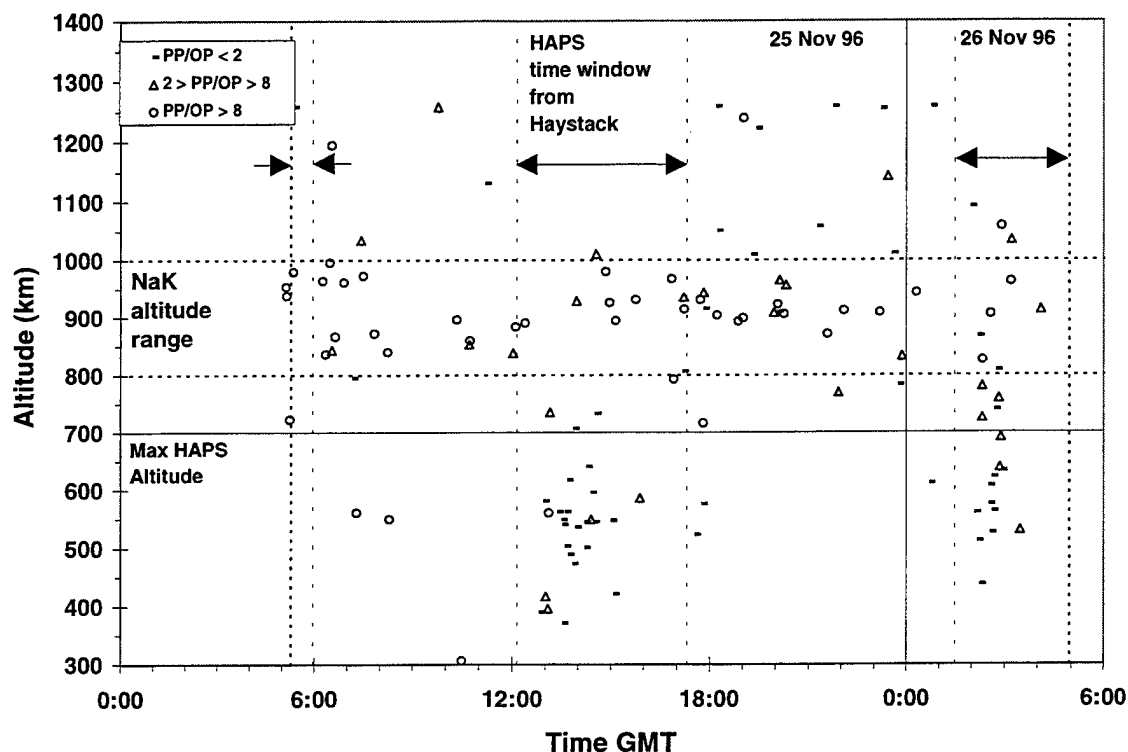


Figure 5. Altitude versus Time-of-Day

Figure 6 shows the same data plotted for orbital inclination versus time-of-day. Note that the NaK debris falls between a narrow inclination band associated with the RORSAT satellites and these debris objects were detected randomly throughout the measurement campaign. This debris family has existed for several years, which has allowed the debris' right ascension to spread out more-or-less uniformly due to perturbations. However, the small HAPS debris were only detected in the Haystack time-windows associated with the cataloged objects. These pieces were detected five months after the breakup event, which was not enough time for perturbations to spread out the HAPS objects' right ascension. Data collection soon after an event may be used to characterize the breakup in terms of count, size distribution, and estimated mass.

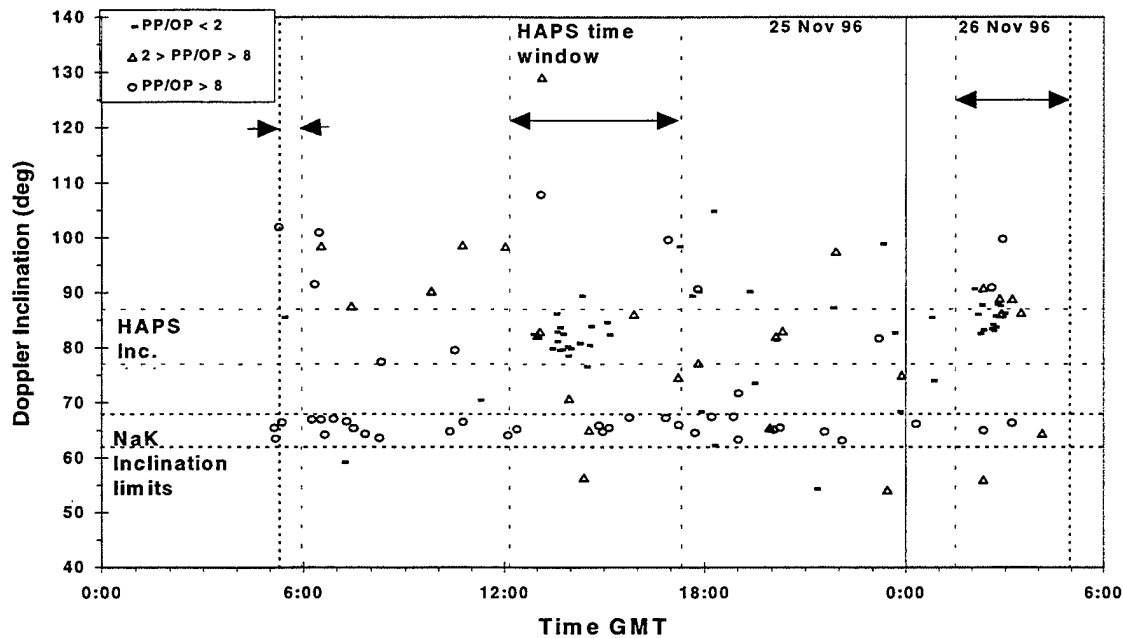


Figure 6. Orbital Inclination versus Time-of-Day.

Figure 7 depicts estimated size (m) versus time-of-day. Again, the vertical dotted lines are the Haystack time-windows when the HAPS debris was observable. The largest object detected during this campaign was approximately 5 cm in diameter. None of the objects correlated with a USSPACECOM satellite number.

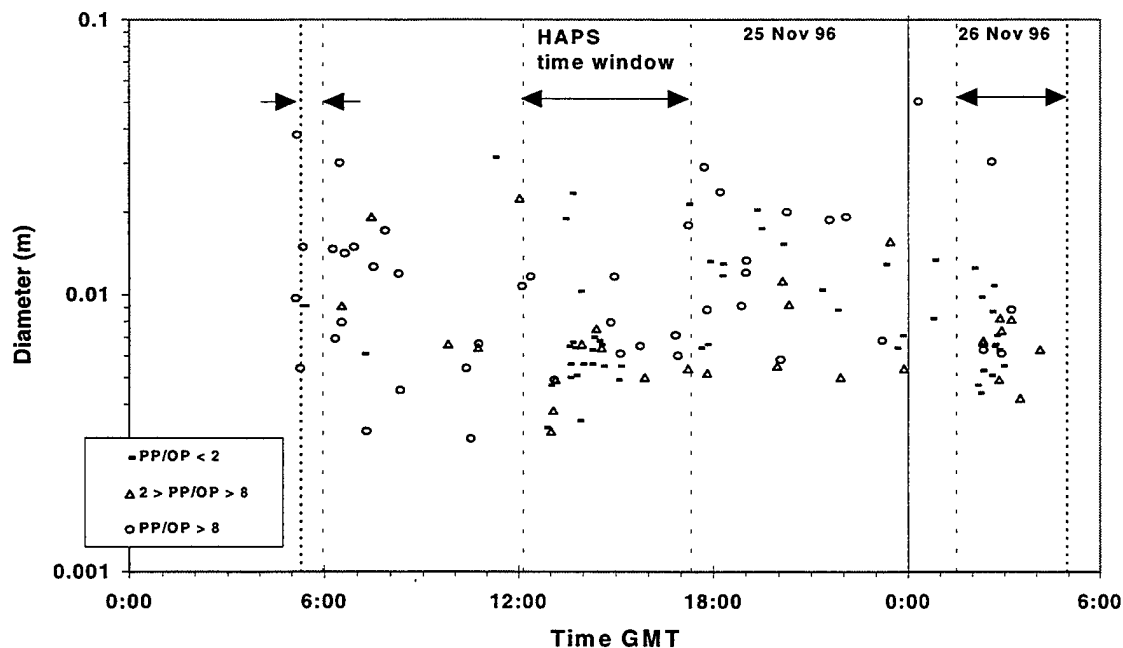


Figure 7. Estimated Diameter versus Time-of-Day.

TRADEX Measurements

TRADEX is a dual frequency radar operating at L-band and S-band. Only the L-band results were supplied to NASA/JSC. TRADEX was operated in a stare and chase mode. As the name implies, the radar is pointed at a fixed position and waits until an object passes through the radar beam. Once an object is detected, real time processing of the monopulse channels provides information on the direction of travel. The radar is accelerated in that direction in order to "catch up" with the object and begin tracking.

TRADEX was operated for 25.15 hours during this experiment starting at approximately 06:10 UT on December 2, 1996 and ending at approximately 07:19 UT, December 3, 1996. TRADEX successfully detected and tracked 50 objects. Also 10 verified detections were not successfully tracked. No data exists for these detections. Of the 50 tracked objects, 22 were known, cataloged objects and 28 were uncorrelated targets (UCTs). The NASA Size Estimation Model was used to estimate the physical size of the 28 UCTs from the measured RCS data. When a track was correlated to a cataloged object, the track was terminated quickly. The historical RCS data from the U.S. Space Command was used to estimate size for these objects.

Figure 8 shows the distribution of inclinations vs. altitude of the semi-major axis for the TRADEX detections. JSC did not receive the altitude at which the object was detected during Stare operations, which would be equivalent to the altitudes reported from the Haystack data. The altitude at closest approach was provided for UCTs, but not for the cataloged objects. The altitude for cataloged object shown is the mean altitude. Since only 50 objects were detected with orbital elements, no major conclusions are drawn from this data set. The primary reason for using TRADEX was to cover orbits that are not visible to the other two radars. Of the tracked objects, only 6 (approximately 13%) of these objects would not have been detectable by Haystack or TIRA. Four of these had inclinations below 40° and two had inclinations above 140° . Only 2 of these objects were UCT's.

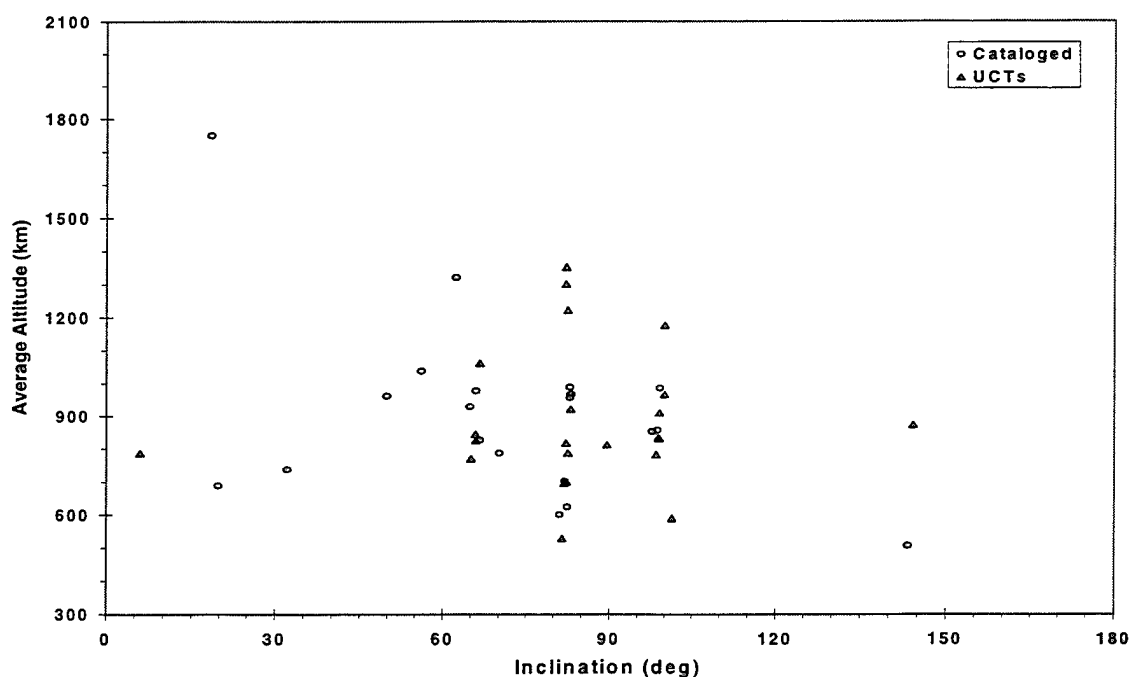


Figure 8. Scatter plot of the Average Altitude vs. Inclination for UCT and cataloged objects

The TRADEX detected satellites grouped into three highly populated inclination bands: $\sim 65^\circ$, $\sim 82^\circ$, and $\sim 99^\circ$. Sixty-five degrees is, of course, the inclination band of the NaK debris from RORSAT satellites. There were 3 cataloged objects and 4 UCTs near 65° inclination. It is debatable that any of these objects are NaK droplets

because the Haystack data has shown that most of NaK debris is 3 cm diameter or smaller, below the threshold of detection for TRADEX. One of the cataloged detections; however, has been identified as the reactor core from COSMOS 1412, possibly the source of some of the NaK.

Seventeen objects were detected in $\sim 82^\circ$ orbits. Seven of these were cataloged and 10 were UCTs. This is the inclination band that HAPS debris is in. All of the UCT detections in this band occurred during periods when the cataloged HAPS debris orbit planes were passing over as shown in Figure 9. One of the cataloged objects is also HAPS debris. Five of the 10 UCTs in this inclination band have PP/OP ratios of 1.26 or less. These are most likely HAPS debris.

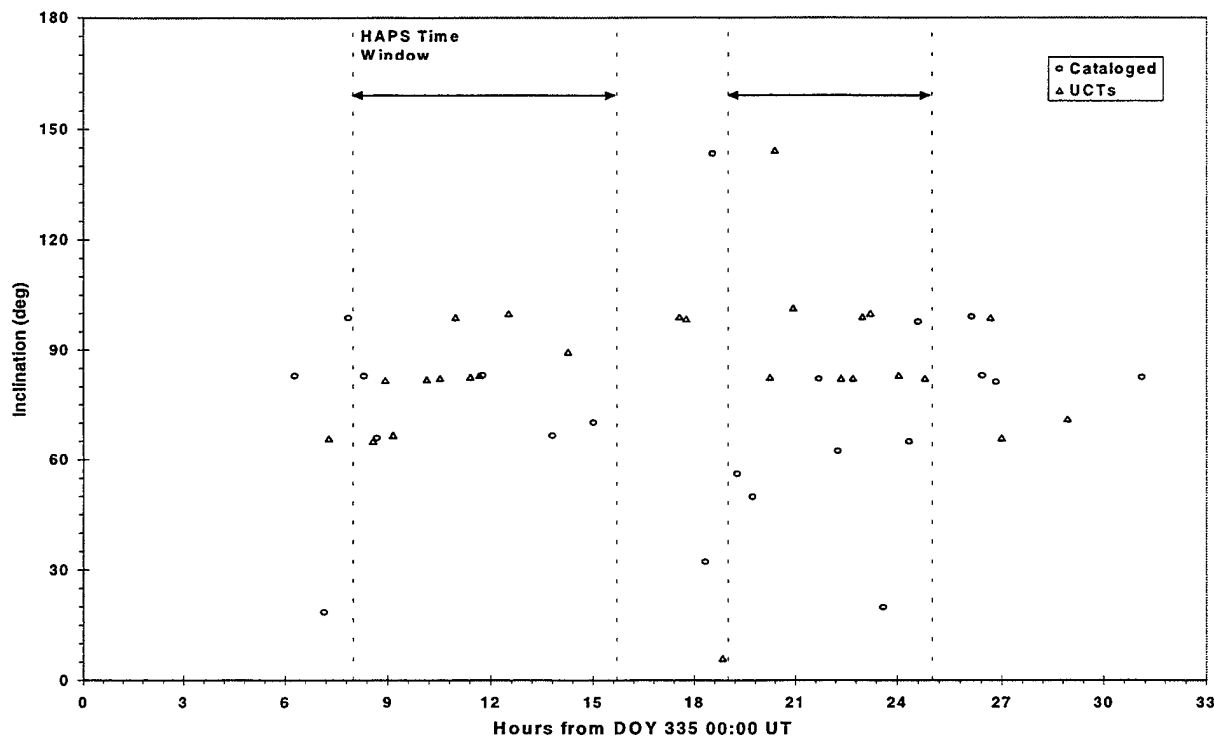


Figure 9. Scatter plot of the inclination of each tracked object vs. the time of the detection.

Eleven objects were detected in orbits with inclinations near 99° . Three of these were cataloged while eight were UCTs. Although the statistics are poor, it may be significant that two of the objects have inclinations near 144° . There have been very few launches into this inclination band.

Figure 10 shows the size distribution for the TRADEX data and the Haystack data collected (over the same altitude range) during the CoBeam test. Although there is very little overlap between the two size distributions, the results are consistent within the measurement uncertainties. Haystack, having the higher sensitivity and small beam width, detects smaller objects. But, during this campaign did not detect any cataloged objects. TRADEX, on the other hand, has a much larger beamwidth and therefore statistically expects to more large objects. The size distribution formed by combining these two data sets is consistent with the size distribution from a larger Haystack data set covering enough time to statistically expect to see the larger sizes. This larger data set for 1996 is also shown.

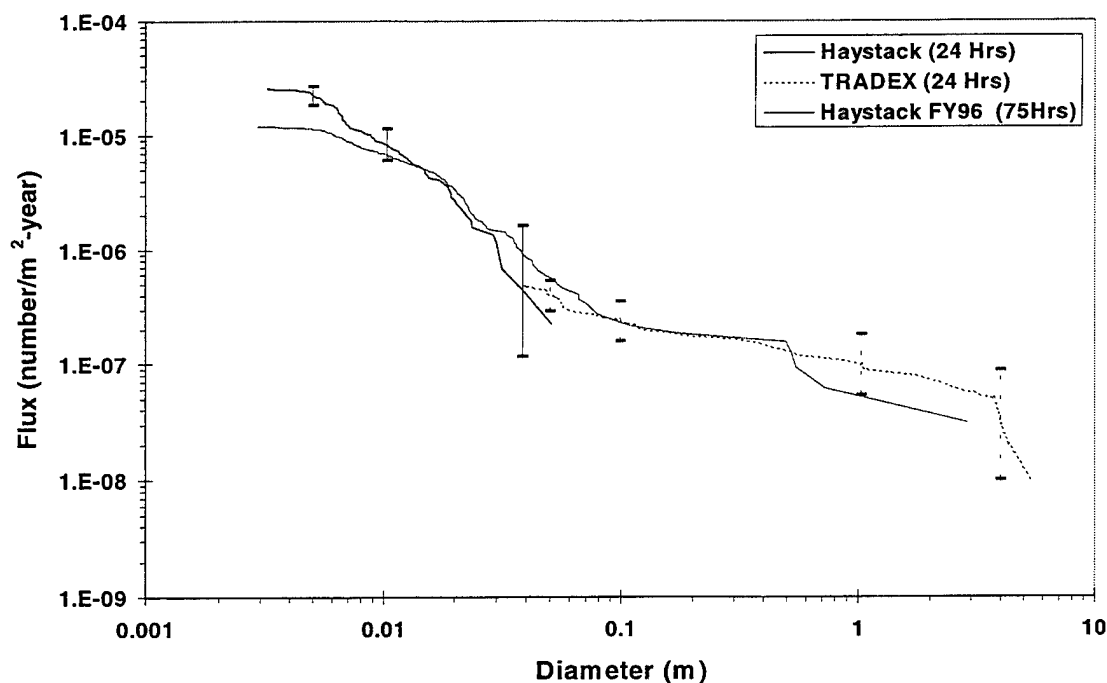


Figure 10. Comparison of Haystack, TRADEX, and Haystack FY96 measured size distributions

TIRA/EFFE Results

The German Research Establishment operates TIRA for Applied Science (FGAN). TIRA has conducted two 24-hour debris campaigns with funding from the European Space Agency/European Space Operations Centre (ESA/ESOC). The first was performed on December 13/14, 1994. The second was performed on November 25, 1996 and was designated the CoBeam Experiment. During the second campaign, The Max Planck Institute for Radioastronomy (MPIfR) operated the 100-m Effelsberg (EFFE) radio telescope as a bi-static receiver. The TIRA/EFFE configuration provided ~21 dB SNR gain in sensitivity over the monostatic TIRA configuration. This configuration was specifically designed to try to verify the existence of the NaK RORSAT debris. The two beams crossed at an altitude range of 750-980 km with the centers crossing at 850-km altitude.

To compare the TIRA/EFFE data to the Haystack results, a judicious choice of scaling parameters was employed. First, the altitude distributions were examined. Figure 11 shows the detections per hours versus altitude for both TIRA/EFFE and Haystack. Several methods were used to compare the Haystack data to the two German systems. The most accurate method was to scale the detection rates by the ratio of their beamwidths, then, to limit the sensitivity of the Haystack data to that of each German systems. The TIRA radar can detect 2-cm objects, EFFE can detect 0.9-cm, and Haystack radar can detect 0.5-cm objects at 1000-km range. The plot shows a fair agreement between the Haystack and the TIRA/EFFE data, but it appears that the EFFE is more sensitive than Haystack. One possible explanation for this difference is that the Haystack data only contains debris objects, which are detected within the half-power points of the main beam. The EFFE receiver does not have angle channels to determine where a detected object passes through the main beam. Therefore, the EFFE data set probably included detections beyond the half-power point of the main beam and possibly some from the sidelobes.

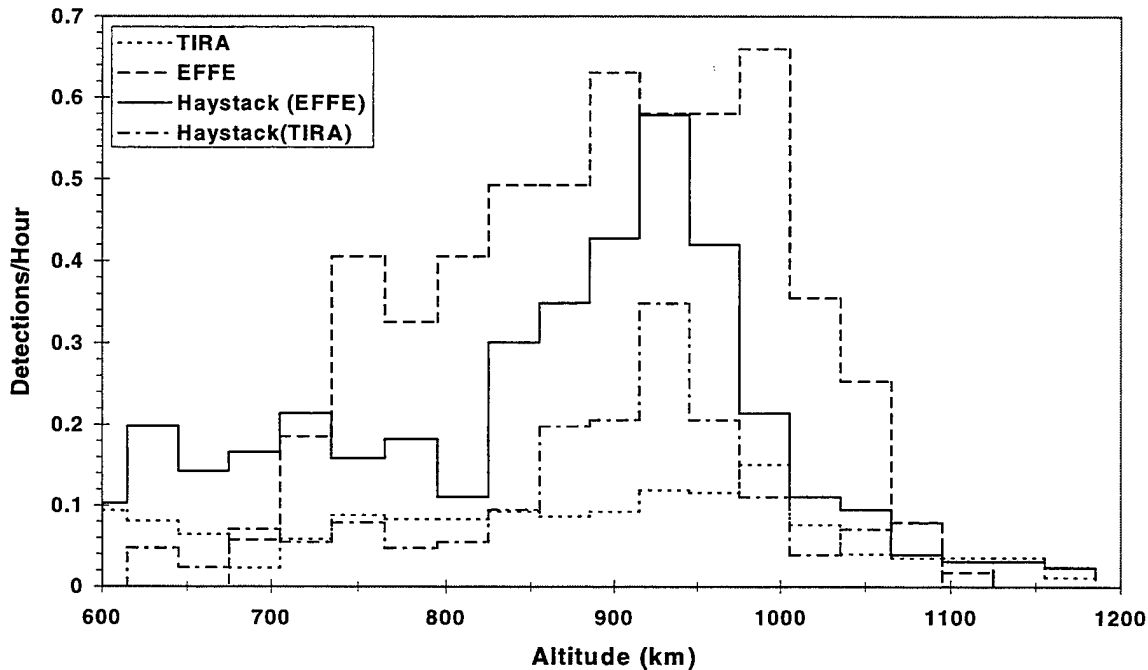


Figure 11. Altitude Distribution

The comparison of inclination distributions had a different set of difficulties because the German data combined the measurements from TIRA and EFFE. Although it was stated that most detections smaller than 2 cm were observed by EFFE, it was difficult to scale the data sets for comparison. The solution was to convert the detection rate for TIRA/EFFE and Haystack to counts and then scale the data to the same total count. Figure 12 and 13 show the resulting inclination distributions. Although there is fair agreement, the Haystack data peaks at 65°, 82°, and 98° are sharper than the TIRA/EFFE data. These narrow peaks seen in the Haystack data are in close agreement to the US Space Command Catalog inclination distribution. In addition, further examination of the TIRA/EFFE data peak centered near 65° inclination shows that it exhibits a broader distribution than the Haystack data. For the size ranges depicted, it has been shown that the primary data source of this debris is the sodium-potassium droplets generated by leaking RORSAT reactor cores. Measurements since 1990 from both Haystack and Goldstone indicate that this debris is very near 65° inclination and the spread is ± 2.5 . It is possible that the range rate accuracy used to calculate the Doppler inclination caused this wider distribution. A range rate difference of 0.1 km/s leads to a 3-4° error in Doppler inclination depending on range and range rate.

Considering this was only a 24-hour snapshot of the space debris environment, the data sets compare quite well. Differences are understood and will be verified once the complete data sets are exchanged. More importantly, both data sets clearly depict the RORSAT and Pegasus (a major breakup at 82° inclination and 500-700 km altitude which occurred in 1996) debris families.

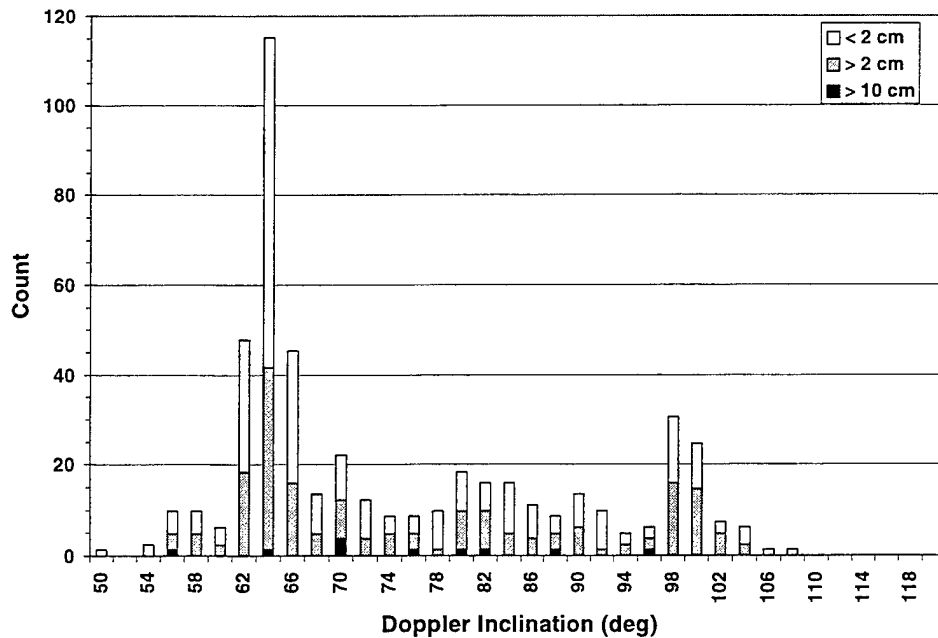


Figure 12. Haystack Data, Inclination Distribution, Altitude 600 - 1200 km, Size > 0.9 cm

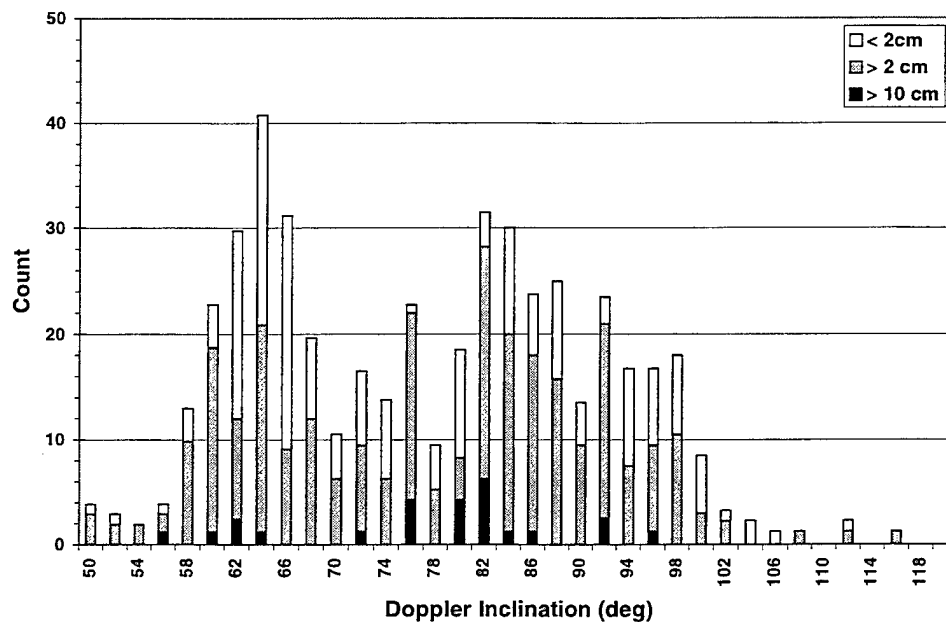


Figure 13. TIRA/EFTE, Inclination Distribution for Altitude 600 - 1200 km

CONCLUSIONS

This paper reviews radar measurements for the November 1996 Cooperative Beam Experiment. Agreement between the radars involved was very good. Tests such as the CoBeam allow critical comparisons of analysis techniques and assumptions, which improve the understanding of the space debris environment. In general, a better job needs to be done to define collection areas and detection algorithms so that comparisons between measurements and the accuracy of the results provided to modelers can be improved.

NASA/JSC Optical Orbital Debris Program: Results from the Liquid Mirror Telescope (LMT) and the CCD Debris Telescope (CDT)

J. L. Africano¹, T. J. Settecerci², J. V. Lambert¹, and E. G. Stansbery³

¹Boeing North American, Inc.

²Lockheed Martin Engineering and Sciences

³NASA/Johnson Space Center

LIQUID MIRROR TELESCOPE

NASA Johnson Space Center (JSC) has built a zenith-staring, three-meter aperture liquid mirror telescope (LMT). This telescope was built to characterize the optical orbital debris environment, especially in the important but hard to track one to ten centimeter size range. The primary mirror of an LMT is a parabolic dish of mercury. As the dish spins, the mercury spreads over the dish to form a reflective surface. The three-meter dish spins at a rate of ten revolutions per minute to form an $f/1.7$ primary mirror.

While the concept of a liquid mirror telescope is simple, its practical execution is not. Liquid mirror technology was pioneered by Ermanno Borra of Laval University, Quebec¹. Borra introduced techniques that made the mirror practical. The main problem with liquid mirrors is vibrations, that produce ripples and waves which destroy the optical quality. Borra took several measures to reduce vibrational effects to a tolerable level. He found that it was necessary to make the mercury layer as thin as possible, with a practical limit of about 2.5 mm. At this thickness, surface tension helps damp waves in the liquid. He made the supporting dish as stiff and as strong as possible, and supported the dish on a high-quality air bearing to provide vibration-free rotation. The rotation speed of the mirror had to be held constant to within 1 part in 100,000, which Borra accomplished with a simple belt drive system. By 1989, he had developed a 1.5 meter diameter $f/2$ liquid mercury mirror that was diffraction-limited. Although mercury poses a significant safety issue, Borra discovered that a thin layer of mercury oxide forms on the mirror surface after a few hours. This layer reduces the mercury vapor concentrations over the mirror to safe levels while having a negligible effect on the reflectivity of the surface. Even so, stringent safety precautions are mandatory for handling the mercury, especially during times when fresh mercury surfaces are exposed while the mirror is being formed or cleaned.

Mirrors larger than 1.5 meters encountered problems with the design of the supporting dish because of escalating requirements for stiffness and strength. Detailed structural analysis of the requirements of larger mirrors was performed². The analysis determined that by using construction techniques adapted from the aircraft industry, it should be possible to construct liquid mirrors as large as 10 meters in diameter.

The greatest advantage of a liquid mirror over a glass mirror is cost. The LMT was built for a cost of about one million dollars while traditional telescopes of similar size cost about ten times as much. One disadvantage is the inability to point an LMT in any direction other than the zenith. This is not a limitation for statistical characterization of the orbital debris population. The telescope can observe the orbital debris that passes overhead through its field of view.

The dish for the $f/1.7$ three-meter aperture NASA liquid mirror was designed and constructed by Paul Hickson and his associates at the University of British Columbia². The mirror, associated optics, and astronomical detector were first assembled and evaluated at the NASA Johnson Space Center in Houston. It was then transported to Cloudcroft, New Mexico, where it was installed in the Cloudcroft Facility operated by the National Solar Observatory at Sunspot, New Mexico. First light for the LMT at the Cloudcroft Facility was in 1995. Performance testing and initial observations with the LMT have been described by Potter and Mulrooney³.

ORBITAL DEBRIS OBSERVATIONS

The use of a long-exposure astronomical CCD camera for observations of LEO orbital debris is impractical because the orbital velocities of these objects carries them out of the field of view within a few seconds. For this reason, an intensified video camera operating at the standard 30-hz television rate was installed on the LMT. The limiting magnitude was measured to be below 17.5 M_v , corresponding to a two centimeter diameter orbital debris object with an albedo of 0.1, at an altitude of one thousand kilometers. Upgrades to the video system with a short exposure CCD and digital cameras have now resulted in fainter limiting magnitudes. Using time-delayed integration (TDI) techniques, the LMT can now see stars down to 23 M_v . The actual detection sensitivity for orbital debris is a function of an object's velocity as it limits the effective dwell time per pixel.

At first glance, one would think little could be learned about an object that passes through the field of view of a telescope in just a few tenths of a second or less. The plane of the orbit, defined by the inclination and RAN derived from an object's field-of-view crossing angle, is reasonably well determined. This is accomplished by measuring the entrance and exit positions of the object's path through the field-of-view. By assuming a circular orbit, the altitude of the object can be estimated based upon its velocity through the field-of-view. The orbital altitude is less well determined largely due to departures from the circular orbit approximation used in the calculations. The size of the object can also be estimated by comparing the object's brightness to the background stars and assuming an albedo (typically 0.1)⁴. This estimate of size is prone to error because the albedo can range from 0.05 to 0.8.

The time available for conducting optical observations of low altitude orbital debris is limited to just a few hours per night. The sun must be far enough below the observer's horizon so the sky is dark, yet not so far that the debris object is in the Earth's shadow.

OBSERVATIONAL RESULTS

The results from the first forty-seven video tapes collected by the LMT are reported. In these observations, 62 correlated objects and 231 UCTs were detected. As discussed above, the altitude of objects detected by the LMT are computed from the observed angular rate assuming that the objects are in a circular orbit. If an object is actually in an eccentric orbit and near perigee (apogee), its observed angular rate will be higher (lower) than that of an object in a circular orbit. Hence, the computed altitude will be lower (higher) than its true physical altitude.

The accuracy with which the orbital parameters for a debris object can be computed was determined from detections of the cataloged objects tracked by the SSN. The orbital parameters derived from these observations were compared to the

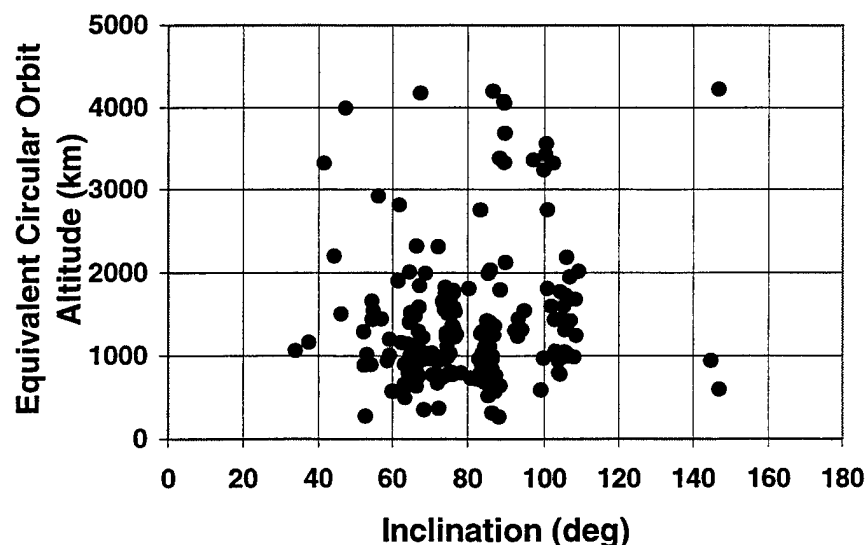


Figure 1. Altitude-Inclination Distribution of Objects Detected by the LMT.

SSN cataloged values. For known LEO satellites with nearly circular orbits ($e < 0.1$), the average error in the equivalent circular orbit altitude determination is about 80 km. The average errors in the inclination and the RAN for all of the detected cataloged objects are about 1.7 and 0.5 degrees, respectively.

Figure 1 shows the altitude versus inclination distribution of the orbital debris detected by the LMT. The orbital debris distribution corresponds closely with known satellite operational altitudes and inclinations. There are fairly tight groupings of uncataloged objects. These groupings have been correlated to satellite breakups⁵ and agree with radar data collected for orbital debris monitoring.

The sizes of objects can also be estimated from these observations. An object's observed brightness is compared to the background stars using techniques similar to visual magnitude estimates made by variable star observers. This observed or apparent magnitude, M_{app} , is then normalized to an absolute magnitude, M_{abs} , at a range of 1000 km where the range is the derived orbital altitude. The size of the debris object is estimated by computing the diameter, D , of a specular sphere having the same absolute magnitude. Figure 2 compares the calculated absolute magnitudes for the correlated objects to their SSN cataloged radar diameters. The three lines in the plot represent the brightness of specular spheres having physical cross-sections corresponding to the radar diameters with albedos of 1.0 (maximum), 0.1, and 0.01. It is interesting to note that the absolute magnitudes cluster around the 0.1 albedo line. There is a suggestion from these and from other observations that the larger, intact cataloged objects may have higher albedos (around 0.2) than the cataloged debris objects. The absolute magnitude of the UCT's is plotted on the left side of Figure 2.

The peak of the distribution occurs at 14th magnitude, which corresponds to a 9-cm diameter sphere. Assuming an albedo of 0.1 for the debris objects, we are detecting objects down to about 3 cm in diameter. About 30 of these UCT's may be associated with the RORSAT sodium-potassium (NaK) droplets. Optical measurements indicate that these droplets are highly reflective. The measured albedo is about 0.8 for these droplets⁶. When 0.8 is used as the assumed albedo, the

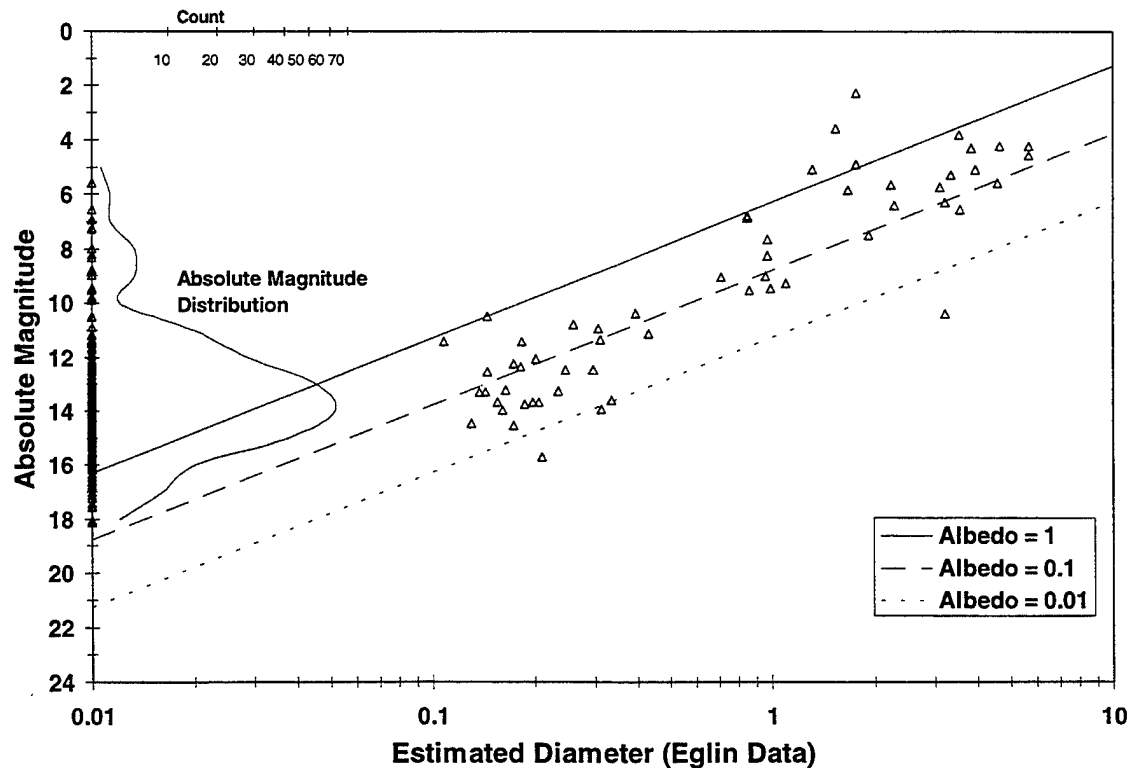


Figure 2. Comparison of Absolute Magnitudes and Catalog Radar Diameters.

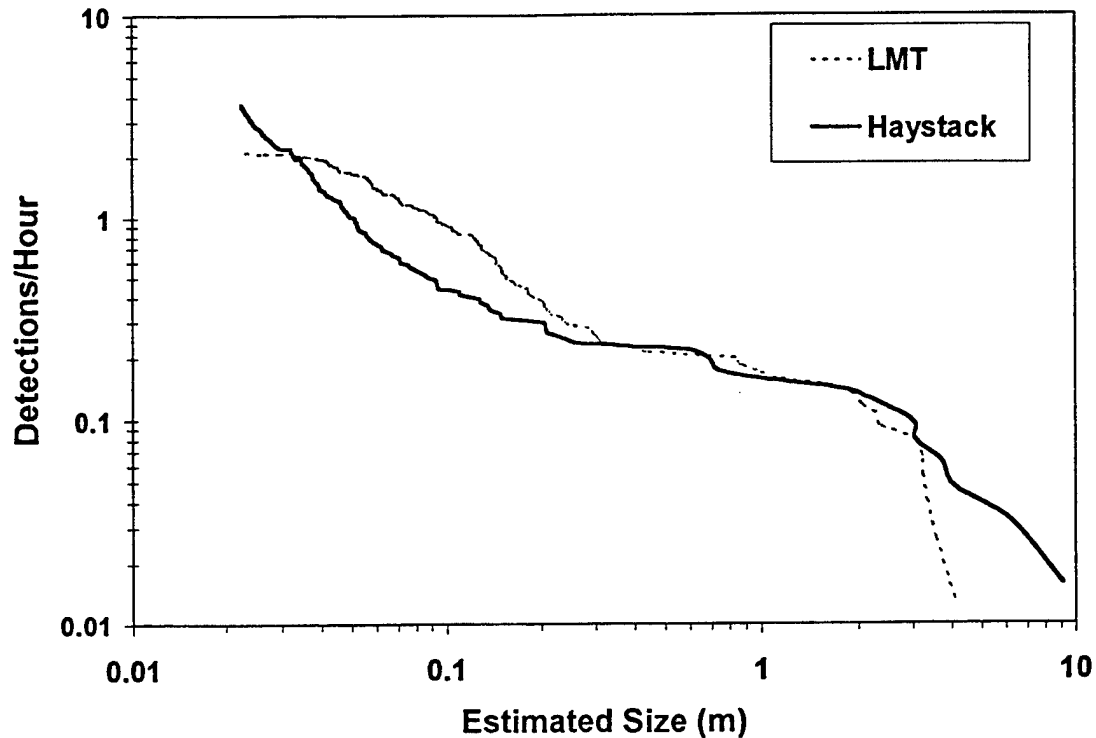


Figure 3. Comparison of Optical and Radar Size Distributions.

diameter estimate for these objects decrease. This implies the LMT is able to detect objects (with a 0.8 albedo) as small as 1.5 cm.

Figure 3 compares the LMT and the Haystack radar detection rates as a function of object size. The observed Haystack detection rate was increased by a factor of 5.2 to account for the difference between the LMT (0.24 degrees) and Haystack (0.05 degrees) beam width. While there are still several additional observational biases to be considered in processing the LMT data, the optical results are very consistent with the radar results. The main difference occurs in the 3 to 30 cm size range. We are exploring possible explanations for these differences.

CCD Debris Telescope (CDT)

One of the limitations of the LMT is that it cannot observe debris in geosynchronous orbits due to the fact it is located at 33 degrees North latitude and is restricted to zenith staring with a relatively small (0.3 degree) field-of-view. The CCD Debris Telescope (CDT) is employed for observations of the geosynchronous Earth orbit (GEO) debris environment. It is an automated 32-cm aperture, portable Schmidt telescope presently co-located with the LMT. The CDT is equipped with a CCD camera capable of detecting 17th magnitude (~0.8-meter) objects at 36,000 km. The CDT is currently conducting nightly systematic searches of the near-GEO environment as part of an international measurement campaign under the auspices of the Inter-Agency Space Debris Coordination Committee (IADC). Testing for this campaign took place in late 1997 and data collection began in January, 1998. About 500 hours of observations totaling more than 50,000 frames have been collected on seventy-two nights for calendar year 1998.

Figure 4 presents a typical CCD exposure. The telescope is pointed to a particular azimuth and elevation. The telescope is allowed to settle with the drives turned off, then a 20 second exposure is taken. Because the telescope is not tracking, stars leave trails, geosynchronous objects leave short trails, and geostationary objects are points.

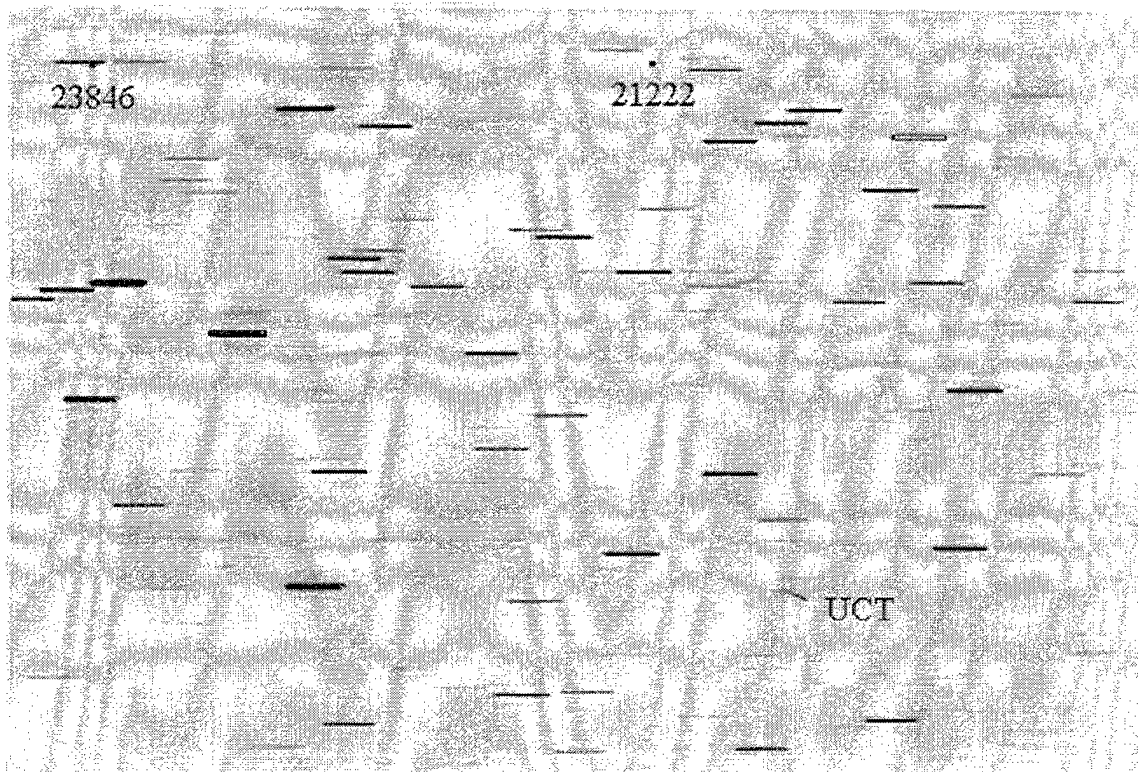


Figure 4. Typical CDT Image.

Automated data reduction software is used to process each frame to find moving objects and report the positions, magnitudes, and times of each detection. At present, the CDT data are transferred electronically to Maui for reduction using software developed by the Maui branch of the Air Force Research Laboratory (AFRL) for their *RAVEN* small telescope program. Processing these data over the Internet takes from five to thirty minutes per frame depending on network activity. Arrangements have been made between NASA and AFRL to transfer this software to JSC during the spring of 1999. Processing these images will then take sixty to ninety seconds per frame!

To date, we have manually reviewed over seventeen thousand CDT frames. The initial results indicate that forty-nine percent of the frames contained at least one moving object, twenty-seven percent of the frames had exactly one object, thirteen percent had two objects, and nine percent had three or more objects. Each night about 130 objects are found in the CDT data; about 30 of these objects are UCTs.

CONCLUSIONS

NASA JSC has developed and demonstrated the LMT technology as a very cost-effective way of monitoring the orbital debris environment. Although this approach does have limitations, it has already demonstrated its usefulness for orbital debris detection and characterization. The LMT is now routinely collecting the first optical measurements of orbital debris objects smaller than five centimeters. The CDT demonstrates a cost-effective method for using small, automated telescopes for monitoring the orbital debris environment at GEO. Weather permitting, observations are made on a nightly basis, excluding the week around full moon. The results of these observations are complimentary to radar measurements, providing critical insights into the nature and distribution of these potentially hazardous objects.

REFERENCES

1. E. F. Borra, R. Content, M.J. Drinkwater, and S. Szapiel, "A Diffraction-Limited $f/2$ 1.5 Meter Diameter Liquid Mirror", *Ap. J.* Vol. 346, 1989 L41-L44.
2. P. Hickson, B.K. Gibson and D.W. Hogg, "Large Astronomical Liquid Mirrors", *P.A.S.P.* Vol. 105 1993 pp. 501-508.

3. A. E. Potter and M.K. Mulrooney, "Liquid Metal Mirror for Optical Measurements of Orbital Debris", *Adv. Space Res.* Vol. 19, 1997 pp. 213-219.
4. K. Henize and J. Stanley, "Optical Observations of Space Debris", *AIAA*, 90-1340, Baltimore, MD., April 1990.
5. N. Johnson, A. Bade, P. Eichler, E. Cizek, S. Robertson, and T. Settecerci, "History of On-Orbit Satellite Fragmentations", *JSC - 28383*, Houston, TX., July 1998.
6. D. J. Kessler, M. J. Matney, R. C. Reynolds, R. P. Bernhard, E. G. Stansbery, N. L. Johnson, A. E. Potter, and P. D. Anz-Meador, "The Search for a Previously Unknown Source of Orbital Debris: The Possibility of a Coolant Leak in Radar Ocean Reconnaissance Satellites", *JSC - 27737*, Feb. 1997.

SPACE SURVEILLANCE OPERATIONS WITH THE SPACE-BASED VISIBLE

Curt von Braun[†]

Since April 1996 the Space-Based Visible (SBV) sensor on the Midcourse Space Experiment (MSX) satellite has been gathering data as part of a technology demonstration of space-based space surveillance. The first year and a half on orbit was dedicated to validating the concept of space-based space surveillance and to assessing the sensor's performance. During this period it was shown that conducting space surveillance on orbit was not only possible but highly productive, and that SBV could serve as an operational asset to the Space Surveillance Network (SSN). On this basis, commencing in October 1997, the SBV was transitioned from that of an experimental sensor to that of a Contributing Sensor within the SSN. This transition occurred as part of an Advanced Concept Technology Demonstration (ACTD) sponsored by the Office of the Secretary of Defense, the Ballistic Missile Defense Organization and U.S. Space Command, with the first operational space-based space surveillance observations supplied to Space Command in April 1998. This paper will begin with an overview of the SBV sensor and its capabilities in support of space surveillance. A discussion of both the routine ground and space operations will be provided, with emphasis on enhancements to mission planning and geosynchronous search capabilities. Finally, a detailed presentation of the performance of SBV as a Contributing Sensor will be given, with particular focus on the comparisons with the existing Ground-based Electro-Optical Deep Space Surveillance (GEOSS) cameras.

INTRODUCTION

Since April 1996 the Space-Based Visible (SBV) sensor on the Midcourse Space Experiment (MSX) satellite (Figure 1) has been gathering data as part of a technology demonstration of space-based space surveillance. The first year and a half on orbit was dedicated to validating the concept of space-based space surveillance and to assessing the sensor's performance. During this period the Space Surveillance Principal Investigator Team conducted a variety of experiments and showed that space-based space surveillance was not only possible but highly productive, and that SBV could serve as an operational asset to the Space Surveillance Network (SSN). On this basis, commencing in October 1997, the SBV was transitioned from that of an experimental sensor to that of a Contributing Sensor within the SSN. This transition occurred as part of an Advanced Concept Technology Demonstration (ACTD) sponsored by the Office of the Secretary of Defense, the Ballistic Missile Defense Organization (BMDO) and U.S. Space Command, with the first operational space-based space surveillance observations supplied to Space Command in April 1998.

[†] Technical Staff Member and MSX Surveillance Principal Investigator, Massachusetts Institute of Technology Lincoln Laboratory, Lexington

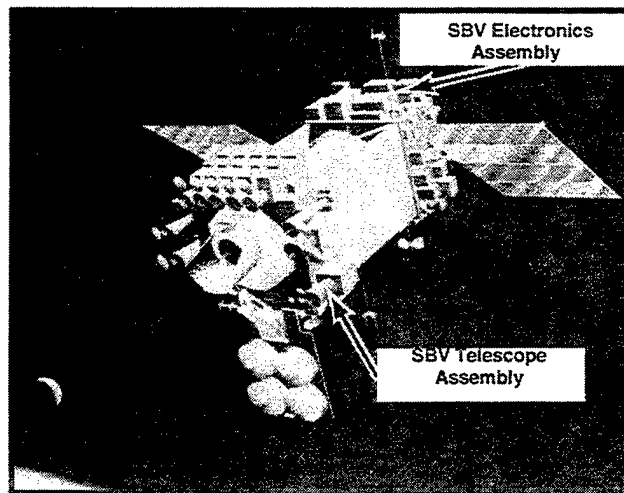


Figure 1 The SBV on the Midcourse Space Experiment

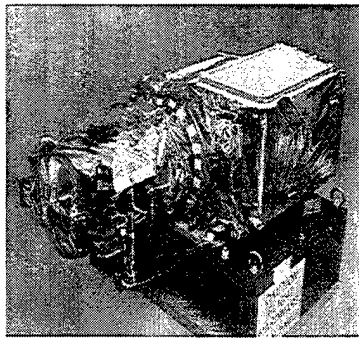
The Space-Based Visible program has a number of general objectives that were established in the late 1980s during the early design phase. Since the inception of the Space-Based Space Surveillance Operations (SBSSO) ACTD in late 1997, specific objectives were added to address needs within the SSN. For a detailed outline of the SBV program objectives during its experimental phase, the reader is referred to Ref. 1. However, the objectives associated with the ACTD operations are given as follows:

- a) Integration of the SBV sensor into the SSN. This involves exercising the Space Defense Operations Center in Cheyenne Mountain (SPADOC) with real space-based space surveillance data;
- b) Operational demonstration of the fusion of SBV data with data from the ground network;
- c) Demonstration of routine response to space surveillance tasking from Space Command; and
- d) Performance of wide-area searches of the geosynchronous orbital belt.

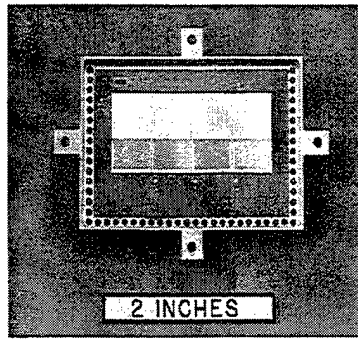
The overall goal of SBV program is to establish a legacy for future space-based space surveillance systems and to facilitate in the transfer of technology to the eventual operational system. This paper will provide an introduction to the SBV sensor, will give a discussion of the routine operations, and will show results achieved over the first year of operations as a Contributing Sensor to the SSN.

THE SBV SENSOR

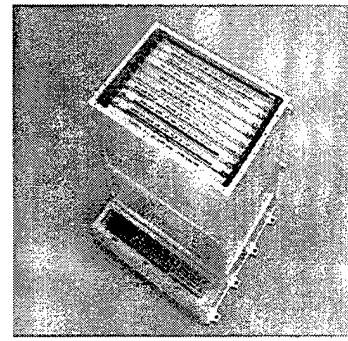
Prior to SBV becoming a Contributing Sensor to the SSN, the Surveillance Principal Investigator Team used the SBV to successfully demonstrate the concept of space-based space surveillance. During the experimental phase of the MSX / SBV program, a number of technologies were demonstrated with the SBV. The hardware associated with these is illustrated in Figure 2. This figure also shows the three key technologies that were used to demonstrate space-based operations. The first technology is that of the high stray-light rejection design of the SBV telescope, which allows for the detection of faint targets in high



High Stray-light Rejection



Focal Plane Arrays



Signal Processor

Figure 2 Major technology demonstrations on the SBV

background environments near the lit earth-limb. The next key technology incorporated into the design of the SBV is the low-noise charge-couple device (CCD) focal planes, also shown in Figure 2. These four abutting 420x420 pixels arrays, each with a frame store region for rapid readout, were fabricated by the Lincoln Laboratory Semiconductor Division in the late 1980's. The last major technology utilized by the SBV is that of the Signal Processor (SP). During routine space surveillance operations, SBV data are gathered by staring at a chosen location in the sky and integrating through a sequence of frames, referred to as a frameset. A typical frameset includes as many as 16 frames, resulting in almost three million pixels of information. The quantity of raw data generated by this process is far too large to be down-loaded on the 1 Mbit/sec communications link available to the MSX. Thus, the SP takes these three million pixels of information per field area and distills out only the information most vital for space surveillance, thus reducing the data volume by as much as a factor of 1000. The remaining information consists of a selection of stars needed to determine the sensor's pointing and any streak signatures left by resident space objects (RSOs) moving through the field-of-view. The effect of the SP is illustrated in Figure 3, which shows both the superposition of 16 raw frames (left) and the signal processed image (right). In these images, the stationary point sources are star detections and the streaks indicate the detection of satellites.

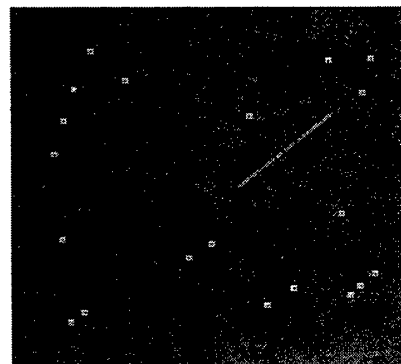
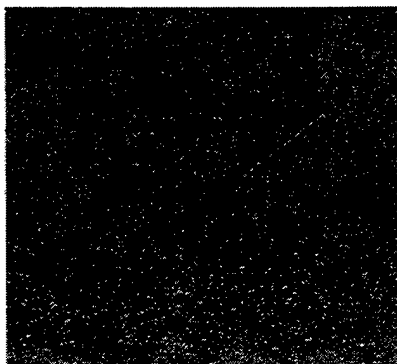


Figure 3. SBV Raw Full-Frame and Signal Processor Images

SBV DATA PROCESSING

Prior to assessing the ability of SBV to conduct space-based space surveillance activities, it was necessary to determine both the metric and photometric characteristics of the sensor. The metric positioning of targets in SBV's field-of-view requires both knowledge of the precise pointing of the sensor's boresight and of the position of SBV on orbit at that time the data are gathered. Using the pointing information, beginning and endpoints of the streaks detected on the focal plane (Figure 3) can be transformed into two angular measurements on the sky, such as right ascension and declination. Each endpoint is considered to be a metric observation of the target. These observations can then be merged with other ground-based optical and radar observations on the same target in order to establish the target's trajectory.

The process of producing a metric observation involves several steps. With SBV in a staring mode, the raw sensor data, as described above, is gathered on-board. The information contained in the each raw frame is then passed to the SP, which extracts the pixel values and intensities associated with a pre-selected number of star detections. In addition, a Moving Target Indicator (MTI) algorithm within the SP identifies any objects moving relative to the stationary background. Pixel intensities and focal plane coordinates for both the selected stars and the moving targets are down-loaded in a so-called SP Report. In the SPOCC, the star detections are centroided and the pattern and exact positions of detected stars are matched to a catalog of known stars. This process allows for a highly accurate determination of the sensor's pointing, without the use of sensors such as on-board gyroscopes. Through this technique, the pointing determination is routinely established to the level of a few tenths of an arcsecond. In addition, pointing is determined independently for each "look", avoiding common problems such as the drift and random walk commonly associated with gyroscopes. Once pointing is determined, this information is used to map the endpoints of the streaks on the focal plane to absolute angular positions on the sky, thus producing an observation (Ref. 2)

While the process described above is sufficient to produce angular measurements on targets from a space-based sensor, it is insufficient for the complete incorporation of these data into a ground-based tracking network. To accomplish this, it is necessary to determine the position, or ephemeris, of the MSX at the time the data were gathered. As part of an independent processing pipeline, Lincoln Laboratory has maintained the MSX ephemeris to an accuracy of 6 meters, surpassing the original goal of 15 meters (Ref. 3). The determination of the MSX ephemeris is accomplished by processing S-band ranging data from the Space Ground Link System (SGLS), a network of ground telemetry sensors used by the Air Force to track its space assets.

In order to assess the metric performance of the sensor, routine on-orbit metric calibration is conducted. This is accomplished by observing satellites for which the positions are well established and by comparing these known positions with SBV-observed positions. During the design phase of the SBV program, the goal of producing 4-arcsec (1-sigma) metric observations of RSOs was set. This 4-arcsec error budget is comprised of a wide variety of error sources, ranging from the estimated position of the sensor on-orbit to systematic uncertainties within the established star catalogs. This 4-arcsec goal has been met, with improvements in these results likely to be realized (Ref. 4 and 5).

In addition to gathering metric observations of targets, the SBV also acquires photometric observations simultaneously. As mentioned earlier, intensity and pixel coordinates for streaks detected on RSOs are downloaded into the SBV Processing Operations Control Center (SPOCC) as part of the routine telemetry stream. The intensity information is used to determine an average brightness for the target during the data collection. The brightness of an object is quantified by the so-called SBV magnitude, a logarithmic scale, with larger numbers representing dimmer objects. The reader is referred to Ref. 6 for details on the processing of SBV photometric data and on the value they offer to space surveillance.

SBV ACTD OPERATIONS

The success of the demonstration phase of the SBV led to interest on the part of U.S. and A.F. Space Command into the use of the SBV as a Contributing Sensor to the SSN for deep space surveillance. This transition from an experimental sensor to an operational sensor was achieved by means of an Advanced Concept Technology Demonstration (ACTD) program through joint funding from the Office of the Secretary of Defense (OSD), the BMDO and U.S. Space Command. The transition began in October 1997 with its completion in April 1998. The function of a Contributing Sensor to the SSN, as with any member of the Network, is to gather observations on targets requested from AF Space Command's 1st Command and Control Squadron (1CACS) in Cheyenne Mountain. On any given day, a so-called tasking list is sent out to the sensor site and, in a timely manner, the site is to respond to the list. A detailed discussion of daily operations of the SPOCC and the SBV will now be given.

Contributing Sensor Operations

The problem of space surveillance is separated into two classes, that of low altitude surveillance and that of deep space surveillance. Low altitude surveillance involves the acquisition, tracking and cataloging of any RSO with a period of 225 minutes or less, while deep space surveillance performs the same tasks for objects with periods greater than 225 minutes. Acquiring and tracking object in low altitude are addressed quite adequately with the use of phased array radar. These radar are often designed to form a fence, such that any object that passes through the fence and is within the range of the radar will be detected, and metric observations will be gathered. While these radar serve low altitude surveillance well, they are not able to address the deep space surveillance problem. In addition, the network of ground sensors has limited capacity and coverage for deep space tracking and, as a consequence, a significant coverage gap existed in the eastern hemisphere of the geosynchronous belt. For these reasons and since SBV has coverage of the entire geosynchronous belt, the sensor was designed to focus on the problem of deep space surveillance.

The operational philosophy of the SBV, as described below, takes the characteristics of the sensor and the constraints of its platform into account. Further, the software that operates the SBV both on the ground and in space is tuned to optimize the productivity of the system by exploiting the advantages while minimizing the impact of the constraints. The means by which this occurs is through the ground operations with the SPOCC and at the Applied Physics Laboratory at Johns Hopkins University (APL), which is responsible for MSX satellite bus and subsystems. The ground network, which allows for communications between 1CACS and the SPOCC and between the SPOCC, APL and the MSX/SBV, is shown in Figure 4.

Daily SPOCC Operations

The operation of the 1CACS-SPOCC-APL network functions in the following manner. Space Command's First Command and Control Squadron generates tasking at the Space Control Center (SCC) and forwards it to the SPOCC located at Lincoln Laboratory. This transmission occurs via the communications node at the Millstone Hill radar. Upon receipt of the tasking list, the SPOCC schedules operations and generates SBV/MSX commands, which are sent via electronic link to APL for upload to the satellite. Once the commands have been uploaded, the process of data collection begins. These data on targets are acquired by the SBV and the results are stored in a RAM buffer in the instrument, until the next available 1 Mbit/sec downlink.



SBV as a Contributing Sensor

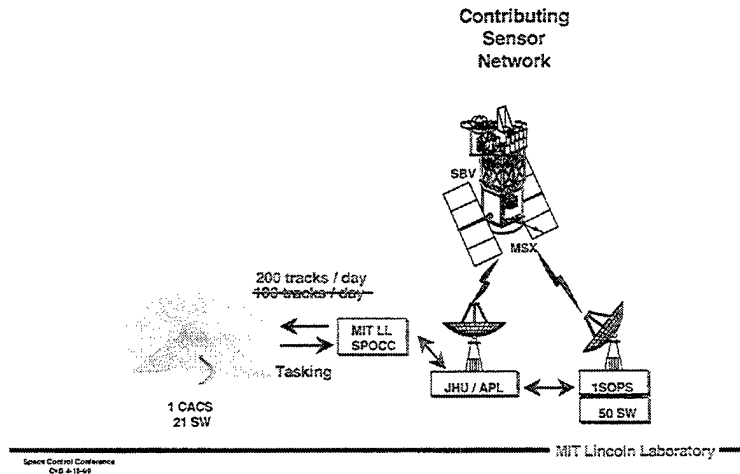


Figure 4. MSX / SBV Ground Network

The data are then sent to the SPOCC for the processing of the observations. The right ascension and declination positions on the tracked targets are then sent to 1CACs in Cheyenne Mountain via the same Millstone communications link that was used to distribute the tasking. In addition to the generation of the observations, the SPOCC is also responsible for establishing the MSX ephemeris and for monitoring the health and status of the SBV. It is the combination of the right ascension and declination positions of targets and the MSX ephemeris at the time the data was gathered that comprise a complete "observations". This entire process occurs 8 hours per day, 7 days a week, with one day a week permitted for routine maintenance and development. It is performed in a highly automated way, with only minimal staffing required. During off-hours the operators are paged by an automated monitoring system, should a problem with the SBV of the SPOCC system arise.

Unlike with ground-based sensors, there is no real-time access to the SBV. The data collection events must be planned ahead of time and sent to the Operations Planning Team at APL. The commands are checked to assure that the safety of both the sensor and the spacecraft will not be jeopardized by that day's activity. The planning for a day's event actually starts six to eight weeks earlier, with a process known as Monthly Planning. The planning is then refined at the weekly level, with the actual set of commands being created at the daily level, in response to that day's tasking list. This process is an artifact of the early phase of the mission, when the spacecraft was shared between eight Principal Investigators. Nonetheless, the goal of distributing observations within a 24-hour window from the latest possible tasking time was set prior to commencement of operations. Figures 5 shows that this goal has been achieved. This timeline is comparable to the response time for a GEODSS site, which must wait for night-fall to gather observations.



Timeliness of Tasking Response

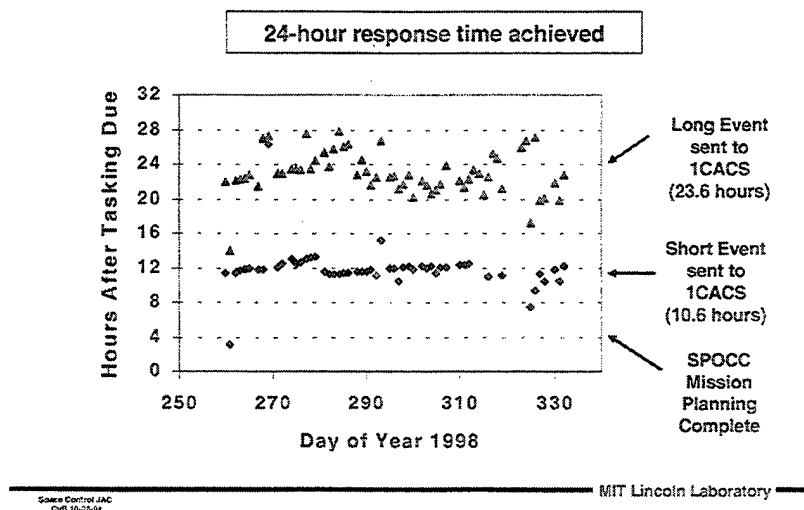


Figure 5. Operational timeline for the SBV as a Contributing Sensor

Since the SBV resides on a 6,000-lb. satellite, re-positioning the platform from one attitude to another is a rather slow process. This is illustrated by the following timeline for a single frameset of data collection:

Re-orienting the satellite to the desired attitude: 3 – 5 minutes
Data collection: 12 – 25 seconds
Signal processing of the data: 35 seconds
Orienting the satellite to the next desired attitude: 3 – 5 minutes

It is clear that operating in this mode is quite inefficient. As a consequence, two techniques were developed to help mitigate this effect. Firstly, an important piece of software that is used for choosing some optimal scheduling of objects was re-designed with the strengths of SBV in mind. The Conjunction-Optimized-Look-Ahead Scheduler (COLA) takes the submitted tasking list of objects, which is to be utilized on any given day, and seeks out regions of space in which objects are in apparent conjunction. A conjunction is defined such that at least two objects are visible simultaneously within the same FOV. With this approach, SBV typically sees at least two objects per CCD, thus increasing throughput considerably. Secondly, attention has been given to accurately modeling how long maneuvers last, so that data collection can begin at the earliest possible moment after the spacecraft has settled from the slew. The impact of the new maneuver model on SBV's productivity can be seen in Figure 6.

The COLA Scheduler

As described earlier, the SBV is an inherently wide field-of-view instrument, with each CCD covering approximately $1.4^\circ \times 1.4^\circ$ and all four together covering a total field-of-regard of $6.6^\circ \times 1.4^\circ$. It is immediately evident that the SBV can use this strength to increase productivity when tracking objects in the geosynchronous belt. However, a small study indicated that conjunctions also occur between objects which

are in dissimilar orbits but which happen to be appear at the same point in the sky at some given time. This allows for increased productivity for non-geosynchronous deep space RSOs as well. The COLA scheduler was specifically written to take advantage of such conjunctions in scheduling, so as to maximize the sensor's productivity and enhance its utility to Space Command.

Space surveillance operations depend on timely and reliable data flow on observations of RSOs. Hence, it is vital to have 7-day/week availability of sensors. The SBV, under its previous paradigm as an experimental sensor, was operated 5 days/week, and only for short periods, typically of 20 minutes in duration. However, as a Contributing Sensor to the SSN, the SBV is operated 7 days/week, with one of those days reserved for maintenance and developmental activities.

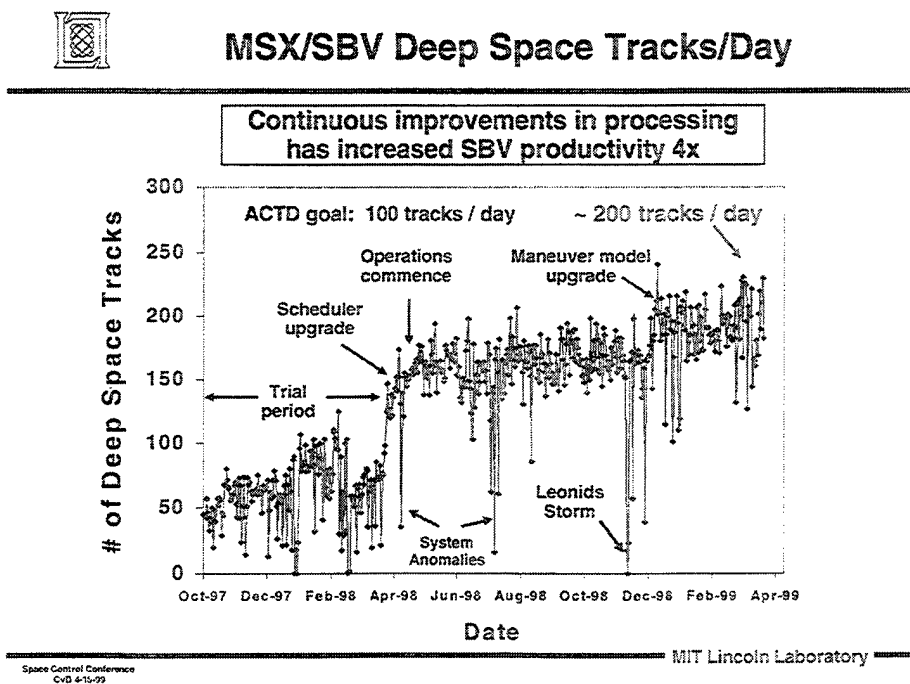


Figure 6. Effects of SBV productivity enhancements

The time series shown in Figure 6 gives the history of the SBV's productivity for the entire ACTD period. The first noticeable improvement in the productivity occurred when the COLA scheduler was implemented into operations. Prior to this time, the Space Surveillance Interface Processor (SSIP), with no optimization for conjunctions, was the standard scheduler used. The distinct improvement in productivity with COLA is evident in the figure in April 1998, shortly before SBV became fully operational. The second significant improvement in capacity occurred after the implementation of the new maneuver model. The goal of producing 100 tracks per 8-hour day during full operations was set for SBV. As of this writing, the SBV is supplying about 200 tracks per 8-hour day – clearly a result of a number of improvements undertaken to increase the productivity of the sensor.

SBV Geosynchronous Belt Surveillance

The SBV has two unique capabilities that make it well suited for surveillance of the geosynchronous belt. The first capability, as described earlier, is the wide FOV, allowing for multiple objects to be seen in one "look". The other characteristic of the SBV is that, being on orbit, it has access to the entire geosynchronous belt, as illustrated in Figure 7. In comparison, it requires at least three ground-based sensors to achieve full coverage of this orbital regime. With regard to SBV's coverage of the geosynchronous belt, a few comments are warranted. First of all, the SBV is restricted from looking within 80 degrees of the sun. This so-called dead-zone, as seen in Figure 8, restricts SBV's view of portions of the geosynchronous belt during certain times of the day.

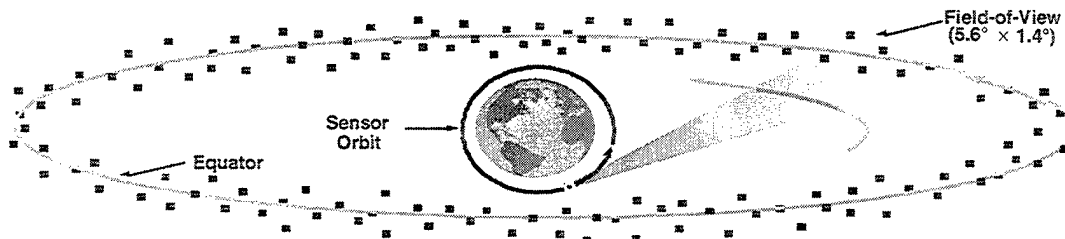


Figure 7. SBV's access to the entire geosynchronous belt

Given this restriction and that SBV is currently funded to operate for 8 hours per day, there is a well-defined region of the belt that SBV can not see during its observing periods. As a consequence, the placement in time of this 8-hour window will have significant bearing on which regions of the belt can be observed.

From April through November 1998, the SBV conducted operations based on two difference viewing periods, or Events, during the day. The first, or Short Event, commenced around 22:00GMT and

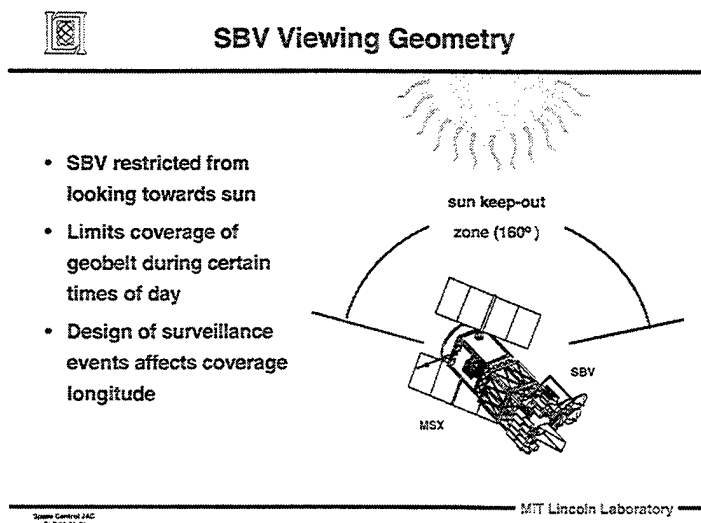


Figure 8. SBV Viewing Geometry



SBV Geosynch Coverage (Apr - Nov '98)

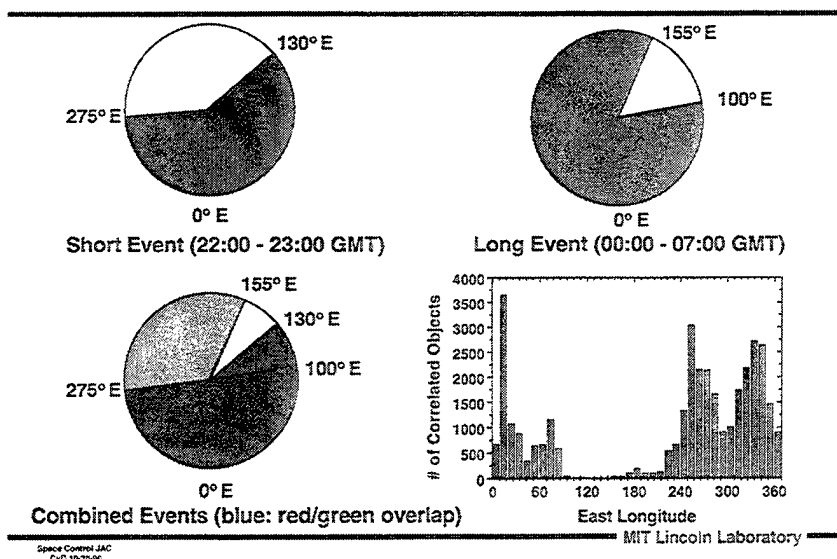


Figure 9 SBV Geosynchronous Coverage April - November 1998

ran for approximately 70 minutes until shortly after 23:00GMT, while the second event, the so-called Long Event, proceeded for nearly 7 hours, from approximately 00:00GMT until 07:00GMT. Figure 9 shows how the timing of these two events translates into regions on the belt. It is clear from this figure that, while the original choice of times allowed for coverage of most of the geosynchronous belt, a gap in which SBV could not track still remained. As a consequence, as of December 1998, two new times were chosen for these events, in order to fill this coverage gap within the belt. Figure 10 shows how this gap has been filled, now giving SBV total coverage of the geosynchronous belt.

Geosynchronous Search

With the capability to see the entire geosynchronous belt and with the sensor's wide field-of-view, the SBV is well-suited to conduct search scenarios through the geosynchronous belt. As a consequence, the SPOCC has dedicated at most 2 hours per day to searching the belt, with the remaining 6 hours devoted to SCC tasking response. From mid-September until early December 1998, the periods of time devoted to geosynchronous search were shared between both the Short and the Long Events. Search was conducted during the Short Event for approximately 1 hour, with the coverage ranging from 0° to 90° East longitude. The second hour of search was in the Long Event, with coverage between 220° to 310° East, as well as further coverage from 0° to 90° East. Commencing in December 1998, after the transition to two four-hour Events, coverage was shared equally in both the first and second Event. Before presenting the findings of these search studies, a description of the strategy and algorithms will be given.

First of all, it was mentioned earlier in the paper that SBV has four abutted CCDs, each with a FOV of $1.4^\circ \times 1.4^\circ$. Search of the geosynchronous belt can be conducted, either by aligning the array along the belt and by slewing the vehicle by approximately 5° steps across the region of interest, or by aligning the array perpendicular to the belt and by slewing the vehicle by approximately 1.5° steps. The former approach is used since it requires less motion of the 6000-lb MSX and because it allows for more rapid coverage. The only key advantage to aligning the array normal to the belt is that objects at inclinations between 0.7° and 2.8° can be detected. Figure 11 shows how the CCD array is oriented relative to the belt for routine search operations.

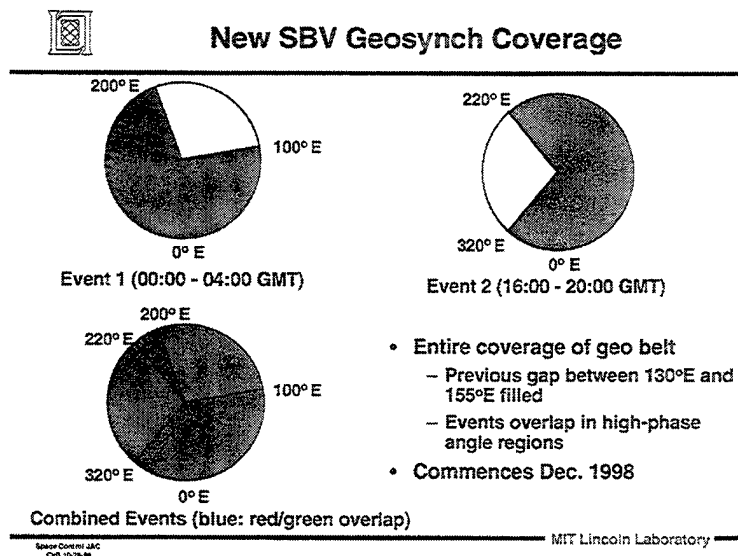


Figure 10. SBV Geosynchronous Coverage December 1998 – Present

It is well known that the ascending nodes of satellites in geosynchronous orbit tend to cross the equator in narrow regions of longitude. Since luni-solar perturbations induce a 53-year period in the inclination of these orbits, satellite owners tend to place the orbit node at specific locations, in order to control the direction of this perturbation. By choosing the launch window carefully, the maneuvers required to maintain the orbits can be minimized, thus increasing the lifetime of the spacecraft. This phenomenon is evident in Figure 11. It is partially for this reason that SBV's search region spans from 0° to 90° East and from 220° to 310° East. Concentrating on the regions around these nodal crossing will tend to maximize the observations gathered, since all geosynchronous and near-geosynchronous satellites cross the equator in this region. However, the region between 0° and 90° East was chosen for an additional reason. Prior to the deployment in southern Spain in mid 1998 of the Transportable Optical System (TOS), a Lincoln 0.5-m class electro-optical telescope also using CCD technology, a significant coverage gap of the geosynchronous belt existed within the SSN. As a consequence, a significant number of objects have been lost from the RSO catalog in this region in recent years. It was felt that SBV would be more successful at finding lost objects in this region than in any other along the belt. In fact, a total of 38 objects were discovered from November 1997 to December 1998, by means of both serendipitous observations during tasking, as well as observations gathered during search. For a more detailed explanation of how objects are discovered, based on new observations from SBV, the reader is referred to Ref. 7.

Preliminary results from geosynchronous search periods have revealed a number of findings. First of all, as was originally expected, the total productivity of SBV during a period of search was less than that during a comparable period of tasking. After analyzing a sample of 25 data collection events from SBV, it was found that, by devoting an average of 1.6 hours per 8-hour day to geosynchronous search in the regions prescribed above and with the approach mentioned, total productivity declined by 12%. Clearly, this value depends on the region of the sky surveyed, as well as the strategy used to search. However, under the same set of conditions, it was found that SBV was 1.5 times more efficient per unit of time at finding uncorrelated targets (UCTs). These UCTs frequently translate into the discovery of maneuvered and lost objects. Thus, under the given scenario, a sacrifice of 12% in overall productive is made for a 50% increase in efficiency at finding UCTs. Whether the benefits outweigh the losses, of course, depends



Geosynchronous Search

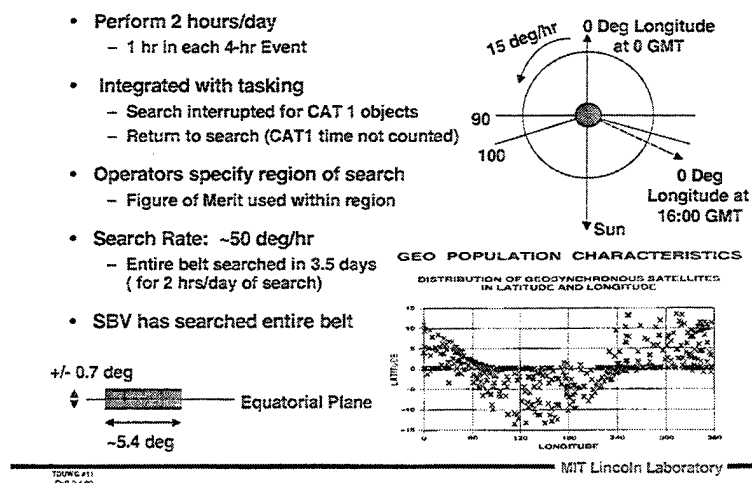


Figure 11. SBV Geosynchronous Search Strategy

entirely on the goals of the program. However, given that SBV is exceeding its overall productivity goals by about 100% (200 tracks per day, as compared with the goal of 100 tracks per day), and given that SBV is making a significant contribution to the discovery of lost objects, a 12% decrease production would seem to be a reasonable sacrifice for the increase in UCTs. It should be noted that this loss would likely be gained back, since significant steps are currently being made to increase the productivity of the SBV on other fronts.

SBV CONTRIBUTIONS TO THE SSN

Sensor Productivity

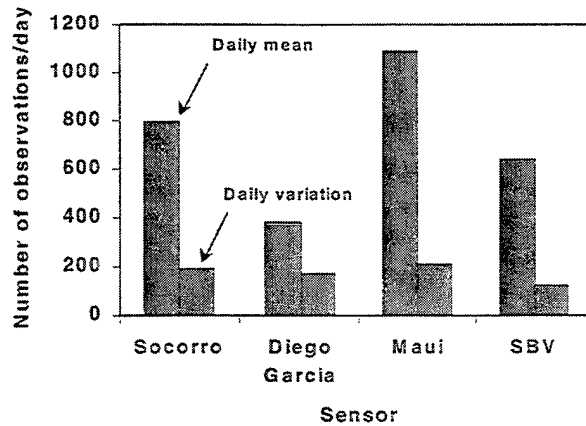
The impact of the COLA scheduler on overall productivity, as is apparent in Figure 6, has been substantial. This impact is even more striking when viewed in terms of SBV's overall contribution to the SSN. On this note, it would seem that the most relevant question, regarding any new sensor, pertains to how it performs relative to others within the network. This is addressed in Figure 12, in which overall productivity, in terms of total observations per day, is shown for SBV and the three GEODSS sites at Socorro, Diego Garcia and on Maui. The mean number of observations produced for each site is presented, as is the daily variation. The variation gives an indication of the reliability of a site at producing a steady stream of observations on a daily basis. It is most closely tied to weather conditions at the site, but can also be related to site operations. It is clear from these results that SBV is competitive with all three GEODSS sites, and that it has low variability on a daily basis. It should be noted that SBV is a single 15-cm telescope, while the GEODSS telescopes have 1-meter apertures and have multiple telescopes per site.

As mentioned earlier, the operations of SBV is focused on addressing the problem of deep space surveillance. Within that regime, a significant amount of SBV observing is dedicated to the geosynchronous belt. By combining this approach with both a wide field-of-view sensor and the COLA scheduler, the SBV can produce a significant amount of tracking data on objects within the



Comparison of Optical Sensors

MSX/SBV productivity comparable to an entire GEODSS site



Space Command JSC
CNS 10-25-98

MIT Lincoln Laboratory

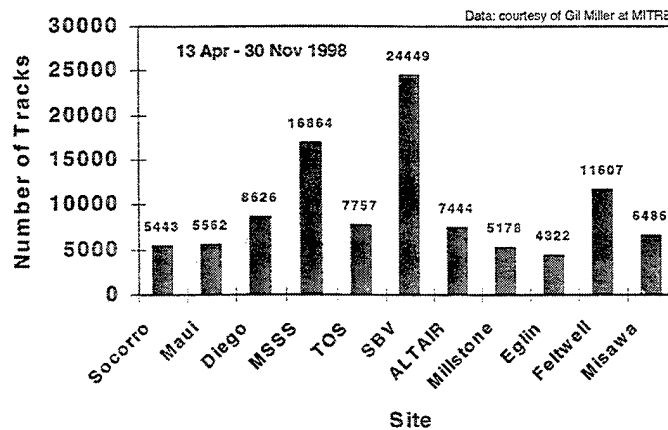
Figure 12. SBV Daily Productivity

geosynchronous belt. As a consequence, during its first 7 months of operations, the SBV gathered more observations on geosynchronous objects than did any other sensor within the network. This comparison is shown in Figure 13.

Finally, one of the most significant contributions that SBV has made to Space Command and the maintenance of the RSO catalogue is to the average age of an element set within the catalogue. The element set associated with any object in the catalogue is used to point sensors within the SSN to gather



Tracks on Cataloged Geosynch Satellites



Data: courtesy of Gil Miller at MITRE

SMO
CNS 12-15-98

MIT Lincoln Laboratory

Figure 13. Number of Tracks on Cataloged Geosynchronous Satellites by Optical Site (April - Nov '98)



Average Elset Age of Geosynch Objects

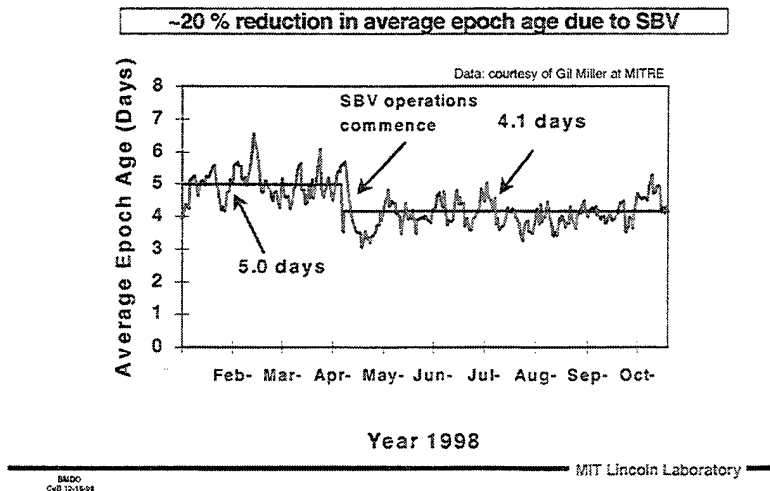


Figure 14. SBV's contribution to the average age of an element set within the RSO catalogue

more tracking data on that object. The tracking data from all of the sites are then merged and, after the orbit determination process is completed, the element set can be updated. If the element set is not updated in a timely manner, there is a risk that the pointing information that is sent to the sensors will not be of a sufficient accuracy to place the object with the FOV or beam-width of the instrument. If no sensor is able to find the object, its element set will continue to degrade and the object will be, effectively, lost from the catalogue. This can also occur if the object performs a significant maneuver and the sensors do not gather tracking data on it in timely manner. As a consequence, it is generally desirable to keep element sets updated frequently. This could be accomplished through more efficient use of existing SSN resources or by adding a sensor to the network. The latter was the case with SBV, and Figure 14 shows the impact on the average age of an element set, when SBV became operational in mid-April 1998.

Category 1 Tracking

Many years ago, the SCC established a hierarchical structure for the tasking of objects on any given day, so that it would be assured of gathering data on objects it considered most vital. This structure is based on categories, ranging from the most important (Category 1) to the least important (Category 5), with varying degrees given at each level. Based on this idea, Space Command tasks sensors on a daily basis with each object accompanied by a rating or category. Since Category 1 objects are established as being the most important to be tracked on any day, it is vital that each sensor within the SSN strive to achieve high performance in tracking these objects. Figure 15 shows the performance of SBV with regard to the daily tracking of Category 1 objects. Illustrated in the diagram is the number of Category 1 objects which SPOCC is tasked to track, along with the number on which observations were successfully gathered. Over the course of three months, SBV performed at greater than 90%, with regard to its response to these requests. This is in comparison with GEODSS sites which respond, typically, at the 20 – 50% level.



SBV CAT 1 Performance

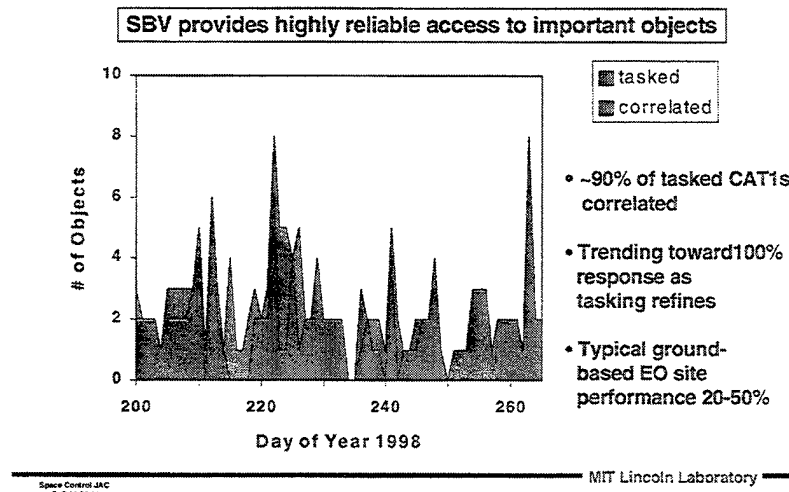


Figure 15. SBV's Category 1 Tracking Performance

SUMMARY

The Space-Based Visible sensor has achieved its primary objective of demonstrating space-based space surveillance operations. The success of the SBV in the technology demonstration phase has resulted in the sensor being incorporated into the operational Space Surveillance Network (SSN) as a Contributing Sensor. When operating as a Contributing Sensor eight hours per day, the SBV has proven to be as productive as a GEODSS site, with respect to the number of observations gathered. In addition, it produces considerably more accurate observations than does a GEODSS site. Further, the SBV has demonstrated the operation of a wide range of technologies, including staring focal planes, high off-axis rejection optics and on-orbit signal processing. An effective Concept of Operations (CONOPS) for space-based space surveillance has been developed, implemented in a highly automated way in the SPOCC, and validated under the current Space-Based Space Surveillance Operations (SBSSO) ACTD program.

The success of the SBV program has been the result of understanding the needs of the operational elements of Space Command and taking a systems approach to developing an effective solution to the needs of the Space Command operators.

REFERENCES

1. Stokes, G., "SBV Program Overview", *Proceedings of the 1997 Space Control Conference*, STK-249 Vol. II, MIT Lincoln Laboratory, Lexington Massachusetts, March 25-27, pp. 17-23.
2. Sharma, J., C. von Braun, E.M. Gaposchkin, "SBV Metric Data Reduction", *Proceedings of the 1997 Space Control Conference*, STK-249 Vol. II, MIT Lincoln Laboratory, Lexington Massachusetts, March 25-27, pp. 37-48.

3. Abbot, R.I., E.M. Gaposchkin, C. von Braun, "MSX Precision Ephemeris", *Proceedings of the 1997 Space Control Conference*, STK-249 Vol. II, MIT Lincoln Laboratory, Lexington, Massachusetts, March 25-27, pp. 63-71.
4. von Braun, C., J. Sharma, E.M. Gaposchkin, "SBV Metric Accuracy", *Proceedings of the 1997 Space Control Conference*, STK-249 Vol. II, MIT Lincoln Laboratory, Lexington Massachusetts, March 25-27, pp. 49-62.
5. von Braun, C., E.M. Gaposchkin, "Improvements to SBV Metric Accuracy Using Spacecraft Drift Corrections", submitted to the *AIAA Journal of Guidance, Control and Dynamics*, October 1998.
6. Lambour, R., R. Bergemann, C. von Braun, E.M. Gaposchkin, "SBV Space Object Photometry: Initial Results", *Proceedings of the 1998 Space Control Conference*, STK-253, MIT Lincoln Laboratory, Lexington Massachusetts, April 14-16, pp. 102-118.
7. Zollinger, G., M. Lewis, J. Sharma, "SBV UCT Automation", *Proceedings of the 1999 Space Control Conference*, MIT Lincoln Laboratory, Lexington Massachusetts, April 13-15

Contributions of the Space-Based Visible Sensor to Catalog Maintenance

J. G. Miller (The MITRE Corporation), W. G. Schick (ITT Industries, Systems Division)

The Space-Based Visible (SBV) sensor, built by Massachusetts Institute of Technology Lincoln Laboratory for the Ballistic Missile Defense Organization's (BMDO) Midcourse Space Experiment (MSX), was one of a suite of sensors on board the MSX satellite to collect data over a wide-wavelength range on ballistic missiles and the earth's background. When the infrared sensor's cryogenic coolant was depleted, the BMDO experiments were concluded. Not needing cryogenic coolant, SBV has become a contributing sensor to the Space Surveillance Network (SSN) as an Advance Concept Technology Demonstration (ACTD).

The Space Defense Operations Center (SPADOC) system was modified in vertical release 97-1 to process space-based observations, i.e., observations from a sensor on board a satellite. The Space Control Center (SCC) at Cheyenne Mountain Air Station began tasking the SBV sensor from SPADOC on 13 April 1998. The sensor tasking software in SPADOC was not modified to handle space-based sensors, but instead a set of fictitious ground-based optical sensors was added to SPADOC's database to simulate the global coverage of a space-based sensor.

Since the ACTD only provided for eight hours of operation six days a week, the visibility constraints of this schedule did not give the SBV sensor global coverage of the geosynchronous belt. Due to the time of the eight-hour period of operation, the SBV sensor could not see the geosynchronous belt from approximately 80 degrees east to 220 degrees east. Two fictitious optical sensors on the equator were entered in SPADOC's database to represent SBV's coverage. One was placed at 21 degrees east with a minimum elevation of 23 degrees. Its coverage of the geosynchronous belt is from 322 degrees east to 80 degrees east. The other ground-based sensor was placed at 271 degrees east with a minimum elevation of 31.6 degrees. Its coverage of the geosynchronous belt is from 220 degrees east to 322 degrees east. See Figure 1 for a depiction of the SBV sensor coverage. Although near-earth satellites are visible to SBV, it has only been utilized for deep-space satellites (periods greater than 225 minutes). Since 15 December 1998, the daily eight hours of operation has been changed to two separate four-hour periods of operation, with the effect of providing global coverage of the geosynchronous belt.

Table 1 shows the number of deep-space satellites on 31 December 1998, broken down by cataloged and analyst satellites and by orbit type. Figure 2 shows that the number of deep-space satellites has grown slowly in 1998. The number of analyst geosynchronous satellites (difference between the two lower graphs in Figure 2) is a small proportion of the total number of geosynchronous satellites. However, the number of deep-space analyst satellites (difference between the upper two graphs in Figure 2) is a large proportion of the total number of deep-space satellites. This is due to the Uncorrelated Track (UCT) processing at the Alternate Space Control Center (ASCC) from Naval Space Command Fence detections on deep-space objects with low perigee. The ASCC generates analyst satellites from these UCTs, and the SCC tasked them to the SSN for more observations from other sensors. If these analyst satellites cannot be maintained by observations from the SSN, they are deleted from the catalog when the epoch age exceeds 60 days. Such analyst satellites are constantly being added and deleted from the satellite catalog, and this accounts for the daily fluctuations in the upper graph in Figure 2.

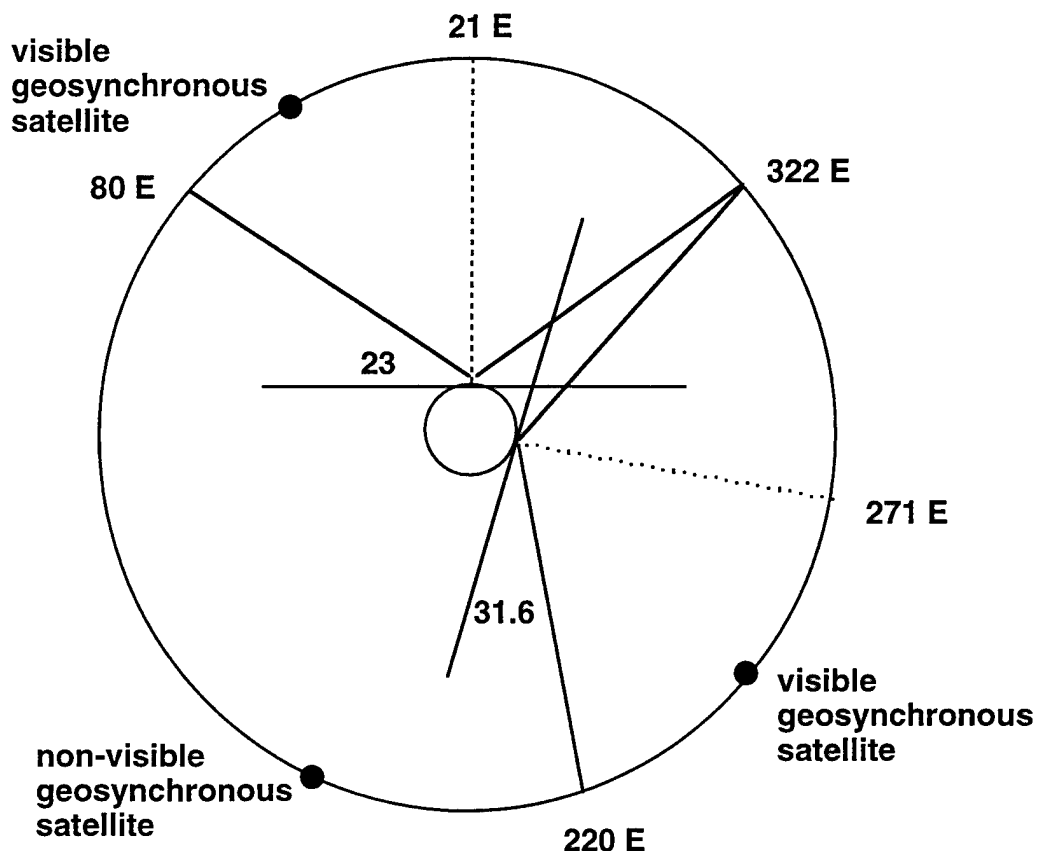


Figure 1. SBV Sensor Coverage

Table 1. Number of Deep-Space Satellites on 31 December 1998

	Deep-Space	Geosynchronous	Deep-Space Other
Cataloged Satellites	1772	711	1061
Analyst Satellites	883	102	781
Total	2655	813	1842

This paper attempts to show SBV's contributions to catalog maintenance. It is difficult to show how any one sensor impacts the satellite catalog. It is even more difficult to show that SBV has made significant contributions to catalog maintenance because the Transportable Optical Sensor (TOS) came on line in Moron, Spain at about the same time as SBV. The SCC began tasking TOS for observations on 18 March 1998. Figure 3 shows the number of tracks from SBV and TOS from their initial operations through 31 December 1998. TOS has contributed nearly as many tracks as SBV. With the addition of two new deep-space sensors to the SSN in 1998, one would expect improvements in the catalog maintenance of deep-space satellites. Our analysis shows that the SBV sensor has contributed significantly to improvements in the catalog maintenance of a subset of the deep-space satellites, namely geosynchronous satellites.

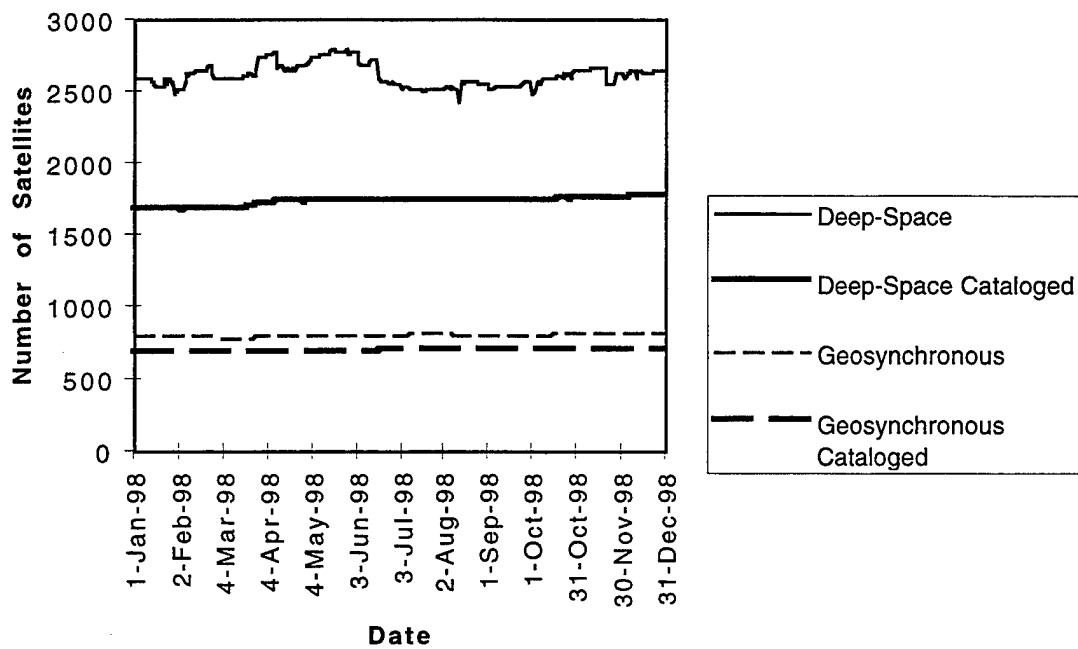


Figure 2. Deep-Space Catalog Growth During 1998

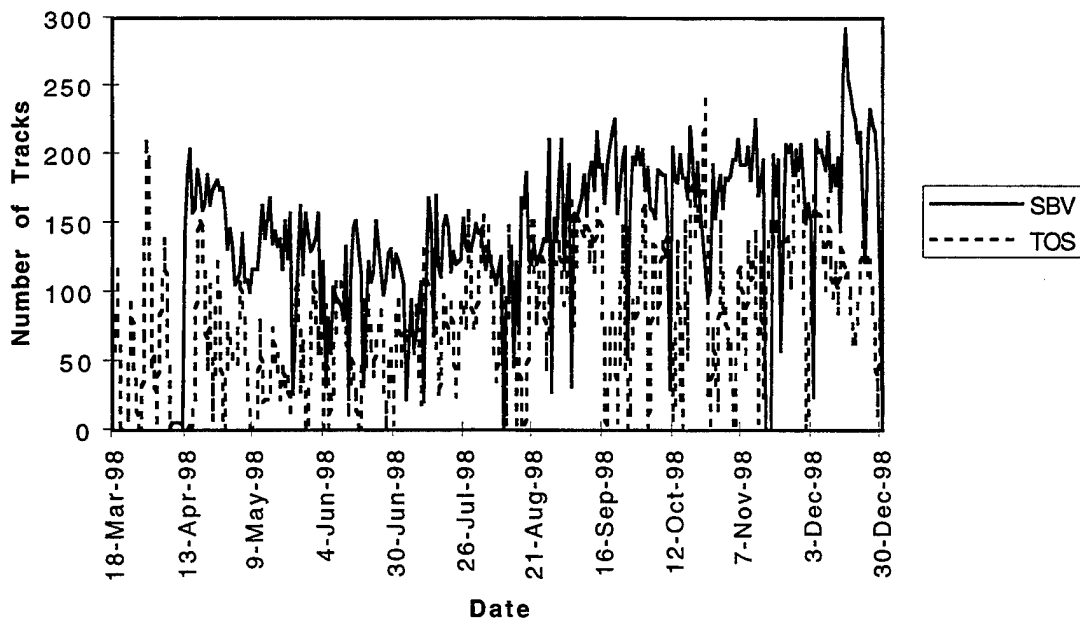


Figure 3. SBV and TOS Tracks

Figure 4 shows the contributions of each SSN site in tracking deep-space satellites from 13 April through 31 December 1998. The Naval Space Command Fence (NAV) and the Eglin radar have contributed by far the most tracks on deep-space satellites. However, most of the tracks in Figure 4 from these two sensors are on non-geosynchronous satellites. The contributions of TOS and SBV to tracking deep-space satellites are small compared to the rest of the SSN. Therefore, statistics on the deep-space subset of the satellite catalog have not significantly changed since the addition of TOS and SBV to the SSN. However, statistics on just geosynchronous satellites have shown improvements since SBV became operational. Sensors that can track geosynchronous satellites are the Eglin (EGL), Millstone (MIL), and ALTAIR (ALT) radars; the RF passive sites at Feltwell (FLT) and Misawa (MSW); the Ground-Based Electro-Optical Deep-Space Surveillance (GEODSS) sites at Socorro (SOC), Maui (MAU), and Diego Garcia (DGC); the Maui Space Surveillance System (MSSS); and TOS and SBV. Among these sensors, SBV's contribution to tracking deep-space satellites is second only to MSSS.

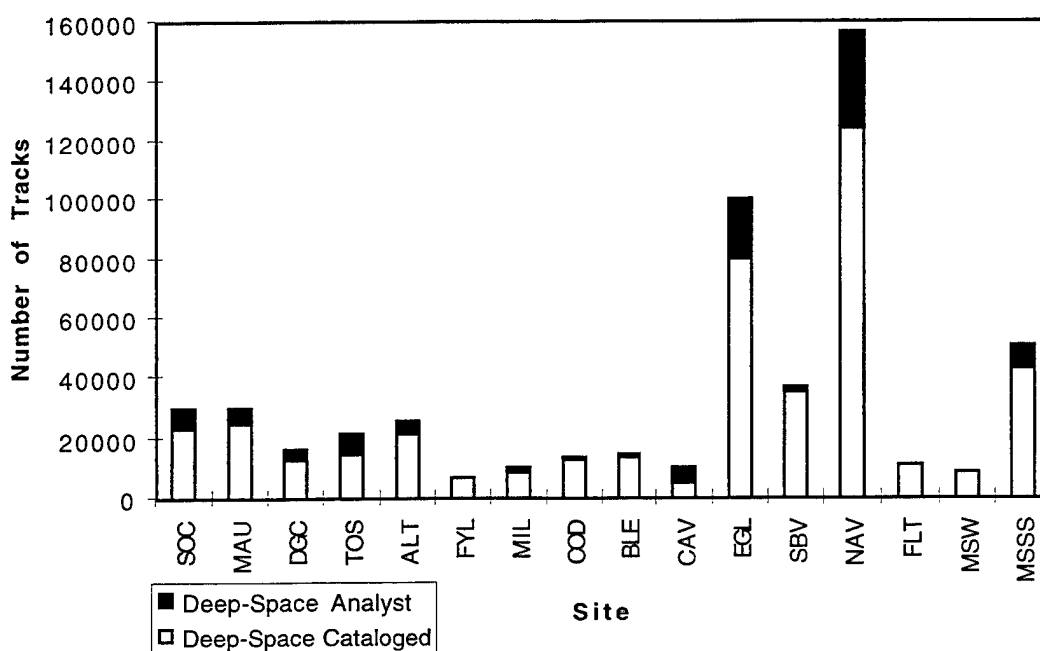


Figure 4. Tracks on Deep-Space Satellites from 13 April through 31 December 1998

Figure 5 shows the contributions of each site in tracking geosynchronous satellites from 13 April through 31 December 1998. SBV's contribution on this subset of the catalog exceeds MSSS, and is rather large compared to the rest of the SSN. Statistics on the epoch age and error growth rate of geosynchronous cataloged satellites show dramatic improvements after 13 April 1998 when SBV became operational. Figure 6 shows a drop in average epoch age of geosynchronous cataloged satellites by 0.8 days. Figure 7 shows a drop in the average number of geosynchronous cataloged satellites on the attention list (epoch age between 5 and 30 days) by 44 satellites. Figure 8 shows a drop in the average error growth rate (EGR) of geosynchronous cataloged satellites by 1.0 km/day.

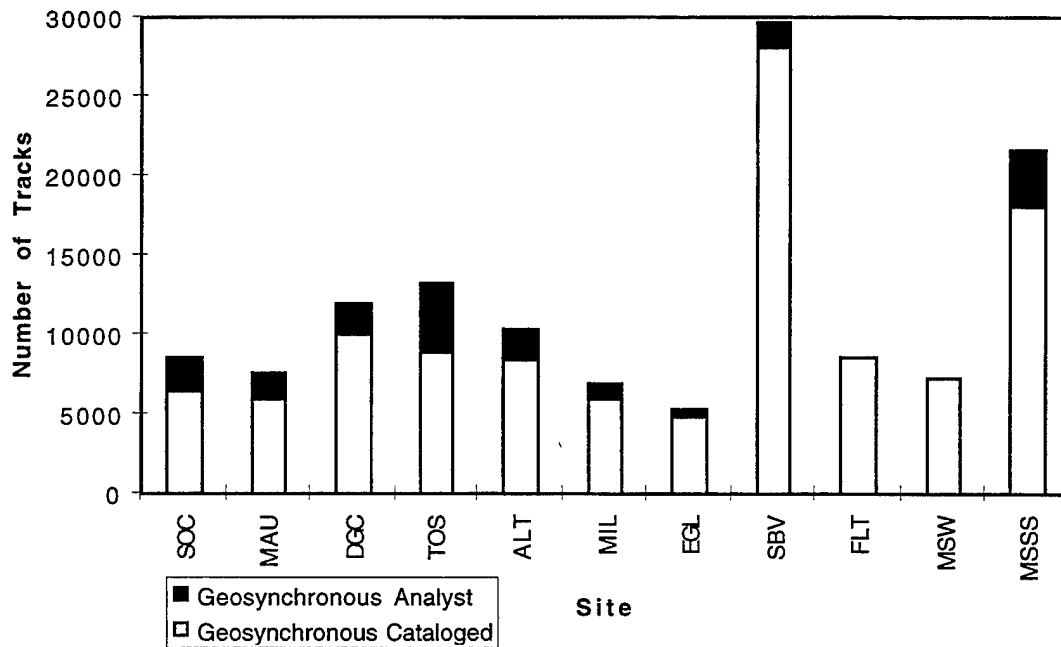


Figure 5. Tracks on Geosynchronous Satellites from 13 April through 31 December 1998

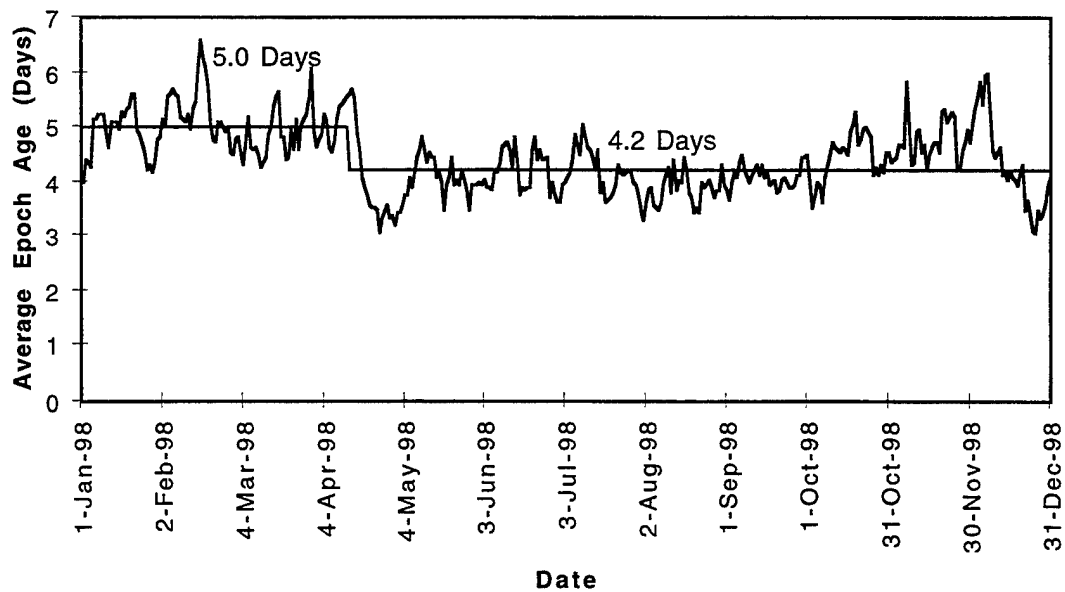


Figure 6. Average Epoch Age of Geosynchronous Cataloged Satellites

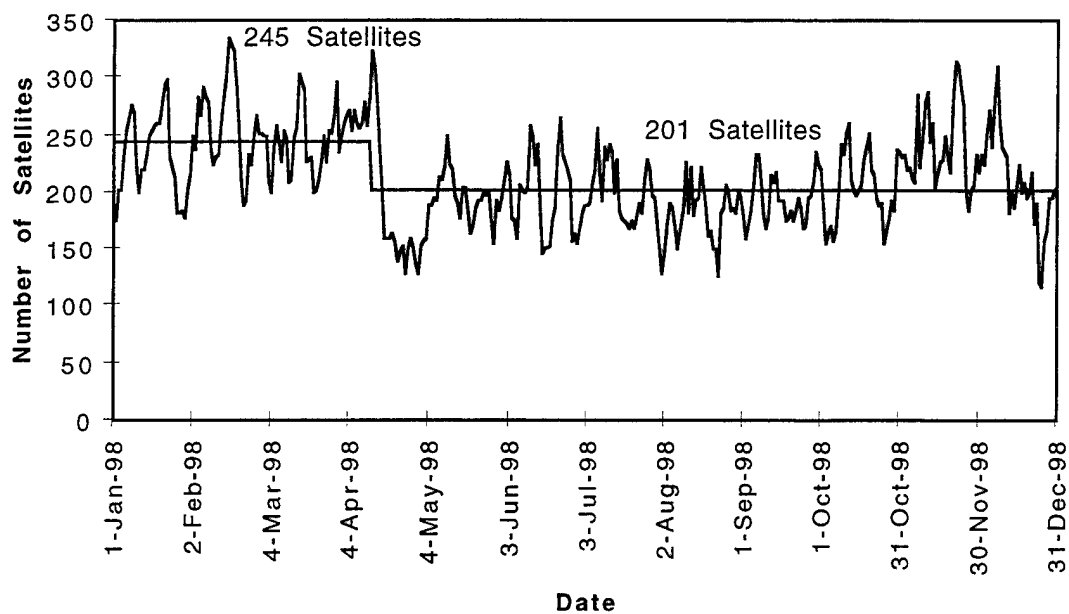


Figure 7. Number of Geosynchronous Cataloged Satellites on Attention List

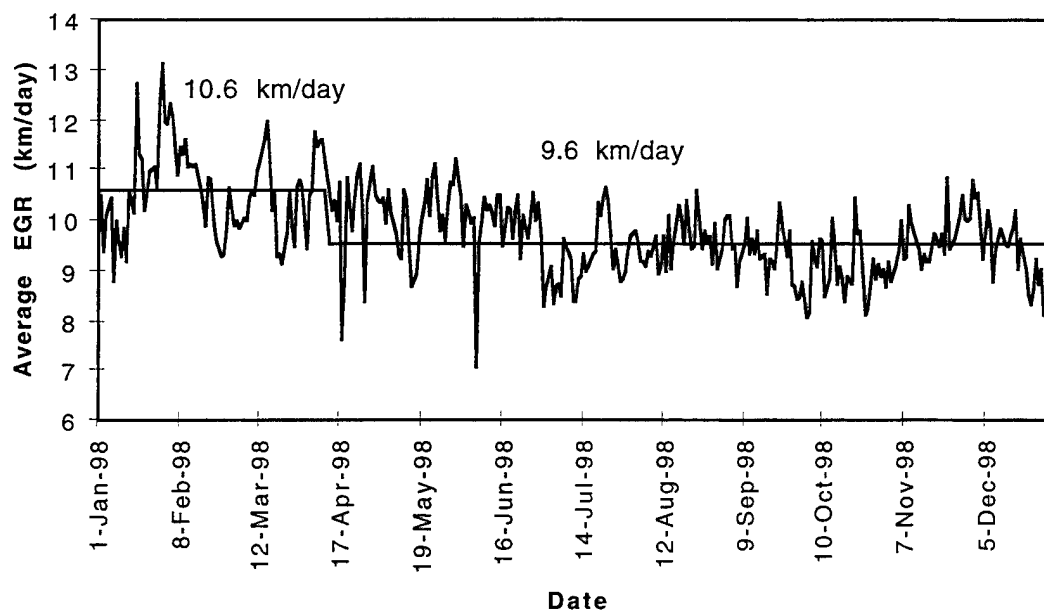


Figure 8. Average Error Growth Rate of Geosynchronous Cataloged Satellites

An EGR value for each satellite in the catalog is computed once a day in SPADOC using a previous element set and the observations from all sensors since the epoch time of the element set. The element set is propagated by Simplified General Perturbations 4 (SGP4) to the time of each observation, and the vector magnitude (VMAG) between the propagated point and observation is computed. A linear least-squares fit to the VMAGs is computed. The EGR value is the slope of the regression line, measured in km/day. The observations are also used in a differential correction to update the epoch time and element set parameters. The element set is saved for the computation of the satellite's EGR the next day as new observations are received by SPADOC. EGR is more a measure of the propagation errors of SGP4 than a measure of the observation errors of the sensors, although the latter does influence EGR. For a given EGR value, it would be difficult to separate the errors due to SGP4 and the observation errors of the sensors. Individual sensor errors are determined from the sensor calibration program developed by ITT.

The sensor calibration program uses reference orbits generated from laser ranging observations obtained from NASA's Crustal Dynamics Data Information System. Reference orbit fits of centimeter-level root mean square (RMS) are generated for Lageos 1 (SSC satellite number (SATNO) 8820), Lageos 2 (SATNO 22195), Etalon 1 (SATNO 19751), and Etalon 2 (SATNO 20026). Additionally, declassified Global Positioning System (GPS) precise ephemeris files are obtained from the National Imagery and Mapping Agency (NIMA) for GPS satellites 34, 35, and 36 (SATNOs 22779, 22877, and 23027, respectively). The deep-space sensors are routinely tasked to track these satellites, and observations on these satellites are compared against the reference orbits. Residuals are calculated against the reference orbits, using two weeks of sensor observations. The mean, one sigma standard deviation, and RMS of all the individual observables are computed from the residuals. Where sufficient observational data are available, the results (biases and sigmas) were very consistent for 1998. The average biases and sigmas for right ascension (RA) and declination for 1998 for each sensor are displayed in Figures 9 and 10, respectively. MSSS consists of three different telescopes, MOTIF(MOT), AMOS(AMS), and the Beam Directed Tracker (BDT). By far, most of the observations from MSSS are from the BDT telescope. AMOS did not provide sufficient observations to accurately determine its bias and sigma.

Note that SBV had no discernable bias for either right ascension or declination, while the other optical sensors definitely displayed biases, especially in right ascension. By accounting for sensor biases in the differential corrections of element sets, the biases can be removed. However, SPADOC does not use sensor biases in the differential correction of element sets, and the biases introduce errors in the differential correction process. The one-sigma standard deviations also reflect upon the quality of the observations going into the orbit determinations. Figure 10 shows that SBV observations are of higher quality than the ground-based optical sensors. This is consistent with the improvement in the average error growth rate of geosynchronous cataloged satellites since SBV became operational, as seen in Figure 8.

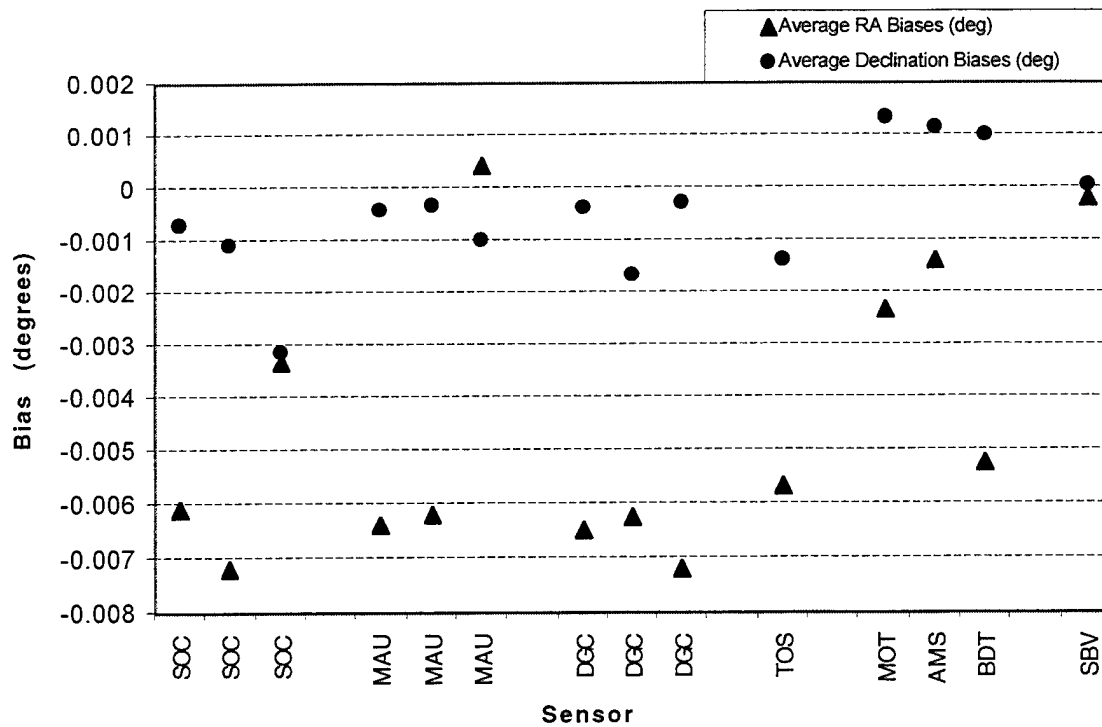


Figure 9. Average Biases of Optical Sensors for 1998

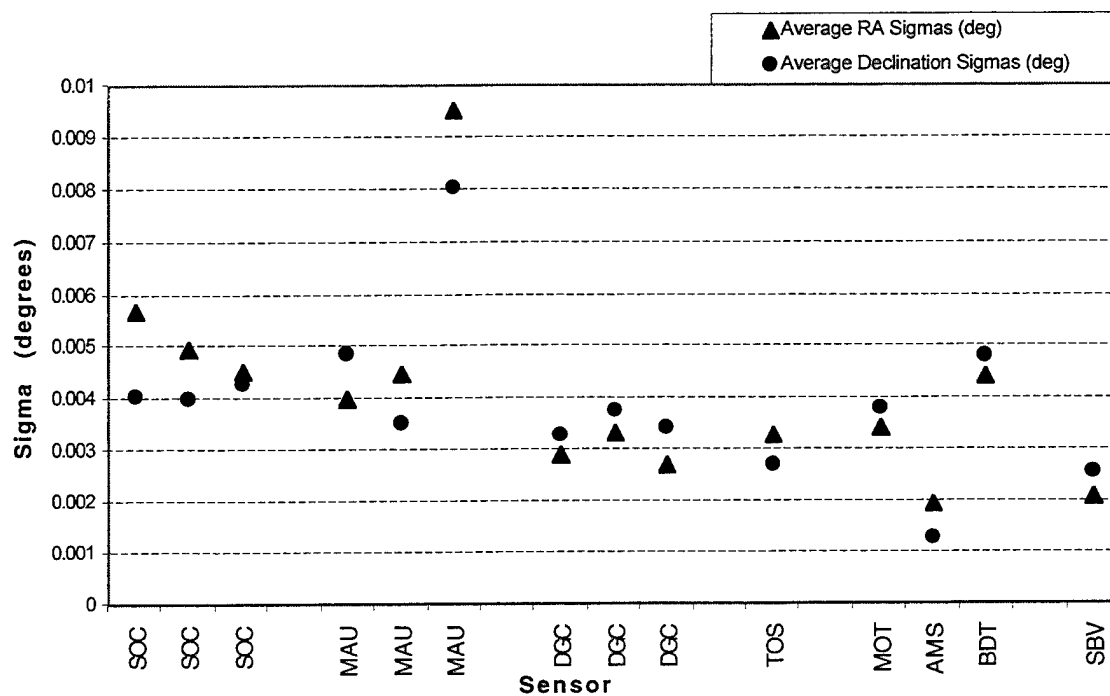


Figure 10. Average Sigmas of Optical Sensors for 1998

Finally, the optical sites' response to tasking is considered. After SBV was operational, Lincoln Laboratory developed a Conjunction-Optimized Look-Ahead (COLA) scheduler to optimize track throughput. The COLA scheduler gives higher priority to tasked objects that are on the focal plane of SBV at the same time, generating streaks on multiple objects from the charged coupled device (CCD). This produces tracks on multiple objects for the cost in time of one slew of the SBV sensor, which is done by reorienting the MSX satellite since SBV is not gimbaled. In order to provide SBV a large enough set of objects to feed the COLA scheduler with opportunities to simultaneously track objects, the sensor tasking from SPADOC was changed from 300 to 800 tracks per day. Beginning in September 1998, the increased track throughput of the COLA scheduler to over 200 tracks per day can be seen in Figure 3. Although SBV's percentage response to tasking decreased when the number of tasked tracks increased from 300 to 800, the actual track throughput increased.

There was some concern that the optimization in the COLA scheduler for simultaneous tracks would not appropriately consider the tasking category, which prioritizes the importance of the satellites to the user. In particular, category 1 tasking occurs on high priority satellites and a higher response rate from the sensors is expected. Lincoln Laboratory's COLA scheduler also prioritizes the satellites by category based on a weighting scheme to ensure the appropriate response on high priority satellites, even though this conflicts with the priority to get simultaneous tracks on multiple objects. Figure 11 shows SBV's response to tasking by category from September through December 1998. Although the number of tasked tracks on category 1 satellites is small, the percentage response has been high.

SPADOC tasked TOS for 250 tracks per shooting period (time site is in darkness). Figure 12 shows TOS's response to tasking by category from September through December 1998. TOS is also responding appropriately to category 1 tasking. TOS is not tasked for category 4 and 5 satellites because its capacity is filled by the time SPADOC attempts to task category 4 and 5 satellites. SPADOC orders the satellite catalog by tasking category before each daily tasking run. Although TOS's percentage response to tasking is higher than SBV's percentage response, SBV's track throughput is higher, as can be seen from Figure 3.

Figure 13 shows the track and observation throughput from SBV and TOS on deep-space satellites from September through December 1998, broken down by acquired tracks/observations in response to tasking and extra tracks/observations (either more tracks/observations than required on a tasked satellite or tracks/observations on an untasked satellite). The large number of extra tracks/observations from SBV is due to the fact that 2 hours per day are spent searching the geosynchronous belt and only 6 hours per day are devoted to responding to SPADOC's tasking. SBV has the greater track throughput, but the observation throughputs are nearly equal.

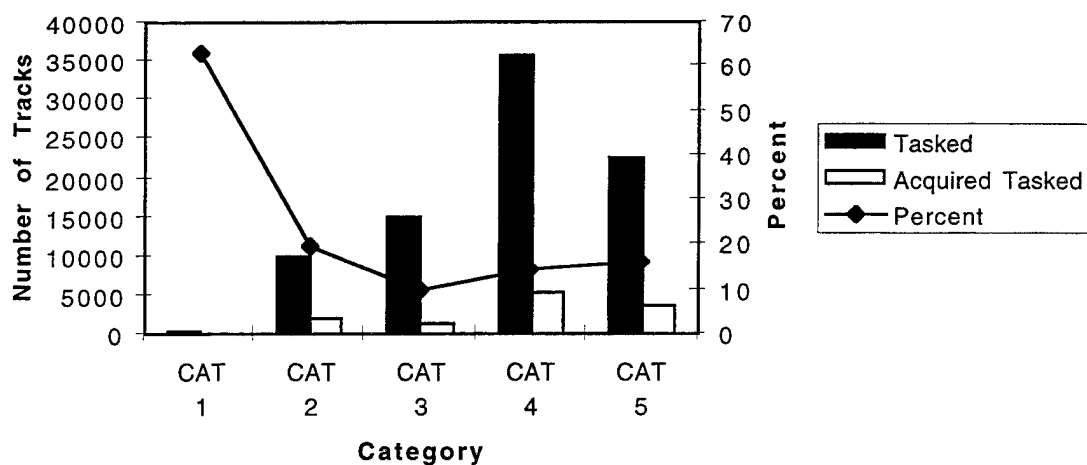


Figure 11. SBV's Tasking Response by Category from September through December 1998

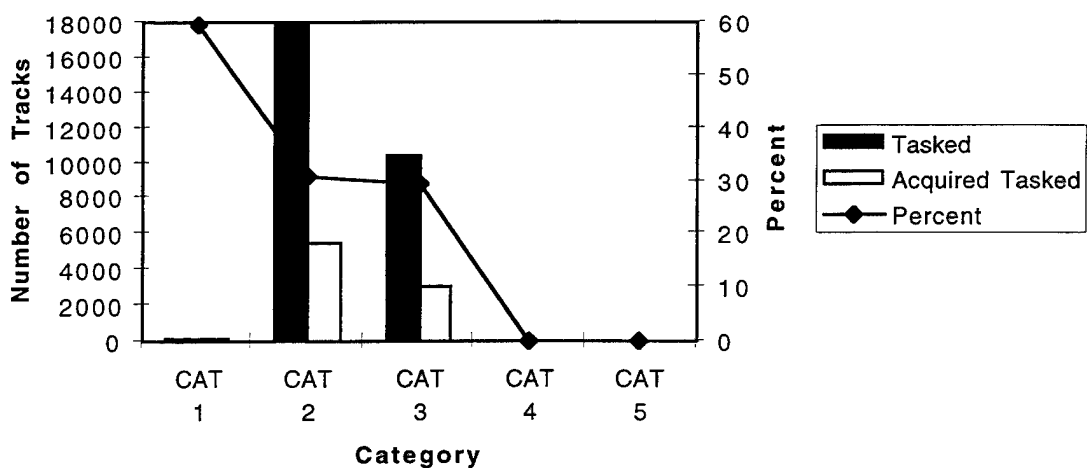


Figure 12. TOS's Tasking Response by Category from September through December 1998

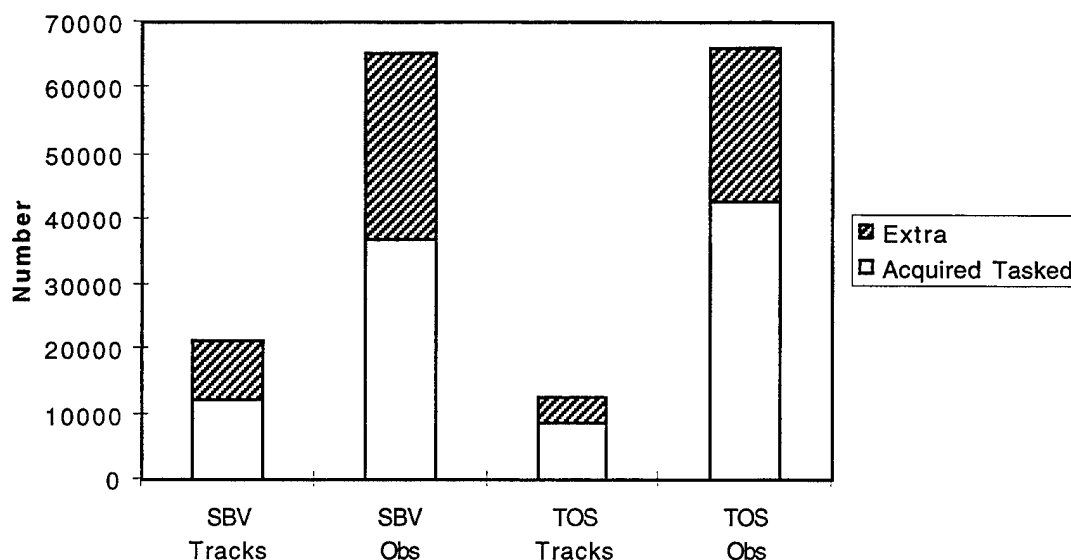


Figure 13. Track and Observation Throughput from September through December 1998

Figure 14 shows the histogram of SBV's observations per track from September through December 1998. SBV is being tasked by SPADOC according to Regulation 55-12, and the most commonly used tasking suffix by SPADOC requires 4 observations per track. Each streak on the CCD produces two observations, corresponding to the endpoints of the streak. To get the 4 required observations on a satellite, two streaks must be processed. Figure 14 shows that SBV is providing more one-streak tracks than two-streak tracks. Two reasons account for the one-streak tracks with only two observations: (1) two hours per day are spent searching the geosynchronous belt and the continuous scanning prevents acquiring the second streak, and (2) the COLA scheduler centers the focal plane array on the primary tasked object and the serendipitously tracked object may only be in the field of view for one streak.

The ground-based optical sites are being tasked by SPADOC according to UI 10-40, which superseded Regulation 55-12. The most commonly used tasking suffix used by SPADOC for the ground-based optical sites requires 5 observations per track. Figure 15 shows the histogram of TOS's observations per track from September through December 1998. Most of TOS's tracks contain 5 observations.

In conclusion, the SBV sensor has contributed to improvements in the statistics on the epoch age and error growth rate of geosynchronous satellites. Since SBV became operational, it has contributed more tracks on geosynchronous satellites than any other sensor in the SSN. SBV's track throughput has increased with the development of the COLA scheduler. SBV's observation throughput has been comparable to TOS's observation throughput. The accuracy of SBV's observations has exceeded the accuracy of the ground-based optical sites.

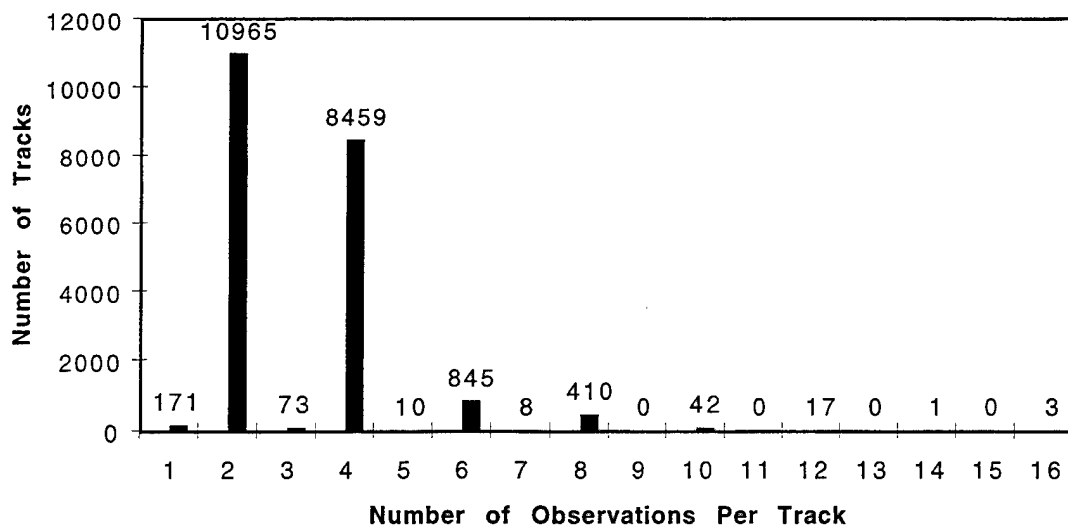


Figure 14. SBV's Obs Per Track from September through December 1998

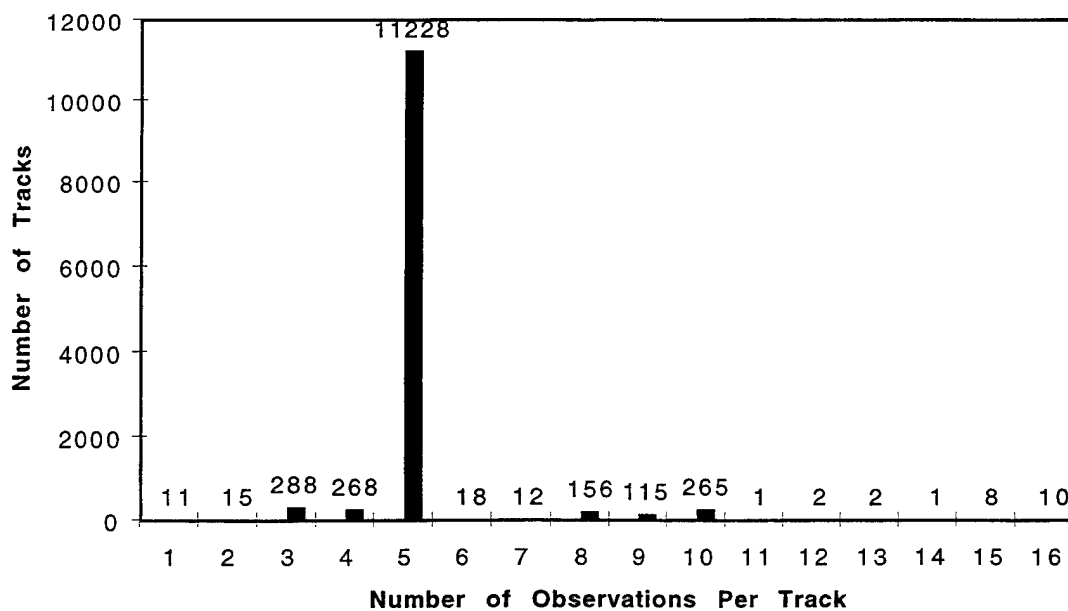


Figure 15. TOS's Obs Per Track from September through December 1998

SBV Uncorrelated Target (UCT) Processing

George R. Zollinger, Jayant Sharma, Marilyn J. Lewis
MIT Lincoln Laboratory

1. Introduction

MIT Lincoln Laboratory has built, and continues to operate, a space-based visible optical sensor (SBV) for space surveillance. SBV is being operated as a contributing sensor as part of the Advance Concept Technology Demonstration (ACTD) program. Work continues to extend and fully utilize the deep-space surveillance capabilities of SBV. One of these areas of research is a focus on the objects detected by the SBV which do not match known catalog objects, referred to as raw uncorrelated targets (UCT). The large (1.4x1.4 deg) field of view of the SBV sensor combined with its signal processor permits the simultaneous detections of multiple RSOs. The wide field of view also provides an inherent search capability that allow RSOs to be detected when they do not match the predicted location or are not in the RSO catalog. To take full advantage of this search capability, the UCT data have to be efficiently processed. This paper will describe the current capability at Lincoln Laboratory to process SBV UCTs. The goal of the processing is to identify the UCTs that correspond to known objects and to develop elements for UCTs that are uncataloged.

A pair of SBV observations, generated from the endpoints of a detected streak, is defined as a UCT if any one of the observations are not within 125 mdeg of the predicted position of a known resident space object (RSO). Raw UCT observations can be categorized as one of the following:

1. True UCTs: Observations that do not match any object in the current catalog of known space objects, and the UCT observations have been linked together to generate a new element set.
2. Catalog Objects: UCT is really a catalog object with an old or poor quality element set. Some of these objects may qualify as Lost Objects¹.
3. Unlinked UCTs: Detections that can not be linked together to generate element sets.
4. False Detections: Erroneous detections caused by factors such as spacecraft motion, radiation events, or signal processor anomaly

If a raw UCT can be identified as a catalog object, the element set's age and quality can be significantly improved. Figure 1 depicts a lost rocket body associated with a Meteosat payload found by the SBV. This figure shows the predicted and detected locations of satellites projected on the SBV focal plane. The Intelsat and NATO satellites predicted and actual locations are very similar and hence the data processing was able to generate correlated observations. However, there is a substantial difference in the actual and predicted locations of Meteosat. At the time, the element set for Meteosat rocket body was 38 days old. As the element set ages, the predicted location becomes less

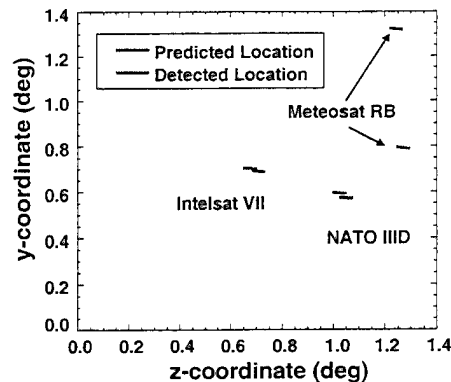
¹ A Lost Object is a RSO that has not been tracked in over 30 days.

accurate and does not match the detected location. In this case, initial data processing marked the Meteosat observation as a UCT, but UCT processing turned this observation into a correlated observation. The SBV is extremely useful in these cases because a large field of view creates the possibility of still detecting an RSO even if the actual location of



UCT Detection Results in Finding a Lost RSO

Satellite	SBV Magnitude	Age of Elset (Days)
Meteosat RB	14.5	38
NATO IIID	10.0	7
Intelsat VII	11.7	< 1



Wide field-of-view is instrumental in the recovery of lost objects

UCT Processing-4
GRZ 12/2/96

MIT Lincoln Laboratory

the object is far from the predicted one.

Figure 1. Lost object found by the SBV.

Once it was understood that not all raw UCTs are true UCTs but could be false detections or catalog objects, a series of tools and techniques were developed for filtering these UCTs into the appropriate category.

2. Historical Approach For Fitting UCTs

MIT Lincoln Laboratory has been a leader in space surveillance since the beginning of artificial satellites. In 1957 Millstone, operated by MIT Lincoln Laboratory, was the first radar to track SPUTNIK. Over the decades, a great deal of software and techniques has been developed for fitting and processing of observations (catalog or UCT). Two software packages have proven useful in processing SBV UCTs. The first program is ANalytical Orbit DEtermination (ANODE) and is primarily used to generate elements from observations. The second program is the UnCorrelated Target Processor (UCTP) and is used to identify observations by propagating all known element sets to the time of the SBV observation and displaying the resulting position differences. However, these tools require user interaction to input data and review the outputs for UCT processing. To improve the efficiency of UCT processing, repetitive analyst tasks were automated. The goal of the automation is to effectively identify UCTs that are readily identified as catalog objects or false detections, and allow the analyst to focus on linking UCTs and generating new element sets.

3. Improvements in Data Processing

Four key areas of software development for improved UCT processing are:

1. Data reduction filters
2. Automated element set generation (Batch ANODE)
3. Automated UCT processing
4. UCT processing tools

3.1 Data Reduction Filters

Data reduction is the process of taking signal processor data, which consist of star and streak detections, and reducing them into correlated metric observations². Data reduction examines each streak detected to determine if it is a valid RSO detection by examining the signature quality along the streak. This first filter removes detections that result from radiation events on the focal plane. Once a streak is considered valid, then data reduction attempts to fit the streak against the RSO catalog. If the streak does not match the catalog, then it is tagged as a raw UCT.

One of the early problems with this method was spacecraft motion. The SBV takes data by staring at a fixed star field and letting a satellite streak through the field of view. However, if the spacecraft is still moving while taking data, then the stars are moving and become detected as streaks. Figure 2 demonstrates a signal processor image where this has happened. In this image, there are 20 streaks detected³ and most of the streaks are the same length. Each of these streaks has excellent streak quality because the star intensity is consistent along the length of the streak. Since these streaks have excellent streak quality, early processing tagged these streaks as UCTs.

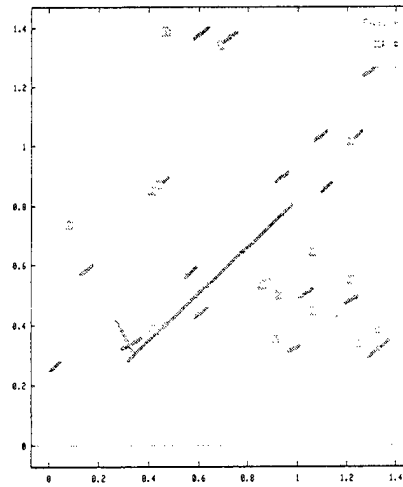
² For more information consult: Sharma, J., *SBV Space Surveillance Performance*, Proceedings of the 1998 Space Control Conference, Report STK-253, MIT Lincoln Laboratory, Lexington, MA, 14-16 April 1998.

³ There would be more but the memory limit for detected streaks is 20, which is a reasonable limit considering the record number of satellite detected is 9.



Data Reduction Filters

- Excessive spacecraft motion results in stars streaking through the focal plane
- Data Processing used to consider these streaks UCTS
 - this was responsible for the about ~40% of all UCTS detected
- Improvements
 - Data Reduction can identify star motion UCTS as false streaks.
 - new maneuver model prevents spacecraft motion during imaging.



UCT Processing-8
GRZ 12/2/98

MIT Lincoln Laboratory

Figure 2. Effects of spacecraft motion.

The effect of a large number of raw UCTs detected due to spacecraft motion can be seen in Figure 3. This plot shows the ratio of data that is considered UCT data. Near the beginning of the year, spacecraft motion caused the number of UCTs detected daily to reach almost 30%. Once the problem of spacecraft motion was understood, a second filter was set up to recognize these streaks as star motion and tag them as false detections. This modification significantly reduced the variability of the number of UCTs detected.



Percent of SBV Data that are UCTs

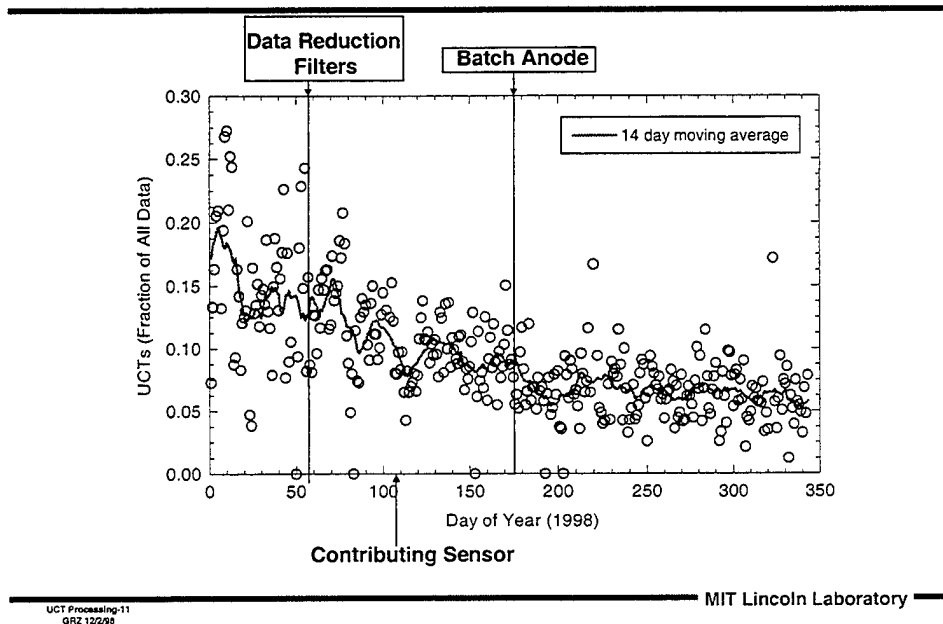


Figure 3. Fraction of SBV data that are UCTs.

3.2 Automated Element Set Generation

The quality of an element set can play an important role in the process of correlating a streak to a catalog object. If the quality of an element set is poor, then the streak will not correlate and becomes a UCT. One key factor in element set quality is the amount of time since the RSO has been tracked, usually referred to as the age of an element set. If the age of an element set reaches five days, then it is called an attention list object because the accuracy of the element set has atrophied to the point that tracking the object is difficult. Therefore it is important to track RSOs frequently and to keep element sets current.

A program based on ANODE was designed to address this very problem by trying to generate new element sets every time an object is tracked. This program is known as Batch ANODE. A communication hub at the Millstone Radar augments this process of element set fitting with a wealth of data acquired from sites such as SBV, TOS, GEODSS, FPS-85, and ALTAIR. For every observation received at Millstone, Batch ANODE will attempt to fit a new element set.

Batch ANODE works as an automatic process which emulates the steps that a user would take to fit an observation using the software ANODE. This program takes into account factors such as the class of object (geo-belt, low altitude, high eccentricity) and how to weight the data quality of a given site. Following a series of recent improvements, Batch ANODE is able to fit element sets for approximately 87% of all deep space tracks (previous batch processing techniques yielded fewer than 50%). At any time, 72 % of the Millstone deep space catalog element sets are generated by Batch

ANODE and the remaining 28% are from other sources (typically Space Command). This is an inverse of the situation prior to the recent improvements where 40% of the element sets were from Millstone and the remaining element sets were from other sources.

Figure 4 displays the quality of the element sets created by Batch ANODE and the previous batch processing. The x-axis shows the correlation residuals for objects detected by the SBV (low correlation residuals are better). The y-axis displays the number of streaks correlated with that residual. The wide blue lines represent the previous batch processing with a mean residual of about 20 mdeg. The red thin lines show the results of the new Batch ANODE processing with a mean residual of about 10 mdeg, which is about 50% improvement in element set quality.

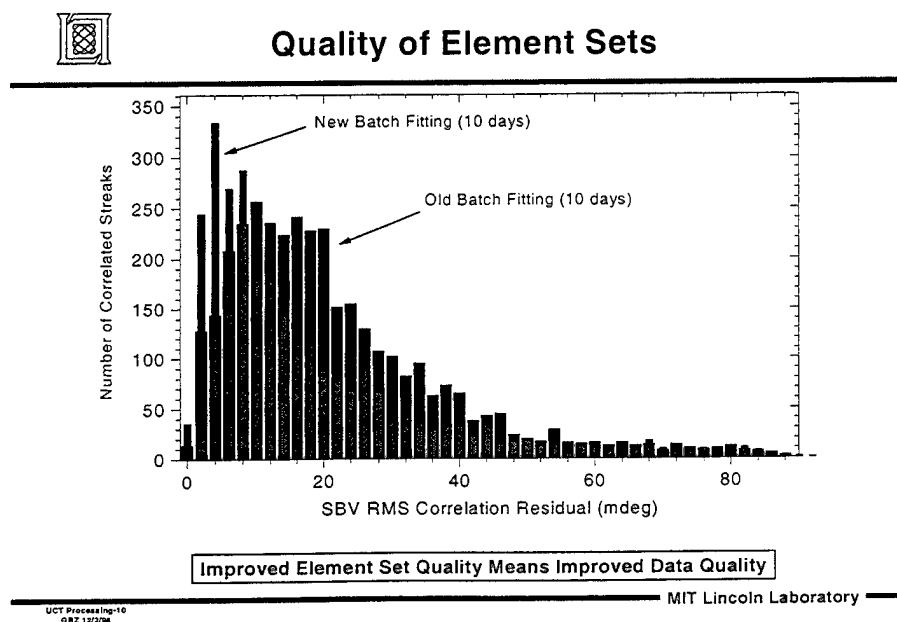


Figure 4. Quality of element plot.

The end result of Batch ANODE is up-to-date element sets with higher accuracy. These element sets improve the chances of correlating a streak to a catalog object rather than marking it as a UCT. Figure 3 shows when Batch ANODE was installed. At that point in time, UCTs represented about 10% of all SBV daily data. This plot shows a downward trend in the ratio of UCT data to total observations. Currently, the combination of data reduction filters and Batch ANODE has reduced this ratio to about 5%.

3.3 Automated UCT Processing

The previous two sections cover how to prevent routine data reduction processing from mistagging a streak as a raw UCT. These methods are an improvement but still there is 5% of SBV data that is tagged as UCT, and these UCTs fall into the three categories outlined in the introduction. These next two sections deal with automation and tools built to supplement the existing data reduction processing.

The automated UCT processing uses the UCTP program to generate candidate objects for the identity of the UCT and summarizes the results for an analyst. This program is executed when the data arrives and is processed at Lincoln Laboratory. Normally this processing is done outside normal working hours, and the results are ready to be reviewed at the beginning of each day. The automated UCT processing attempts to categorize all UCTs as one of the following:

1. Catalog object
2. False detection
3. Best guess catalog object

The best guess given by automation represents the object that best fits the UCT but has a correlation problem. This problem could be as simple as the fact that the correlation residuals are above a certain threshold or that the UCT is moving faster/slower than the matched catalog object. Another difference is that UCT Automation UCTs are sent directly to the User tool (see next section). Hence UCT Automation is performing standard steps followed by a user and will make a recommendation as to what it thinks a UCT could be, but ultimately it is the user's decision about retagging the UCT observation.

While this type of automation may seem limited, there are several things to consider. The first is that this automation improves the speed of hand processing by a factor of ten. The second is that Data Processing Filters and Batch ANODE remove the easily filtered UCT cases and leave the harder cases like Lost Objects. The final reason is that UCT Automation has the ability to automatically retag UCT observations, but this ability is deliberately inactive because this program is a relatively recent development; and there is still a need for more experimental data about its performance. It is important to ensure that UCT Automation is running correctly with few or no mistagged observations. Automation successfully identified almost 50% of all UCTs, and manual processing in the same time frame identified 67% of the UCTs.

3.4 UCT Processing Tools

The historical method for fitting UCT observations revolved around interactive programs using text based inputs and outputs to display information. The wealth of information generated by SBV and its unique status as a space-based sensor led to the development of graphics based tools. These tools were developed in a web environment and were designed to allow users access to the data in an easy to use GUI, combined with a series of applications that lets the user evaluate and retag UCTs. The use of a web browser as an interface ensures ease of access and portability. The primary goal of this tool is to separate UCTs into the appropriate category, so if a UCT is a catalog object, then that observation should be tagged and sent to Space Command.

The first key feature of this tool is the ability to show what is in the same field of view as the UCT. This feature is demonstrated in Figure 5. This image shows what was in the field of view around the UCT 99787. In this image there are 4 detected streaks.

The first three streaks match the predicted location of catalog objects. The fourth streak, however, deviates substantially, about .2 degree from any predicted object. Looking at this image, one would correctly assume that the UCT is 25492.

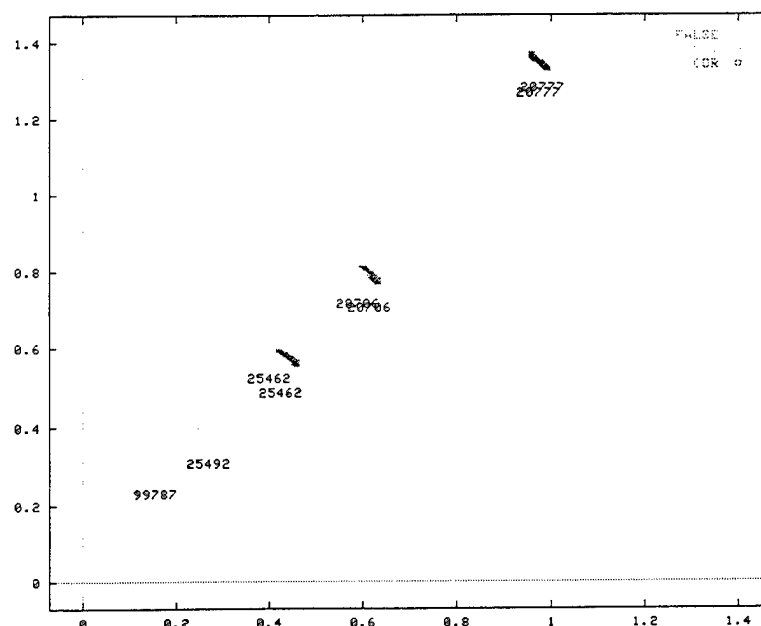


Figure 5. Typical SBV field of view image.

Figure 6 shows some additional information that is displayed alongside each signal processed image. The first column displays the results of hand processing which in this case selected 25492 as a match for the UCT 99787. The second column is the results of UCT automation which also picked 25492 as the candidate object. Looking at the age column, 25492 has an age of 4.9 day, which accounts for the error in the predicted location. If the user clicks on the UCT in the ID column, the detail results from UCTP can be seen (Figure 7). This fit shows the correlation residuals of each object in the field of view⁴. This is the exact same screen that fitting a UCT by hand would show, but with the key difference that the UCT Automation has saved the analyst a long series of manual operations that must be repeated for all the UCTs.

⁴ Showing all of the correlation residuals can be important if the user disagrees with the candidate picked via automation.

UCT	AUTOFIT	CATEGORY	ID NUMBER	Magnitude	Phase	Range	LAT	LONG	Rate	Streak	Sig	AGE
		OBJ	25462	11.88	70.4	39941.7	-0.023	28.184	4.4	1	1	1.10
		OBJ	20777	13.02	71.3	39814.3	-0.005	29.119	4.4	2	2	1.00
		OBJ	20706	12.54	70.7	39934.2	-0.044	28.466	4.4	3	3	1.10
25492	25492 -0.148000 0.008000	UCT	92787	13.5			0.021	27.789	4.3	1	1	
		VIS	20777	11.80	71.3	39814.3	-0.004	29.134	4.3			1.00
		VIS	20706	12.70	70.7	39934.2	-0.020	28.457	4.3			1.10
		VIS	25462	12.60	70.4	39941.7	-0.011	28.171	4.3			1.10
		VIS	25492	12.50	70.1	39951.4	0.015	27.927	4.4			4.90

Automation Recommendation

Results of Hand Processing

Figure 6. UCT tool information screen.

DAY 334 TIME 02:31:53			NUMBER OF OBJECTS:18075			CURRENT DAY 334 TIME 10:59:43		
MEASURED VALUES AND <+/-BOUNDS>								
SITE	RA	DEC	RANGE	RDOT	RADOT	DECDOT	LONGITUDE	LATITUDE
ID	(DEG)	(DEG)	(KM)	(M/SEC)	(MDEG/SEC)		(EAST)	(NORTH)
LSC	130.28	-8.66			-0.1	4.3	28.24	0.96
<+/->	1.26	1.25	50.000	125.00				
OBJNO							[R]	XSEC WIDTH EPOCH MATCH
20706	-0.714	0.049	(39864)	(-6000)	0.0	4.4		334.00
25462	-0.408	0.038	(39872)	(-6000)	0.0	4.4		332.90 *YES*
25492	-0.148	0.008	(39882)	(-6000)	-0.1	4.4		329.10 *YES*
25491	1.056	0.047	(39881)	(-6000)	-0.2	4.4		329.13
ORBITAL UPDATE ERROR, ID: 10422 10423								
>>> Closest Satellite: 25492. Vector Magnitude Difference: 102.14 Km. <<<								

Figure 7. Typical UCTP output.

If this information was not sufficient information for retagging the UCT, the tool enables the user to link multiple UCT either by searching looks where a specific RSO should be or via observations taken at the same longitude using the interface in Figure 8. The geocentric latitude and longitude of an UCT is calculated by mapping the UCT observation on to sphere with a radius of 42,164km. With the position of SBV known, it is possible to complete the triangle shown in Figure 7b, and to calculate the earth fixed coordinate.

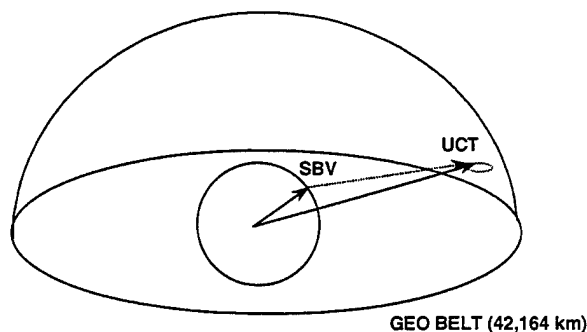


Figure 7b. Calculation of UCT latitude and longitude.

From this interface, the user can view the images such as displayed in Figure 5. But more importantly, if the user can link several UCT observations together, a new element set can be created and used to collect additional data. An element set is useful in identifying the object as maneuvered or relocated object or a previously uncataloged object. Figure 9 displays some of geosynchronous objects that were detected by SBV as UCTs, and were subsequently identified by generating an element set from the UCT observation. In the last year alone, the SBV has found 38 lost objects (2 uncataloged objects), and this is an important contribution to maintaining an accurate catalog of RSOs.

UCT color code Correlates in a cluster duplicate streak correlates but could be a false streak

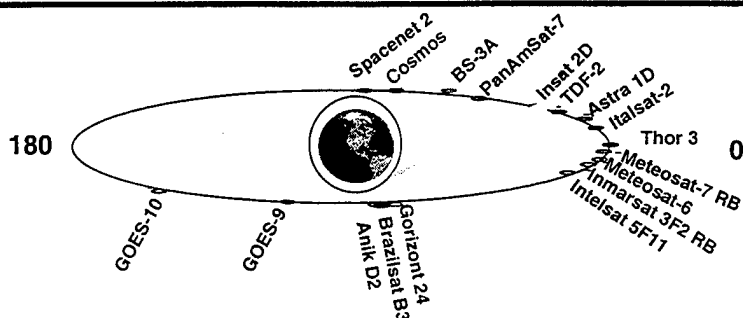
rate problem bad res

Pick	Look Num	Status	Auto Status	UCT id	Magnitude	Rate	Streak ldx	Lat	Long	Year	Day	Hour	Min	Sec
<input type="checkbox"/>	237021	12183	12183 -0.046000 -0.131000	99794	12.2	9.7	3	1.238	256.185	1998	334	7	6	53.364
<input type="checkbox"/>	237020	12183	12183 -0.040000 -0.146000	99793	12.2	10.0	4	0.698	256.838	1998	334	7	6	6.358
<input type="checkbox"/>	236985	11304	11304 -0.003000 -0.019000	99791	9.8	109.9	1	-2.167	263.107	1998	334	6	13	1.363
<input type="checkbox"/>	236951	false	false	99789	10.9	12.6	1	0.047	248.917	1998	334	5	20	45.370
<input type="checkbox"/>	236934	5216	5216 0.019000 0.006000	99788	10.6	169.3	1	-2.190	264.483	1998	334	4	54	37.364
<input type="checkbox"/>	236846	25492	25492 -0.148000 0.008000	99787	13.5	4.3	4	0.021	27.788	1998	334	2	31	42.364
<input type="checkbox"/>	236845	25492	25492 -0.147000 0.008000	99786	13.8	3.9	1	0.019	27.788	1998	334	2	30	53.367
<input type="checkbox"/>	236777	4598	4598 -0.012000 -0.136000	99783	7.2	135.2	3	1.021	1.896	1998	334	0	46	21.366
<input type="checkbox"/> object is secret	object: <input type="text"/>			<input type="checkbox"/> don't append obs		<input type="checkbox"/> do a fit, skip fit		<input type="button" value="run job"/>		<input type="button" value="Reset"/>				
<input type="checkbox"/> object is unclassified														

Figure 8. Linking multiple UCTs together.



Lost Objects Found by the SBV



SBV discovered/recovered 38 objects in the last year

UCT Processing-17
GRZ 12/2/98

MIT Lincoln Laboratory

Figure 9. Lost objects found by the SBV.

The last major feature of this application is that it can retag and transmit observations from the SPOCC to Space Command, which is the ultimate goal for using this tool.

4.0 Success of Hand Processing

Versions of the UCT tool have existed since the SBV became a contributing sensor in April of 1998. The early versions did not have the full range of applications possessed by the current version, but when combined with UCTP, it enabled analyst to begin processing raw UCT data.

During this time period from Day 103 to 337 of 1998 there were

- 3993 Raw UCTs detected (about 17 UCTs per day)
- 2888 of these UCTs were retagged by hand (72.3% total UCTs) where
 - 446 true UCTs (11.1%)
 - 1951 catalog objects (48.9%)
 - 491 false detections (12.3%)
- 1105 Unlinked UCTs (27.7%)

The end result of this fitting is that 60% of all raw UCTs are being retagged as a catalog object or true UCT, and are sent to Space Command. Overall this means that UCT processing has improved the observation throughput by about 3%. By identifying UCTs, the age and quality of the object's element set can be significantly improved. This improvement prevents objects from getting lost, and represents an important contributor to an accurate catalog of RSOs.

5.0 Success of UCT Automation

Processing UCT observations automatically with UCTP is still a relatively recent software installation of the last forty days. Since this is an evolving process, the automation is running in a suggestion mode in which it recommends a candidate object for each UCT detected. The reason for this caution is the desire to prevent mistagging of catalog objects.

However, the early results for UCT automation are promising, as shown in Figure 10. The first row represents what fraction of the raw UCTs was categorized. Automation was able to come up with possible identifications of almost all of the UCTs, but the bulk of these identifications were the best guess case. Best guess means that Automation has a possible correlation with a catalog object, but there is a problem with that correlation (poor residuals, rate problem, etc.). The second row is the number of true UCTs. Currently, automation does not have a technique for categorizing raw UCTs as true ones. The other two areas: UCTs retagged as False Detections or Catalog Objects shows that hand processing outperforming UCT automation by about 38%.



Comparing Automation Versus Hand Processing

- Timeline: Day 306 to 337 of 1998
- 501 Raw UCTs

CATEGORY	MANUAL PROCESSING	AUTOMATED PROCESSING
Tagged	339 (67.7% of UCTs)	490 (97.8%)
True UCTS	24 (4.8%)	0
FALSE DETECTIONS	85 (16.9%)	57 (11.4%)
CATALOG OBJECTS	230 (45.9%)	169 (33.7%)
Best Guess Case	0	264 (52.7%)

UCT Processing-18
ORZ 12/2/94

MIT Lincoln Laboratory

Figure 10. Comparing automation versus hand processing.

The statistics in Figure 10 reflect the fractional breakdown of the amount of processing performed by both Automation and Hand processing. However, it does not cover how often the two methods disagree. When comparing UCTs categorized as false detections by UCT automation, in every case, hand processing agreed with automation. When comparing the UCTs tagged as catalog objects, there were seven cases (automation mistag rate of 4%) where the two methods disagreed. These seven mistags were the result of two factors: One candidate was an object in a dense cluster where it becomes hard to

correctly identify the UCT as to which is the correct cluster object. The second reason for disagreement occurs when hand processing picked an object not in the field of view of UCT Automation. This is the result of an analyst having special knowledge about an RSO such as that an object has maneuvered to a certain longitude or is station-kept. Currently this information is not available to UCT Automation and hence it cannot make correctly correlate in such cases.

When comparing the automation best guess case with hand processing, there are 31 additional cases where hand processing agrees with UCT automation. This means that UCT Automation has correctly identified 49.9% of all UCTs detected, as opposed to 67.7% tagged via hand processing.

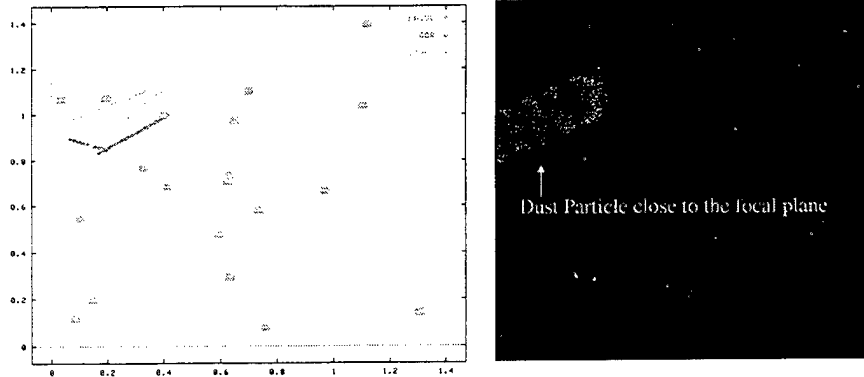
6.0 Additional UCT Processing

The current methods for processing UCTs still leave 28% of the observations unidentified. Work is continuing to utilize these remaining UCTs. The first goal is to identify UCTs as possible geosynchronous objects. SBV primarily performs observations on geosynchronous objects, and has had more success in collecting multiple observations on geosynchronous UCTs. The UCT processing tool allows the user to mark UCTs as likely geo-belt or nongeo-belt UCTs. If a UCT is a geo-belt object, SBV can collect additional data on the UCT by looking near the same longitude. An element set can then be generated by linking together multiple UCT observations. It is more difficult to link together observations on objects with smaller orbital periods (< 24 hr), but in a few instances SBV UCT data has been used to generate element sets for high eccentricity objects that pass near the geo-belt.

Work is also ongoing to ensure that the SBV data quality remains high and that the UCTs represent valid detections of RSOs. As previously mentioned, UCTs resulting from radiation events and spacecraft motion are currently being identified. It is vital to ensure that UCT observations are valid for effective processing of the UCT data. Recently an interesting, but small, source of UCT data has been identified. The SBV is an optical telescope focussed at infinity. When a dust particle (micron sized) appears in the telescope's field of view a few meters away from the focal plane, it is not in focus and results in a moving diffuse image being projected on the focal plane. Figure 11 shows an example of dust detection. The image on the right shows an intermediate level image generated by signal processor, and the image on the left show the output streak detections from the signal processor. The signal processor extracted 4 streaks from this data set. Two streaks were determined to be valid, and were labeled as UCTs. The diffuse characteristic of a dust detection produce streaks with a more uniform intensity distribution than streaks generated by RSOs. Currently it is possible for the analyst to identify detections due to dust particles. Preliminary indications are that these detections are responsible for at most a few percent of the SBV UCT data.



Non RSO Streak Detection



UCT Processing-23
GR2 12/2/98

MIT Lincoln Laboratory

Figure 11. Dust particle detection.

7.0 Summary

The SBV is another successful Space Surveillance sensor developed by MIT Lincoln Laboratory. The large field of view of SBV has an inherent search capability that permits the detection of RSOs that are lost or uncataloged, resulting in UCT detections. The ability to utilize the UCT data is important in preserving the accuracy of the catalog of RSOs. This problem has been attacked from several methods: improving element quality, false detection filters, automated UCT process, and new UCT processing tools. These successful methods were built upon the foundation of software and analyst techniques developed at other MIT Lincoln Laboratory sensors, but took a step further through the use of automated processing and graphic based web tools. These tools are responsible for SBV being a major contributor in finding Lost Objects and has improved the data quality and throughput of the system.

SBIRS LOW Adjunct for Space Surveillance

Ronald W. Sayer & Grant H. Stokes
MIT Lincoln Laboratory

Abstract

Currently, SBIRS LOW system is seen as the next generation objective Space-Based Space Surveillance sensor. Though designed for missile tracking, SBIRS LOW should have considerable capability for addressing many, but not all, Space Surveillance functions. This paper suggests the addition of an adjunct sensor to three of the SBIRS LOW satellites, which will conduct the Space Surveillance functions not expected to be inherent to the SBIRS LOW system. The suggested adjunct system is designed to observe the Deep Space population several times each day. The current design point for the adjunct will be sensitive enough to detect a 30cm diffuse sphere in the geosynchronous belt and will have a search capacity exceeding 3,000 square degrees per hour to a limiting magnitude of 17.3.

Introduction

The feasibility and capability of Space-Based Space Surveillance have been successfully demonstrated by the SBV system, both during a technology demonstration phase and as an operations demonstration under the current SBSSO ACTD (von Braun 1999). The SBV was constructed using technology that is now a decade old and since the late 1980's considerable advances have been made in the areas of staring focal planes, on chip stabilization and space qualified processors. Thus, systems with considerably more observation capacity could now be constructed, and point designs have been suggested for systems of free flyers dedicated to Space Surveillance (Stokes 1998).

Within the past year, Lt. General Dekok, then the commander of SMC, suggested that the appropriate way to conduct Space Surveillance from space was to construct an adjunct Space Surveillance sensor to be placed on some number of the SBIRS LOW satellites. SBIRS LOW is currently viewed as the objective system for operational Space-Based Space Surveillance; however, the SBIRS LOW is designed primarily as a missile tracking system and its Space Surveillance functionality has been viewed as an "as capable", low cost, add-on mission. It should be noted that since there are many similarities between surveillance of low altitude satellites and missile tracking, SBIRS LOW will have considerable natural capability for timely tracking of many important payloads and will have an unmatched capability for tracking new launches (Table 1). However, since the SBIRS LOW system is designed for primarily observing missile targets near the Earth, it has certain inherent deficiencies for some other important Space Surveillance tasks. These are:

- 1) The system is inherently down-looking, which makes Deep Space Objects difficult to schedule and observable only at extended ranges, and in the enhanced background near the earth;

- 2) The sensitivity of the SBIRS LOW tracking sensor may not be sufficient for doing Geosynchronous surveillance or for small satellites at any altitude;
- 3) The relatively small field of view of the SBIRS LOW tracking sensor makes searching a large area or searching for a specific lost resident space object more time consuming than desirable.

These Space Surveillance deficiencies could be approached in a number of ways:

- 1) Driving Space Surveillance requirements, which address the above issues, could be placed on the primary SBIRS LOW sensors – Exercising this option is likely to be more costly than practical and would result in more Space Surveillance capacity than justifiable due to the large number of SBIRS LOW satellites.
- 2) SBIRS LOW inherent Space Surveillance capability could be enhanced by a small number of dedicated satellites.
- 3) SBIRS LOW inherent Space Surveillance capability could be enhanced by a small number of adjunct sensors placed on a few of the SBIRS LOW satellites or some other host satellites.

It is the third of these options, specifically putting the adjunct sensors on a few SBIRS LOW satellites, that is addressed by this paper.

SBIRS LOW, it should be made clear, is not the ideal satellite to host the adjunct sensor. The high radiation environment is harmful to the sensor's long-term function; also, the prompt effects (detection of numerous radiation events on the focal plane) make the signal processing considerably harder (for the primary missile tracking mission also). In addition, the altitude of the SBIRS LOW sensors is higher than desirable for Space Surveillance operations. Given these issues with the non-optimal orbit, if a credible adjunct can be designed for SBIRS LOW, it will work on a broad range of host satellites.

Technology

As was mentioned above, considerable technology advances have been made since the era of the SBV construction. The technology available to the adjunct sensor package today (1999) is covered in Table 2 along with that in the SBV for comparison.

Lincoln Laboratory's GEODSS upgrade CCD technology will provide the sensitivity and large format necessary for Space Surveillance search operations. The CCD has high quantum efficiency (66% solar weighted) and a large number of pixels (2048 X 2048), necessary for maintaining high accuracy metric observation of Resident Space Objects (RSOs) over a wide field of view. In addition, new technology allows large format CCDs to be fabricated as orthogonal transfer devices. Orthogonal transfer means that the charge packets may be moved in either the X-axis or Y-axis during the integration of a frame to compensate for jitter in the sensor pointing. An example of the function of an orthogonal transfer CCD is shown in figure 1. On-chip stabilization allows the elimination of stringent bus stability requirements and allows the adjunct sensor to be compatible with a broad range of host vehicles.

A portion of the signal processing will require two special-purpose, but available, space qualified processors (such as a Mosaic020 by Daimler-Benz Aerospace). The rest of the computation requirements (sensor health and status monitoring, correlation with the catalog, catalog update, maneuver detection, etc.) of the sensor may be satisfied with a general-purpose, space qualified processor (such as a Lockheed Martin Federal Systems RAD 6000 processor).

Sensor Design

An initial design of the adjunct sensor has been made and is shown in Figure 2. The sensor contains a gimbaled, on-axis Cassigrain telescope, which is less expensive and considerably less massive than the off-axis design used in the SBV. The need to reject off-axis light is reduced for two reasons: the telescope need not look near the Earth since the SBIRS LOW track sensor will track the LEO objects, and the adjunct sensor will be operated such that it will not point within 90 degrees of the Sun. This last requirement will not hurt timeliness greatly since three sensors will be in three different orbital planes.

The telescope will have 9 inch diameter optics and be capable of detecting objects as faint as 17.3 visual magnitudes. This corresponds to detecting diffuse objects as small as 30cm (Appendix A) at the geosynchronous belt for typical reflectivities (0.3), phase angles (45 degrees), and sky backgrounds (22 visual magnitudes). The telescope has been designed with a field of view of 3 degrees X 3 degrees, which allows wide areas of the sky to be searched to find objects with old element sets, find new objects, or find lost objects. Given the format (2048 X 2048), the field of view of the adjunct sensor, and the SBV experience, metric observations with an accuracy of 2 arcseconds will be attainable. The comparison of the SBV and the adjunct sensor is as follows; the adjunct has a field of view that is roughly twice as large as the SBV and has roughly four times as many pixels as the SBV. The SBV attains 2 to 4 arcsecond accuracy at present (von Braun 1997) and is limited by the stability of the MSX bus. The adjunct telescope design has been engineered such that the percentage energy that falls into a single pixel from a point source is 60 to 90%, similar to the SBV. Thus, observations from the adjunct sensor should be twice as accurate as observations from the SBV.

Concept of Operations

The objective of the adjunct system is observation of all Deep Space RSOs several times daily with small gap times for almost all objects. An additional product of this system could be observations on demand.

In order to assess the capability of a system composed of three adjunct sensors on SBIRS LOW satellites, a simulation of the system was run. A very simple CONOPS was chosen as a vehicle to estimate of the system capability. The system was operated in a tasked mode for all areas of the sky except for a third (the section at the best solar phase angle) of the object-rich Geosynchronous belt, which was searched once per orbit of the adjuncts. The search could be accomplished using only 7% of the system resources,

leaving the other 93% for tasked operation. The tasking algorithm was quite simple but effective. A list of the entire deep space catalogue was made. A scheduling attempt was made for the first satellite on the list. If the satellite was successfully observed, it went to the bottom of the list. If it could not be observed, it maintained its position on the top of the list and the next entry on the list was attempted. After successfully observing an entry, the scheduler went back to the top of the list and started again. This "bubble sort" scheduling results in all of the objects on the list being seen and minimizes the gap times for difficult objects (such as high eccentricity objects whose apogee is at poor solar phase angles, or "in the sun"). This analysis assumed a step/settle/acquire cycle of 30 seconds. In addition, the signal processing time must be less than 30 seconds, which is credible based on the SBV experience scaled to the adjunct processor. Finally, the simulation treated a number of realistic constraints, such as maintaining an exclusion zone of 90 degrees from the Earth and the Sun.

System Performance

The performance of the 3 adjunct sensor system was assessed by running the numerical simulation across an interval of four days. During this time the system operated with an unclassified catalogue containing 1565 objects. Initially, the catalog is listed in a random order. The sensors then task detectable objects preferentially at the top of the list. An object is detectable if it is sunlit and does not require the sensor to look closer than 90 degrees to the Sun or the Earth. All Deep Space, cataloged objects that have current elsets should be large enough to detect with this sensor under these observing circumstances. Once an object is detected, it is moved to the bottom of the list. This tasking method is constructed to minimize the largest Gap Time of each Deep Space target.

The results of the four-day simulation are as follows: 1510 out of 1565 objects were detected at least every 15 hours (Table 3). The other 55 objects are high eccentricity objects; only 6 out of the 55 objects are active payloads, thus 316 out of 322 active Deep Space payloads were detected at least every 15 hours. Also, the average target object is detected 8.0 times per day (Figure 3). There were 12,370 detections per day, or 1.4 streaks on average per pointing. In summary, almost the entire Deep Space catalog can be maintained with several revisits to each object every day. Gap times for most objects are 15 hours or fewer (Figure 4).

Summary

Deficiencies in the natural SBIRS LOW capability for Space Surveillance can be addressed by a small number of adjunct sensors. These sensors, based on evolved SBV technology, could be made compatible with a wide range of host satellites, and impose few requirements on the host. The sensors could be made to operate on and provide considerable capability from three of the SBIRS LOW satellites even though the currently expected orbits of the SBIRS LOW constellation are not considered optimal for Space-Based Space Surveillance. The suggested SBIRS LOW adjunct system could observe almost all cataloged, Deep Space objects several times daily.

References

Opar, T.; Sridharan, R.; "SBV Experimenter's Guide", Project Memorandum No. 91PM-SPC-030, Lincoln Laboratory, August 1992.

Stokes, G.; Sayer, R.; "Space-Based Space Surveillance: Thoughts on the Next Step", Space Control Conference 1998

von Braun, C.; Sharma, J.; Gaposchkin, M. E.; "SBV Metric Accuracy", Space Control Conference 1997

von Braun, C.; "Space Surveillance Operations with the Space-Based Visible", Space Control Conference 1999

Table 1
SBIRS LOW : The Objective System for Space-Based
Space Surveillance FOC ~2007

•Natural Strengths for Space Surveillance:

Low Altitude Satellites

- Timeliness
Proliferated constellation
- Launch to Insertion Tracking
New Foreign Launch
from proliferated launch
sites
- Large Capacity for SOB
Objects
Gimbaled sensor on
proliferated constellation

• Natural Weaknesses for Space Surveillance:

- Small Objects
Lacks sufficient sensitivity
- Search Operations
Small field of view
- Deep Space Objects
Inherently down-looking,
lacks search rate and
sensitivity
- Efficiency
Small field of view

TABLE 2		
Year	SBV 1989	SBIRS Adjunct ~2007 (1999 Technology)
# of sensors	1	3
Sensitivity	15.5 vmag	17.3 vmag
Telescope	6 inch	9 inch
Quantum Eff.	27%	66%
Search Rate	100 sq °/hr	3,240 sq °/hr
CCD	420x420	2048x2048
Fov	1.4° x 1.4°	3° x 3°
Processing	10 MIP	200 MIP/sat
Gimbaled	No	Yes

Table 3
Summary of Maximum Gap Time in Simulation for
1565 Deep Space Objects

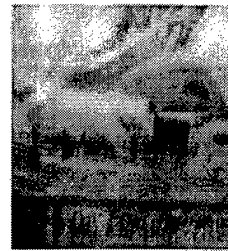
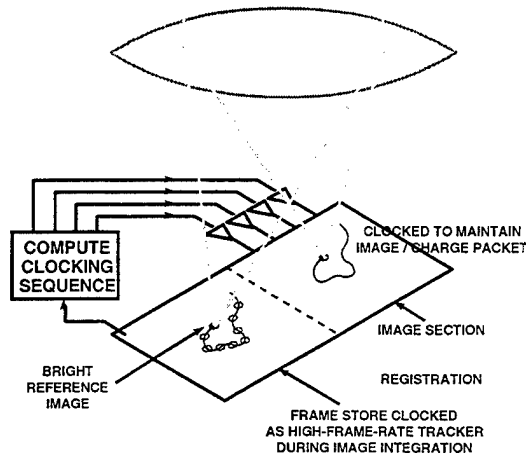
# DS Objects	# DS payload	Maximum Gap Time
1510	316	< 15 hours
29	3	15 - 24 hours
22	2	1 - 2 days
4	1	> 2 days

High
Eccentricity
Objects

Jitter Compensation: Demonstration of OTCCD

➔ Jitter compensation is critical
Improves metric accuracy
Reduces "settle" times

CCD CAMERA
BOUNCING ON A SPRING:



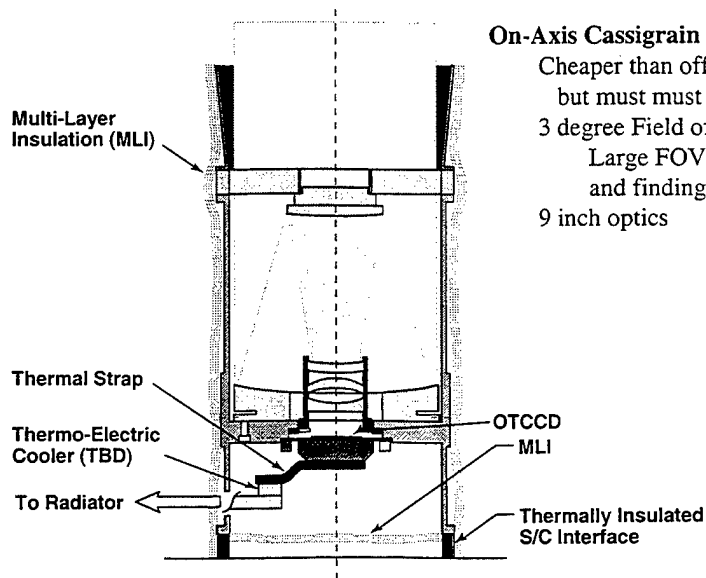
NO MOTION
COMPENSATION



WITH MOTION
COMPENSATION

Figure 1

Adjunct Telescope



On-Axis Cassigrain design

Cheaper than off-axis design,
but must look $> 90^\circ$ from Sun

3 degree Field of View

Large FOV critical for search operations
and finding "lost" objects

9 inch optics

Figure 2

Daily Sightings of Deep Space Population - 3 Adjunct Sensors

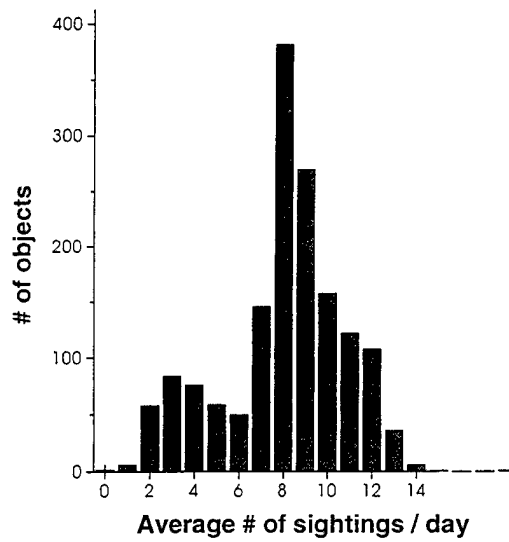


Figure 3

Maximum Gap Times for Deep Space Population - 3 Adjunct Sensors

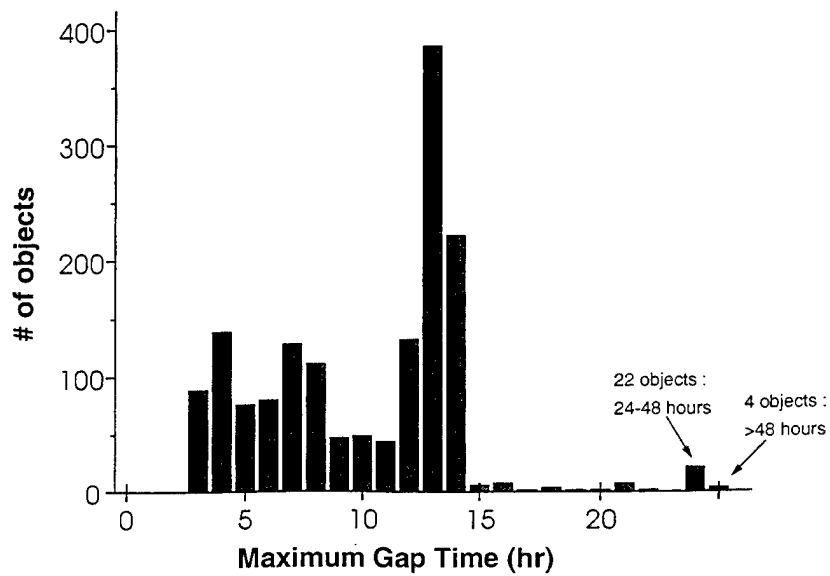


Figure 4

Appendix A

A method for calculating the limiting magnitude of the SBV has matched the SBV's demonstrated performance (Opar 1992), and is used to calculate the limiting magnitude achievable by the adjunct sensor. The variables listed below are pertinent to the calculation.

	Value	Note
SNR	4.12	Limiting signal to noise ratio, empirically determined
A_{Eff}	0.0268	effective area, m^2 , 9 inch optics, 17% obscuration by lens assembly
QE	0.66	quantum efficiency
T	0.72	transmission coefficient, due to 3 mirror bounces and 6 glass – air interfaces
N	5.85×10^8	photons / ($\text{m}^2 \text{ s arcsec}^2$), GEODSS upgrade chip value
k_f	0.66	“straddle” factor
T_d	0.5	Dwell time in single pixel, Same as exposure time, this is best case
T_{Exp}	0.5	Exposure time
α	5.27	single pixel Field of View, arcseconds
B_{vis}	22.0	background, Visual magnitudes, reasonable dark sky number
N_{DC}	10.5	electrons/second/pixel, dark current
σ_o^2	5	electrons/pixel, system noise

The result is a limiting magnitude of 17.3 visual magnitudes. The small detectable object detectable can then be calculated given these variable values:

ρ	0.33	reflectivity, typical values range between .2 and .45
A	$\pi(\text{radius})^2$	area of a sphere
ϕ	0.17	phase function for a diffuse sphere at a typical phase angle : 45 degrees

The resulting limiting radius of detection is 15cm, or a 30cm diameter object. Note that sensitivity will be worse for objects moving quickly, as the dwell time, T_d , will be reduced.

REPORT DOCUMENTATION PAGE

Form Approved
OMB No. 0704-0188

Public reporting burden for this collection of information is estimated to average 1 hour per response, including the time for reviewing instructions, searching existing data sources, gathering and maintaining the data needed, and completing and reviewing the collection of information. Send comments regarding this burden estimate or any other aspect of this collection of information, including suggestions for reducing this burden, to Washington Headquarters Services, Directorate for Information Operations and Reports, 1215 Jefferson Davis Highway, Suite 1204, Arlington, VA 22202-4302, and to the Office of Management and Budget, Paperwork Reduction Project (0704-0188), Washington, DC 20503.

1. AGENCY USE ONLY (Leave blank)		2. REPORT DATE 13-15 April 1999		3. REPORT TYPE AND DATES COVERED Project Report	
4. TITLE AND SUBTITLE Proceedings of the 1999 Space Control Conference				5. FUNDING NUMBERS F-19628-95-C-0002	
6. AUTHOR(S) L.B. Spence (Editor)					
7. PERFORMING ORGANIZATION NAME(S) AND ADDRESS(ES) MIT Lincoln Laboratory 244 Wood Street Lexington, MA 02420-9108				8. PERFORMING ORGANIZATION REPORT NUMBER STK-254	
9. SPONSORING/MONITORING AGENCY NAME(S) AND ADDRESS(ES) ESC Hanscom Air Force Base Bedford, MA 01730				10. SPONSORING/MONITORING AGENCY REPORT NUMBER AFSPC/DOY	
11. SUPPLEMENTARY NOTES This report is based on studies performed at Lincoln Laboratory, a center for research operated by Massachusetts Institute of Technology. The work was sponsored by the Department of the Air Force, AFSPC/DOY, under contract F-19628-95-C-0002. Papers appearing in this Proceedings were sponsored by multiple sources.					
12a. DISTRIBUTION/AVAILABILITY STATEMENT This document is available to the public through the National Technical Information Service, Springfield, VA 22161.				12b. DISTRIBUTION CODE	
13. ABSTRACT (Maximum 200 words) The seventeenth Annual Space Control Conference sponsored by ESC and co-hosted by MIT Lincoln Laboratory and the AF Research Laboratory was held on 13, 14, and 15 April 1999. The purpose of this series of conferences is to provide a forum for the presentation and discussion of space control issues. This <i>Proceedings</i> documents those presentations from this conference that were received in time for pre-conference publication. The papers contained were reproduced directly from copies supplied by their authors (with minor mechanical changes where necessary). It is hoped that this publication will enhance the utility of the conference.					
14. SUBJECT TERMS				15. NUMBER OF PAGES 210	
				16. PRICE CODE	
17. SECURITY CLASSIFICATION OF REPORT Unclassified	18. SECURITY CLASSIFICATION OF THIS PAGE Unclassified	19. SECURITY CLASSIFICATION OF ABSTRACT Unclassified	20. LIMITATION OF ABSTRACT Same as report		